Investigation of mesoscopic superconductivity and quantum Hall effect by low temperature Scanning Tunneling Microscopy

David Wander

THÈSE

Pour obtenir le grade de

DOCTEUR DE L'UNIVERSITÉ GRENOBLE ALPES

Spécialité : NANOPHYSIQUE

Arrêté ministériel : 25 mai 2016

Présentée par

David WANDER

Thèse dirigée par **Clemens WINKELMANN**, Université Grenoble Alpes
et codirigée par **Hervé COURTOIS**,Enseignant-chercheur, Université Grenoble Alpes
et co-encadrée par **Elke SCHEER**, Universität Konstanz
préparée au sein du **Laboratoire Institut Néel - CNRS**
dans **l'École Doctorale Physique**

Investigation de la supraconductivité mésoscopique et de l'effet Hall quantique par microscopie à balayage tunnel à basse température

Investigation of mesoscopic superconductivity and quantum Hall effect by low temperature Scanning Tunneling Microscopy

Thèse soutenue publiquement le **12 septembre 2022**,
devant le jury composé de :

Monsieur Stefan HEUN
DIRECTEUR DE RECHERCHE, CNR, Rapporteur
Monsieur Christophe BRUN
CHARGE DE RECHERCHE, CNRS, Rapporteur
Madame Alexandra PALACIO MORALES
MAITRE DE CONFERENCE, Université Paris-Saclay, Examinatrice
Monsieur Wulf WULFHEKEL
PROFESSEUR, Karlsruhe Institute of Technology (KIT), Examinateur
Monsieur Franck BALESTRO
PROFESSEUR DES UNIVERSITES, Université Grenoble Alpes, Président

Abstract

Since its development in the 1980s, the scanning tunneling microscope (STM) has become a workhorse in solid state physics. It offers a combination of atomically resolved topographical as well as spectroscopic information inaccessible by other means. In recent years, ultra-low-temperature STMs working at millikelvin temperatures have been developed to resolve smaller and smaller energy scales. In my thesis, I built such a setup operating at an effective temperature of 140 mK in a 50 mK refrigerator. Additionally, the setup is equipped with an ultra-high-vacuum preparation chamber operating at 2×10^{-10} mbar for controlling the sample surface on an atomic level.

After benchmarking this system, I show its first application on epitaxial monolayer $NbSe_2$, a material hosting exotic Ising superconductivity and being a great platform for investigating superconductivity in the two-dimensional limit. In combination with magnetic superstructures, topological superconductivity in form of Majorana zero modes is expected to arise. Being topologically protected from decoherence, these states are promising candidates for topological quantum computing.

Finally, I discuss another low-temperature STM study investigating the quantum Hall broken-symmetry orders in graphene. Under strong magnetic field, electrons are forced into flat bands which quenches their kinetic energy. Electron interactions can then induce a large variety of broken-symmetry states with distinct topological and lattice-scale orders. The nature of the ground state realized in standard sample systems has been unknown and intensely debated for more than a decade since all evidence stemmed from indirect transport measurements. In our study we exploit the ability to locally map the system's wave function combined with spectroscopic measurements to unambiguously identify the ground state order. We furthermore demonstrate the ability to explore the phase diagram by means of substrate-induced screening of the Coulomb interaction.

Résumé

Depuis son développement dans les années 1980, le microscope à effet tunnel (STM) est devenu un outil indispensable à la physique de la matière condensée. Il offre une combinaison d'informations topographiques et spectroscopiques à résolution atomique inaccessibles par d'autres moyens. Ces dernières années, des STM à ultra-basse température travaillant à des températures de l'ordre du millikelvin ont été développés pour résoudre des échelles d'énergie de plus en plus petites. Dans ma thèse, j'ai construit un tel dispositif fonctionnant à une température effective de 140 mK dans un réfrigérateur de 50 mK. De plus, le dispositif est équipé d'une chambre de préparation sous ultravide fonctionnant à 2×10^{-10} mbar pour le contrôle de la surface de l'échantillon à un niveau atomique.

Après avoir étalonné ce système, je montre sa première application sur une monocouche épitaxiale de $NbSe_2$, un matériau abritant une supraconductivité d'Ising exotique et constituant une excellente plateforme pour l'étude de la supraconductivité dans la limite bidimensionnelle. En combinaison avec des superstructures magnétiques, une supraconductivité topologique sous forme de modes zéro de Majorana est prédite. Étant topologiquement protégés de la décohérence, ces états sont des candidats prometteurs pour l'informatique quantique topologique.

Enfin, je présente une autre étude STM à basse température portant sur les ordres de symétrie brisée de l'effet Hall quantique dans le graphène. Sous un fort champ magnétique, les électrons sont forcés de se placer dans des bandes plates, ce qui annule leur énergie cinétique. Les interactions entre électrons peuvent alors induire une grande variété d'états de symétrie brisée avec des differents ordres topologiques et spatiales. La nature de l'état fondamental réalisé dans les systèmes d'échantillons standard est inconnue et fait l'objet d'un débat intense depuis plus d'une décennie, car toutes les preuves proviennent de mesures indirectes du transport. Dans notre étude, nous exploitons la possibilité de cartographier localement la fonction d'onde du système, combinée à des mesures spectroscopiques, pour identifier sans ambiguïté l'ordre de l'état fondamental. Nous démontrons en outre la possibilité d'explorer le diagramme de phase au moyen d'un écrantage de l'interaction coulombienne induit par le substrat.

Acknowledgements

Just like every big project, my PhD would not have been possible without the support and contribution of a multitude of people. Here I want to thank everyone who was directly implicated in my work, but of course many others supported me personally during the last four years without which I could not have accomplished this work either. I am deeply grateful to all those people as well.

First and foremost, I would like to thank my supervisors Clemens Winkelmann, Hervé Courtois and Elke Scheer for offering this PhD project as well as for their advice and support. A special thanks goes to Hervé for managing the QuESTech Marie-Curie training network that my project was part of and which enriched my PhD experience through additional training, internships abroad and which made me meet a great group of other PhD students and researchers.

I also want to thank the other PhD students and post-docs of my group. Thanks to my predecessor Alessandro de Ceccco for introducing me to the STM measurements and the functioning of the dilution fridge. Thank you to Rini Ganguly for working together with me on the STM measurements for more than a year. A big thank you also goes to Alvaro García-Corral, Danial Majidi, Efe Gumus and Bivas Dutta for the time we spent together and the discussions we had about physics and technical issues of our setups and experiments.
I also want to thank the internship students that worked with me on my project and invested their time and effort into its advancement: Thank you Keir Logan, Elisa Bossard and Corinna Fohn!
During the six months of down time of my setup, I was very lucky to be received by Benjamin Sacépé and Alexis Coissard from our QNES group at Institut Neel as a support of Alexi's project. This collaboration created a nice win-win situation and resulted in a great publication. Thank you very much for welcoming me this nicely and for the professional and efficient interactions we had.
I also want to acknowledge the discussions with the remaining members of the QNES team, specially with Pierre Mallet and Jean-Yves Veuillen.
In the context of the $NbSe_2$ project I also worked and discussed with Vincent Renard, Claude Chapellier and Matthieu Jamet from CEA Grenoble. Thank you for preparing the samples and for the discussions we had!
Similarly, I would like to thank Valérie Guisset, Philippe David and Johann Coraux for preparing a graphene on rhenium sample that allowed me to characterize the electronic temperature achieved in my STM setup.

Since my work was heavily focused on instrumentation, I also had plenty of interactions with all the technical services at the institute and received a lot of support from them.
An outstanding role played Stephanie Garaudée who managed an important part of the UHV related topics.
For all my work related to mechanics, I received great help from Laurent Del-Rey, Julien Jarreau, Denis Maillard and Didier Dufeu from the ExpE mechanical workshop. Thank you a lot for introducing me to 3D CAD, the use of the workshop machines and for helping me out readily whenever I came up with a new urgent problem to be solved. Another big thank you goes to Eric Eyraud for his advice and help concerning the Sionludi dilution fridge.

My work also included a significant part on electronics and electronic noise filtering. For this, I collaborated with the electronic workshop of the Institute, specially with Jean-Luc Mocellin and Olivier Exchaw. Thank you for your help!
I would also like to thank the SERAS mechanical workshop of CNRS for their sporadic support when assembling heavy parts of the setup, for fabricating a few mechanical pieces and for helping me clean the contaminated UHV parts delivered by Axess Tech.
Even though it finally did not lead to fruitful results, I also spent some time in the clean room, fabricating nanostrucutred samples. Thanks to the Nanofab team for their help during that time. A special thank you goes to Simon le Denmat, for his help with the ambient AFM systems which where very helpful for characterizing my STM samples prior to measurement.
I would also like to thank the financial service of the Institute, namely Angelique Simoes, for treating all my order requests whenever I had to buy components for the setup.

I also want to thank the people who welcomed me warmly during the two internships I did during my PhD project. Thank you to Naveen Shetty, Hans He, Samuel Lara-Avila and Sergey Kubatkin at Chalmers and to Khaled Karrai and Constanze Metzger at attocube.

Last but not least, I appreciate the work and invested time of the reviewers and jury members of my thesis for careful revision of my manuscript and interesting discussions during the defense.

Finally, the entire project required a substantial amount of money. I therefore want to acknowledge the generous funding from the following agencies: This project has received funding from the European Union's Horizon 2020 research and innovation programme under the Marie Skłodowska-Curie grant agreement No 766025 and from the Agence Nationale de la Recheche in the framework of the JOSPEC project. The work on graphene in the quantum Hall regime has received funding from the European Union's Horizon 2020 research and innovation programme ERC grants QUEST No. 637815 and SUPERGRAPH No. 866365.

List of abbreviations

AFM	Atomic Force Microscope
ARPES	Angle-Resolved PhotoEmission Spectroscopy
BCS	Bardeen Cooper Schrieffer
BLG	BiLayer Graphene
CAF	Canted Anti Ferromagnetic (order)
CDW	Charge Density Wave
DFT	Density Functional Theory
F	Ferromagnetic (order)
FFT	Fast Fourier Transform
FWHM	Full Width at Half Maximum
KB	Kekulé Bond (order)
KD	Kekulé Distortion
LL	Landau level
MBE	Molecular Beam Epitaxy
MZM	Majorana Zero Mode
RHEED	Reflection High Energy Electron Diffraction
RMS	Root Mean Square
SOC	Spin Orbit Coupling
SPM	Scanning Probe Microscope
STS	Scanning Tunneling Spectroscopy
TMD	Transition Metal Dichalcogenide
TSP	Titanium Sublimation Pump
UHV	Ultra High Vacuum
YSR	Yu Shiba Rusinov

Contents

1 Introduction

With their first observation of the characteristic exponential current decay with tip-sample distance on March 16th 1981, Binnig and Rohrer lay the foundations for scanning tunneling microscopy (STM), a technology that should revolutionize surface science and solid state physics in the following decades.
Even though their initial motivation was to perform local tunneling spectroscopy, they soon realized the ability of this technique to record atomically resolved surface topography images[1]. The first application became indeed microscopy because of the increased technical difficulty when working at low temperatures required for high resolution spectroscopy measurements. The big breakthrough which incited the interest of large parts of the surface science community was the first real space observation of the 7x7 reconstruction of a silicon surface, concluding a long standing debate in the community[2]. Soon after, Tersoff and Hamann[3] provided the first theory of the tunneling processes in an STM geometry, giving the method a more solid physical foundation and showing that the STM can image the local amplitude of quantum mechanical wave functions in real space. In the years after and the decades since then, the technology has advanced tremendously and has been applied to a vast field of different applications. Among those, there are measurements of chemical reactions and catalysis on surfaces[4,5], low temperature STM for spectroscopy[6,7], combined scanning electron microscopy and STM[8] with multiple tips for four probe measurements[9], spin-polarized STM[10–13], STM in air[14] and water[15] etc. At the same time, the STM is not limited to observing the surface. It can also be used to modify it in a controlled way. The most prominent examples for this are atom or molecule displacements by means of the tip. This can be used to form artificial structures, such as quantum corrals[16] or magnetic chains for the quest of Majorana zero modes[17].

Motivated by quantum effects occurring on sub-milli-electron-volt energy scales, one branch of the STM developments aimed at operating at lower and lower temperatures for reducing the spectroscopic resolution limitations imposed by the smearing of the Fermi distribution at finite temperature. Our group was one of the pionieers in this field, demonstrating a dilution temperature STM featuring atomic resolution and an effective electron temperature of 210 mK in 2001[18]. A few years later, even lower electronic temperatures of around 65 mK have been reported by the Quantronics group in Saclay[19] and in 2013 38 mK in Stuttgart[20].

Since our group is coming from the device and transport community, the first two versions of our millikelvin STM were not equipped with in-situ sample preparation capabilities and were just operated in the cryogenic vacuum of around 10^{-6} mbar. This is sufficient for the study of a few very robust systems such as graphene. However, many other interesting materials oxidize or show other degradation at ambient conditions, requiring in-situ surface preparation. The additional advantage is that the precise control of the surface state and atomically clean samples make good quality measurements a lot easier since one is no longer bothered by residual dirt in the tunnel junction.

In **Chapter 2**, I present the main task of my PhD project which was building the third version of our millikelvin STM, this time operating inside an ultra-high-vacuum (UHV) environment with in-situ sample and tip preparation capabilities. Implementing this required massive

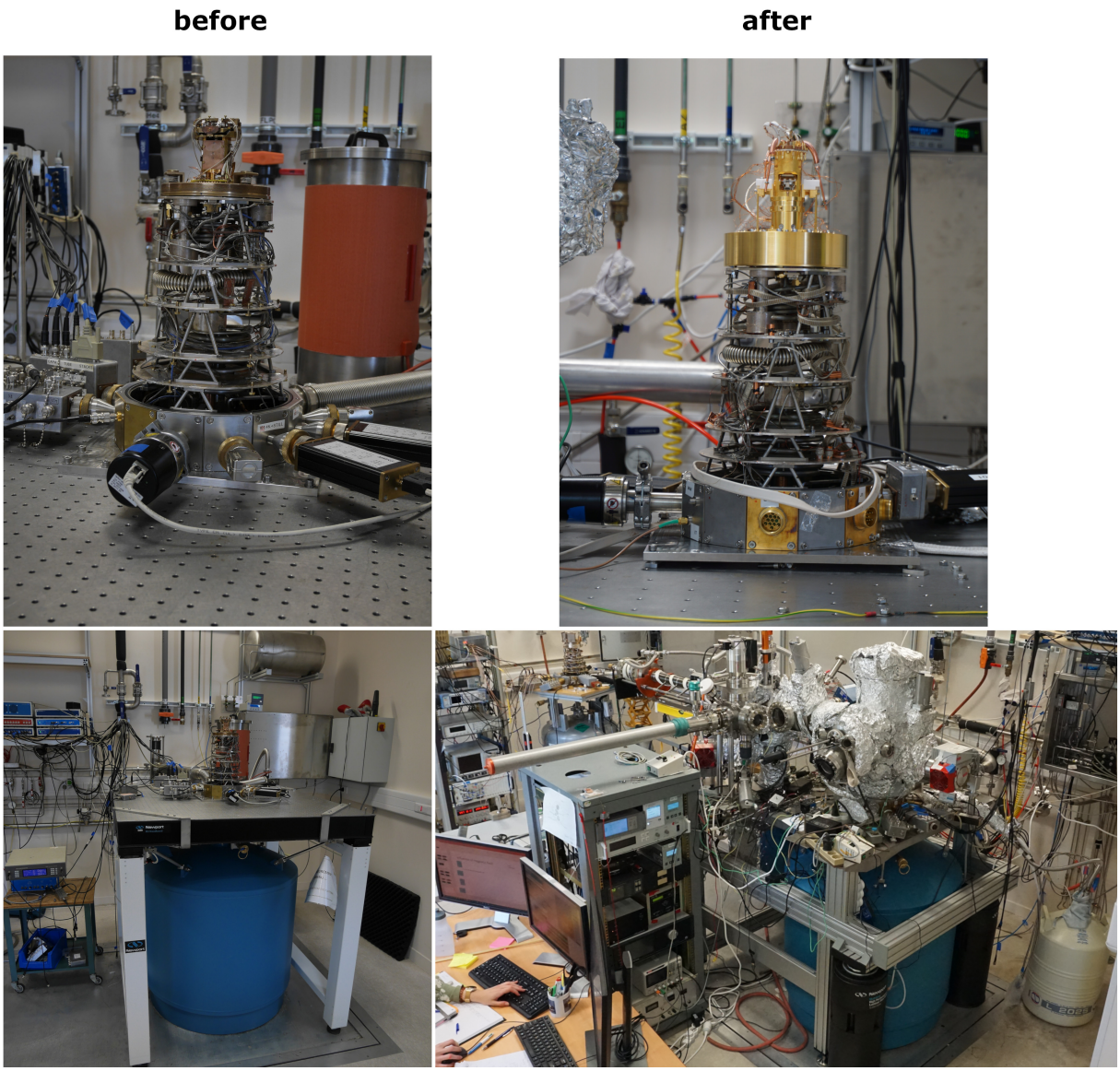

Figure 1.1: Comparison of the setup before and after my PhD. Both, the inside (top) as well as the outside (bottom) of the vacuum chamber have evolved tremendously. The only part that stayed the same is the dilution refrigerator.

changes of the whole setup, as illustrated in Figure 1.1. The changes go from the replacement of the STM measuring head which, in its old version, was not compatible with in-situ sample exchange via the redesigning of the radiation screens to allow access to the sample under vacuum to the construction of the UHV surface preparation chamber attached to the dilution fridge. Finally, the weight of the entire apparatus increased by a few hundred kilograms requiring a new suspension system. We used this occasion to also redo the entire wiring of the setup, adding radio frequency filters to improve the effective sample and tip temperature. As we will see in Section 2.6.2, we now achieve approximately 140 mK. Furthermore, we added an RF line and antenna which allows irradiating the tunnel junction with RF photons for photon-assisted tunneling or electron spin resonance measurements.

In **Chapter 3**, we then turn to the first scientific project in this new setup: epitaxial monoalyer $NbSe_2$ on bilayer graphene. This material hosts exotic Ising superconductivity and is a great platform for studying superconductivity in the two-dimensional limit. Given its strong

spin-orbit-coupling, it is also a good building block for engineering superconductor-magnetic hetero-structures in which topological superconductivity is expected. We are part of a consortium that just started working on this system. In particular, we obtained the first monolayer $NbSe_2$ samples grown at CEA Grenoble. Therefore the first task presented here is the characterization of the grown films, to compare them to what has been reported before and to gain as much understanding of the occurring features and effects as possible. As we will see, the quality of the films is good. The sample mostly behaves as expected and incites for further studies including magnetic impurities.

In **Chapter 4**, I finally present results obtained in a different STM setup. Here we did not work at extremely low temperatures but instead, at large magnetic fields of up to 14 T. Under these conditions, the energy spectrum in graphene condenses into flat bands which quenches the electron's kinetic energy. Inter-electron interactions can then induce a large variety of broken-symmetry states with distinct topological and lattice-scale orders. The nature of the ground state realized in standard sample systems has been unknown and intensely debated since all evidence stemmed from indirect transport measurements. In our study, we exploit the ability to locally map the system's wave function combined with spectroscopic measurements to unambiguously identify the ground state. We furthermore demonstrate the ability to realize different ground states by means of substrate induced screening of the Coulomb interaction.

2 Dilution-Temperature Ultra-High-Vacuum Scanning Probe Microscope

Scanning Probe Microscopies (SPM), and in particular Scanning Tunneling Microscopy (STM), are very powerful tools for the study of structural and electronic properties of a wide range of samples. In contrast to most other measurement techniques which usually measure an average over large sample areas, SPM gives local access on the (sub) atomic scale. The STM's capability of directly imaging wave-functions of quantum systems together with its micro electron-volt spectroscopic resolution has made it a workhorse in solid state physics. In this work, we are interested in studying quantum systems and interactions in the deep sub-meV regime, which is why we install our STM within a dilution temperature refrigerator operating at 50 mK.

In this chapter, I will describe our Dilution Temperature Scanning Probe Microscope setup. Building this machine, starting from an existing "Sionludi" dilution fridge, was one of the main tasks of my PhD project.

After a short review of previously built ultra-low temperature SPMs in Section 2.1, we proceed with a brief overview of the full setup in Section 2.2. We will then take a more detailed look at its four main building blocks: the Ultra-High Vacuum (UHV) surface preparation chamber in Section 2.3, the table-top dilution refrigerator in Section 2.4, the wiring we designed for low noise measurements in Section 2.5 and finally the Scanning Probe Microscope and its performance in Section 2.6.

Contents

2.1 State of the art

As stated in the introduction, our goal is to study quantum physics in mesoscopic systems on the local scale. Of particular interest is the combination of superconducting materials with (atomic scale) magnetic impurities which give rise to interesting interaction phenomena such as the Kondo effect and the formation of Yu-Shiba-Rusinov states. Probing this with a Scanning Tunneling Microscope and mapping out spatial variations on the atomic scale will give complementary information to transport measurements and therefore allow us to better understand the underlying physics.
From an experimental point of view, these experiments require a setup providing:

- dilution temperatures well below 1 K, for μeV-range spectroscopic resolution and the study of superconductors with low critical temperature
- preparation capabilities for surface control on the atomic level
- ultra-high vacuum pressures in the 10^{-10} mbar range for the conservation of the pristine sample surfaces
- low vibration levels for atomically resolved imaging

In order to better understand the design choices we made for our setup, let us take a brief moment to review the state of the art of ultra-low-temperature UHV STMs fulfilling these requirements.
Starting with the ultra-low temperature aspect, the first 50 mK STM was built at the AT&T Bell Laboratories in 1991 [21] and was used to characterize $NbSe_2$ by scanning tunneling spectroscopy. The published spectrum (Figure 3.1 a)) shows feature widths on the order of 500 µeV which is much larger than the thermal broadening of $3.5k_BT = 15\,\mu eV$. Even though they did not publish a detailed description or characterization of their setup, this probably means that their electronic (tip) temperature was much higher than the 50 mK base temperature. In the years after, people improved the spectroscopic resolution and thus the corresponding effective temperature to 210 mK [18] in 2001, 65 mK in 2007 [19] and finally 38 mK in 2013 [20]. The key elements for reaching these low electronic temperatures are:

- good thermal anchoring of the STM and all wires going down to the STM,
- passing all entering signals through low pass filters to remove picked up high frequencies,
- avoiding bias voltage fluctuations by avoiding ground loops or by actively compensating them,
- shielding the sensitive wires (bias, current, z-tube).

At temperatures below 1 K interactions with the electromagnetic environment of the tunnel junction described by the $P(E)$-theory as well as single electron charging effects leading to charge noise become significant compared to the thermal resolution limit. The precise temperature where this becomes dominant depends on the tip-sample capacitance and therefore on the shape of the tip, but in most cases this happens above 100 mK [22]. The $P(E)$ and the charging noise decay much slower with temperature than the thermal smearing of the Fermi distribution. Cooling to temperature far below 100 mK therefore only results in little improvements of the spectroscopic resolution. For the vast majority of applications, including our studies, 100 mK are sufficient.
A common way of characterizing the spectroscopic resolution is to measure the density of states of a (BCS) superconductor as it is shown in Figure 2.1. At the gap edge, the BCS density of states features a step from zero conductance to the infinitely high coherence peak. In a real experiment, this sharp feature is broadened by temperature, bias noise, the effect of the environment according to $P(E)$ theory and gap anisotropy of the superconductor. Since they all

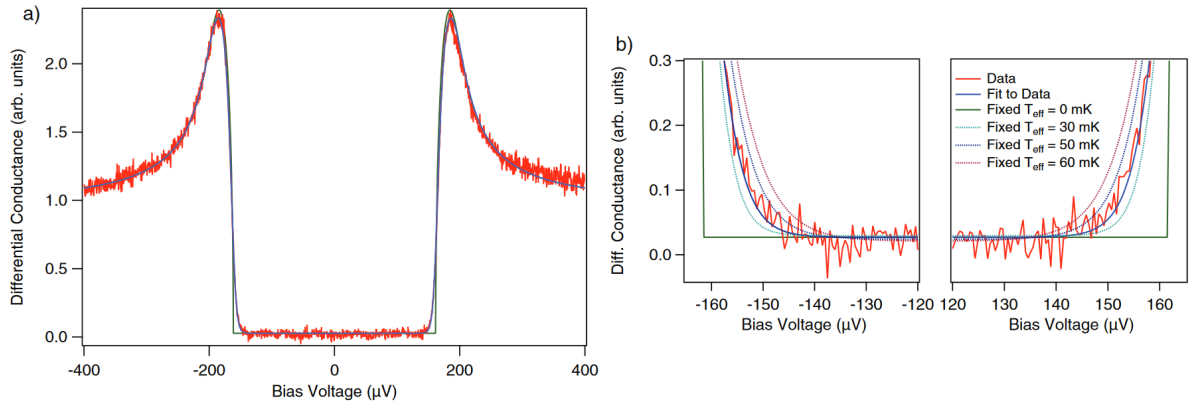

Figure 2.1: Tunneling spectroscopy of an Al tip on Cu (111) measured at 15 mK for bench-marking purposes. In red the measured data, in green a 0 K Maki theory. Dashed lines: Maki theory broadened by a finite effective temperature. The fit to the data yields 38 mK. Adapted from Assig et al.[20].

contribute in a similar manner, we quantify the sum of these effects in terms of an effective temperature, which is generally higher than the physical temperature. Pair breaking caused by spin-orbit coupling limits the height of the coherence peaks to a finite size, but leaves a sharp onset of the conductance at the gap edge, as can be seen by the green 0 K theory line in Figure 2.1 b).

When combining ultra-low temperatures and ultra-high vacuum, one of the biggest difficulties is implementing a reliable mechanism for sample and tip exchange. In the measurement position, the STM is inside the hermetically closed radiation screens and potentially surrounded by a big coil and therefore not well accessible from the outside. The most widely used strategy consists in top- or bottom-loading. For this, a long vertical translator is connected to the cryostat along its central axis. The radiation screens are equipped with a hole that can be opened and closed by shutters. For accessing the STM, the shutters are opened and usually the entire STM head is removed from the dilution fridge and brought to a more accessible UHV chamber attached above or below the cryostat. An example for such a setup is the ULT STM at NIST shown in Figure 2.2 a). The disadvantage of this design is that the length of the translator and the cryostat add up and result in a very tall (> 7 m) setup. Another, much less common strategy for ULT STMs is side loading, implemented at KIT as shown in Figure 2.2 b). There, the openings for accessing the STM are implemented in the lateral walls of the cryostat. Due to the curved surface, this is a bit more challenging than for the top-loading approach. Additionally, the STM still needs to be displaced slightly to leave the coil surrounding it in the measurement position. However, the big advantage is that this lateral access allows for a much more compact design of the overall system, which is why their entire setup fits on a single table and into a standard laboratory room.

The second big difference between the two setups shown in Figure 2.2 is the vibration damping system. The NIST system (a) relies on inertial damping. There, the STM is rigidly connected to the dilution fridge, which itself is mounted on a 6 t granite table. This table is suspended by air dampers, standing on another, even bigger, concrete slab of about 110 t which is also suspended by air dampers. The latter has external dimensions of about 4.3 m $\times$ 5.6 m $\times$ 3.1 m and therefore already occupies a full room on its own. Nevertheless, plenty other setups have been built following the same strategy[23–26]. The KIT system on the other hand just uses a single air damping system to suspend the UHV chamber and the dilution fridge in combination with a spring suspension of the STM inside the dilution fridge. Nevertheless, they find sufficiently low vibration levels of below 300 fm/$\sqrt{\text{Hz}}$. Once again, this design makes the system much more

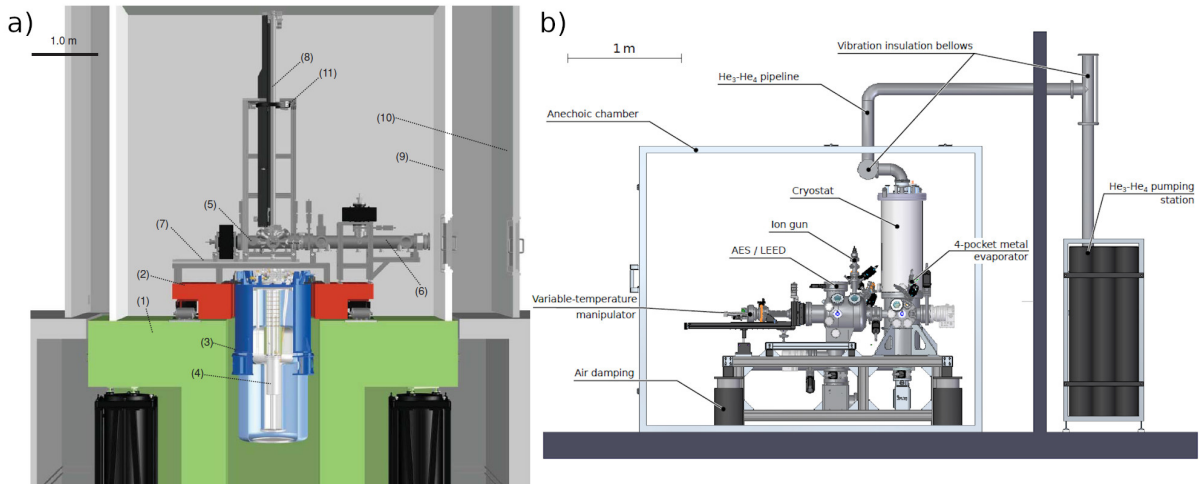

Figure 2.2: Two different design schemes for ULT UHV STM setups. a) Cross-sectional view of the NIST STM which uses a top loading mechanism and an inertial vibration damping system. (1) 100 t concrete slab, (2) 6 t granite table, (3) cryostat, (4) dilution insert, (5) UHV chamber, (6) interlab vacuum line, (7) rails for moving the UHV chamber, (8) vertical translator for top-loading of the STM, (9) & (10) acoustic enclosure. Adapted from [27]. b) The mK setup at KIT using a side-loading mechanism and a spring suspension of the STM to allow for a much more compact design. Adapted from [28].

compact and imposes much less constraints on the building where the setup can be placed in. Since a few years, ULT UHV STMs are now also available commercially. The only manufacturer so far is UNISOKU Co., Ltd. from Japan. Their USM1600 and USM1600J reach a base temperature of about 40 mK and can be equipped with different magnetic coils, up to 15 T. The guaranteed working pressure in the preparation and observation chamber is 3×10^{-10} mbar. Oddly, in their brochure, they only specify a energy resolution of < 1 meV, which corresponds to an effective temperature of about 3.3 K and could be reached even with a Joule-Thomson STM.

In the historical perspective, the first ultra-low temperature STMs were not UHV compatible. When adding in-situ UHV sample preparation using a top-loading mechanism, the setups grew a lot in size, occupying most of the time two stories of a building. In the last couple of years, developments now go to more compact side-loading designs. With our development, we want to continue this trend. Exploiting the ultimate compactness of the "Sionludi" dilution refrigerators developed in Grenoble, we aim at an even smaller footprint than the KIT setup. Compared to the commercial systems we also cut the price by a rough factor of two.

2.2 Overview

An overview of the setup is shown in Figure 2.3. Let us go through its different parts following the work flow of a standard experiment. First, the sample has to be introduced into the setup through the load-lock highlighted in red on the left side of Figure 2.3. Once the vacuum in the load-lock is sufficiently low (usually in the 10^{-8} mbar range), the sample can be transferred to the main preparation chamber, highlighted in green. At this position, we can make use of the techniques described in the next section to prepare the sample's surface state under vacuum conditions down to 2×10^{-10} mbar. Then, the sample is transferred to the microscope that is mounted inside the dilution fridge (highlighted in orange) using the long manipulator of

the preparation chamber as well as the wobble stick of the fridge. Sample transfers can be performed while the microscope is at 4 K. During the transfer process it heats up to about 30 K but can be brought to base temperature within roughly 2 h. Thus, it is possible to do up to three preparation and measurement cycles per day, which can be interesting while optimizing a preparation recipe.
The liquid helium required for the operation of the refrigerator is stored in the blue dewar below the table. It can accommodate about 250 l of liquid, enough for more than a week of operation. Compressed air dampers in the legs of the table suppress unavoidable building vibrations.

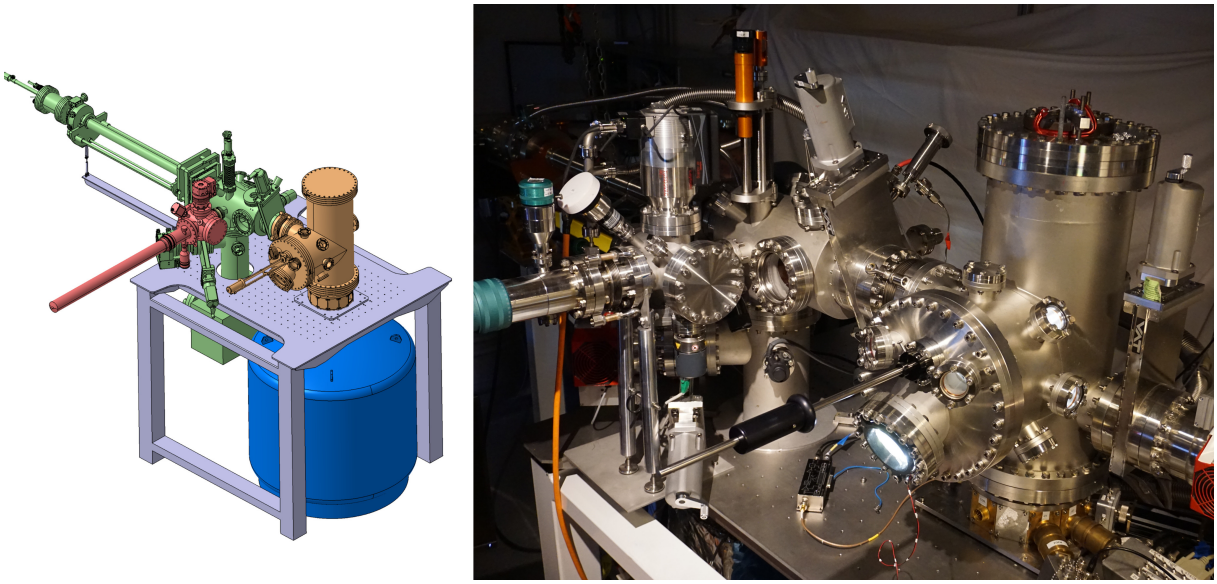

Figure 2.3: Overview of the dilution temperature UHV SPM setup. Left: 3D model showing in green the surface preparation chamber reaching base pressures of 2×10^{-10} mbar, in orange the dilution fridge operating at 5×10^{-9} mbar and 50 mK and in red the load-lock usually kept at 1×10^{-8} mbar. Furthermore, you see the ^{4}He reservoir in blue and the optical table with compressed air dampers in each leg in grey. Right: photo of the real setup.

2.3 In-situ Ultra-High Vacuum preparation chamber

Solving the Schrödinger's equation for a simplified 1D tunnel barrier, one finds that the current flowing through this tunnel junction decays exponentially with the barrier thickness i.e. the tip-sample distance. The characteristic decay length for common materials is on the order of 50 pm which implies that mainly the first atomic layer of the sample is probed. While this allows us to be extremely sensitive to surface effects and probing the properties of 2D materials, it also implies that a mono-layer of impurities heavily disturbs the tunneling signal. On top of that, impurities on the surface can alter the electronic properties of the sample over a significant length scale[29]. Finally, most of the elementary superconductors oxidize quickly and form a non-conducting oxide layer when exposed to air[30]. For these reasons, after preparing the sample's surface, it is of utmost importance to protect it against impurities and oxidation until the very end of the measurements. The only way of achieving this is by evacuating the entire system and by preparing the samples *in-situ*. To get an idea of the pressure we need to work at, one can calculate the time τ it takes for the sample surface to be covered by a monolayer of impurities. Using the simplified assumption that all impinging molecules adsorb and none

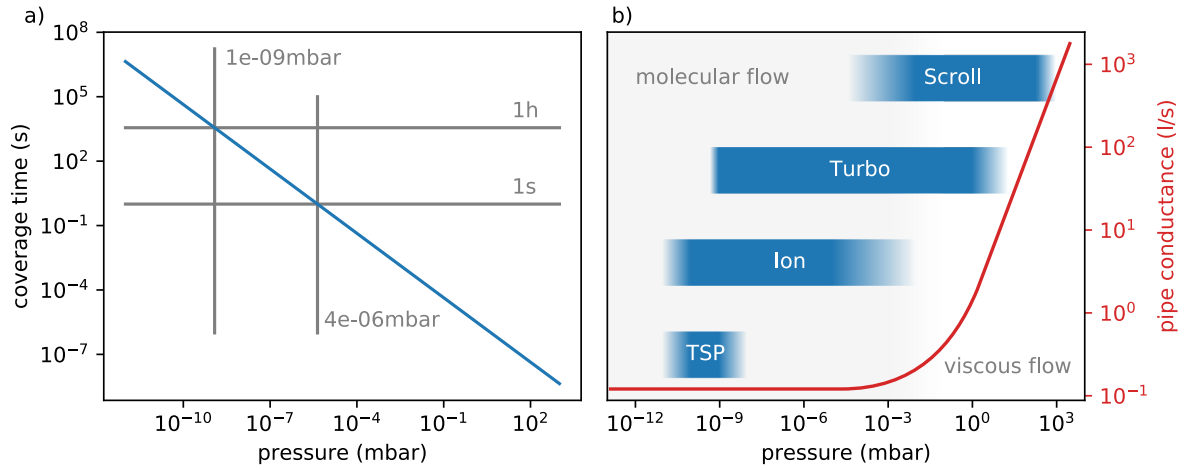

Figure 2.4: a) Motivation for working under UHV conditions: time to cover the sample surface with one monolayer of adatoms, assuming 100 % sticking probability. For keeping a clean surface during the entire manipulation time of several hours, a pressure of less than 1×10^{-9} mbar is required. b) Operating pressure ranges for the pumps used in our setup and the pressure dependence of the pipe conductance, here for $l = 100\,\text{cm}$ and $d = 1\,\text{cm}$.

desorb, this time is given by[1]

$$\tau = \frac{\sqrt{2\pi m k_B T}}{P A_m} \,. \tag{2.3.1}$$

It depends on the molecular mass m, the temperature T and the pressure P of the gas as well as on the surface area A_m covered by each adsorbed molecule. This relation is depicted in Figure 2.4 a) for Nitrogen at room temperature. It shows that for a working time of about one hour, the pressure has to be in the range of 1×10^{-9} mbar or lower.
Of course, our measurements take more than one hour and the working temperature is usually 4 K or less. According to Equation 2.3.1, at lower temperatures the time to cover the surface is even smaller, however, inside the SPM head, the sample is surrounded by cold surfaces which act as strong cryopumps. Hence, the pressure in the base-temperature volume is orders of magnitude lower, giving us plenty of time to perform our measurements. This means, that the relevant time are the about 30 min between the preparation of the sample and its insertion into the cold SPM. In conclusion, we have to work in the 10^{-10}-10^{-9} mbar range. In the next section, I will detail how we achieve these pressures.

2.3.1 Achieving Ultra-High Vacuum

Differently from what one could naively think, the main task of the pumps used in a ultra-high vacuum system is not to remove the laboratory air that was trapped in the chamber when closing it but to fight against the constant flux of new gas entering it. This gas can come from leaks, diffusion, permeation and desorption which will be discussed more in detail later on. Each of this sources contributes with its incoming particle flux Q, measured in $\text{mbar}\,\text{l}\,\text{s}^{-1}$. Opposed to that, we have the pumps removing particles with their total pumping speed $S = \frac{dV}{dt}$ measured in $\text{l}\,\text{s}^{-1}$. This defines the ultimate reachable pressure

$$p = \frac{Q_{tot}}{S} = \frac{Q_L + Q_{perm} + Q_{des}(t) + Q_{diff}(t)}{S}. \tag{2.3.2}$$

[1] for a full derivation see Appendix A

Let us have a brief look on the different particle sources and how to minimize their fluxes.
Q_L: Leaks in the vacuum chamber are the most obvious source of incoming particles. They often occur on weld seams and on the seals of flanges. However, they can be found and eliminated using a helium leak detector. Therefore, in a running system that was properly tested, leaks should not contribute significantly. Apart from leaks to the outside environment, there are also virtual leaks. These are closed volumes, e.g. behind a screw in a blind hole, which are inside the vacuum chamber but can not be pumped out properly. They slowly emit their gas through small gaps leading to an enormously increased pumping time. This kind of virtual leak has to be avoided by carefully designing all parts inside the vacuum system.
Q_{perm}: Permeation through the walls of the vacuum system is mainly possible for small molecules like Hydrogen and Helium. However, due to their low abundance in the laboratory air, this effect is negligible for UHV systems.
Q_{des}: Desorption of molecules that are adsorbed on the surfaces of the vacuum system is the dominating process slowing down the pumping of a recently opened vacuum system. The main contribution comes from the unavoidable water film that quickly forms on surfaces exposed to air. However, also finger prints or grease residues from the manufacturing process can be problematic, which is why all parts have to be cleaned and handled carefully. The desorption rate depends on the vapor pressure of the material which can be increased tremendously by heating the entire system. This process is called bake-out and is indispensable for reaching pressures in the 10^{-10} mbar range in a reasonable time on the order of a few days. Consequently, all parts of the vacuum system that can not be removed for the bake-out have to be designed to sustain elevated temperatures of at least 120 °C.
Q_{diff}: Diffusion to the surface and subsequent release of elements absorbed in the materials used in the vacuum system, e.g. Hydrogen and CO in stainless steel, is the main source of gas in a clean, baked UHV system. It has to be minimized by choosing the proper materials such as stainless steel, glass and ceramics. Materials with a high vapor pressure and materials that can absorb volatile compounds such as plastics, organic materials but also some metals like Zinc and Lead have to be avoided. Since the diffusion is a slow process, its emission rate decreases very slowly over several months. The ultimately unavoidable source is hydrogen from stainless steel, which can be reduced by a high temperature annealing of the chamber before assembly[31]. However, this requires special furnaces, increases the price and is dispensable for reaching 10^{-10} mbar.

Now that we know through which processes gas can intrude into the vacuum system, let us have a closer look on how to remove it from there. Since we are reducing the particle density in our setup by 13 orders of magnitude compared to atmospheric pressure, various properties of the gas are changing on the way down to the ultimate pressure. For this reason, no single pump exists that could cover the full range from room pressure down to 10^{-10} mbar. We rather have to use several different pumps, using different working principles.
The first stage is the fore pump, which works based on the spatial compression of the gas. There are several technical implementations like rotary vane, diaphragm, screw, roots or scroll pumps. For a UHV system it is highly recommendable to use a dry pump, i.e. a pump that does not need any oil for greasing etc. We opted for a scroll pump[2] which is a dry pump based on two interleaving scrolls for compressing the gas. Its main operation range is from 1 bar to about 1×10^{-3} mbar which corresponds roughly to the viscous flow regime, depicted in Figure 2.4 b). In this regime, the particle density is still high enough to have a mean free path smaller than the size of the system. This implies that particles mainly scatter with one another and like this

[2] Agilent Technologies IDP-7; 120 l/s; ultimate pressure 4×10^{-3} mbar

quickly propagate pressure differences. Thus, by pumping at one point, one can "suck" out the gas from the entire volume.
Things drastically change when further lowering the pressure to the point where the particle's mean free path becomes much larger than the system's dimensions. In this molecular flow regime, particles basically only scatter at the chamber walls. A pressure gradient generated by a pump no longer leads to a force on a single molecule, driving it towards the pump. The only effect of the pump is then to remove particles from the system that, through random scattering events, happen to arrive at its input. This has severe implications for conductances of pipes connecting the pumps with the main chamber. For viscous flow, the conductance of a plain, straight pipe for air at 20 °C is

$$C_{\text{pipe,vis}} = 1.35\frac{d^4}{l}\overline{p}$$

with the diameter d in cm, the length l in cm and the mean pressure $\overline{p}$ in Pa. Whereas for molecular flow it is

$$C_{\text{pipe,mol}} = 12.1\frac{d^3}{l}$$

with d and l in cm. The difference becomes easier to grasp when plotting the conductance as a function of p, as it is done in Figure 2.4 b). Hence, the molecular conductance of a pipe is orders of magnitude smaller than its conductance at atmospheric conditions in the viscous regime. As a consequence, all pumps that will be described in the following and which work in the molecular flow regime have to be placed as close as possible to the vacuum chamber in order not to loose a big part of their pumping speed by the pipe connecting it to the chamber.
The next pump with which, in combination with a bake-out of the chamber, pressures in the range of 5×10^{-10} mbar can already be reached, is the turbo-molecular (or just turbo) pump[3]. Its main component is a set of quickly (1000 rpm) rotating rotor blades. These blades are inclined such that when they hit a molecule, it gets a kick toward the outlet of the pump. Between adjacent rotating blades, there is a static stator blade inclined the opposite way, redirecting the molecule's radial velocity into an additional outward velocity. The compression of such a pump increases strongly with its rotation speed and with the molecular mass of the gas. This implies that light gases such as Hydrogen and Helium can not be efficiently removed with this type of pump.
Pumping Hydrogen can be accomplished with the last two pumps installed on our setup. The first of them is the Ion-getter-pump[4]. Unlike the scroll and the turbo-molecular pump, this pump is not a gas-displacement but a gas-binding pump. It usually consists of a stainless steel cathode and a titanium anode on which a high voltage of several kV is applied. Through field emission, electrons are emitted from the cathode and accelerated by the field. If these electrons happen to hit a molecule, they ionize it. The then charged molecule gets accelerated by the strong field and crashes into the titanium anode. This has two effects: first, due to its high energy, the ion can be implanted deeply into the titanium and be bound due to this effect. On the other hand, the impinging molecules sputter off the top titanium layers, creating a clean titanium surface. This surface is chemically very reactive and can bind most of the common gasses in a UHV system (H_2, CO, CO_2, N_2, O_2 etc.). Another big advantage of this type of pump is that it does not use any moving components. For this reason, it does not cause any vibrations and can keep running while vibration sensitive STM measurements are performed.
The last pump we use is a titanium sublimation pump (TSP). It also exploits the chemical reactivity of a clean titanium surface which is created by sublimation from a heated titanium

[3] Pfeiffer Vacuum HIPACE 300; 260 l/s; ultimate pressure $< 5 \times 10^{-10}$ mbar
[4] Agilent Technologies VacIon Plus 300; 240 l/s; ultimate pressure $< 1 \times 10^{-11}$ mbar

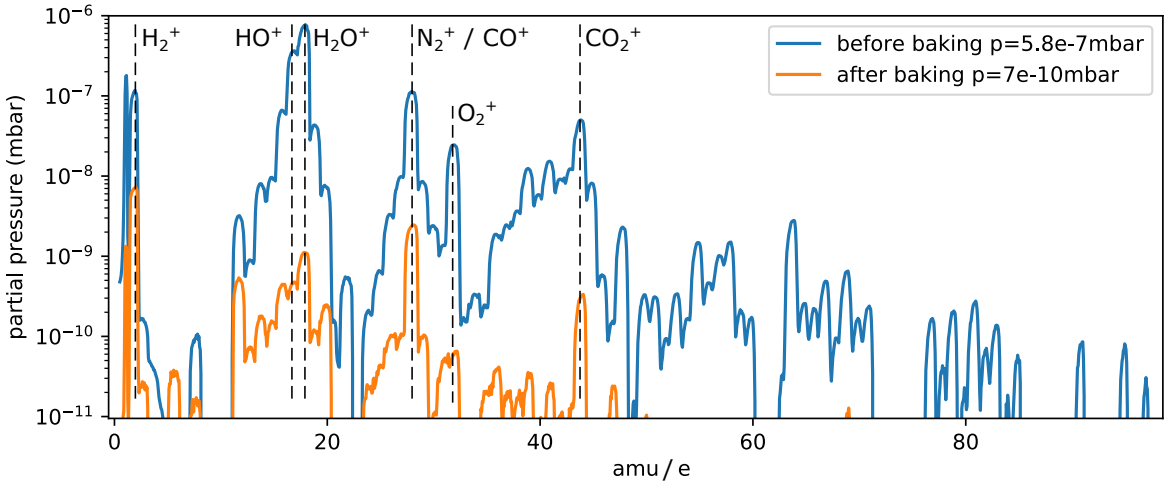

Figure 2.5: Exemplary RGA spectra recorded before (blue) and after (orange) the baking of the preparation chamber. Before baking the H_2O^+ peak is dominant. After baking the H_2 from the stainless steel constitutes the main contaminant. Since the RGA is not calibrated, the absolute values of the partial pressures are not correct. Nevertheless, for our purposes, relative values are sufficient.

filament. The walls of the pump can be cooled with liquid nitrogen which increases the reactivity of the titanium and makes it act as a cryo-pump as well.
For effective troubleshooting and for making sure the pumping works as expected, it is very helpful to know the composition of the gas inside the vacuum system. This can be measured with a residual gas analyzer (RGA). It ionizes the gas with electrons emitted from a filament. The beam of ions is then accelerated and shaped before it passes through a quadrupole mass filter that allows only ions with a specific ratio of $\frac{m}{q}$ to pass. At the end, the ion flux is measured with a Faraday cup or an electron multiplier. Finally, full mass spectra can be recorded by changing the voltages applied to the quadrupole which tunes the $\frac{m}{q}$ ratio allowed to pass the filter. The ionization stage of the RGA does not only charge the molecule, it can also crack it into its fragments. For this reason, one molecule usually generates a pattern of several peaks with a precise ratio of the peak amplitudes. This is a unique fingerprint, which allows to disentangle the contributions of several gases present in the chamber.
Two exemplary spectra of our chamber before and after baking are plotted in Figure 2.5. As mentioned above, before baking, the water adsorbed on the surfaces is the main contributor to the resiudal gas. The relevant peaks it generates are the H_2O^+ peak at 18 amu/e and the HO^+ peak at 17 amu/e, but it also causes several other minor peaks.[5] After baking, most of the water has been removed and the dominant peak is the H_2^+ at 2 amu/e generated by the residual hydrogen.
Using the RGA, we could also detect air leaks, exploiting the characteristic abundance ratios $N_2/O_2 = 78/21 = 3.7$ and $N_2/Ar = 78/1 = 78$. Leaks can also be detected by spraying He on the outside of the chamber and observing the response of the 4 amu/e peak. At the beginning, some parts of the main manipulator were delivered without proper cleaning, which we observed by the presence of large peaks at high molecular masses (50 amu/e and above).

[5] O^+ at 16 amu/e, H_2O^{2+} at 9 amu/e, $H_2{}^{18}O^+$ at 20 amu/e, etc.

2.3.2 Preparing clean surfaces

The main focus of preparing surfaces lies on removing impurities. They can either come from the bulk of the sample or from the environment and adsorb on the surface or chemically alter the surface e.g. by oxidation. However, this is not the only goal of surface preparation. Just as important is the ability to control other properties of the sample such as surface roughness, crystalline structure (of thin films), surface reconstructions etc.
In our setup, we implemented the most common preparation techniques which we will discuss in the following sections.

Annealing

Annealing, i.e. controlled heating of the sample to a certain temperature, is the simplest but extremely important technique for sample preparation. Many processes such as the diffusion of impurities in the bulk, their solubility in the host crystal, the diffusion of atoms across the surface, the desorption or sublimation of adsorbates, the breaking of chemical bonds, etc. are strongly temperature dependent. Therefore, heating the sample can be used to tune many of its properties. On the other hand, heating for changing one of the properties might result in changing several others as well. Thus, the full procedure (temperature, temperature ramp, time) must be controlled as precisely as possible for obtaining reproducible results.[32]
In our setup, we dispose of two different ways for heating the sample: a tungsten filament and contacts for direct current heating.
The core component of the **filament heater** is the 0.4 mm Tungsten filament consisting of eight windings of approximately 6 mm diameter. As depicted in Figure 2.6 a), it is mounted a few millimeter below the sample holder. There is no direct contact of the filament and the sample holder. The heat transfer mechanisms are therefore heat conduction through the sample acceptor stage and thermal radiation. Thus, the overall heat flux depends as

$$\dot{Q} = a\,(T_\mathrm{F} - T_\mathrm{S}) + b\left(T_\mathrm{F}^4 - T_\mathrm{S}^4\right)$$

on the filament temperature T_F and the sample temperature T_S. a and b are geometry and material constants. Hence, low temperature heat transport is dominated by conduction and high temperature transport by radiation.
Since the temperature coefficient of the wire resistance is positive, the power source should be used in constant voltage mode. In constant current mode, a catastrophic chain reaction of heating, leading to higher resistance resulting in more heating, could occur and destroy the filament.

As mentioned above, we want to keep track of the sample temperature at all time. For this, we installed a k-type thermocouple below one of the two clamps holding the sample holder, where it is as close as possible to the sample (see Figure 2.6 b)). However, there remains an unavoidable distance between the thermometer and the sample position, which will manifest in a different temperature reading as well. We calibrated this temperature difference using a special Mo sample holder onto which we fixed a second thermocouple. From 700 °C onwards, thermal radiation becomes strong enough to measure the sample temperature optically. Since we do not know neither the precise emissivity of the sample holder material (expected to be around 0.1) nor the transmissivity of the chamber's windows, we use a bi-chromatic pyrometer. The temperature readings of the different thermometers during a ramp to maximum power are compared in Figure 2.6 c). The temperatures shown in this figure are the equilibrium temperatures. Below approximately 700 °C, the system reacts rather slowly, taking several minutes to reach a thermal equilibrium. At high temperatures above 900 °C, this only takes a few seconds.

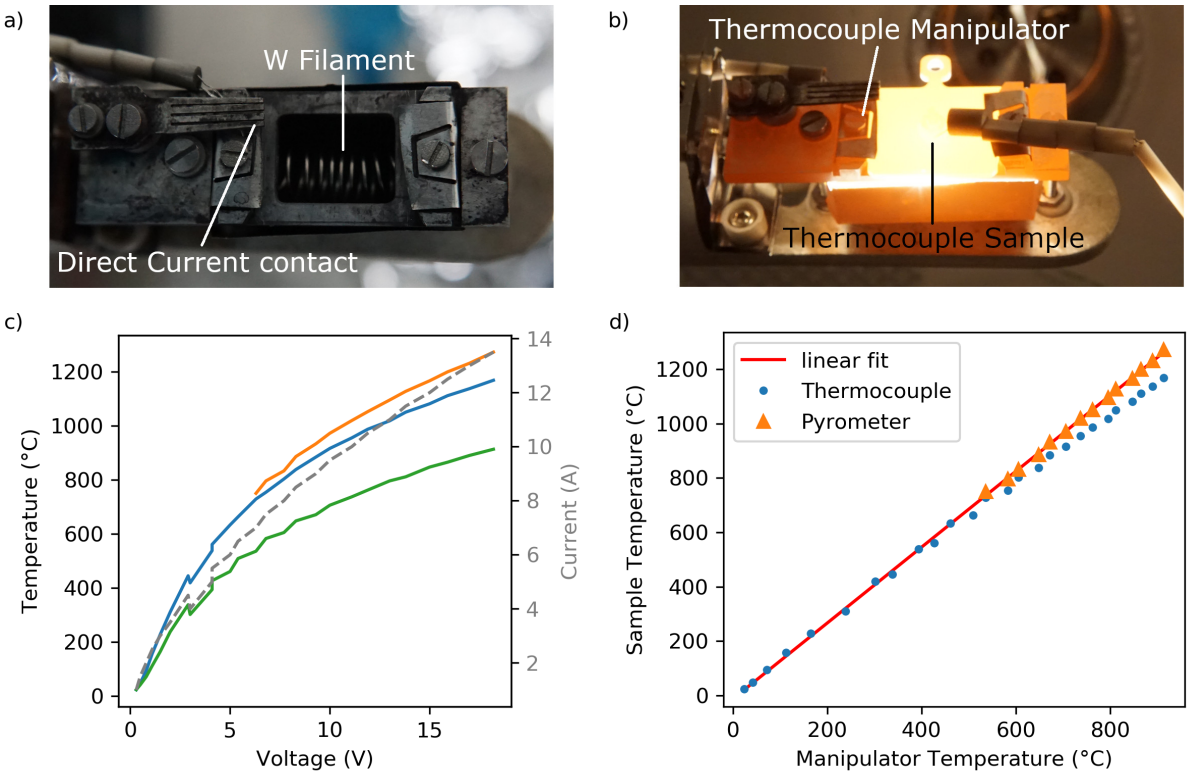

Figure 2.6: Calibrating the filament heater. a) The heating stage offers two heating methods: a Tungsten filament and contacts for direct current heating. b) For calibrating the manipulator's thermocouple, we temporarily fixed a second thermocouple directly on the sample holder. c) Temperatures measured with the manipulator thermocouple (green), the sample thermocouple (blue) and a bi-chromatic pyrometer (orange) as function of the voltage applied to the filament. The dashed grey line shows the current flowing through the filament. d) In equilibrium, the sample temperature T_S is proportional to the temperature of the manipulator thermocouple T_M. Linear fitting yields $T_S = (1.395 \pm 0.008) T_M - (12 \pm 5)°C$.

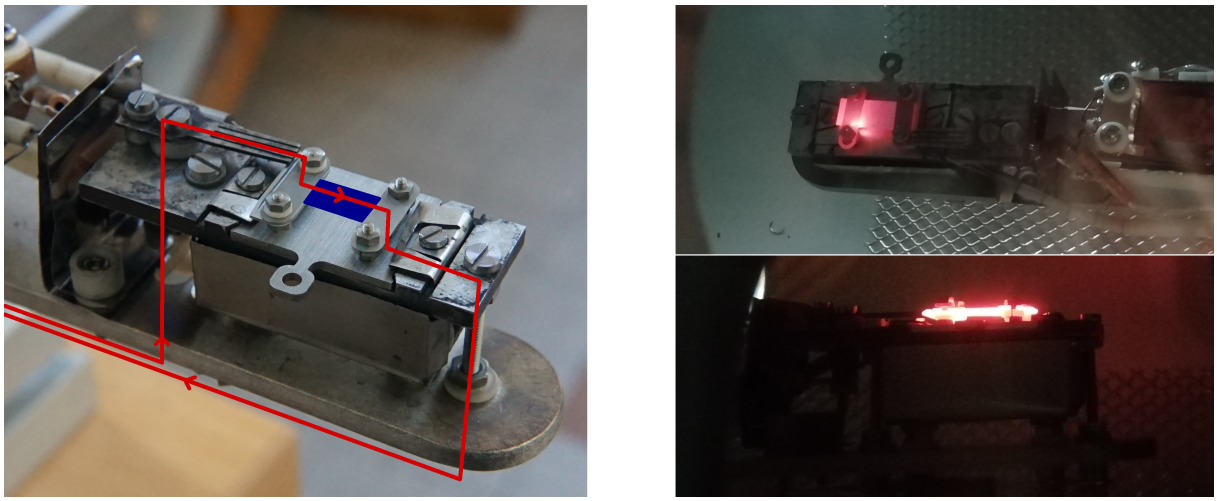

Figure 2.7: Direct current heater. Left: the special sample holder in place on the manipulator. The current flows as indicated by the red line. The connection from the manipulator to the sample holder is established through the flexible comb on the left and through the clamp holding the sample holder on the right. Right: Heating a silicon sample.

Clearly, there is a big discrepancy between the thermocouple on the manipulator and the two other measurements. Nevertheless, with this data in hand, it is easy to calibrate the sample temperature as function of the manipulator temperature. As we can observe in Figure 2.6 d), the sample temperature T_S increases linearly with the manipulator temperature T_M. A linear fit to the thermocouple data for temperatures below 700 °C and to the pyrometer data for temperatures above 700 °C which yields

$$T_S = (1.395 \pm 0.008) T_M - (12 \pm 5)°C.$$

We can use this relation to approximate the sample temperature from the reading of the manipulator thermocouple. For **direct current heating**, we can connect a power source to the special sample holder shown in Figure 2.7. As sketched, the current flows directly through the sample and returns via the manipulator ground. The resistive heating taking place in the sample allows to heat it to about 1200 °C at steeper temperature ramps than with the filament because of the much smaller mass to be heated and by avoiding the need to transport the heat from the place of generation to the place of interest. Another advantage is that for short heating pulses (often called „flash annealing“), the manipulator does not heat up as much and therefore degases less, which can help keeping the sample surface clean. However, this technique is limited to samples with an intermediate resistance. It should be much higher than the wire resistance but still small enough in order to dissipate a few watt using reasonable voltages. For this reason, it is mainly used for semiconducting samples such as silicon. Due to the negative temperature coefficient of the semiconductor resistance, the power source should be used in constant current mode.
On the right side of Figure 2.7 it becomes clear that the heating is not necessarily occurring homogeneously across the sample. In the shown case, a slightly increased contact resistance on one of the sample clamps leads to local heating at this point.
The temperature measurement using the manipulator's thermocouple is not practical because of its bad thermal coupling and slow reaction. Instead, a pyrometer should be used.

Sample cooling

The sample temperature is an important parameter for the growth dynamics of thin-films. Previously, we discussed how we can heat the sample above room temperature to increase the

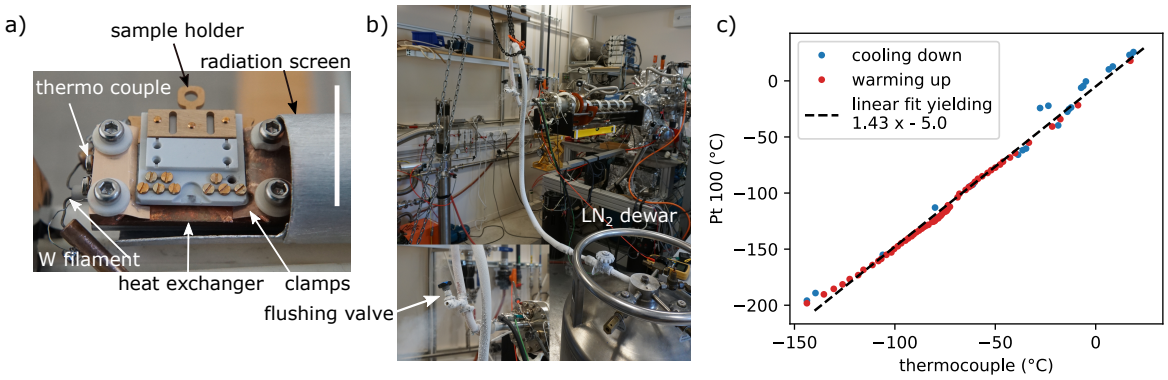

Figure 2.8: Sample cooling in the preparation chamber. a) Photograph of the sample stage which can be cooled by injecting liquid nitrogen into the heat exchanger. The temperature can be measured by a K-type thermocouple. Scalebar: 18 mm. b) Injection of liquid nitrogen from a pressurized dewar. We use a valve right before the entrance of the manipulator to flush and precool the transfer pipe. c) Calibration of the thermocouple versus a Pt100 resistor mounted on a sampleholder plate.

diffusion rate. However, sometimes we want to have little or no diffusion on the surface e.g. for the deposition of single molecules or adatoms when we want to prevent them from clustering. To this end, the main manipulator of the preparation chamber possesses a second sample stage which is depicted in Figure 2.8 a). The sample holder plates are fixed in place and thermalized by two clamps on each side, pressing it against the heat exchanger made of copper. From the outside, we can inject liquid nitrogen into the heat exchanger to cool it to approximately 77 K. Its temperature can be monitored through a K-type thermocouple fixed on the left. To reduce the radiative heat load on the liquid nitrogen supply pipe, it is surrounded by the return pipe which is cooled by the cold gas and, as a second insulation layer, the aluminum radiation screen that can be seen on the right side of Figure 2.8 a).
The company that supplied the manipulator did two design errors: first, the tungsten filament also shown in Figure 2.8 a) was intended to be used for heating the cold stage and in this way stabilize intermediate temperatures between 300 K and 77 K. However, the heat transfer to the heat exchanger happens only through radiation and is therefore much weaker than the cooling power of the liquid nitrogen bath. Second, the return pipe ends with a piece of very small inner diameter (approximately 1 mm over 15 cm) which constitutes a large impedance for the exhaust gas. This complicates the initial cooling when the cooling is provided by a cold gas flow. Given the maximum over-pressure at which we can inject (about 2 bar), the gas flow through this restriction is critically limiting the cooling power. Overall, it is not sufficient to cool the transfer pipe from the nitrogen dewar to the manipulator inlet and the manipulator at the same time. As shown in Figure 2.8 b), we circumvent this problem by flushing the transfer pipe through an extra outlet right before the injection into the manipulator. In this way, we directly inject liquid nitrogen into the manipulator. This flushing has to be repeated several times during the cool-down procedure. Once everything is cold and filled with liquid, the cooling power is sufficient to reach a steady state. Unfortunately, due to its lower specific heat, injecting liquid helium is not possible, so we are limited to temperatures above 77 K.
For calibrating the thermocouple, we used a sampleholder with a mounted Pt100 resistor. The comparison between the two temperature readings is plotted in Figure 2.8 c). We record both temperatures while cooling down (blue dots) and when warming up again (red dots). Since both curves coincide, we conclude that the coupling of both thermometers is good and that there are no long thermalization time constants. Second, we note that we really reach the boiling temperature of liquid nitrogen at −196 °C which once again shows the good thermal coupling of the

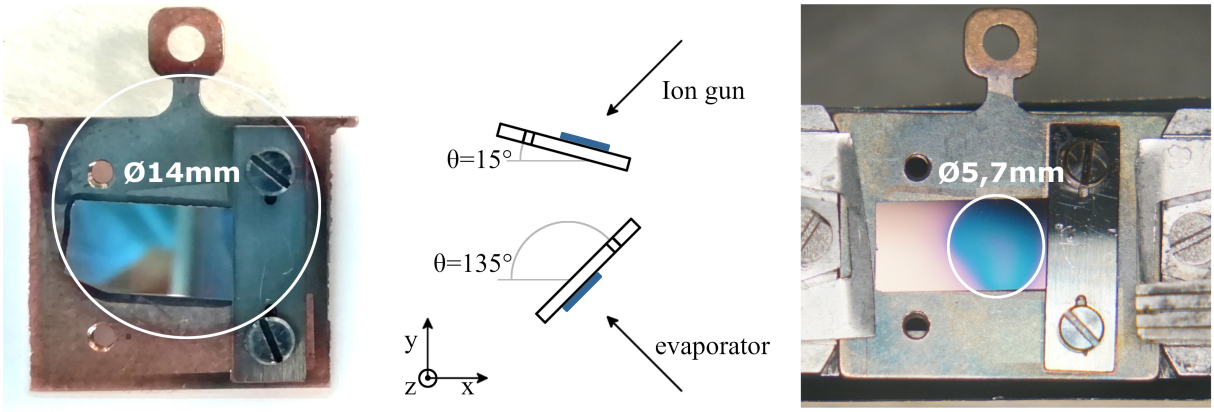

Figure 2.9: Evaporator and Ion gun beam sizes. Left: Spot size of the evaporator after an Indium calibration evaporation. The manipulator position was not optimized yet, which is why the evaporation is off-center. Center: Illustration of the sample orientation within the chamber during ion bombardment (top) and evaporation (bottom). Right: In blue, a hole etched in a Ti/Au thin film for determining the ion gun spot size, which is roughly 5.7 mm in diameter.

sample to the liquid bath. Furthermore, the two temperatures are approximately proportional to one another, which is underlined by the fact that the linear fit represented by a dashed line overlays very well with the data points. However, there is a surprisingly large factor of 1.43 between the two calibrations which we do not have a good explanation for. Possibly, the two wires of the thermocouple are shorted at a second, warmer point, but in that case it is surprising to not see a hysteresis between cooling down and warming up. Either way, for our application it is sufficient to apply the calibration factor for obtaining the real sample temperature.

Ion milling

Removing thin layers of the surface is another step, often used in sample preparation recipes. In our setup, we have a commercial ion milling system[6] for this purpose. During operation we can inject a small amount of Argon or Neon. We typically work at a pressure reading of $p \approx 4.5 \times 10^{-5}$ mbar of Neon. However, the sensitivity of the ion gauge used for measuring the pressure depends on the gas in the chamber. It is more sensitive to Neon than to air, hence the actual Neon pressure is $0.3 \cdot 4.5 \times 10^{-5}$ mbar $= 1.35 \times 10^{-5}$ mbar.
In the ion source, this gas is ionized and Neon ions are accelerated to energies between 0.12 keV - 5 keV and directed to the sample. When hitting the surface, the ions scatter at the sample's atoms which are kicked out of the lattice. They can then scatter again with other atoms, leading to a cascade of removed sample atoms. Finally, they are pumped off or redeposited. Like this, the surface gets slowly sputtered off.
Due to the cascade of scattering events, the first few atomic layers get mixed during the sputtering process, thus for a monolayer of impurities, several atomic layers of the sample need to be sputtered off to assure a full removal of the impurities. Damages of the crystalline structure are usually repaired by a subsequent annealing step during which implanted Argon or Neon atoms desorb as well.[32]
Since the sputtering process is of purely physical nature, this method works for basically every material.
The sputter rate depends on various parameters such as the process pressure, acceleration voltage, angle of impact on the surface etc. For our typical parameters, summarized in Table 2.1,

[6] Prevac IS40C1

the rate is roughly on the order of 0.5 nm/min. A precise estimation of this value has not been necessary for our purposes. Our ion gun generates a very focused beam of ions. As can be seen

$p_{reading}$	$p_{corrected}$	I_{emis}	V	I_{ion}	α	sputter rate
4.5×10^{-5} mbar	1.35×10^{-5} mbar	5 mA	1500 V	3 μA	30°	0.5 nm/min

Table 2.1: Typical sputter parameters used in our setup. α denotes the angle of incidence of the ions on the sample surface with respect to normal incidence.

in Figure 2.9, its diameter at the sample position is only about 5.7 mm. Therefore, it is very important to carefully position the manipulator.[7] If the spot is off-center, its position can be corrected by moving the along x, taking into account the 15° rotation angle sketched in Figure 2.9. If the sample is thick, the effective sputtering position moves downwards on the sample holder plate. This has to be compensated by reducing the y position of the manipulator.

Electron beam evaporation

The controlled deposition of materials is another crucial step in many sample preparation recipes. While in some cases this can be done ex-situ in dedicated facilities, followed by a sputter cleaning of the contaminated surface, in other cases it is indispensable, or at least more practical, to do the deposition in-situ.
In our setup, we have a commercial electron beam evaporator[8] for this purpose. It hosts a filament which starts emitting thermal electrons when a current of approximately 1 mA is applied. These electrons are then accelerated by a field of up to 2000 V and finally hit and heat a rod of the material to be deposited. When sufficiently hot, the rod material starts sublimating and eventually gets deposited on the sample when opening the manual shutter. Instead of rod evaporation, one can also mount a tungsten crucible containing a small quantity of the evaporant.
The evaporator also features a flux monitor for continuous monitoring of the evaporation rate and the evaporated thickness. It consists of an ion collector at the beam exit whose measured signal is proportional to the evaporation rate but which depends on the evaporation parameters such as the evaporant position, the emission current and the e-beam energy as well. Therefore, it needs to be calibrated before each evaporation, once the desired evaporation conditions are stabilized. For this purpose, we installed a quartz balance opposite of the evaporator. The size of the evaporation spot shown in Figure 2.9 is only about 14 mm large and does not exceed the sample holder. Thus, during the evaporation on the sample, the quartz balance is shadowed by the sample and can therefore not be used for real-time monitoring of the deposition rates.
Summarizing, the procedure for an evaporation is the following:

- Retract the manipulator enough to clear the axis between the evaporator and the quartz.
- Start the evaporation and ramp to the desired emission current and voltage.
- Once all parameters are settled, calibrate the evaporator's flux monitor against the quartz.
- Close the shutter. Advance the manipulator to place the sample in front of the evaporator.
- Open the shutter. Measure the evaporated thickness by integrating the flux signal. Close the shutter once the desired thickness is attained.
- Ramp down the emission current and voltage and switch off the evaporator.

[7] x=25 mm, y=27 mm, z=224 mm (for sample on hot stage – z=277.5 mm on cold stage), h=208 mm, θ=15°. See Appendix C for a definition of the axes.
[8] Focus EVC 300S

The evaporation controller can use the flux monitor signal to regulate the e-beam energy such that the evaporation rate stays constant. For us, this feature worked nicely for Indium, which has a comparatively low melting point. When evaporating Niobium at the maximum power limits of the evaporator, sparks inside the evaporator occur which lead to sudden peaks in the flux signal and disturb the controller. Therefore, the constant current mode has to be used which does not allow for flux regulation. Recording the flux signal, which we do using a home made program, then becomes crucial in order to keep track of the actual film thickness.

Given that the quartz balance and the sample are not at the same position, once at the beginning, we have to estimate the so called tooling factor

$$T = \frac{T_\mathrm{m}}{T_\mathrm{x}}$$

of the quartz balance which is used to calculate the film thickness T_m on the sample from the film thickness T_x on the quartz. Since this factor is of purely geometrical origin, it stays constant as long as the evaporator position is kept the same.
For estimating the tooling factor, one has to evaporate a film of a certain nominal thickness, remove the sample and measure its actual thickness. However, as mentioned above, we can not measure the evaporation rate with the quartz during the evaporation but have to track the film thickness with the flux monitor. Thus, we first calibrated the quartz balance against the flux monitor, giving 37 843 Å/C at an initial tooling factor $T_0 = 100\,\%$. The nominally evaporated film thickness was $t_\mathrm{n} = 56.45\,\text{Å}$, but AFM measurements of the actual film thickness showed an actual thickness $t_\mathrm{a} = 396\,\text{Å}$. The resulting tooling factor is

$$T = \frac{t_\mathrm{a}}{t_\mathrm{n}} \times T_0 \approx 700\,\% \; .$$

This value is reasonable since the balance is at about twice the distance from the source than the sample and the evaporation spot is probably not perfectly centered on it.

Molecule evaporator

The main focus of our experiments lies on the investigation of superconductivity in inhomogeneous systems, for example around magnetic impurities. An elegant way of introducing such impurities is the deposition of single, magnetic molecules on the sample surface. Due to their large mass, less cooling is required for freezing out their surface diffusion as compared to single adatoms. Furthermore, by choosing different organic structures hosting the magnetic impurity atom, one can, in principle, tune the coupling to the superconductor. It is also possible to displace molecules in a controlled way using the STM tip and to design molecules to assemble in complex, atomically controlled structures[33,34].
We use the home made evaporator[9] shown in Figure 2.10. It is made of a 0.375 mm molybdenum filament that is mechanically supporting the quartz crucible and serves as a resistive heating element at the same time. By applying currents of a few ampere, the crucible can be heated well above 200 °C[35]. For monitoring its temperature, a K-type thermocouple is attached to the crucible. We decided to mount the evaporator inside the load lock in order to avoid contamination of the main preparation chamber and for being able to refill or change the evaporant without venting the main chamber.

[9] built by Keir Logan and Stéphanie Garaudée

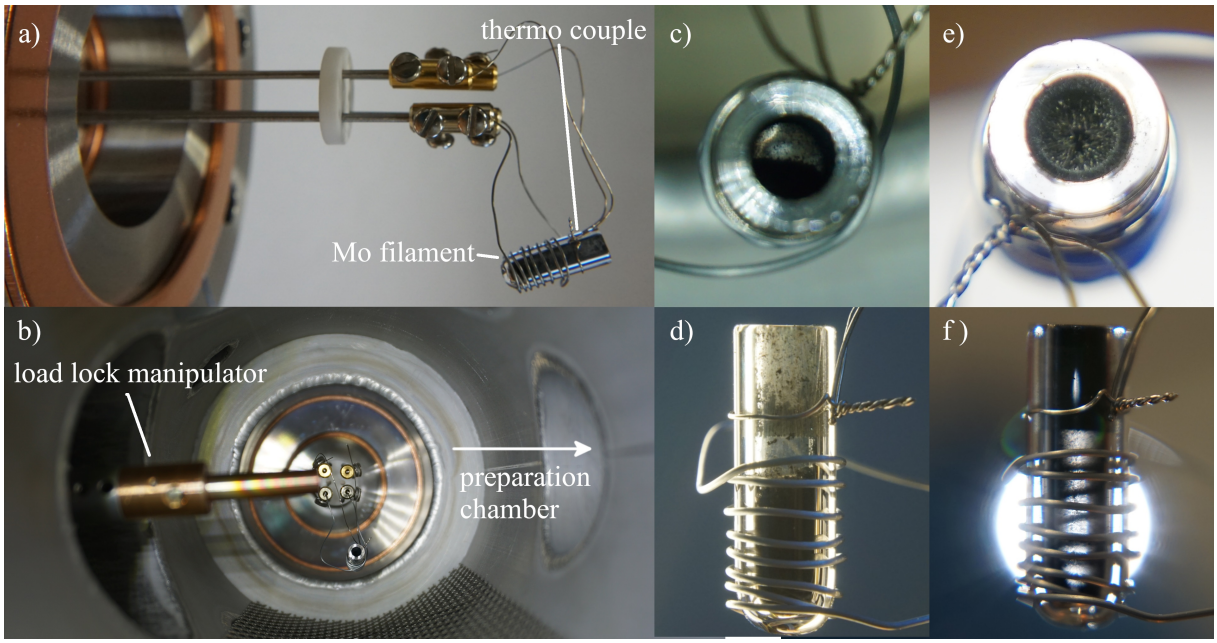

Figure 2.10: Molecule evaporator. a) Overview of the molecule evaporator. The powder of molecules gets loaded into the quartz crucible. Resistive heating of the filament wrapped around it starts the molecule evaporation. The temperature can be monitored using a thermo couple attached to the crucible. b) The evaporator mounted on the load lock, pointing towards the sample which is held by the load lock manipulator. Top view (c) and side view (d) of the crucible after molecule filling. e) and f): After strong and long heating, the molecules evaporate at the bottom and recondense at the colder top of the crucible and can clog the full diameter.

For preventing the evaporant from falling out of the crucible, it is mounted at an angle of approximately 16° from the horizontal position, which means that the sample needs to be rotated by 106° with respect to the horizontal orientation in order to face the crucible.
During the calibration of the deposition rate, the evaporator was hot for several hours and potentially at temperatures leading to large evaporation rates. As a result, almost all molecules at the bottom of the crucible evaporated. However, as shown in Figure 2.10, a large part of them re-condensed at the colder top of the crucible, which is not surrounded by the filament. Eventually, this completely clogs the crucible so that no more molecules are evaporated. An improved evaporator design would therefore have the filament be wrapped around the entire length of the crucible to provide homogeneous heating and would use a wider crucible which would not get clogged that quickly. Another possibility is to use a crucible with a large diameter as it has been done by Danilo Longo in their MnPc evaporator[36].

Nevertheless, once the parameters are optimized, small amounts of molecules can be evaporated without risking to clog the crucible. We used a trial and error approach over multiple cycles of evaporation and testing the success by STM to find the following procedure that works well for the deposition of a submonolayer of molecules:

- preheat 1-2 h at 1.7 A
- ramp up to 3.9 A and stabilize for 5-10min
- expose for 30 s
- resulting coverage: approx. 20 %

However, these parameters are not at all universal. Obviously, they will be different for a different kind of molecules which generally have a different sublimation temperature. Furthermore, the precise geometry of the crucible inside the filament as well as the position of the molecules

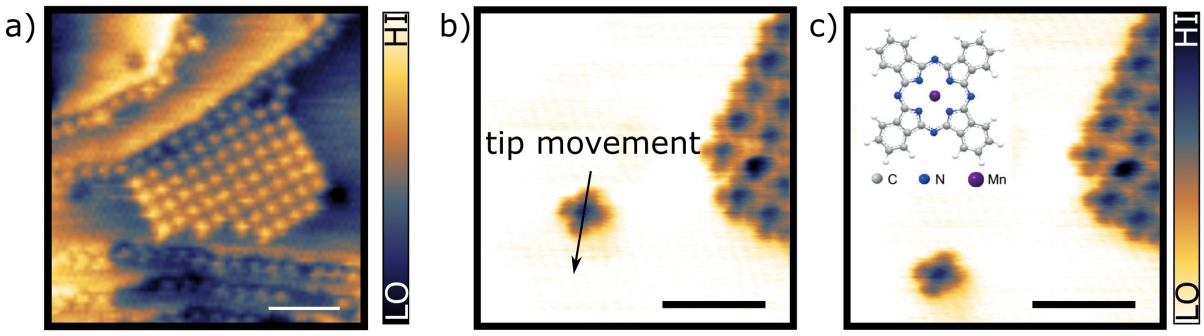

Figure 2.11: MnPc molecules on Pb (111), evaporated at room temperature. a) Topography image of a molecule patch. Molecules also arrange along steps of the substrate. b) and c) Topography images ($V_b = -200\,\mathrm{mV}$, $I = 12\,\mathrm{pA}$) of a single molecule with the corner of a patch as a reference. Between the two images, the tip was brought closer to the surface ($V_b = -200\,\mathrm{mV}$, $I = 1\,\mathrm{nA}$) and scanned across the molecule once as indicated by the black arrow. In the subsequent image at large tip distance, the molecule is at a different position. Scale bars are 5 nm. The inset in c) shows the molecular structure of MnPc, adapted from [37].

inside the crucible can play a role. Therefore, after each filling of the crucible and definitely when changing the crucible to a different molecule species, the evaporation procedure has to be fine-tuned again.

STM topography images of deposited molecules on Pb(111) at room temperature are depicted in Figure 2.11. The thermal energy at this temperature is sufficient to allow for molecule diffusion such that they arrange in their thermodynamically most favorable position. This means that they accumulate at the substrate steps and form regular islands. In both cases, they have more neighboring atoms and are therefore more tightly bound than on the flat surface of a terrace. We expect to see individual molecules when evaporating on a substrate that was precooled by liquid nitrogen. However, this remains to be tested.

Having a more precise look at the zoomed images in Figures 2.11 b) and c), we note the cross like structure of the molecules. Each arm corresponds to a benzene ring which can be found on each corner of the molecular structure sketched in the inset of c). We are also sensitive to the high density of states generated by the manganese atom in the center, resulting in a peak in topography.

Finally, the molecules are rather weakly bound to the surface. On one hand, this means that we have to scan at very large tunneling resistances ($V_b = -200\,\mathrm{mV}$, $I \leq 12\,\mathrm{pA}$) for not moving the (single) molecules through mechanical interactions with the tip. When they form large clusters, slightly higher currents of about 30 pA still work. On the other hand, this implies that we can manipulate the molecules in a controlled way by pushing them with the STM tip. One example of such a manipulation is illustrated in Figure 2.11 b) and c). First, we took the image in b) at large tunneling resistance ($V_b = -200\,\mathrm{mV}$, $I = 12\,\mathrm{pA}$). Then, we moved the tip to the starting point of the black arrow, decreased the tunneling resistance ($V_b = -200\,\mathrm{mV}$, $I = 1\,\mathrm{nA}$) and moved the tip across the molecule following the black arrow. We then came back to the imaging settings ($V_b = -200\,\mathrm{mV}$, $I = 12\,\mathrm{pA}$) to check the effect of the tip manipulation. The resulting topography image is shown in c) and indeed shows that the molecule moved by a few nanometers. The big patch of many molecules next to it serves as a reference and allows us to exclude that it has been the tip which changed between the two measurements. This procedure is robust and reproducible and would in principle allow to fabricate more or less complex structures of molecules on the surface.

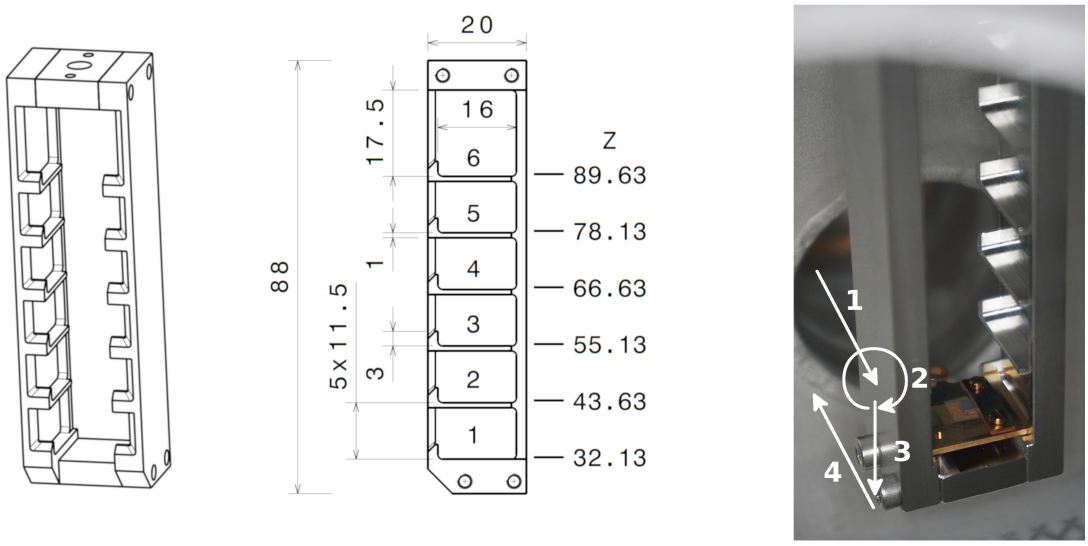

Figure 2.12: The sample storage shelf inside the preparation chamber. It consists of six shelfs, each equipped with a stop on both sides to prevent samples from falling. Samples are manipulated using the load-lock manipulator. For removing a sample, the indicated steps have to be followed: 1) advance the manipulator 2) lock the bayonet by rotating the manipulator 3) lower the shelf to lift the sample above the stop 4) retract the manipulator with the sample on it. For placing a sample in the shelf the same steps have to be followed in the reverse order.

UHV storage system

A last feature of the sample preparation chamber is the sample storage shelf. It allows to store up to six samples or tips simultaneously. It is convenient to leave all commonly used substrates inside the chamber to protect them from the harmful ambient conditions and to have them more accessible without needing to perform the entire loading and cleaning procedure at each time. The shelf is mounted vertically above the load-lock axis and is equipped with a manual drive that allows lowering it for sample exchange operations.
The shelf is shown in Figure 2.12. It is designed for the Omicron sample holders used in our setup. Since the sample holders are just lying on the shelfs, without being held in place by springs, all shelfs are equipped with mechanical stops on both ends to ensure that they do not fall unintentionally. For overcoming the mechanical stop at the front, the procedure sketched in Figure 2.12 has to be followed when picking up a sample from the shelf:

1. advance the manipulator
2. lock the bayonet by rotating the manipulator
3. lower the shelf by 3 mm to lift the sample above the stop
4. retract the manipulator with the sample on it

For placing a sample in the shelf the inverse procedure needs to be followed. The central sketch of Figure 2.12 lists the z-positions of the vertical drive for accessing the different levels of the shelf.

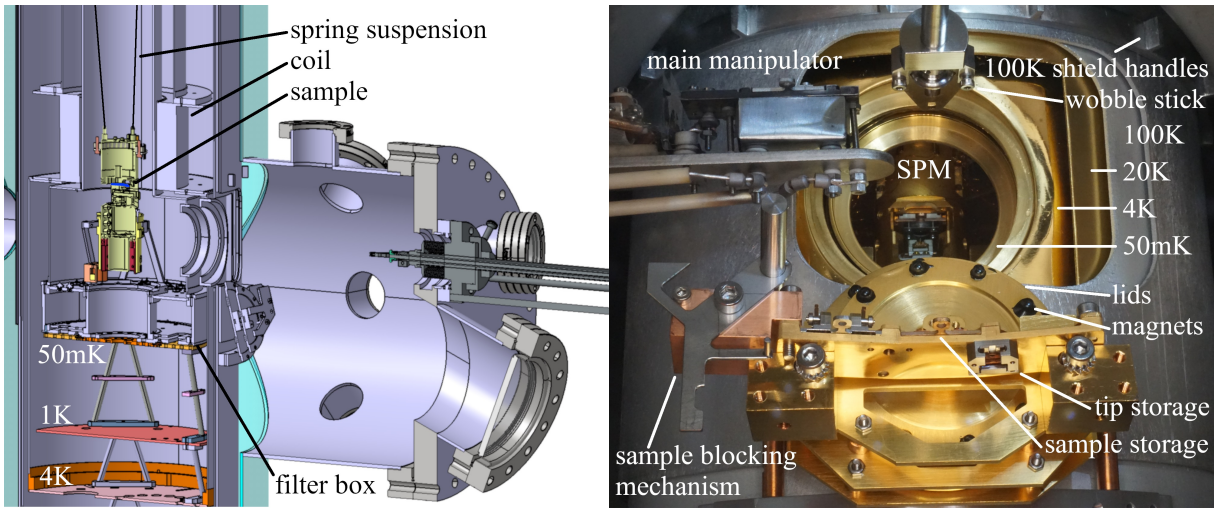

Figure 2.13: Radiation shields with open windows. The lids of the 50 mK and the 4 K shield are stored on a shelf which is fixed to the 100 K shield. This shelf also features three pockets for storing samples as well as one tip storage slot. The sample holder on the left most slot can be locked in place using the mechanism mounted on the left of the shelf. This is necessary for detaching a new tip from its transport plate.

2.4 A table-top dilution refrigerator with in-situ sample access

The refrigerator used here is an inverted dilution refrigerator called "Sionludi", that was developed and fabricated at the Néel Institute and was previously used in a home made low temperature STM [38]. It uses the well known principle of diluting ^{3}He in a ^{4}He rich ^{3}He-^{4}He mixture [39] and reaches a base temperature of below 50 mK. It consists of several stages that thermalize at temperatures of about 100 K, 20 K, 4 K, 1 K and 50 mK. On the left side of Figure 2.13, the upper three stages are visible. As it is sketched there, unlike most other dilution refrigerators, it has its coldest stage at the highest point and thus an inverted architecture. The cooling power at 100 mK is on the order of 200 µW.
Its big advantages for this project are its very compact design and the fact that it does not use radiation shields filled with liquid helium or nitrogen. This simplifies the task of adding lateral windows into these shields which are necessary for the in-situ sample and tip exchange. In the following, I will focus on how we implemented these windows and on the other modifications I realized and refer the reader to the bibliography [38,40,41] for further details on the dilution refrigerator.

Figure 2.13 shows on the left a cross-sectional view of the 3D model of the cryostat. The components for the refrigerator itself are accomodated on several platforms, with decreasing temperature from the bottom to the top. The base of the 100 K and the 20 K platform as well as the actual pipes of the refrigerator are omitted for clarity. The top most platform is connected to the mixing chamber of the dilution refrigerator and hence cooled to temperatures of about 50 mK. The electronic filters which are placed inside the donut shaped box on top of this platform as well as the SPM head are connected to this platform as well and thermalize at similar temperatures. To protect all cold parts of the system from the radiative heat load from the surrounding world, every platform carries a cylindric shield that completely encloses all colder parts. We implemented two different types of windows in these shields for enabling access to the SPM at the core.
The 50 mK and the 4 K screen possess round openings to which on the inside - and therefore

not visible on the image - small neodymium magnets are glued[10]. In Figure 2.13, the setup is shown with open windows, so the lids for closing the openings are stored in their dedicated storage shelf fixed to the 100 K screen. As can be seen on the right side of the figure, the lids are also equipped with magnets which hold them in place once picked up from the shelf and installed on the screen using the wobble stick. Apart from storing the lids, the shelf can also accomodate up to three samples and one tip, which is very handy during exchange operations. On the leftmost sample place, we additionally installed a mechanism which allows to lock the sample holder in place. This is needed when taking a tip from its transfer plate, an operation during which one has to pull on the tip holder but wants the carrier plate to stay in place.
Spatial constraints did not allow to install a window on the 20 K screen, which therefore just has a permanent opening. Since the cooling power on the next colder 4 K stage is still rather large and the radiation coming from 100 K is, according to the Stefan-Boltzmann law, already about 80 times smaller than that coming from room temperature, a hole in the 20 K screen is less problematic than in any other radiation screen.
On the 100 K screen, the spatial constraints were the smallest, such that we could opt for a different, more user friendly system. It consists of two concentric cylinders that both posses a hole. The outer cylinder can be rotated such that the two holes can be aligned for opening or be misaligned for closing the window. The rotation is controlled by pushing with the wobble stick on the screen's small handles above the window. An easy movement even under UHV conditions is ensured by a ball bearing based suspension. The moving part of the screen is thermalized through copper braids.
The 4 K screen hosts a superconducting coil which generates approximately 1.6 T for a current of 10 A. Note that in Figure 2.13 on the left, the SPM head is shown in its suspended position, i.e. in the measurement position. The sample, highlighted in blue, then resides just at the lower end of the coil. Numeric calculations show that at this position the maximum field is approximately 1 T. We also calculated the stray field of the magnets used for the lids at the sample position and found a value on the order of 100 μT, which is roughly comparable to the earth magnetic field.

Unfortunately the wire of the coil broke during the mounting to the screen. I therefore could not perform any magnetic field dependent measurements. In the near future, it will be replaced by a new, fully UHV compatible coil providing a slightly larger field (about 3 T in the center of the coil).

2.5 Low-noise setup for high resolution spectroscopy

In the previous section, I briefly described the big effort we take for cooling to temperatures around 50 mK. In order to get the maximum benefit of these low temperatures in terms of spectroscopic resolution and electronic temperature of the sample, it is very important to carefully design its electrical connections to the outside world.
There are two main problems to consider:

- Every cable coming from higher temperatures introduces an additional heat load on the refrigerator and therefore increases the achievable base temperature.
- At very low temperatures, phonons freeze out, leading to a very weak coupling of the electron bath to the cooling stage. Therefore, (black-body) plasmons traveling down the wires from higher temperatures can excite the sample's electrons and increase significantly the electron bath temperature with respect to that of the phonon bath.

[10] 10 times N45 ⌀3x3 mm each, glued using Stycast 2850 FT

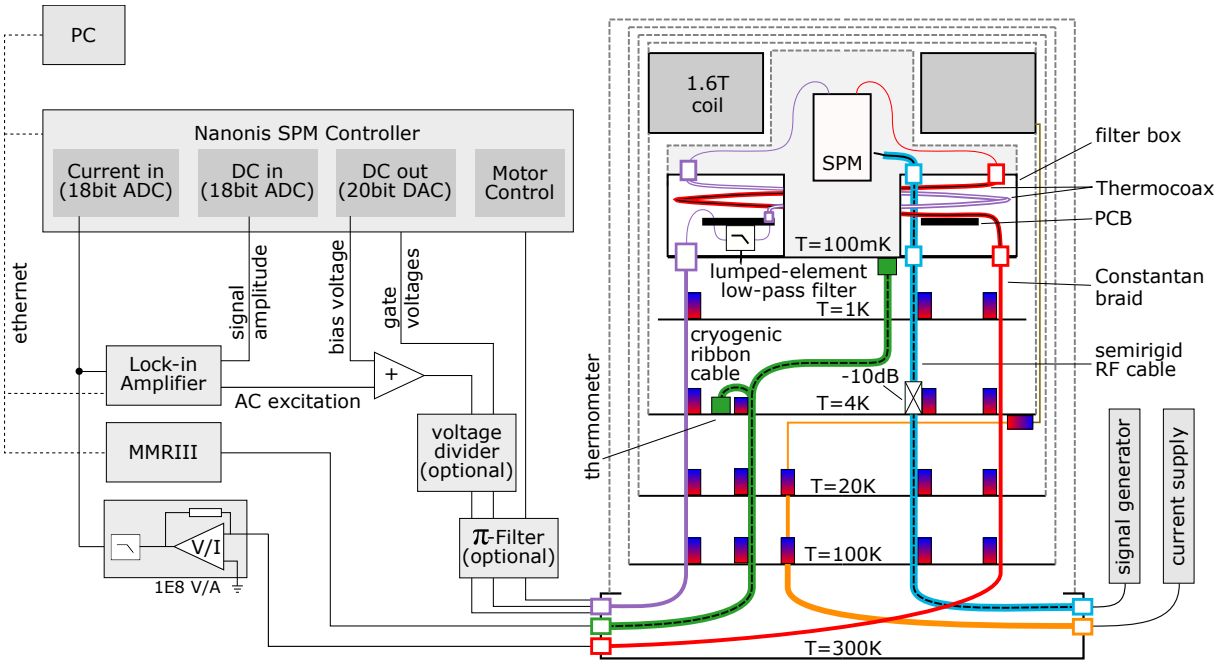

Figure 2.14: Schematic representation of the wiring in the experimental setup. All wires outside the cryostat's vacuum chamber are coaxial cables. Inside the chamber, coaxial cables are represented by a dashed central line on a solid background and unshielded wires by solid lines. For clarity, only one line of each type is shown here. In purple: DC, blue: RF, red: tunnel current, orange: coil supply, green: thermometer. The length of the Thermocoax cables is 1 m for all low voltage lines and 25 cm for the high voltage lines supplying the SPM's piezo elements.

In the next two subsections, I will discuss how we solved these problems in our setup.

2.5.1 Minimizing the heat load

For the simple case of a wire with a constant cross-sectional area A, the heat load coming in from the next higher temperature stage follows[42]

$$\frac{\mathrm{d}Q}{\mathrm{d}t} = -k(T)\,A\,\frac{\mathrm{d}T}{\mathrm{d}x}\,. \tag{2.5.3}$$

Therefore, there are four knobs for minimizing this heat flux:

- Choosing materials with a low thermal conductivity k, specially at low temperatures. Good options are stainless steel, constantan (CuNi) or NbTi. NbTi becomes superconducting at about 10 K, which additionally decreases its thermal conductivity because Cooper-pairs do not contribute to thermal transport. Far below the critical temperature, this can decrease the thermal conductivity by several orders of magnitude[43].
- Decreasing the wire diameter decreases the cross-sectional area A, but a good trade-off with mechanical stability and the wire resistance needs to be found.
- Increasing the wire length increases $\mathrm{d}x$ but also increases the wire resistance. Furthermore, too long wires are difficult to accommodate. We usually use lengths of about 25 cm between the different cryostat stages.
- Minimizing the temperature difference $\mathrm{d}T$ across the wire which can be ensured by a good thermal anchoring of the wire at the next higher temperature. This is particularly important because the cooling power decreases dramatically at lower temperatures.

As depicted in Figure 2.14, there are five different types of wires in our cryostat which will be detailed in the following.

There are in total 34 DC lines going to the SPM head. They are split in three cryogenic ribbon cables[11] consisting of 12 twisted pairs of NbTi wires held together by a nylon mesh (see Figure 2.15 a)). One of the two wires per pair is grounded at base temperature and has a floating end at room temperature. It provides some shielding of the signal wire which is of course not as good as that of a coaxial cable. However, given that all DC lines will be filtered at base temperature anyways (see Section 2.5.2), this twisted wire solution is sufficient and causes a smaller heat load on the base temperature stage. At each intermediate temperature, the ribbon cables are thermalized by clamping them between two copper plates with a thin Kapton film between the cable and the copper plate to avoid shorting the cable to ground through small damages of the wire's coating. The wire diameter is 100 µm which results in an electrical resistance of 52 Ω/m at room temperature. The big advantage of NbTi is its low thermal conductivity which is about $10^{-2}\,\mathrm{W\,m^{-1}\,K^{-1}}$ at 1 K and which, due to its superconducting character, drops quickly for sub-kelvin temperatures, reaching about $10^{-4}\,\mathrm{W\,m^{-1}\,K^{-1}}$ at 100 mK[44]. For comparison, at 1 K, this is approximately a factor of 3 lower than stainless steel and a factor of 2000 less than copper (RRR=20)[45]. To give an upper limit of the injected power, we assume a constant thermal conductivity of $10^{-2}\,\mathrm{W\,m^{-1}\,K^{-1}}$ along the full 25 cm, giving 0.3 nW per wire, or 20 nW for all DC lines. This is negligible compared to the 200 µW of cooling power.

The thermometers are connected using three twisted, superconducting coaxial cables[12], shown in Figure 2.15 b). They consist of a NbTi central wire in a CuNi matrix, surrounded by a Teflon core insulation and a CuNi shielding. The wire resistance at room temperature is 67 Ω/m. We measure the thermometer resistance using a three-probe measurement setup. This measurement principle is only accurate if the difference of the three wire's resistances is negligible compared to the sample resistance. Since we use identical wires of the same length that are twisted together and therefore follow the same temperature trajectory, their resistances should not differ by more than 1 Ω. For the Carbon thermometer, at 5 K the resistance is 880 Ω and its sensitivity is 310 Ω/K. An error of 1 Ω in the resistance measurement therefore corresponds to an error of 3 mK in temperature. In analogy, for the RuOx at 100mK the error is 2 pK. Therefore, the three-probe measurement allows us to reduce the heat load by 25 % as compared to a four-probe measurement without a significant loss of accuracy.
The most important signal of any scanning tunneling microscope is the tunnel current. Due to the large impedance of the tunnel junction (usually on the order of 10^7 Ω - 10^{11} Ω), the observed currents are very small, reaching down to the pA range. For this reason, the signal can be easily disturbed by electromagnetic noise, thus strong shielding would be beneficial. On the other hand, one has to avoid capacitances larger than a few nF at the entrance of the current amplifier and heavy heat loads on the base temperature stage that would be transported by a copper shield. We used a braid of three 1.5 m Constantan wires with a wire diameter of 0.1 mm and 67 $\Omega\mathrm{m}^{-1}$ giving approximately 100 Ω total resistance. Two out of the three wires are grounded to provide shielding to the third wire, carrying the current. As shown in Figure 2.15 b), thermal anchoring at the different temperature stages is accomplished by wrapping the braid around a copper post and fixing it there using Stycast epoxy. We also tried using a thermocoax coaxial cable, but had the impression that it induces noise, probably originating from mechanical vibrations, inducing small currents through the triboelectric effect.
The wires supplying the coil have to be able to sustain 10 A, which leads to very different criteria than for all the other wires discussed above. Due to the large currents, even small resistances can lead to significant Joule heating. Therefore, we need to use a good electrical conductor even

[11] sold by CMR-Direct, Model 02-32-064
[12] sold by GVL Cryoengineering Dr, George V. Lecomte GmbH, Product reference: GVLZO3

T (K)	d (mm)	ρ (nΩm)[46]	R (mΩ)	P_{Joule} (W)	$\int_0^T k(T)dT$ (W/m)[45]	$P_{Conduction}$ (W)
300		17.00			180000	
100	1.00	5.00	3.25	0.32	100000	0.42
20	0.60	0.10	2.65	0.27	30000	0.13
4	0.35	0.10	0.16	0.02	1000	0.02

Table 2.2: Characteristics of the 15 cm long copper wires supplying the coil. Each wire is listed at the temperature of its colder end. The resistance is an upper limit, assuming that the entire wire is at the temperature of its hotter end. The thermal conductivity is calculated using thermal conductivity integrals $\int_0^T k(T)dT$, assuming a constant cross sectional area and a linear temperature gradient.

though, according to the Wiedemann Franz law, this comes hand in hand with a high thermal conductivity. Down to 4 K, we use copper wires with decreasing diameters. The exact numbers are summarized in Table 2.2 together with the approximate heat loads P_{Joule} generated by Joule heating at the maximum current of 10 A as well as the heat flux $P_{Conduction}$ due to the thermal gradient in each wire segment. We chose the wire diameter and length such that both heat sources contribute about the same amount in order to minimize the total heat load.
Finally, there is the cable for injecting RF photons into the tunnel junction. Due to their high frequency of several GHz, these signals can not be transported on a simple DC line as the ones described above. Instead, they are carried by a semi-rigid coaxial cable wave guide. For a reduced thermal load, the shielding is made of stainless steel which has a comparatively low thermal conductance. Thermal noise on the signal is reduced by attenuating it by 20 dB at 4 K and another 20 dB at base temperature. The thermalization of the wire is assured by silver sheets soldered to the outer shield, shown in Figure 2.15 c).

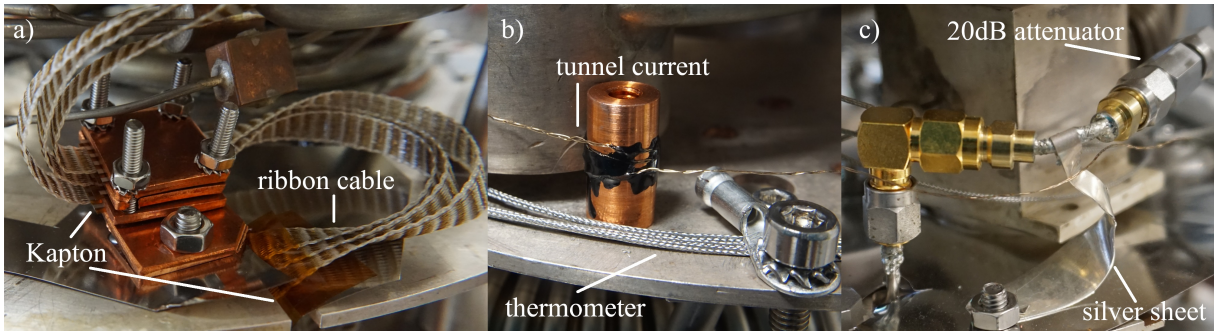

Figure 2.15: The different wire types and their thermalizations. a) Cryogenic ribbon wire consisting of 12 twisted NbTi superconducting wires, thermalized at each stage by clamping between copper plates. b) Top: braid of three Constantan wires carrying the tunnel current wound around and glued to a copper cylinder for thermalization. Bottom: superconducting coaxial cables used to connect the thermometers. c) Rigid coaxial cable for RF excitation and its thermalization using a silver sheet.

2.5.2 Filtering high frequency radiation

As mentioned at the beginning of this sub chapter, all effort spent on reaching the lowest possible base temperature is in vane if high frequency photons can travel down the lines and drive the electrons of the sample out of thermal equilibrium. Noise coming from the environment, e.g. wireless telecommunication, can be avoided by consistently shielding all wires outside the cryostat's vacuum chamber and by applying a low-pass filter to all lines right before feeding

them into the cryostat. However, one intrinsic source of THz radiation remains: the thermal black-body radiation. Its spectrum is depicted in Figure 2.17 a) for the relevant temperatures in our setup. If we want to prevent the thermal radiation from heating the electrons, we have to block all frequencies above the 50 mK spectrum. Hence, a low-pass filter with a cut-off frequency of 1 GHz or less is desirable. Naturally, at its output, this filter also emits the thermal radiation corresponding to its temperature. Consequently, it can only be placed at base temperature.

There are several ways of physically implementing low-pass filters[47,48]. The straight forward approach is using RC-, LC- or RLC filter circuits made of discrete electronic components which allow to easily design a compact filter with the desired characteristics. However, due to parasitic capacitances, high frequency signals can bypass the filter, leading to a decreased attenuation from the GHz range on. Therefore, these filters have to be combined with a second filter type, the so called distributed element filters.

As the name suggests, distributed element filters consist of an elongated element which geometrically decouples the input from the output. There are three mechanisms that can be deployed for filtering:

Dissipation in a dielectric (magnetic) material surrounding the conductor, in which polarization (magnetization) processes lead to dissipation characterized by the imaginary part of the complex permittivity ε (permeability μ).

One can also make use of the **low-pass characteristics of a coaxial cable** that due to its intrinsic resistance, inductance and capacitance acts as a distributed RLC low-pass element.

The third option is exploiting the **skin effect** which expels the field of high frequency signals from the bulk to the surface of the conductor. Therefore, the effective cross-sectional area for charge transport decreases, leading to a higher resistance and therefore bigger attenuation. This effect is strongly amplified in powder filters where the signal passes through a box filled of small metal powder (often copper or stainless steel). The individual grains are usually of a size around 30 µm and are insulated from each other by a thin oxide layer or by embedding them in an insulating matrix. This geometry dramatically increases the effective surface area on which skin effect damping takes place[49].

There are a variety of concepts exploiting these effects for filtering purposes. The most common are powder filters in different geometries such as (induction-compensated) coils or on chip as well as dissipative coaxial lines with different dielectric fillings[47]. We opted for the well known and characterized[50], commercially available Thermocoax coaxial cable. They provide a smooth transmission curve without resonance peaks often observed in powder filters and they are relatively easy to accommodate in our setup.

In our design, we decided to place all low-temperature filters in a cylindrical copper box, labeled “filter box” in Figure 2.14. It takes the lines from the electromagnetically “dirty” lower volume, applies a low-pass filtering and feeds them into the “clean” upper volume that houses the SPM head. The implementation and characteristics of this filtering system will be presented in the following section.

Let us first consider the DC lines, which represent by far the biggest number of cables inside the box. As mentioned above, they arrive on three cryogenic ribbon cables which are terminated by a Micro-D connector. Thus, they enter the box via the Micro-D feed-through shown in Figure 2.16 a). The backside of the feed-through is connected to the input contact pads of the lumped-element low-pass filters with 0.16 mm insulated copper wires. The filters themselves are mounted on the bottom of the PCB. One example is shown in Figure 2.16 c). We use a π-filter architecture that is sketched in Figure 2.16 d). Its input capacitor shunts high frequencies to ground, the transmitted signal then passes the inductor that also opposes to quickly chang-

f_{cut} (MHz)	C_{in} (nF)	L (nH)	R (Ω)	C_{out} (nF)
0.1	1	15.7	50	10
10	1	15.7	10	1

Table 2.3: Values of the components used in the lumped-element filters.

ing currents before finally a second capacitor once again shunts remaining high frequencies to ground. The resistance damps the resonance of the LC-circuit in order to obtain a monotonously falling transmission spectrum. This design is known to give very smooth output signals, has a good voltage gain for low current signals and has a much steeper roll-off than a first order RC-filter.

The coarse motion piezo scanners of our SPM use the so called "stick-slip" principle. It relies on a very fast voltage ramp on the order of $100\,\mathrm{V}\,\mu\mathrm{s}^{-1}$. This implies that the cut-off frequency should not be lower than 1 MHz. Furthermore, the relatively high line resistance of about 100 Ω together with a desired decharging of the coarse motion piezos and capacitances nearby within 1 μs imposes capacitances smaller than 10 nF. In order to have some margin, we opted for a filter capacitance not larger than 1 nF, which is then small compared to the capacitance of the piezo stacks of around 8 nF at room temperature.

For all other lines, there are no such limitations because all signals will be of much lower frequency, usually not exceeding 1 kHz. Therefore, for these lines we decided to push the cut-off frequency as low as possible using reasonably compact components, giving us the values summarized in Table 2.3. As discussed previously, for filtering the thermal radiation of higher temperatures, a cut-off of 1 GHz is sufficient. However, as every real low-pass filter always has a finite roll-off, a lower cut-off frequency leads to stronger attenuation at higher frequencies. The real transmission spectrum of the lumped-element filters is plotted in Figure 2.17 b). To cover a maximum frequency range, the plots combine measurements performed with a Zurich Instruments MFLI Lock-in amplifier (10 Hz - 5 MHz) and with an Agilent E8362C Network Analyzer (10 MHz - 20 GHz). The finite output impedance of the voltage source as well as the resistance, inductance and capacitance added by the coaxial wires used to connect it to the filters significantly alter the recorded signal. Taking into account these parasitic components (dotted lines in Figure 2.17 b)) allows to reproduce the measurements[13]. However, the real transmission of the bare filters is higher. It is obtained from simulations and represented by the dashed lines in the same figure. As expected, the cut-off frequencies are about 100 kHz and 10 MHz. The anticipated increase of the transmission at high frequencies due to the direct coupling of the input to the output can also be observed from about 100 MHz on. This illustrates nicely the need of the second - distributed element - filtering system.

As mentioned above, we use a coaxial cable manufactured by THERMOCOAX SAS, sold under the trademark Thermocoax. It consists of a NiCr(80/20) wire inside a 0.5 mm 304L stainless steel sheath. The wire has a room temperature DC-resistance of $50\,\Omega\mathrm{m}^{-1}$, a capacitance of $0.4\,\mathrm{nF\,m}^{-1}$, a small bending radius of 1.5 mm and can be used from cryogenic temperatures up to 600 °C without a significant change of its properties. The volume between the conductor and the jacket is filled with strongly compacted MgO powder. MgO is a non magnetic insulator, the attenuation therefore relies primarily on the skin effect and the RLC-properties of the coaxial geometry. Its attenuation per unit length is given by the real part of the propagation coefficient γ[50,51],

$$\gamma = \sqrt{j\omega c(r(\omega) + j\omega l)}. \tag{2.5.4}$$

[13] lumped element simulations performed with LTSpice®

r, l and c are the resistance, inductance and capacitance per unit length respectively. For a proper model, it is important to take into account the frequency dependence of the line resistance due to the skin effect:

$$r(\omega) = \left(\frac{\sqrt{\mu\mu_0\rho_\mathrm{w}/2}}{\pi d_1} + \frac{\sqrt{\mu\mu_0\rho_\mathrm{j}/2}}{\pi d_2} \right) \sqrt{\omega}.$$

Here, ρ_w and ρ_j are the wire and the jacket material's resistivity and d_1 and d_2 their respective outer and inner diameter. Injecting the known material properties[14] results in the dotted orange line in Figure 2.17 c) which perfectly reproduces the measured curve for 1 m wire in green. The transmitted voltage goes as $V(z) = V_0 e^{-\gamma z}$, thus the transmission in dB scales linearly with the wire length. Indeed, this is observed in the plot where the dashed green curve indicating $0.25 \times \mathrm{Transmission}_{1\,\mathrm{m,dB}}$ superimposes the measured curve for 25 cm of Thermocoax shown in olive green. In analogy, this allows to extrapolate the transmission for the 1 m wire from the shorter one for frequencies above 4 GHz where the noise-floor of the Network Analyzer is reached.
Combining both filter components results in transmission spectra depicted in Figure 2.17 d). According to Planck's law for the black body radiance (plotted in Figure 2.17 a)), the required attenuation to thermalize radiation coming from the hot temperature T_h to the cold temperature $T_\mathrm{c} = 50\,\mathrm{mK}$ of the base temperature is[47,52]

$$A(\nu) = \frac{e^{\frac{h\nu}{kT_\mathrm{h}}} - 1}{e^{\frac{h\nu}{kT_\mathrm{c}}} - 1}\,. \tag{2.5.5}$$

Comparing this to the attenuation of our filtering system shows that it is strong enough even for $T_\mathrm{h} = 300\,\mathrm{K}$ (dashed red line in Figure 2.17 d)). This lets us conclude that our low-temperature filtering system effectively avoids an increase of the electronic temperature which can therefore be expected to be very close to the cryostat's base temperature of about 50 mK.

Let us now consider the tunnel current line. It carries the pA current signal that is amplified by a factor of $1 \times 10^8\,\mathrm{V\,A^{-1}}$ by a room temperature transimpedance amplifier. Every real amplifier adds its noise gain β^{-1}. In the high frequency limit, it depends on the sample capacitance C_s (dominated by the wiring) and the feedback capacitance C_f of the amplifier as[53]

$$\beta^{-1} = \frac{C_\mathrm{s}}{C_\mathrm{f}}\,. \tag{2.5.6}$$

Increasing C_f decreases the amplifier bandwidth. For this reason, the wiring capacitance must be kept as small as possible. This is why we decided not to use lumped element filters with their 2 nF capacitance being much larger than the 1 m Thermocoax capacitance (0.45 nF) and that of the braided Constantan wire (<200 pF). Hence, in the filter box, the tunnel current line is fed through the bottom by an SMA feed through, adapted to MCX, passed through 1 m Thermocoax and fed through the top from where it goes directly to the SPM head.

The last wire type entering the base temperature cavity is the RF wire. On its whole length it is a coaxial cable, which therefore already serves as a distributed filter. Additionally, as sketched in Figure 2.14, it contains a 20 dB attenuator at 4 K and another 20 dB attenuation at base temperature. When injecting large power signals, the attenuation at base temperature leads to significant heating. Overall, the attenuation allows to remove most of the remaining high temperature radiation. In the filter box, the line is just passed through via a regular, flexible coaxial cable to avoid impedance mismatch problems that could occur by using a Thermocoax cable.

[14] $\rho_\mathrm{w} = 1.08\,\mu\Omega\,\mathrm{m}$, $d_1 = 0.17\,\mathrm{mm}$, $\rho_\mathrm{j} = 0.7\,\mu\Omega\,\mathrm{m}$, $d_2 = 0.35\,\mathrm{mm}$

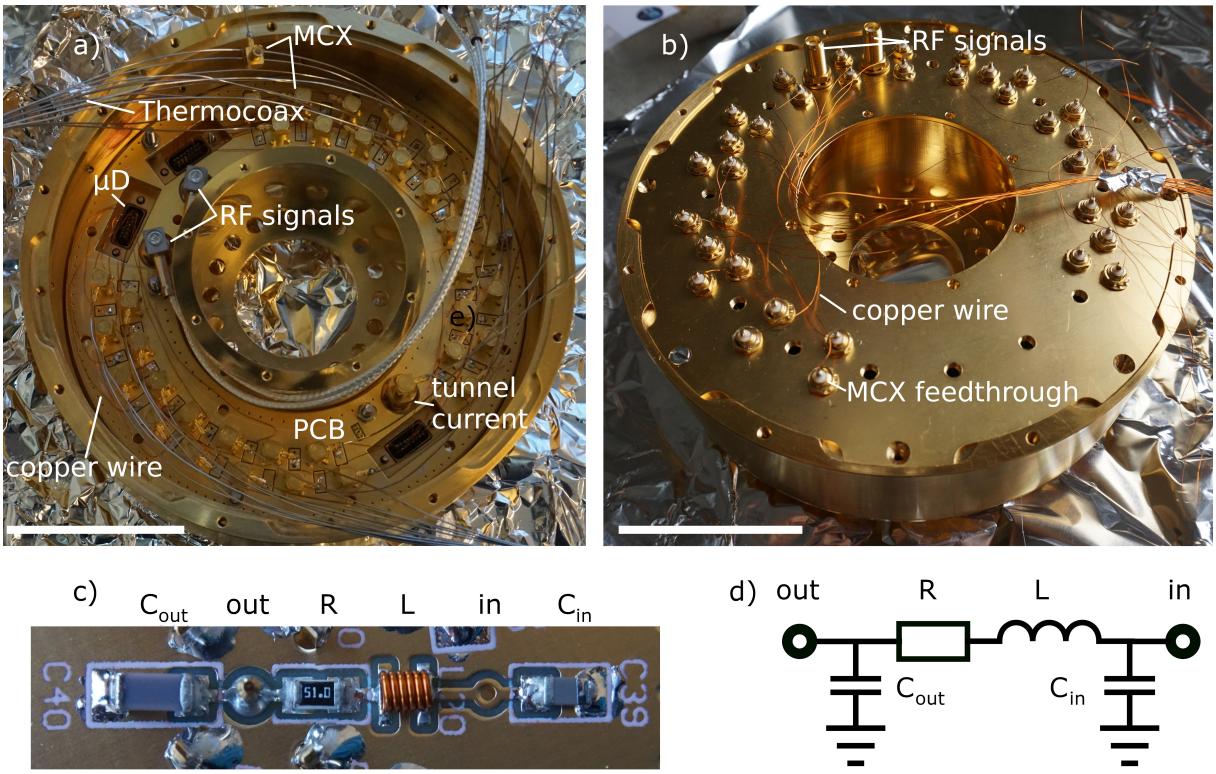

Figure 2.16: Implementation of the base-temperature low-pass filters. a) View in the open box with the PCB carrying the lumped element filters on the bottom. All Thermocoax wires as well as the two RF-cable are already plugged in. b) Top view of the closed box. c) Lumped-element low-pass filter mounted on the bottom face of the PCB. Schematics in d) For the values of the components refer to Table 2.3. Scale bars are 50 mm.

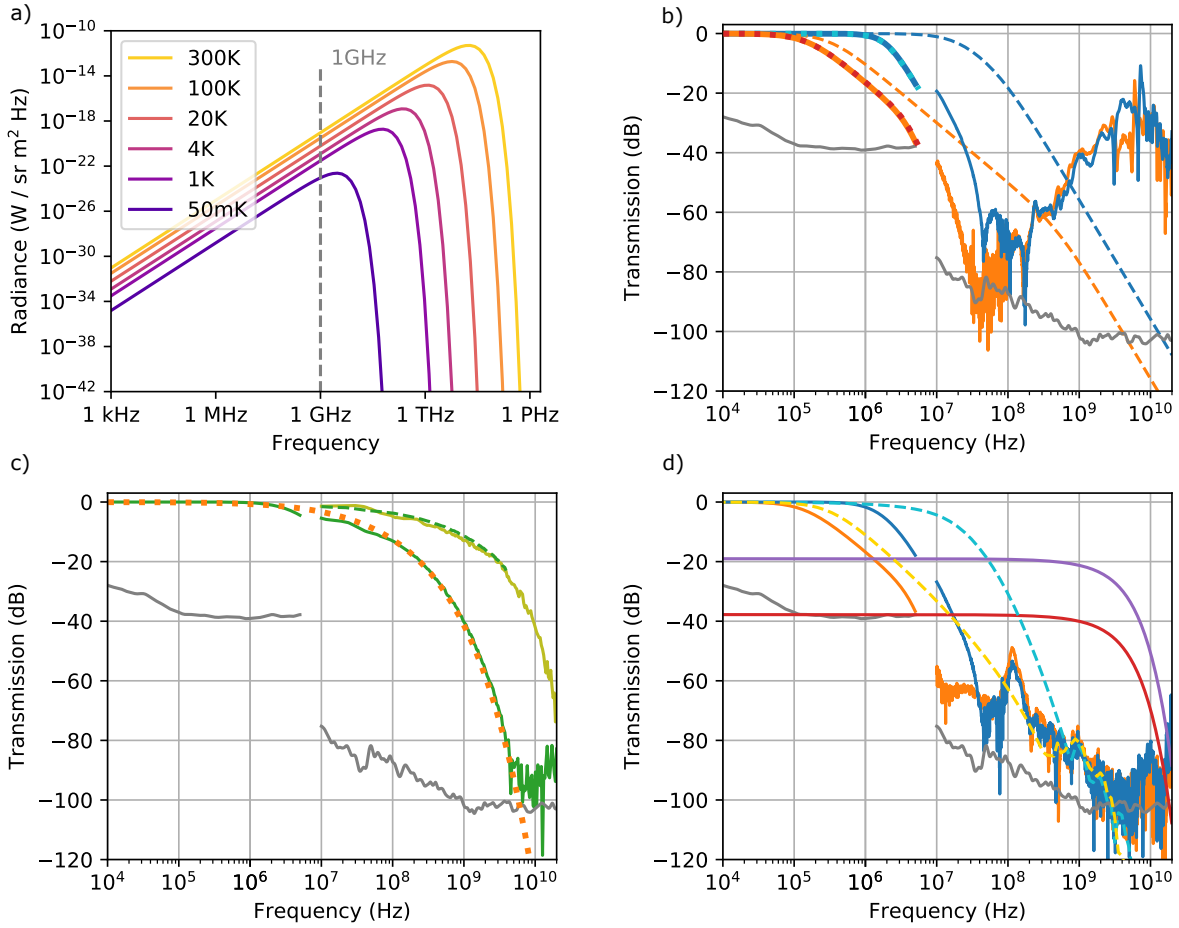

Figure 2.17: Room temperature characteristics of the base-temperature low-pass filters. a) Motivation: Blackbody radiation spectra at several relevant temperatures. Effective filtering from about 1 GHz on allows to block the high temperature thermal radiation coming down along the wires. b) Transmission of the two different types of lumped-element filters showing the expected cut-off frequencies of about 100 kHz (orange) and 10 MHz (blue). The full lines are raw measurement data measured with two different instruments: ZI-MFLI (left) and Agilent VNA[15] (right). The measurements below 5 MHz are altered by parasitic impedances from the instruments outputs and the coaxial wires which is perfectly reproduced by the simulations taking those into account (dotted lines in dark red and light blue). The VNA was calibrated before the measurement to avoid this problem. The dashed lines show the simulated transition of the filters only, neglecting parasitic capacitances. In grey: the noise-floor of the instruments. From around 100 MHz on, signals can circumvent the filters through the finite capacitive coupling of the filter input and output. This illustrates the need for distributed element filters. c) Transmission of 1 m (green) and 25 cm (olive) Thermocoax. The dashed green line is 0.25 times the 1 m curve in units of dB. The dotted orange line is the expected transmission for 1 m Thermocoax, according to Equation 2.5.4. d) Measured transmission of lumped-element filter and Thermocoax in series (same color code as in b)) compared with the required attenuation to keep the sample electronic temperature at 50 mK assuming incoming thermal radiation from 300 K (red) and 4 K (purple). The best approximation of the real transmission of the filters, using the simulation for the lumped element filters up to approximately 200 MHz and the measured transmission for higher frequencies, is represented by the yellow and light blue dashed lines.

2.6 Dilution-temperature SPM for experiments at the interface of transport- and surface-physics

In the previous sections, we discussed the experimental environment for the dilution temperature STM measurements. This section will finally present the core component of the setup: the scanning probe microscopy head. We will also demonstrate the specifications and limits on exemplary measurements on standard Au (111) and Pb (111) samples as well as on graphene on a Re thin-film.

We opted for the commercial TRIBUS Ultra[16] low temperature compatible, non-magnetic SPM head, shown in Figure 2.18. It offers an easy in-situ tip and sample exchange and sample and tip displacement across $4\,\mathrm{mm} \times 4\,\mathrm{mm} \times 10\,\mathrm{mm}$ in x,y and z respectively. The standard sample holder is made for samples up to $10\,\mathrm{mm} \times 6\,\mathrm{mm}$ in size, which are fixed by metallic clamps that will also ensure the electric contact to the surface. The uncovered sample area is then $5\,\mathrm{mm} \times 6\,\mathrm{mm}$ large.
Using the special sample holder displayed on the bottom center of Figure 2.18, up to eleven different voltages can be applied to the sample simultaneously, enabling the combination of transport measurements and microscopy on nano-fabricated devices. However, the experiments performed so far did not require this feature so we have not tested it yet.

The tip is mounted on top of a piezo tube which possesses six electrodes, allowing to apply electric fields in the x, y and z direction and hence bending the tube in x and y and expanding or shrinking it along z exploiting the piezo effect. The latter effect is very weak. At low temperature, the tube expands by $1.3\,\mathrm{nm/V}$ along z. When not amplifying the signal generated by the Nanonis electronics, its 16 bit resolution over a range of $\pm 10\,\mathrm{V}$ translates to a z-resolution of 0.3 pm which is sufficient to even resolve the atomic corrugations of a metallic surface which can be as little as 1 pm in height. Applied voltages on the x and y electrodes bend the tube, resulting in a tip movement of about $10.6\,\mathrm{nm/V}$ at low temperatures. Since we usually apply $\pm 150\,\mathrm{V}$, we can access a scan area of $3.2\,\mu\mathrm{m} \times 3.2\,\mu\mathrm{m}$. At room temperatures, the piezo effect is about five times stronger, increasing the accessible volume accordingly. The exact calibration of all motors for room temperature as well as low temperature are listed in Appendix B.

The TRIBUS tip holder features two lines, one intended for collecting the tunnel current and the other one for reading out the excitation signal from a qPlus tuning fork, hence allowing to perform STM and (non-contact) AFM measurements simultaneously. The tuning fork can be excited mechanically. To this end, there is a separate electrode called "R" on the piezo tube through which an oscillation along the z-axis can be imposed. Detailed pictures of the qPlus tip are shown in Figure 2.18 on the top right. In the qPlus configuration used here, the AFM resonator is a piezoelectric tuning fork of which one prong is rigidly glued to the tip holder whereas the other one can resonate freely. Through the piezo effect, the movement of the free prong generates a small voltage which is read out through the "q+" electrode. The tip that interacts with the sample is a small electrochemically etched tungsten wire that is glued to the end of the free prong. It is connected by a separate electrode for collecting the tunnel current or for applying a bias to the tip for KPFM-type measurements. I confirmed that the AFM excitation works by measuring the resonances of the tips, which usually lie around 23 kHz with a quality factor of around 1300-5000 in air at ambient pressure. In vacuum and when cooling down, the quality factor usually increases reaching values well above 10000. I approached the tip in AFM mode and confirmed that the regulation works properly. However, until now

[16] SIGMA Surface Science, now Scienta Omicron

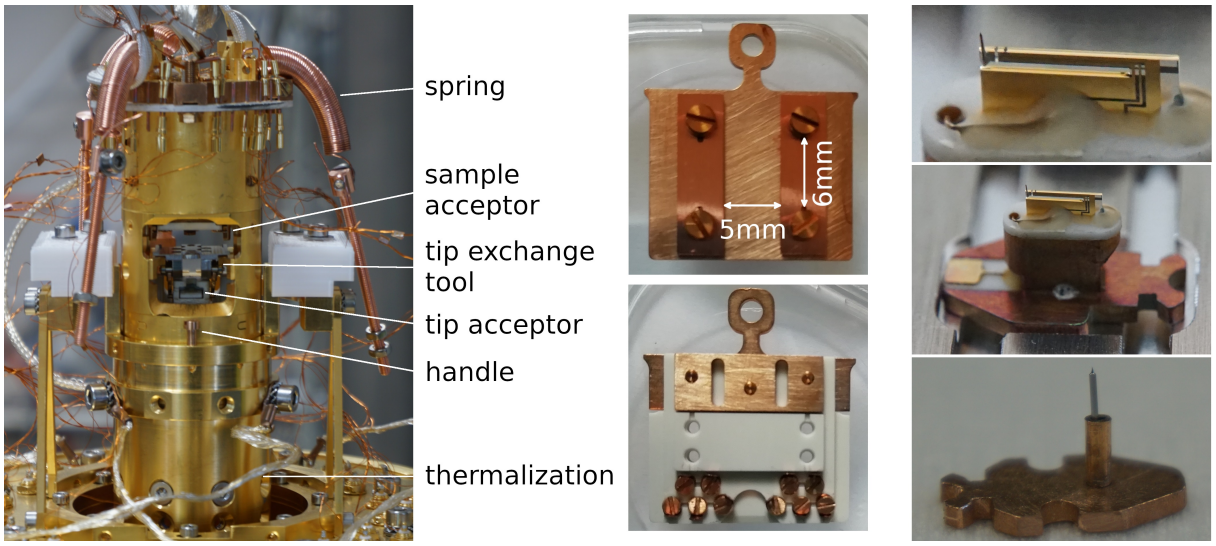

Figure 2.18: The TRIBUS Ultra SPM head. Left: overview of the scan head before suspending it on its springs. Center top: sample holder with two clamps. The sample must not be larger than 6 mm and not longer than 13 mm out of which 5 mm will be accessible for STM measurements. Center bottom: 10 contact sample holder. The sample can be fixed using four screws in the central macor piece. The ten contacts arrive on the screws at the bottom from where they can be wire bonded to the sample. Right top zoom on the qPlus resonator with the STM tip glued to the end of the free prong. Right center: complete view of the qPlus tip. Right bottom: electrochemically etched W tip.

all our experiments only required the STM mode, so I did not characterize the AFM scanning performance extensively.

Vibration damping

For reaching subatomic resolution, the position of the tip must be stable on the same length scale. This requires a very efficient mechanical noise damping system. Usually, these damping systems as well as the microscope head itself can be described as damped harmonic oscillators with an external driving force. Their response to a sinusoidal driving force is therefore given by

$$x(t) = \frac{F_0}{m\sqrt{(2\omega_0\xi\omega)^2 + \left(\omega^2 - \omega_0^2\right)^2}} \sin(\omega t + \phi) \tag{2.6.7}$$

where F_0 is the driving force amplitude, $\xi = \frac{1}{2Q}$ the damping ratio and ω and ω_0 the driving and resonance frequency, respectively. Since all systems are installed in series, the driving force of the next system will be the response of the previous one, effectively multiplying the response terms. From this equation, we can draw two conclusions:

- The **resonance frequencies** of the damping stages should be as small as possible, since for small damping, the response decays as $\frac{1}{|\omega^2-\omega_0^2|}$. At the same time, the resonance frequency of the STM head itself should be as high as possible.
- The **damping ratio** ξ should be large enough to prevent a large amplification of the drive at resonance, but should not be too large either since this would lead to a $\frac{1}{\omega}$ instead of a $\frac{1}{\omega^2}$ response, thus filter high frequencies much worse.

In our case, we place the entire setup on a concrete block of several tons, founded in the basement of the building, to start from a low vibration level. Furthermore, we use two damping

stages. The first one is a compressed air optical table that supports the entire setup including the UHV preparation chamber and the dilution refrigerator with its helium reservoir. The dampers are accommodated in the legs of the table, depicted in Figure 2.3. The suspended mass is roughly 600 kg and the resonance frequency around 1.5 Hz, thus it effectively suppresses building and floor vibrations.[17] However, acoustic vibrations or vibrations coming through the cables and pipes necessary for controlling the experiment can circumvent this damping system. Therefore, we implement a second damping stage by suspending the microscope on springs from the top of the base temperature radiation screen. As mentioned above, the resonance frequency of the oscillator formed by the suspended microscope should be as low as possible. Since the mass of the microscope can not be changed significantly, we can only play with the spring stiffness which is determined by the used wire diameter, the diameter of the spring coils and the number of windings. The viable parameter space is limited mainly by geometrical constraints, for example the available room height limits the length of the springs taking into account that for the assembly of the radiation screens, double their height has to be available. On the other side, during measurements the SPM head's equilibrium position should be partially inside the magnetic field coil, but for sample and tip exchange it has to be lowered by about 40 mm without exceeding the elastic limit of the springs, which imposes a minimum spring length of roughly 120 mm in equilibrium. Taking into account all these constraints, we found a good compromise by using three springs made of 0.5 mm copper beryllium wire wound in 60 coils with a diameter of 7 mm. After suspending the microscope with its mass of about 600 g, the observed resonance frequency is roughly 2 Hz.
In vacuum, the suspended SPM head only experiences very little damping caused by the wires connecting it. Hence, the quality factor of this mechanical resonator is very large, leading to a strong amplification of external excitations around the resonance frequency. To increase the damping factor to the desired, weakly damped range, we add the eddy current damper drawn in Figure 2.19. It is made of a set of static magnets, fixed to the cryostat, and two conductive plates fixed to the SPM that move in the magnetic field generated by the magnets. The induced eddy currents generate a force opposing the movement and hence lead to damping. The advantage of this kind of system is that it creates no mechanical contact between the SPM and the cryostat through which vibrations could be transmitted. Furthermore, this prevents any wear, thus the system is very robust. Finally, its damping is proportional to the velocity and therefore realizes the standard damping force assumed in simple theories. Due to the compactness of the entire system, there were strong spacial constraints on the design of the damping system. This is why we opted for neodymium magnets that generate a much stronger magnetic field than ferrite magnets of the same size. In consequence, much less volume is required to generate the same damping force. A drawback of neodymium is its rather low Curie temperature of around 310 °C compared to 450 °C for ferrite. The neodymium magnets should not be heated above 80 °C since they might get demagnetized otherwise. A drawback of this eddy current damper system in general is the fact that the magnets are at a rather small distance of about 50 mm from the sample. At this distance, their stray field is not yet negligible. A numerical study of our geometry showed that, at the sample position, a field of about 100 µT remains when using all six magnets[35]. This is slightly larger than the earth magnetic field but also only about 1 % of the critical field of aluminium. Thus, the stray field is non negligible compared to the earth magnetic field, but does not significantly affect most samples either. Another consequence of the compact design is that the gap between the copper plates screwed to the SPM and the mag-

[17] With the added weight by the UHV chamber we were working very close to the limits of the dampers shown in Figure 2.3. We recently replaced them by four more powerful Newport S-2000 Stablizer^{TM} dampers and a custom made aluminum support structure.

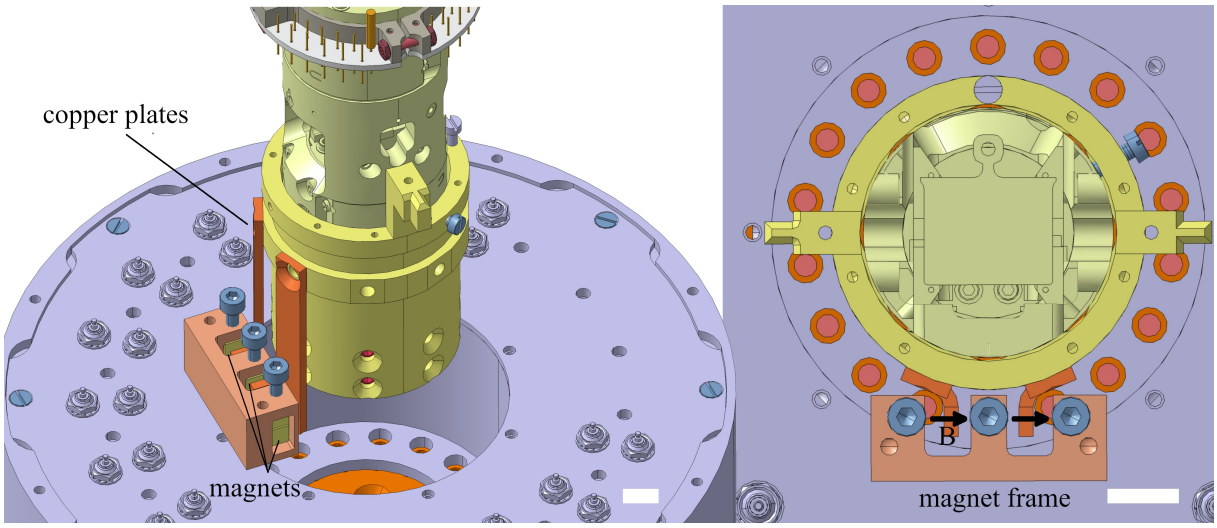

Figure 2.19: The eddy current damper of the SPM suspension system. Up to six 5x5x5 mm^3 neodymium magnets can be mounted in the magnet frame which is fixed on the base temperature filter box. (left) Two copper plates attached to the SPM head can move freely in the space between the magnets (right). The eddy currents induced in the copper plates upon movements of the SPM head lead to a force opposing the movement and thus to contact less damping. Scale bars are 10 mm.

nets is only 2 mm. Careful adjustment of the SPM suspension when assembling the setup is necessary to avoid a mechanical contact between the two.

When designing the damper system, we calculated the expected damping ratio, taking into account the geometries and material properties, such as the magnet's magnetization and the conductivity of the copper plates. However, one big uncertainty is the low temperature conductivity of the copper, quantified by its residual resistance ratio

$$RRR = \frac{\rho_{300\,\mathrm{K}}}{\rho_{0\,\mathrm{K}}} \,. \tag{2.6.8}$$

The low temperature behavior is dominated by impurities in the metal which are not that well controlled in the common commercial materials. For this reason, only the order of magnitude of the RRR, but not its precise value are known. With this in mind, we chose an adaptable design, where the number of magnets and their spacing can be tuned. Indeed, during the first cool down with all six magnets in place we realized that the system was over damped, leading to suboptimal damping, as described above. Finally, a configuration using only the two central magnets gave us a good result at all temperatures with a quality factor of roughly 2 at low temperatures.
The spring suspension and eddy current damper system is effective enough to allows us to scan while the turbo pumps are running. Under these conditions, we are able to resolve atomic steps and single molecules. Only for the highest spatial and spectroscopic resolution, the turbo pumps have to be disabled.

Sample and tip exchange

Apart from stable measuring conditions, another fundamental requirement for successful operation of the SPM is a reliable sample and tip exchange under UHV conditions. First, the SPM head has to be lowered by about 40 mm. This brings the sample from the measuring position, where it is inside the magnetic field coil, to the exchange position, where it can be accessed through the radiation shield's windows shown in Figure 2.13. It then has to be locked in place,

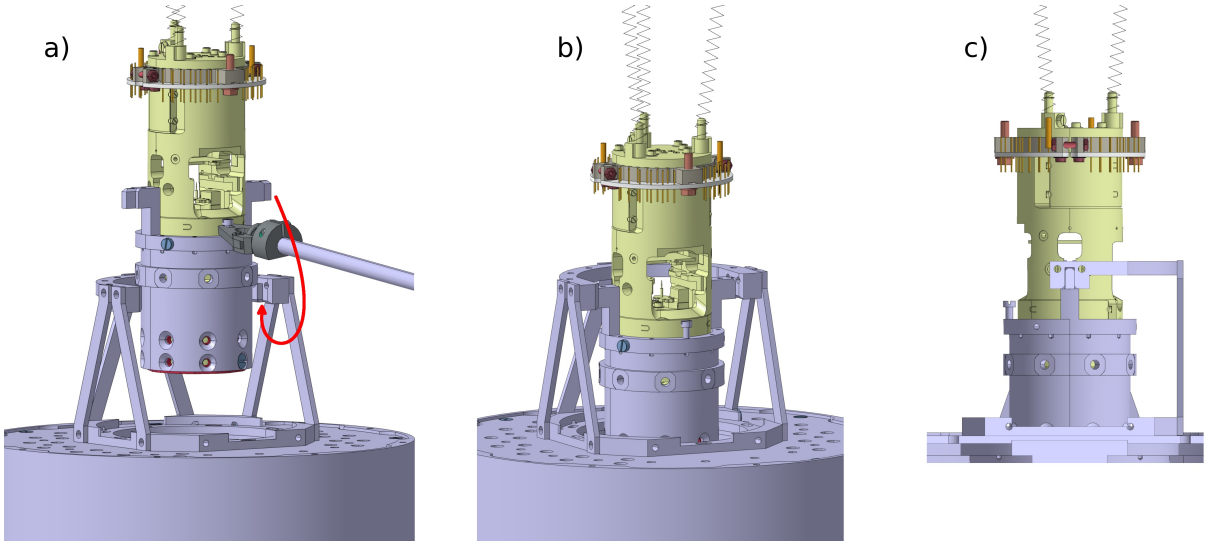

Figure 2.20: Clamping mechanism used to fix the SPM head for tip and sample exchange and for good thermalization during cool downs. a) In the measurement position, the SPM head is suspended on springs. It has a small handle from where it can be grabbed with the wobble stick and be pulled down following the red arrow, such that the two arms on the left and right side of the SPM enter the pocket of the fixed structure at the arrow head. Since the springs still pull upwards, the SPM is locked in place. b) In the fixed position, all movements except down the z axis are blocked. One can then pull on the sample or tip without moving the entire SPM head. c) Cross section through the pocket of the support structure. The SPM arms and the pockets are manufactured with a very tight fit, such that rotations around the x axis are also suppressed.

such that it does not move when pulling out or pushing in samples or tips. For this purpose, I designed the mechanism illustrated in Figure 2.20. At the bottom of the TRIBUS head, I added an additional adaptation piece offering a handle from where it can be grabbed using the wobble stick and two arms for locking it into place. The arms of this piece precisely fit into two pockets of the structure screwed to the cryostat. Once the arms are inserted into the pockets from below, the springs pull up the SPM head and hence keep it in place. Apart from movements in the horizontal plane, the tight fit also blocks rotations around the horizontal axis. The only remaining free movement is therefore a displacement downwards, which is used to free the SPM after finishing the sample exchange.

Changing the sample itself is a rather simple operation. After sufficiently retracting the tip to prevent touching it, one can simply grab the hook of the sample holder plate and pull on it using the wobble stick. Accordingly, a new sample can just be inserted into the sample acceptor stage and pushed all the way in. A tip exchange is slightly more complicated. First, the tip needs to be fully retracted. In its lowest position, several small pins on the lower side of the tip acceptor stage lock into corresponding holes of the SPM frame to take up all forces acting on the acceptor stage upon tip exchange. This protects the piezo tube which is rather brittle and could break when pulling directly on it. The tip holder is clamped by a spring. To liberate it, Scienta Omicron provides a dedicated tip exchange tool that needs to be inserted into the SPM head as shown in Figure 2.18. It compresses the spring holding the tip which is then free and can be exchanged. At the end, the tip exchange tool has to be withdrawn and stored on the 100 K screen's sample storage shelf again.

Through the springs and the very thin copper wires carrying the electronic signals, the SPM has only a weak thermal coupling to the cryostat stage. To ensure that our measurements are performed at the lowest possible temperature and for assuring proper performance of the dilution fridge, we need to increase this thermal coupling without adding strong mechanical connections that would shortcut the vibration damping system. To this end, we opted for a braid of long and

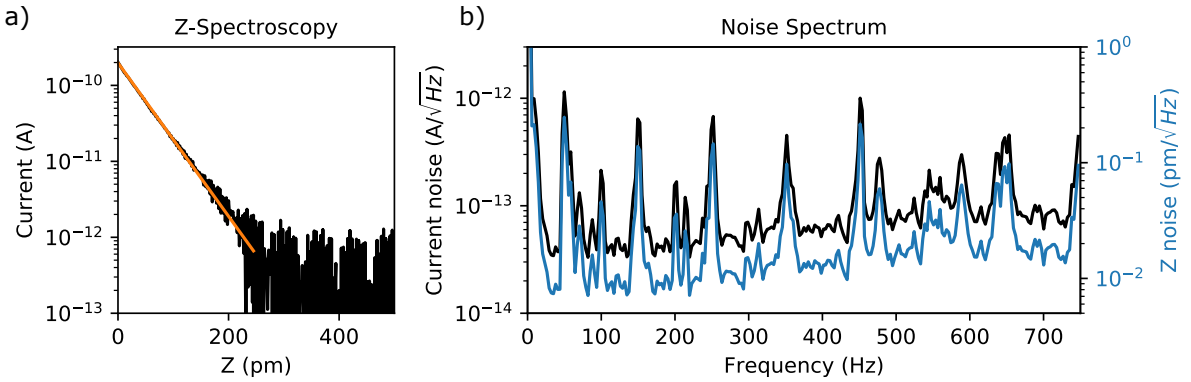

Figure 2.21: Noise level of the STM. a) Distance dependence of the tunneling current for a PtIr-Pb junction. $Z = 0$ is chosen arbitrarily as the position where $I = 200\,\mathrm{pA}$ at the applied voltage of 4 mV. At around 250 pm the current falls below the 200 fA noise floor of our current amplifier. In orange: exponential fit $198\,\mathrm{pA}\,\exp(-Z/43\,\mathrm{pm})$. b) Current noise (black) measured with disabled z-controller and the derived z noise (blue). This noise level is sufficiently low to obtain atomically resolved topography scans of the Pb surface.

thin silver wires. Two braids, visible in Figure 2.18, are screwed to the clamping adapter piece on the SPM head on one side and to the base temperature plate in the central hole of the filter box on the other side.

The thermal contact as well as the cooling power of the refrigerator are such that the microscope comes back to 4 K within approximately 30 min after sample exchange. Condensing and reaching base temperature then takes another 30 min to one hour. Thus, it is possible to investigate two to three samples per day, which is particularly useful when optimizing preparation parameters.

A heating resistance is mounted on the base temperature stage of the cryostat. Using this resistance, intermediate temperatures between 50 mK and 750 mK can be stabilized with fluctuations on the order of 200 μK. For measurements between 750 mK and 4 K the dilution becomes unstable, thus we can ramp to this temperatures only for short times on the order of a few minutes while slowly heating the dilution back to 4 K. The temperature of the STM follows the cryostat temperature with a delay of approximately 1 min.

2.6.1 STM topography imaging

One of the first tests in STM mode is measuring the distance dependence of the tunneling current to confirm the exponential behavior expected for a clean tunnel junction. In our example in Figure 2.21 a), we use a PtIr-Pb tunnel junction. The work functions of the two materials are approximately $\Phi_{\mathrm{PtIr}} = 5.1\,\mathrm{eV}$ [54] and $\Phi_{\mathrm{Pb}} = 4.05\,\mathrm{eV}$ [55]. We very crudely approximate the tunnel junction by a 1D rectangular barrier of the mean height of $\Phi \approx 4.6\,\mathrm{eV}$. Plugging this into the 1D rectangular barrier model $Z_0^{-1} = 2\sqrt{2m_e\Phi/\hbar^2}$, we expect a decay length of roughly $Z_0 = 45.6\,\mathrm{pm}$. Indeed, the measurement in Figure 2.21 a) shows a nicely exponential behavior and a decay length Z_0 of 43 pm in good agreement with the calculation. The remaining difference might be explained by the rough approximation of the tunnel barrier shape. Due to the difference in the work function, a more accurate model would use a trapezoidal tunnel barrier. Uncertainties on the work function values as well as a small error on the piezo calibration can further contribute.

Next, we characterize the stability of the tunnel junction. For this, we disable the z-controller at a current of 200 pA and a bias voltage of 4 mV and measure the power spectral density of the current noise shown in black in Figure 2.21 b). We clearly observe peaks at 50 Hz and its

multiples, most likely being of electronic nature. For spectroscopy measurements we usually use lock-in time constants and integration times of 20 ms in order to average out most of this noise.
The current's exponential distance dependence allows calculating the amplitude of small distance oscillations $dZ \ll Z_0$ from the corresponding current amplitude dI via

$$I = I_0\, e^{-Z/Z_0} \Rightarrow dZ = -\frac{Z_0}{I}\, dI\ . \tag{2.6.9}$$

With the parameters from the Z-Spectroscopy (Fig. 2.21 a)) discussed previously, this gives the Z-noise represented by the blue curve in Figure 2.21 b). Since most of the current noise is probably of electronic origin, we regulate comparatively slow[18] while scanning so that the tip does not follow high frequency oscillations which would just add spurious features to our topography data. The disadvantage of a slow regulation is the slow reaction of the controller to actual changes in topography which means that we have to scan at rather slow speeds on the order of 20 nm s^{-1}.

Let us now look at scanning tunneling microscopy images and the attainable resolution with this setup. The sample we use as a benchmark is a Pb single crystal with a polished (111) surface[19] prepared by ion bombardment and subsequent annealing to roughly 170 °C to obtain an atomically flat and clean surface.
Lead possesses a face-centered cubic (fcc) crystalline structure[56]. Taking into account the unavoidable small miscut angle, the expected surface looks similar to the sketch shown in Figure 2.22 a) and b). We expect to observe two main features: at a larger scale, the mono-atomic steps between adjacent (111) terraces and, when zooming in on one of the terraces, eventually the characteristic hexagonal lattice with a six fold rotational symmetry.
Moving on to the measurements in Figure 2.22 c), we indeed observe the atomically flat terraces with mono-atomic steps between them. From simple geometrical considerations, one can readily derive the fcc (111) step height d to be

$$d = \frac{a}{\sqrt{3}} \tag{2.6.10}$$

where a denotes the lattice constant. For Pb, $a = 495$ pm[57] which implies a step height of 286 pm. Estimating this number from the STM scan allows for a precise calibration of the z-piezo tube.
Due to the delocalized nature of the electrons in metals, the local variations of the electron density of states are very small and so are the corrugations observed by STM. For this reason, seeing atomic resolution on this kind of samples is rather challenging and requires very good tip stability and low noise levels. Nevertheless, as Figure 2.22 d) demonstrates, we achieve observing these features. For this kind of observation, the tip needs to be close to the surface i.e. the tunnel conductance needs to be large. The shown measurement was performed at 15 mV bias voltage and 1 nA current set-point. Note that the only post processing applied to the data is a line-wise subtraction of a parabolic fit to remove the sample tilt, demonstrating nicely the stability of the scanning conditions.

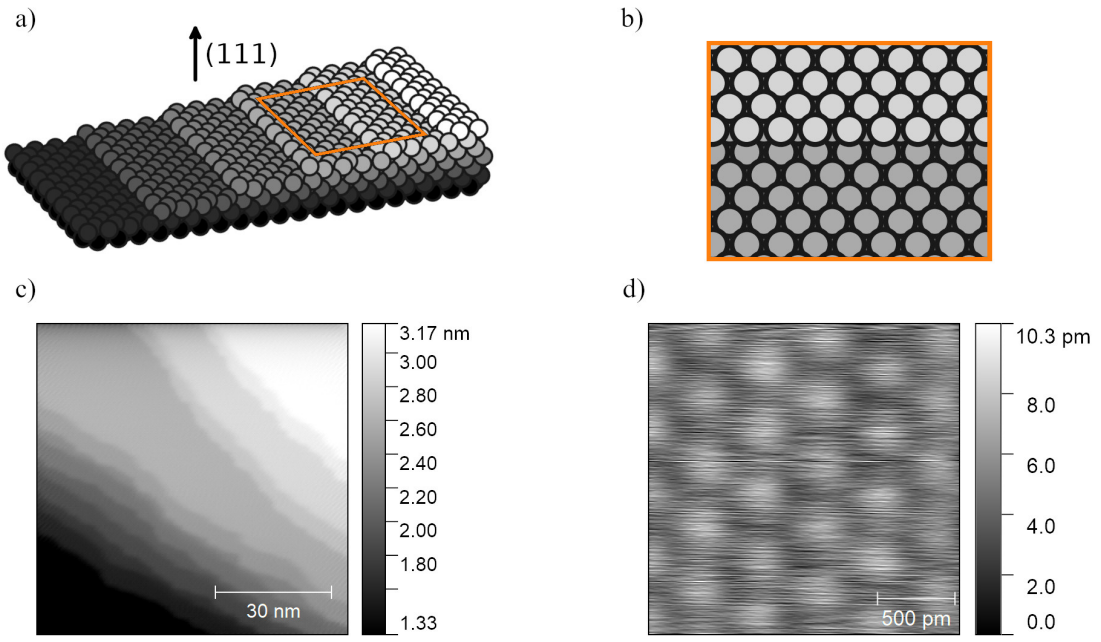

Figure 2.22: STM Topography imaging. a) Perspective and b) top view of a vicinal surface to the (111) face-centered cubic as obtained for the Pb (111) crystal probed here. c) Topography image of Pb (111) terraces measured by STM at low temperature. d) Zoom on one terrace with atomic resolution, measured at 15 mV and 1 nA.

2.6.2 Tunneling spectroscopy

Apart from topographic information, we are particularly interested in the electronic properties of our samples. As we will see in the next paragraph, this information can be accessed through scanning tunneling spectroscopy.
According to Tersoff and Hamann[3], the tunnel current in a STM tunnel junction can be approximated as

$$I(V_\mathrm{b}, z, \vec{r}_0) \propto \int_{-\infty}^{\infty} \left(f(E-eV_\mathrm{b}, T_\mathrm{t}) - f(E, T_\mathrm{s})\right) \rho_t(E-eV_\mathrm{b}) \rho_\mathrm{s}(E) |\Psi_\mathrm{s}(\vec{r}_0)|^2 dE \tag{2.6.11}$$

where $f(E,T)$ denotes the Fermi-Dirac distribution at energy E and temperature T, ρ_t the tip's density of states (DOS) and the term $\rho_\mathrm{s}(E)|\Psi_\mathrm{s}(\vec{r}_0)|^2$ the local density of states of the sample. Hence, for a known tip density of states, recording the tunnel current, or its derivative dI/dV, as function of the applied bias voltage V_b across the junction allows to recover the sample density of states ρ_s.

NIS Spectroscopy

As a first benchmark, we consider two superconducting samples measured at 58 mK cryostat temperature with a metallic PtIr tip. Using a lock-in amplifier, we record the tunneling conductance $\mathrm{d}I/\mathrm{d}V$ at a constant tip position. According to Equation 2.6.11, this is

$$\frac{\mathrm{d}I}{\mathrm{d}V} \propto \int_{-\infty}^{\infty} \frac{\partial f(E-eV_\mathrm{b}, T_\mathrm{t})}{\partial V_\mathrm{b}} \rho_\mathrm{s}(E) \tag{2.6.12}$$

[18] standard feedback parameters are $p = 2 \times 10^{-12}$ m/A, $\tau = 250\,\mu$s, $I_\mathrm{sp} = 300$ pA
[19] supplied by MaTeck GmbH

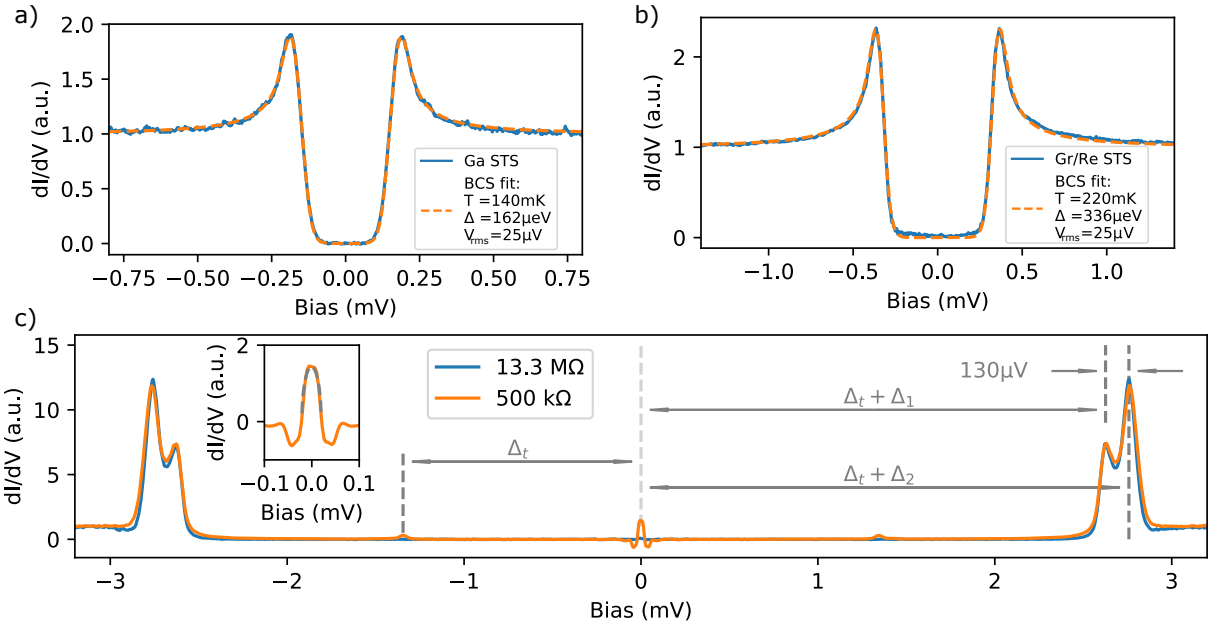

Figure 2.23: Scanning Tunneling Spectroscopy measurements at around 58 mK illustrating the achievable resolution. a) and b) Measurements with a normal PtIr tip and the corresponding BCS fit taking into account the lock-in broadening a) for α-gallium and b) for graphene on rhenium. c) Measurement with a Pb coated tip on Pb (111), forming an SIS tunnel junction. The two gaps of Pb, spaced by approximately 130 μV, are clearly resolved. At low junction resistances, the Josephson peak at $V_\mathrm{b} = 0\,\mathrm{V}$ and a peak at $V_\mathrm{b} = \Delta_\mathrm{tip} = 1.345\,\mathrm{mV}$ from Andreev reflection arise. The inset shows a zoom of the Josephson peak where the grey dashed line represents a delta like feature broadened by the lock-in excitation of $V_\mathrm{rms} = 15\,\mu\mathrm{V}$.

since we approximate the normal tip density of states to be constant over the considered bias range.
For both samples, we employ the BCS density of states

$$\rho_\mathrm{s} = N_0 \frac{E}{\sqrt{E^2 - \Delta^2}} \tag{2.6.13}$$

for fitting the tunneling spectrum of the superconducting gap according to Equation 2.6.12. N_0 here denotes the normal state conductance of the sample and Δ the superconducting gap.
The lock-in amplifier adds a sinusoidal excitation to the bias voltage. In the following, we denote V_AC the peak amplitude and $V_\mathrm{rms} = V_\mathrm{AC}/\sqrt{2}$ the root-mean-square amplitude of this signal. The full width at half maximum (FWHM) of the smearing it causes is $\sqrt{6}\ V_\mathrm{rms}$ [58]. Ideally, V_rms should be chosen such that this value is smaller than the FWHM of all features in the DOS. One can easily derive the exact shape of the broadening. It is given by the broadening function [58]

$$R(E) = \frac{2}{\pi V_\mathrm{AC}} \sqrt{(eV_\mathrm{AC})^2 - E^2}\ . \tag{2.6.14}$$

The measured signal is then the convolution of the broadening function with the samples "real" $\mathrm{d}I/\mathrm{d}V$, yielding:

$$\left[\frac{\mathrm{d}I}{\mathrm{d}V}(V)\right]_\mathrm{measured} \propto \int_{-eV_\mathrm{AC}}^{eV_\mathrm{AC}} \frac{\mathrm{d}I}{\mathrm{d}V}(V+E)\, R(E)\, \mathrm{d}E\ . \tag{2.6.15}$$

Another limiting factor for spectral resolution is the thermal broadening of the Fermi distribution in the tip, which has a FWHM of $3.5 k_\mathrm{B} T$.

Let us first consider superconducting α-gallium. The measurement was motivated by observations of topological properties in α-gallium [59] that rose the question whether this would

affect its superconductiving properties which have been studied for almost a century[60]. To our knowledge, no low-temperature scanning tunneling spectroscopies have been performed on α-gallium so far. In our measurements depicted in Figure 2.23 a), the spectra are very well reproduced by BCS theory and therefore show no signs of unconventional superconductivity. The critical temperature of α-gallium is reported to be $(1.08 \pm 0.01)\,\mathrm{K}$[61] which, assuming BCS like behavior, corresponds to a zero temperature gap of $\Delta = 164\,\mu\mathrm{eV}$ in perfect agreement with our observation. Additional measurements on this system, such as the determination of the temperature dependence of the gap, are currently ongoing but will not be discussed in further detail here.
Turning to the spectral resolution, the BCS fit taking into account the lock-in broadening yields an effective electronic temperature of approximately 140 mK. In this measurement, the lock-in amplitude of $V_{\mathrm{rms}} = 25\,\mu\mathrm{V}$ was chosen too large, since this corresponds to a temperature of $\sqrt{6}eV_{\mathrm{rms}}/(3.5k_{\mathrm{B}}) \approx 200\,\mathrm{mK}$. Thus, reducing the amplitude should lead to sharper coherence peaks. However, since the lock-in effect is taken into account by the fit, the estimated effective temperature should not be too far off.

The second sample consists of monolayer Graphene grown by CVD on a Re thin-film deposited on an Al_2O_3 (0001) substrate[20]. Its measured spectrum in Figure 2.23 b) is well reproduced by the BCS fit when assuming an effective electronic tip temperature of about 220 mK. The value for the superconducting gap $\Delta = 336\,\mu\mathrm{eV}$ is in agreement with a previous study of graphene on rhenium thin films[62] which explains the discrepancy to the gap on bare rhenium ($255\,\mu\mathrm{eV}$) thin films by a modified density of states of rhenium caused by dissolved carbon atoms. For graphene on a bulk Re(0001) single crystal, a gap of $\Delta = (280 \pm 10)\,\mu\mathrm{eV}$[63] was measured. The gap on bulk Re is increased much less since the C atoms are much more dilute in this larger Re volume.
We also note a small but finite conductance in the gap. The precise nature of this is not understood but most likely it is related to the graphene layer which is not intrinsically superconducting. This might also lead to a slightly increased effective temperature for the BCS fit.

From the two measurements discussed above, we conclude that our effective tip temperature is roughly around 140 mK, which corresponds to a FWHM smearing of about 40 µeV. We believe that the difference to the fridge temperature is mainly caused by bias noise since our setup possesses unavoidable ground loops. With a special wiring scheme and a tunneling preamplifier that actively senses and compensates fluctuations Le Sueur et al.[64] achieved 50 mK electronic temperature. Therefore, such a system might be an interesting candidate for improving the spectroscopic resolution in the future.

SIS Spectroscopy

Using a superconducting tip, instead of a normal metallic one, has several interesting implications.
First of all, one can make use of the very narrow coherence peak of the tip density of states to overcome the thermal broadening of the Fermi distribution, which allows to increase the spectroscopic resolution[65–67]. However, this comes at the cost of more difficult to interpret tunneling conductance measurements, since they show the convolution of the tip and sample density of states. Nevertheless, using more refined post processing methods, i.e. deconvoluting

[20] sample preparation by: V. Guisset, P. David, J. Coraux, substrate from B. Gilles

the two, one can recover the sample density of states. In Figure 2.23 on the bottom, we show the raw tunneling conductance data for a superconducting Pb-vacuum-Pb junction. When measuring at large tunnel resistance, shown in blue, one remarks two main differences with respect to the NIS spectrum, both caused by the convolution of the two superconducting densities of states:

- The size of the gap has doubled. In general, it is $2*(\Delta_{\text{tip}}+\Delta_{\text{sample}})$ wide, but since in this measurement tip and sample are made of the same material this simplifies to 4Δ.
- The coherence peaks are much narrower and higher, reflecting the increased resolution with this kind of tip.

A second implication is that when decreasing the tunnel resistance, i.e. approaching the tip closer to the sample, eventually the tunnel current will not only be carried by quasi-particles but also by Cooper pairs. This case is plotted in orange in the same figure which shows that the Cooper pair tunneling gives rise to several sub gap peaks which stem from two different origins:

- At zero bias, a super-current flows between the tip and the sample driven by a phase difference between the overlapping Cooper pair wave-functions in the two electrodes.
- At $V_n = \frac{2\Delta}{ne}$, where n is a natural number, due to Multiple Adreev reflections (MAR). The probability, and thus the spectroscopic weight, of MAR processes decreases monotonically with increasing n, which is why we only observe the peaks up to $n = 2$ [68,69].

A zoom on the Josephson peak at zero bias is plotted in the inset of Figure 2.23 c). In principle, the Cooper pair tunneling only occurs when the two Fermi levels of tip and sample are aligned. Thus, this feature has the shape of the delta distribution. However, experimentally the peak is broadened due to bias voltage fluctuations. As discussed above, for us the dominant source of these fluctuation is the lock-in amplifier. The broadened $\mathrm{d}I/\mathrm{d}V$ is plotted as a dashed grey line in the inset of Figure 2.23 c) using a delta distribution for the sample feature and employing the nominal $V_{\text{rms}} = 15\,\mu\text{V}$ applied by the lock-in. It reproduces the measured curve very well which implies that parasitic bias fluctuations and broadening due to the electromagnetic environment described by the $P(E)$ theory are small compared to these $15\,\mu\text{V}$. Conversely, the resolution of this measurement could have been increased by reducing the lock-in amplitude at the cost of a worse signal-to-noise ratio.
Note that the Josephson effect arising in an SIS junction allows for direct local measurements of the superconducting pairing order parameters [70–72]. This is of special interest for the study of unconventional superconductors such as high-T_c superconductors, heavy fermion materials and disordered superconductors [73–76].

A last feature of the spectra on Pb is that the coherence peaks are split into two peaks at $|eV_{\text{b}}| = \Delta_t + \Delta_1$ and $|eV_{\text{b}}| = \Delta_t + \Delta_2$. The occurence of the two peaks is a material property of lead which possesses two Fermi-sheets with different pairing energy, leading to the observation of the two gaps [66]. From the position of the Andreev peak, we can estimate the tip gap of $\Delta_{\text{t}} = (1.35 \pm 0.01)\,\text{eV}$. Subtracting this value from the coherence peaks at $(2.63 \pm 0.01)\,\text{meV}$ and $(2.76 \pm 0.01)\,\text{meV}$ yields $\Delta_1 \approx (1.28 \pm 0.01)\,\text{meV}$ and $\Delta_2 \approx (1.41 \pm 0.01)\,\text{meV}$. The spacing of $130\,\mu\text{eV}$ we observe between the two peaks is slightly smaller than the $150\,\mu\text{eV}$ observed by Ruby et al [66]. However, the more striking difference is that they observed a very different spectroscopic weight of the two peaks. In their measurements, the Δ_1 peak is a factor of four larger than the Δ_2 peak. However, in our measurement the weight difference is the other way around. The Δ_1 is about half as large as the Δ_2 peak. This looks much more like the spectra Ruby measured on Pb (110). Since we observed the hexagonal atom arrangement characteristic

for the (111) surface of the fcc crystalline structure of Pb, we are sure that we are measuring the (111) face. Thus, the origin of this discrepancy is unclear. Maybe the lead on our tip is not amorphous as we assumed and we are measuring (110) like features of the tip.
The fact that we can clearly resolve this splitting proves once more the good spectroscopic resolution we can achieve with our setup. Note that, unlike the authors of ref.[66] who are working at 1 K, our much lower tip temperature allows us to resolve this splitting even with a normal tip (see appendix D). This has been observed by Randeria et al. in their dilution temperature STM as well[72].

There are plenty of approaches for obtaining superconducting tips[65,77–79]. We use a PtIr tip, cut with a wire cutter at ambient conditions, which we deeply indent into a Pb(111) single crystal. Like this, the tip apex is coated with an amorphous, superconducting Pb film[66], which can be confirmed by spectroscopy measurements. Apart from being very simple to carry out, the advantage of this technique is that it allows to go back and forth between a normal tip and a superconducting tip by means of indentation, for Pb coating, and field-emission, for Pb removal.

2.6.3 Photon-assisted tunneling

As we have seen in the previous section, there are several tunneling processes involved in STS on superconductors. The picture becomes even more complex when considering hybrid systems with e.g. quantum dots, magnetic impurities or semiconductors coupled to the superconducting substrate. The competition of superconductivity with other interactions leads to the formation of supplementary subgap states such as Majorana, Andreev or Yu-Shiba-Rusinov states[80–87], which are not easy to distinguish from tunneling conductance measurements only. A very useful tool for gaining more insight on the underlying tunneling processes is photon-assisted tunneling (PAT), where tunneling spectroscopies are measured under the effect of an external radio frequency electromagnetic excitation[88,89].

Experimentally, we are applying this field by means of an antenna inside the cavity formed by the base temperature radiation screen which contains the SPM head and hence the tunnel junction. As shown in Figure 2.24, this antenna is simply the open end of a coaxial cable fixed at about 30 mm from the tunnel junction. During measurements, we noticed very pronounced resonances for the RF transmission. Good coupling occurs at a frequency of $f_{\mathrm{RF}} = 15.115\,\mathrm{GHz} = \Omega/2\pi$. This corresponds to a wavelength of 19.8 mm which is approximately $3/2$ of the antenna length of about 13.2 mm. We are therefore probably using the $(2/3)\lambda$ mode of the antenna.

Let us first consider the tunneling of quasi-particles, sketched in Figure 2.25 a). Without external excitation, the quasi-particles from the filled states on the left only find empty states on the right which they can tunnel to when $|eV| \geq 2\Delta$, where V is the applied bias voltage and Δ the superconducting gap. This leads to the peak in conductance at $2\Delta \approx \pm 2.75\,\mathrm{mV}$ for zero RF amplitude shown in Figure 2.25 d). However, when irradiating the junction with a finite electromagnetic field, inelastic tunneling processes involving the absorption or emission of photons can occur. Respectively, this means that k photons of frequency $\Omega/2\pi$ participating with their energy of $k\hbar\Omega$, create a peak in conductance when quasi particles tunnel from one coherence peak to the other, thus at a bias of $|eV| \geq 2\Delta \mp k\hbar\Omega$. Due to the quantized nature of this process, we observe a series of sidebands (better visible in Figure 2.25 e)) consisting of individual dots along the bias axis and whose spacing along the bias axis is $\hbar\Omega/e$. In order to understand the outer v-shape of the split peak, it is more instructive to think of the RF excitation in terms of the electric field and therefore the electric potential V_{RF} it induces between tip and sample. The

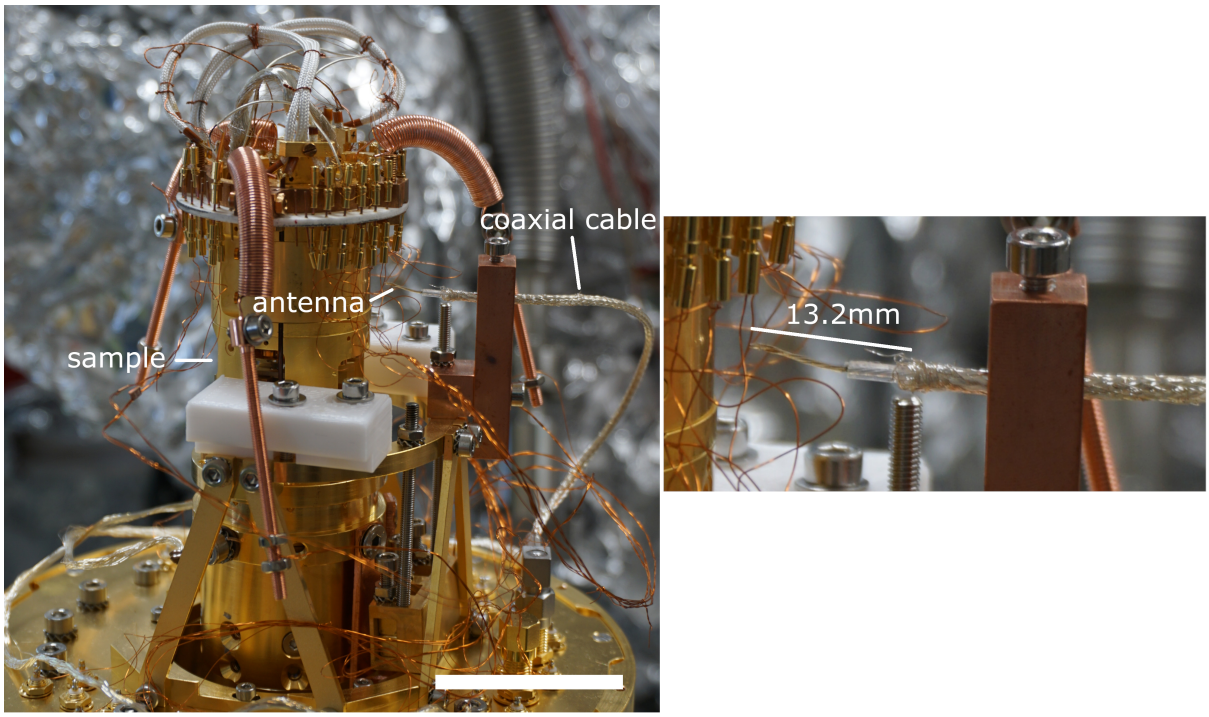

Figure 2.24: Radio frequency antenna for photon-assisted tunneling. Left: The RF-antenna used to inject photons into the tunnel junction. Note that in the measuring position the SPM is about 40 mm higher, such that the antenna is a few millimeter below the sample and at a distance of about 30 mm. Scale bar: 40 mm. Right: Zoom on the antenna, which is about 13.2 mm long.

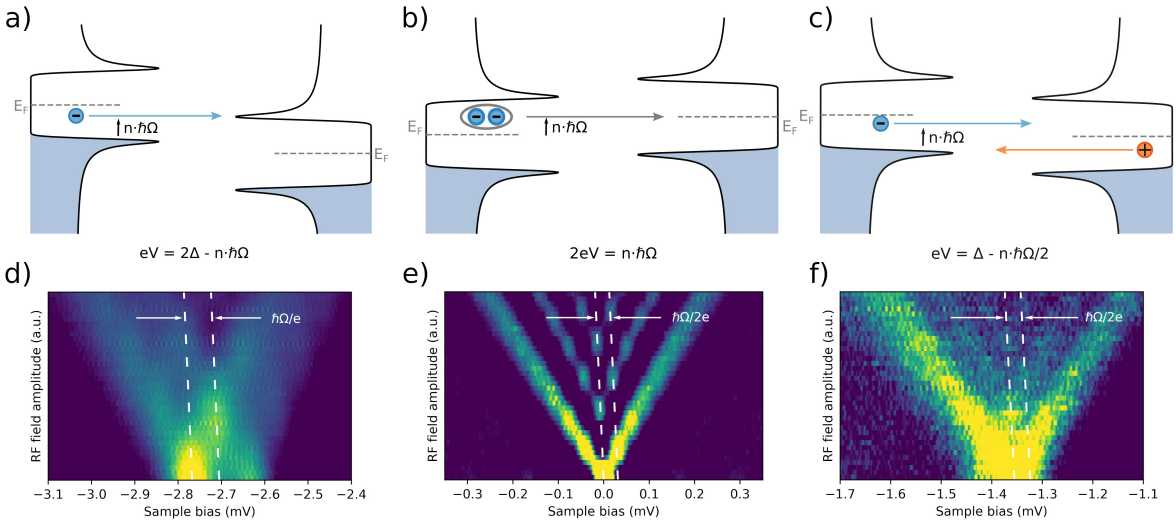

Figure 2.25: Examples of photon-assisted tunneling processes on a Pb (111) sample. a) Quasi-particle tunneling is a single electron process, d) which leads to $\hbar\Omega/e$ splitting of the sidebands. Due to the relatively large width of the coherence peaks and the presence of Pb's second coherence peak at around $-2.65\,\mathrm{mV}$, the features are rather washed out here. b) Cooper pairs transport a charge of $2e$ e) due to which a sideband spacing of $\hbar\Omega/2e$ is observed. c) The same holds for resonant Andreev reflections where an electron and a hole are involved and f) cause the same spacing. Measurements with a Pb tip on Pb. $\Omega = 2\pi \cdot 15.115\,\mathrm{GHz}$, $T = 58\,\mathrm{mK}$.

maximum energy a tunneling quasi-particle can draw from it is eV_{RF} which limits the number of photons Λ that can be involved in a tunneling process to $eV_{\mathrm{RF}} = \Lambda\hbar\Omega$, resulting in the linear field dependence of the outermost peak splitting.
Things slightly change when considering Cooper pair tunneling, sketched in Figure 2.25 b). Cooper pairs form due to attractive interactions between electrons and condense in a collective BCS ground state. According to the Josephson effect, they can also tunnel across a vacuum barrier. At zero RF-amplitude, this requires the energies of the two BCS ground states to be aligned, hence creating a peak in the conductance at zero bias voltage. Similar to the quasi-particle case described beforehand, photon induced inelastic tunneling occurs at finite RF field. The main difference is that the Cooper pairs carry a charge of $2e$, which is why an applied bias voltage changes their electro-chemical potential by $2eV$. As a consequence, sidebands occur at a spacing of $2eV = \hbar\Omega$, which is illustrated in the measurement of 2.25 e).
An analogous reasoning holds for the conductance peak at $\pm\Delta$ caused by an Andreev reflection process, sketched in Figure 2.25 c). In this case, a quasi-particle is retro reflected as a hole, transferring in this way a Cooper pair to the other side. The energy of the photons is shared between two particles, giving a tunnel condition of $|eV| = \Delta - k\hbar\Omega/2$, thus the same spacing as for the Josephson peak.

A more rigorous and quantitative analysis of the observed patterns which also explains the oscillating behavior of the sidebands along the field amplitude axis is given by the Tien-Gordon theory, yielding a tunneling conductance[88,90]

$$G(V) = \sum_n J_n^2\left(\frac{keV_{\mathrm{RF}}}{\hbar\Omega}\right) G^{(0)}(V + n\hbar\Omega/ke)$$

for the n-th sideband. J_n denotes the n-th Bessel function and $G^{(0)}$ the conductance without applied RF field. It reproduces nicely the observed pattern.

For other tunneling processes, the pattern might look different. For example in the case of Yu-Shiba-Rusinov states probed by photon-assisted tunneling, the observed pattern is V shaped for a small tunnel conductance when single-electron tunneling is dominant but changes to a Y shape for large conductance when resonant Andreev reflection becomes dominant[88]. This demonstrates once more that photon-assisted tunneling is a very helpful tool for understanding the underlying tunneling process of (sub-gap) conductance peaks.

Note that the use of the RF antenna is not only limited to this application. When working in an external magnetic field, the radio frequency excitation can be used to excite spin-flips on the sample, a process called electron spin resonance (ESR). Using a spin-polarized tip, the STM allows observing these processes at the single-spin level and with an energy resolution far beyond the thermal limit[91,92]. When combined with a DC-pump probe scheme, one can even observe the time evolution of single spins[93] or coupled spin systems[94], rendering this technique very insightful for the field of (quantum) spintronics.

3 Epitaxial monolayer $NbSe_2$ on graphene

Superconductivity is a fascinating macroscopic quantum effect. While conventional s-wave superconductivity is well explained by the BCS theory, unconventional superconductivity as it is found in high-T_C superconductors and other exotic systems still lacks proper understanding. Since the advent of 2D materials during the last decade, superconductivity has also been studied in the 2D limit. Excitingly, the restriction to two dimensions can significantly influence the superconducting properties.

Here, we want to study an epitaxially grown monolayer of the Transition Metal Dichalcogenide (TMD) $NbSe_2$ to learn more about the possibly unconventional superconductivity it hosts and to use it as a platform for engineering hetero-structures where topological superconductivity is predicted to emerge. With its low critical temperature of about 3 K, requiring measurements at sub-Kelvin temperatures for the opening of a full superconducting gap, as well as its sensitivity to oxidization, requiring handling under UHV conditions, it is a great material to exploit the strengths of our experimental setup.

In Section 3.1, we will first start by reviewing the state of the art and the key experiments required for understanding the motivation for this experiment. The second part of the chapter (Section 3.2) then presents our preliminary data. Since the study is not yet complete, there are no groundbreaking discoveries to be presented. The goal rather is to explain as many features as possible as a base for future work as well as to benchmark the quality of our monolayer $NbSe_2$ growth compared to the data published by Ugeda et al. who are leading this still young field of research.

Contents

3.1 State of the art

3.1.1 Ising superconductivity

In $NbSe_2$ the broken inversion symmetry and the strong spin orbit coupling (SOC) caused by the heavy transition metal leads to so called Ising superconductivity in the thin film limit[95]. In an Ising superconductor, spin orbit coupling creates an effective Zeeman field, which locks the spins in a certain direction (out of plane for $NbSe_2$). This reinforces the spin pairing in this direction such that an external applied magnetic field perpendicular to the internal field must then be much stronger in order to break the Cooper pairs by aligning the electron spins along the external field. Thus, the Pauli paramagnetic limit derived for free electrons can be significantly exceeded[96]. For monolayer $NbSe_2$, the in-plane critical field is about six times the Pauli limit[95].
The unconventional character of the superconductivity in $NbSe_2$ is further highlighted by the observation of a two-fold rotational symmetry of the in-plane critical field[96,97] while, in the absence of exotic effects, the honeycomb crystalline structure of $NbSe_2$ would rather imply a 120° symmetry.
STM data on monolayer $NbSe_2$ is still scarce. In their first studies of this material, the Ugeda group claimed to see signatures of disorder-induced fractal structures of the superconducting energy gap[98] and excitations outside the superconducting energy gap, interpreted as Leggett modes arising from the competition of two pairing channels: standard singlet s-wave and unconventional triplet f-wave pairing[99].

3.1.2 Towards topological superconductivity

Very technically speaking and in the most general definition, a topological superconductor is a superconductor with non-zero topological number such as the Chern number, which means that its wavefunction can not be transformed adiabatically to a combination of atomic wavefunctions. In a narrower sense, sometimes called strong topological superconductors also require a fully opened gap, such that subgap transport is only carried by gapless and topologically protected excitations called Majorana zero modes (MZM) which happen to be Majorana particles (particles which are their own antiparticles) and arise at the surface of the material or at topological defects. The ultimate motivation for studying these systems apart from the rather academic goal of realizing a Majorana fermion is the creation of quantum bits (qubits) which are topologically protected from decoherence[100,101].

Before we can tackle the implementation of applications such as topological quantum computing, we need to properly understand the basic interactions at play and how to tune them experimentally. Current strategies for inducing topological superconductivity rely either on proximity-coupling a semiconducting nanowire with strong spin orbit coupling to an ordinaty s-wave superconductor or by proximity-coupling magnetic nano-structures to a superconductor with strong spin orbit coupling[102]. Here we opt for the second approach, aiming for the fabrication of magnetic structures on the strong SOC superconductor $NbSe_2$. For this approach, the most studied systems are chains of magnetic adatoms, trying to implement the famous Kitaev chain[103] for creating Majorana zero modes[104]. Nevertheless, there are other, less explored, strategies such as two-dimensional magnetic islands in which topological edge states arise[105,106]. The two cited studies following this last approach used self assembled ferromagnetic adatoms on the surface, but with the recent developments of magnetic van der Waals materials such as the ferromagnetic CrI_3[107] an even wider range of combinations becomes

accessible experimentally. For now, there are very few reports on topological superconductivity in such van der Waals heterostructures[108].
Yet another strategy consists in using adsorbed magnetic molecules. The right choice of the ligands allows tuning the interaction to the substrate as well as between neighboring impurities, enabling the self assembly of complex structures[33,109,110].

Let us consider a bit more in detail the interactions between magnetic adsorbates and an underlying superconductor. The exchange coupling between the two materials gives rise to so called Yu-Shiba-Rusinov (YSR) states that appear as sub-gap states in spectroscopy measurements. The competition between superconducting pairing, characterized by the superconducting gap Δ, and Kondo-screening of the unpaired impurity magnetic momentum due to antiferromagnetic exchange coupling with the substrate, characterized by the Kondo temperature T_K, leads to two possible ground-states[111]:

- the Kondo screened singlet for $k_B T_K > \Delta$
- the unscreened doublet state for $k_B T_K < \Delta$

The peaks observed in spectroscopy correspond to the excitation of the system of one of these states to the other one, which will occur at energies inside the superconducting gap. In tunneling spectroscopy, two peaks appear at energies symmetrical around the Fermi energy. However, their spectroscopic weight is in general asymmetric due to a difference in the local weights of the electron and hole wave functions of the YSR bound state[112].
Scanning tunneling spectroscopy has been a very helpful tool for understanding the exchange coupling at the single-atom scale. In 1997, Yazdani et al. discovered localized YSR states around magnetic adatoms. Since then, their orbital structure[29,113,114] as well as the role of charge transfer[115,116] have been investigated.
Exploiting the versatility of the STM, two interesting experiments can be performed. First, mechanical interactions with the STM tip (pushing or pulling on the adsorbate) allow tuning the exchange coupling J and therefore also the Kondo temperature. Like this, one can drive the system through the quantum phase transition[112,117]. Second, atoms can be arranged in a controlled way, such that the coupling of several YSR states can be studied. It has been shown that the YSR states hybridize[118] and even form bands for long chains[17]. Topological superconductivity and Majorana zero modes have been predicted to exist in this kind of system[119], which is why they have been intensely studied in order to precisely understand the conditions for the formation of such topological states[17,120–122].

On three-dimensional superconductors, YSR states decay as $1/(k_F r)$ where k_F is the Fermi wave vector and r the radius from the impurity. Since k_F is small, the decay occurs over sub-nanometer distances, limiting the available parameter space to weak coupling between adjacent magnetic impurities. However, in two-dimensional systems, the confinement leads to a slower decay of the YSR states, namely $1/\sqrt{k_F r}$, which allowed their spatial mapping on a nano-meter length scale, compatible with inter-molecular distances[29]. On bulk $NbSe_2$, chains of impurities such as cobalt phthalocyanine[123] or Fe atoms[17] hybridize and form YSR bands, but without signatures of Majorana zero modes. Even though $NbSe_2$ is a layered material, already showing two-dimensional like behavior in its bulk form, we expect to be able to increase the coupling even further by going to the single layer limit.
Summarizing, the epitaxially grown monolayer of $NbSe_2$ we propose to use here, is a rich platform for investigating (unconventional) superconductivity in two dimensions as well as the influence of a wide range of different impurity structures that can influence the superconductivity through their magnetic properties or through charge transfer.

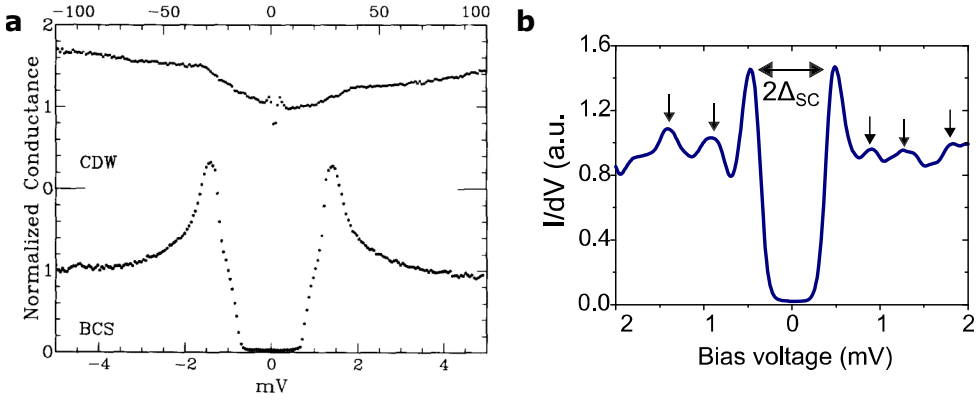

Figure 3.1: a Tunneling spectra on bulk $NbSe_2$ showing the CDW gap measured at 4 K on the top and the superconducting gap measured at 50 mK on the bottom. From ref.[21]. **b** Superconducting tunneling spectrum measured on single-layer $NbSe_2$ on bilayer graphene measured at 340 mK. From ref.[124].

3.1.3 Other properties of $NbSe_2$

In its bulk form, $NbSe_2$ is a well studied material. Here we will focus on the most relevant results for this study.

First and foremost, we already discussed that the reduced dimensionality heavily alters the superconducting properties. The most straight-forward parameter to look at is the critical temperature. Indeed, it decreases with a decreasing number of layers from the bulk value of about 7 K to approximately 3 K in the single layer limit[95,125]. This has two important implications: first of all, $NbSe_2$ stays superconducting even in the monolayer limit and second of all, its critical temperature is significantly reduced, such that for a proper measurement of the fully opened superconducting gap one requires at least a 1 K or even better a sub-Kelvin environment with good electronic filtering, like the one we built and which is described in Chapter 2.

Naturally, the density of states probed by tunneling spectroscopy is also affected. Figure 3.1 compares two such measurements, showing on the left a measurement on bulk $NbSe_2$ and on the right one of the few available spectra on single-layer $NbSe_2$. First of all, the decrease in critical temperature goes along with a decreased value of the superconducting gap from $\Delta_{bulk} \approx 1.4\,meV$[21] to $\Delta_{1L} \approx 0.4\,meV$[124]. The bulk spectrum clearly shows a shoulder which has been interpreted as either a multigap or a strongly anisotropic superconductor. Recent ab-initio calculations attribute to a real-space anisotropy of the gap[126], rejecting the multigap scenario. In the single-layer, the spectrum does not seem to feature such a shoulder. Its band structure must therefore be distinctly different from bulk $NbSe_2$. Another peculiarity in the single-layer case is the emergence of peaks outside the gap, which have been interpreted as superconducting collective modes stemming from competing pairing instabilities[99].

In single-layer $NbSe_2$, the effect of the substrate is potentially strong. A recent study investigated the influence of four different substrates on the superconducting properties of single layer $NbSe_2$[124]: epitaxial graphene on SiC, bulk Au(111), single-layer boron nitride and bulk WSe_2. On the metallic Au(111), a strong coupling and charge transfer from the substrate significantly alter the band structure and destroy superconductivity. On WSe_2, the bandstructure is almost unaffected, but the coupling to the substrate is strong enough to destroy superconductivity. It only persists on the very weakly coupled hBN and graphene substrates. For STM measurements it is much more practical to have a fully conducting sample surface, thus out of the two candidates, the epitaxial graphene on SiC is the only suitable one for us. Furthermore, it is rather easy to produce this kind of substrate and have a homogeneous coverage of the entire sample surface[127,128].

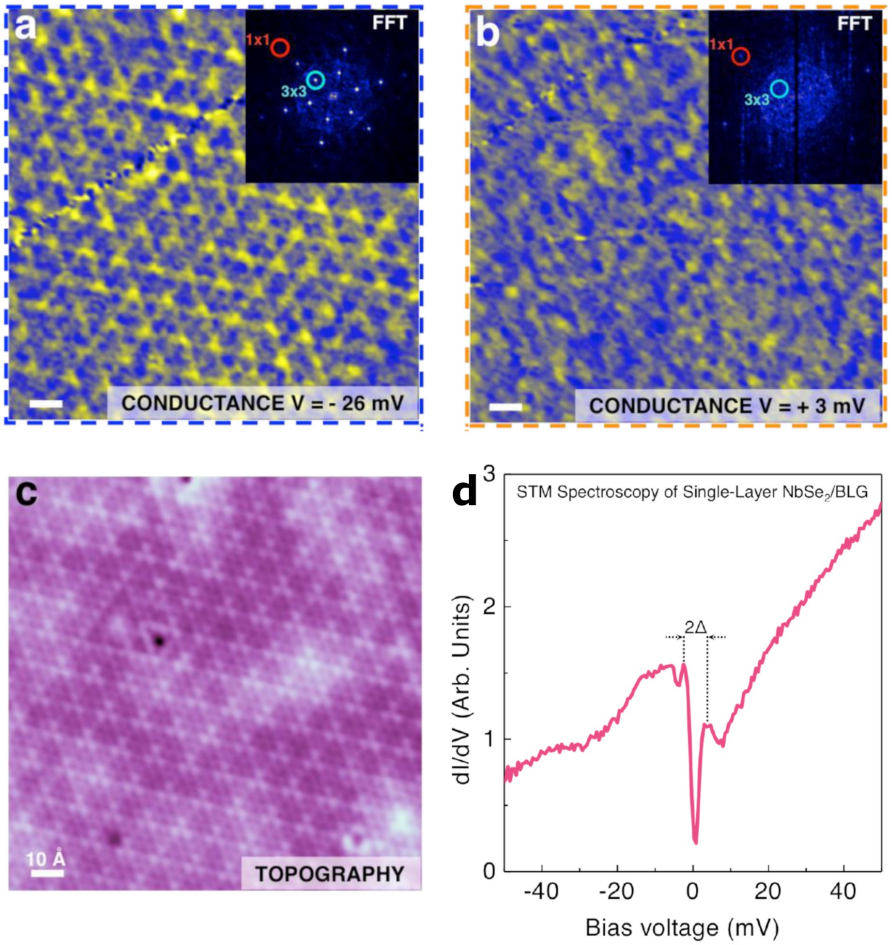

Figure 3.2: Charge Density Wave in monolayer $NbSe_2$ on bilayer graphene. Conductance maps taken at **a** $V = -26\,\mathrm{mV}$ and **b** $V = 3\,\mathrm{mV}$ ($f = 871\,\mathrm{Hz}$, $I = 40\,\mathrm{pA}$, $V_{\mathrm{rms}} = 0.6\,\mathrm{mV}$, $T = 5\,\mathrm{K}$). The FFTs in the insets allow identifying the Bragg (1x1) and CDW (3x3) peaks. **c** STM topograph of the same region as a and b ($V = -17\,\mathrm{mV}$, $I = 40\,\mathrm{pA}$, $T = 5K$). **d** Bias spectroscopy measurement on single-layer $NbSe_2$/BLG showing the CDW gap (Δ) measured at $I = 100\,\mathrm{pA}$, $V_{\mathrm{rms}} = 0.6\,\mathrm{mV}$, $T = 5\,\mathrm{K}$. Reprinted with permission from ref.[125].

Another effect observed in $NbSe_2$ is the formation of a quasi commensurate 3x3 charge density wave below 33 K[125]. The origin of this charge density wave has been controversially discussed and mechanisms such as Fermi-surface nesting[129–131] and saddle point singularities[132] have been proposed but the most recent experiments point to electron-phonon coupling to be causing this CDW[125,133–138]. The above mentioned studies of the CDW consider bulk 2H-$NbSe_2$. However, since the electron-phonon coupling seems to be the origin of the CDW, it might be significantly altered by the substrate in the monolayer limit. Therefore, it is natural to ask if the CDW will persist in monolayer $NbSe_2$. Until now, there are only very few studies, but they confirm the persistance of the CDW in monolayer $NbSe_2$ on several substrate systems[124,125,139], including MBE-grown $NbSe_2$ on bilayer graphene on SiC which is very close to what we use for our experiment.
Figure 3.2 a) depicts a conductance map of the triangular CDW lattice in monolayer $NbSe_2$ on bilayer graphene. This map has been measured outside the dip of about $\Delta \approx 4\,\mathrm{meV}$ which is observed in the tunneling spectroscopy of Figure 3.2 d). When mapping the conductance inside the dip, as it is done in Figure 3.2 b), no signs of the CDW are observed. This becomes very clear when comparing the FFTs of the maps shown in the insets. Outside the dip, the 3x3 peak at $1/3$ of the atomic lattice peaks (1x1) is clearly visible, but within the dip it vanishes com-

pletely. The authors of[125] therefore interpret this dip as the CDW gap. However, a DFT study of freestanding monolayer $NbSe_2$ [140] motivated by these measurements does not find a clear gap opening up due to the CDW which questions the interpretation of the experimental data. Finally, a nicely resolved image of the CDW is shown in the topography image of Figure 3.2 c). Interestingly, even though Figure 3.2 only shows one type of CDW order, theoretical ab-initio calculations[140–142] as well as experiments[139] have shown that in the monolayer limit, several 3x3 CDW distortion patterns have nearly the same stability and can therefore coexist, which leads to spatial phase boundaries. Furthermore, the CDW may show up differently depending on the bias voltage.
Note that the CDW gap is anisotropic and leaves large parts of the Fermi surface ungapped[136], which ultimately allows its coexistence with superconductivity.

3.1.4 The Proximity effect

As we will see below, our sample is not fully covered by $NbSe_2$, so that relatively large areas of the non-superconducting graphene substrate are accessible by STM.

When a normal metal is in contact with a superconductor, the correlations present in the superconductor leak out into the normal conductor, which transfers a part of the superconductor's properties such as the Meissner effect[145], a modified density of states with the opening of a (mini)gap[18,143,146] and the ability to transport supercurrents[147] to the normal material.

The key microscopic process to explain this behavior is the Andreev reflection which we will discuss briefly. When an electron like quasiparticle (later just electron) of energy $E_F + \varepsilon$ with $\varepsilon < \Delta$, momentum $k_F + \delta k/2$ and spin σ coming from the normal metal impinges on the N-S interface, it can not simply continue traveling into the superconductor since there are no available states at this energy. However, in a second order process, a second electron of energy $E_F - \varepsilon$, momentum $-k_F - \delta k/2$ and spin $-\sigma$ can be transferred to the superconductor simultaneously, forming a Cooper pair in the superconductor and leaving behind a hole in the normal metal. The important point here is that this is a coherent process, so that the reflected hole carries phase information of the incoming electron and the superconducting phase. In other words, the two electrons of the normal metal that transit to the superconductor are correlated and form an Andreev pair, which is very similar to a Cooper pair with the difference being that there is no pairing interaction between them. Naturally, the inverse process of a Cooper pair breaking and injecting two correlated electrons into the normal metal is also possible.

In the systems we are interested in, we find ourselfs usually in the dirty limit, where the relevant length scales are larger than the mean free path l, so that the electron transport is diffusive. However, the phase coherence of the Andreev pair is conserved over the much larger coherence length

$$L_\varepsilon = \sqrt{\frac{\hbar D}{\varepsilon}}$$

where $D = v_F l/2$ is the diffusion coefficient, v_F the Fermi velocity and l the mean free path in the normal metal. Only beyond this length, the phase coherence is lost and the Andreev pair breaks[148]. The dynamics of this coherently diffusing system is described by the so called Usadel equation[149].
Let us now discuss the implications of the proximity effect on the density of states in the normal metal by means of the STM data of Le Sueur et al.[143] shown in Figure 3.3 a). The investigated device consists of a normal silver wire contacted by a closed superconducting aluminum lead. The loop like structure allows imposing a finite phase difference across the silver wire by applying an external magnetic field. For the device shown on the top, without phase gradient, the

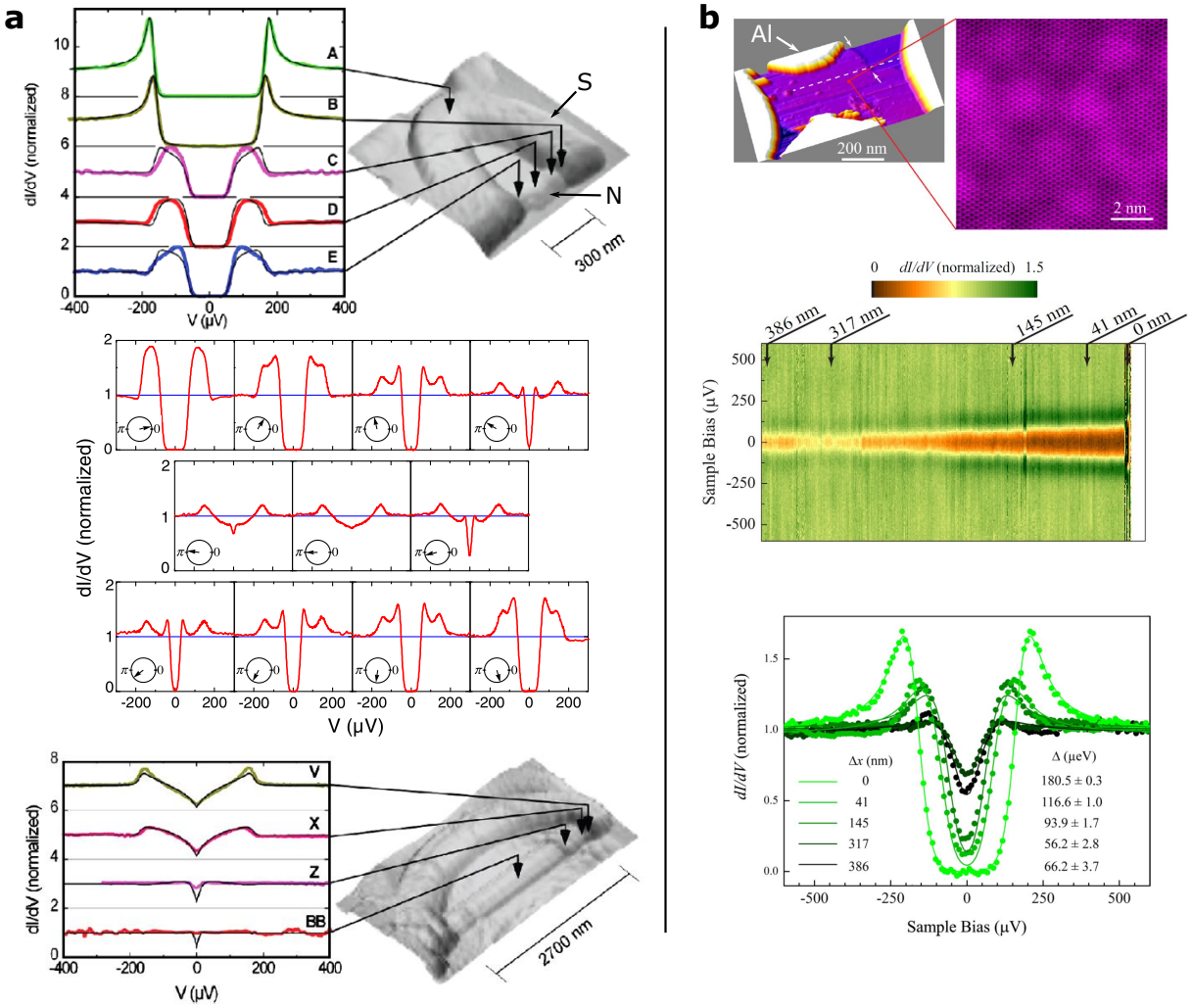

Figure 3.3: STS measurements of the proximity effect. **a** Aluminium (S) / silver (N) SNS junction in a loop like geometry for the generation of a phase difference induced by an external magnetic field. The top plot shows spectra for the field free case. Black lines are simulations. With external field (bottom), a finite phase difference can be imposed. Depending on the parameters position, phase and geometry, a multitude of different spectral shapes can be observed. Reprinted with permission from[143]. **b** Al on islands on few layer graphene on SiC (0001). The conductance map along the dashed white line shows a decay of the minigap induced in graphene over several hundreds of nanometers. Individual spectra are plotted on the bottom. Reprinted with permission from[144].

length of the normal section L is shorter than the coherence length. The normal metal therefore obtains superconducting properties all along its length, with the opening of a minigap $\delta < \Delta$. The size of this gap is on the order of the Thouless energy

$$E_{\mathrm{T}} = \frac{\hbar D}{L^2} \,.$$

All quasiparticles at energies below δ form Andreev pairs and are hence gapped out. We therefore obtain a double peak structure with peaks at Δ and δ. In the shown example, both peaks merge into one broad peak. When imposing a phase difference, the minigap undergoes a 2π periodic suppression, reaching a minimum of $\delta = 0$ at a phase difference of π. We see this very well in the plots in the center of Figure 3.3 where the two inner peaks at δ come closer together when the phase difference approaches π.
Finally, moving on to the long wire on the bottom of 3.3 a), we notice that the tunneling conductance now has more of a triangular shape and only approaches zero at zero bias. In this geometry, the phase coherence length is inferior to the normal metal size. Therefore, the system has to be imagined as being open to one side. Electrons coming from the open end are necessarily uncorrelated and therefore contribute to a finite tunneling conductance and thus prevent the formation of a full gap. As a take home message, we note that the geometry is an important parameter for the shape of the tunneling conductance.
We now consider graphene as the normal conductor. Due to its peculiar dispersion relation and relativistic charge carriers, it is not obvious that this material can be proximitized and carry a supercurrent and that the diffusive model used in metals can be applied. Nevertheless, transport measurements confirmed a robust supercurrent and Josephson effect through graphene sheets[150] and the validity of the diffusive model for junction lengths of $L = 200 - 400\,\mathrm{nm}$[151]. An STM study of the proximity effect in graphene by Natterer et al.[144] is shown in Figure 3.3 b), which investigates a sample structure very close to ours. Their sample consists of superconducting aluminum islands deposited on top of few layer graphene on SiC (0001). The aluminum therefore induces superconductivity in the two-dimensional graphene substrate. Furthermore, there are many aluminum grains that contribute from several sides. The authors investigate the spectra along the dashed line highlighted in the topography image. The resulting spectra are presented in the form of a conductance map in the middle and as a plot of selected individual spectra on the bottom. A clear dip at zero bias is observed even at hundreds of nanometers from the interface. However, unlike on the contact, the tunneling conductance never goes to zero on the graphene, not even at zero bias close to the interface. The dip width is also smaller than the gap on aluminum. Concerning the spatial evolution, the size of the dip decays as the tip moves away from the aluminum island until it starts increasing around 317 nm again, when the tip actually starts approaching another aluminum island. A similar behavior but with a quicker decay has also been observed by Cortés-del-Río et al.[152] in graphene next to Pb islands. We therefore expect to observe something comparable in our sample.

3.2 Preliminary results

In this section, we will discuss the preliminary results we obtained on the first $NbSe_2$ samples. The first step of the study is to understand the structure and properties of the graphene substrate and the bare $NbSe_2$ thin film. Adding magnetic structures is a second step to be realized in future studies.

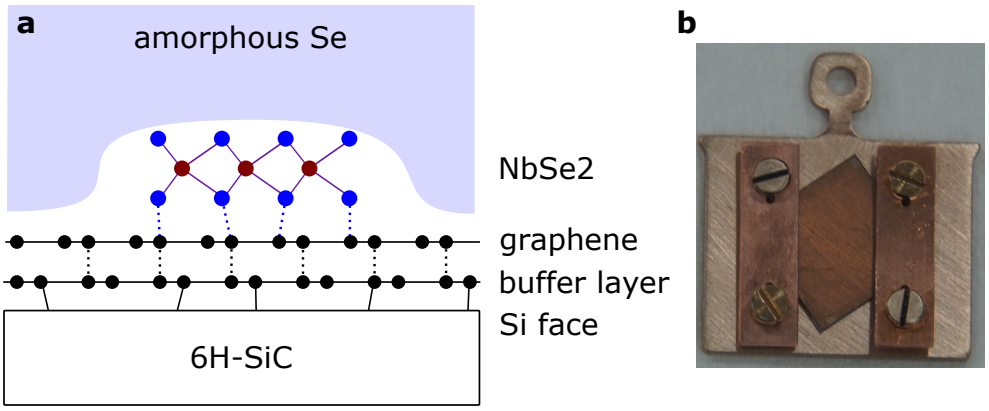

Figure 3.4: The $NbSe_2$ sample. **a** Cross-sectional sketch of the sample. Solid lines represent covalent bonds, dotted lines Van der Waal interaction. Distances are not to scale. **b** Photo of the mounted 10 mm × 10 mm sample before insertion into the UHV chamber.

3.2.1 Sample fabrication

As mentioned above, we investigate monolayer flakes of $NbSe_2$ grown by molecular beam epitaxy on epitaxial graphene on SiC. The coverage of the $NbSe_2$ is on the order of 50 % for the main sample investigated here. It can be monitored by reflection high energy electron diffraction (RHEED) during the growth process. As a result of the sub-monolayer coverage, we expect the formation of individual islands, separated from each other by areas of the bare graphene substrate. Figure 3.4 a) shows a sketch of the sample structure. The bulk 6H-SiC substrate carries a first carbon layer, often denoted as the "buffer" layer since it is still covalently bound to the substrate. This strong bonds alter its electronic properties, so it does not possess a linear dispersion like free-standing graphene. The superposition of the C and the SiC lattice forms an incomensurate 6x6-SiC modulation. On top of that we have one or more layers of graphene, which grows in a Bernal stacked position with respect to the buffer layer. It only has van der Waals bonds to the buffer layer below, leaving its band-structure unaffected. For simplicity, we will refer to this system just as "graphene" in the following. The 6x6 modulation of the buffer induces a 40 pm high honeycomb like corrugation with a wavelength of 1.9 nm in the graphene layer[153]. Note that due to the Bernal stacking, the buffer and the graphene layer do not form a Moiré.
On top of this graphene substrate, the monolayer $NbSe_2$ islands are also only connected through van der Waals forces.
Finally, we deposit a several tens of nanometer thick amorphous Se layer atop the whole structure to protect it against oxidation during the transport through air from the MBE chamber to the STM setup. Thanks to the very low melting point of Se, this layer can easily be desorbed by a light annealing inside the STM's preparation chamber.
Let us briefly review the sample fabrication parameters which were performed by Vincent Renard for the graphene growth and by Mathieu Jamet for the $NbSe_2$ growth. For the **graphene growth**, the 6H-SiC sample is placed inside a graphite crucible in a controlled Ar or Ar/H_2 atmosphere. The crucible can be heated inductively and the temperature is controlled using several pyrometers. The growth involves several steps: first, annealing at 900 °C for 18 min to remove adsorbates, followed by a 30 min 1600 °C etching in Ar/H_2 (9/1) to reconstruct atomically flat terraces about 5 µm wide. The H_2 is then flushed out at 900 °C for 30 min before launching the surface graphitization at 1600 °C in 1 atm static Ar for 20 to 30 min. Finally, the sample is cooled back slowly to room temperature. Since the graphene surface is very robust, the sample can then be transferred through air to the MBE chamber without any special precau-

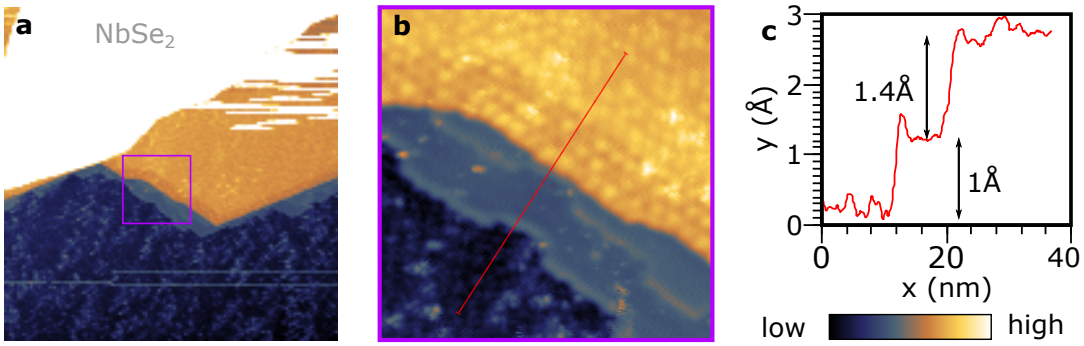

Figure 3.5: Topography data of the graphene substrate. **a** 200 nm × 200 nm scan at $V_b = 50$ mV and $I = 20$ pA showing a step in the graphene substrate. The white area is a $NbSe_2$ flake. **b** 40 nm × 40 nm zoom as indicated by the purple rectangle in a. Same parameters. The top part clearly shows the substrate induced hexagonal modulation which is absent in the central plateau and less clear on the bottom part. **c** Height profile along the red line in b. The overall step height corresponds to a step in the SiC substrate of 2.5 Å.

tion. Adsorbed water will desorb during heating to 650 °C before starting the growth.
The **$NbSe_2$ growth**[1] is performed at 650 °C sample temperature with a niobium evaporation rate of 0.0125 Å/s in a 1×10^{-6} mbar Se atmosphere until the $NbSe_2$ signal can be seen by RHEED. Subsequently, the sample is annealed at 725 °C for 15 min before being capped with about 10 nm of amorphous selenium.
The photo in Figure 3.4 b) shows the 10 mm × 10 mm sample before loading it into the STM preparation chamber. The copper clamps hold the sample in place and assure the electric contact to the graphene layer on the surface. This is crucial, since the SiC bulk is insulating. Once inside a 3×10^{-10} mbar environment, we **remove the protective Se layer** by annealing the sample at roughly 250 °C (measured by a pyrometer) for one to two hours. During this process, the pressure in the chamber increases to roughly 2×10^{-9} mbar when the Se desorbs and then slowy comes back to the 10^{-10} mbar range.

3.2.2 Structural properties

Let us now turn to the STM measurements performed between 50 mK and 4.2 K.

Graphene substrate

The first element to be characterized is the graphene substrate. Figure 3.5 shows topography data of a step in the substrate. In Figure 3.5 a), we distinguish four plateaus. The dark blue, light blue and orange planes belong all to the graphene substrate. The white area is a several Å higher $NbSe_2$ flake. Here we focus on the graphene, and take a closer look on the step in Figure 3.5 b). Clearly, the higher, orange plateau possesses a hexagonal modulation compatible with the 6x6-SiC modulation expected in graphene on SiC. Interestingly, the same structure is not visible on the light blue intermediate plateau. The dark blue plateau has some modulations, but they are not as pronounced as on the orange plateau. If we consider the quantitative step heights as indicated in 3.5 c), we conclude that the overall step of 2.4 Å corresponds to a step of the SiC substrate, which has a nominal height of 2.5 Å [128]. Since the interlayer distance in graphite is about 3.3 Å [154] and therefore much larger than what we see here, we can exclude that the step originates from different numbers of graphene layers grown on top of the SiC

[1] The parameter in the main text are for sample 2502. For 2529 shown in Appendix E, the values are 690 °C deposition temperature, 0.0125 Å/s Nb rate, 780 °C annealing for 15 min.

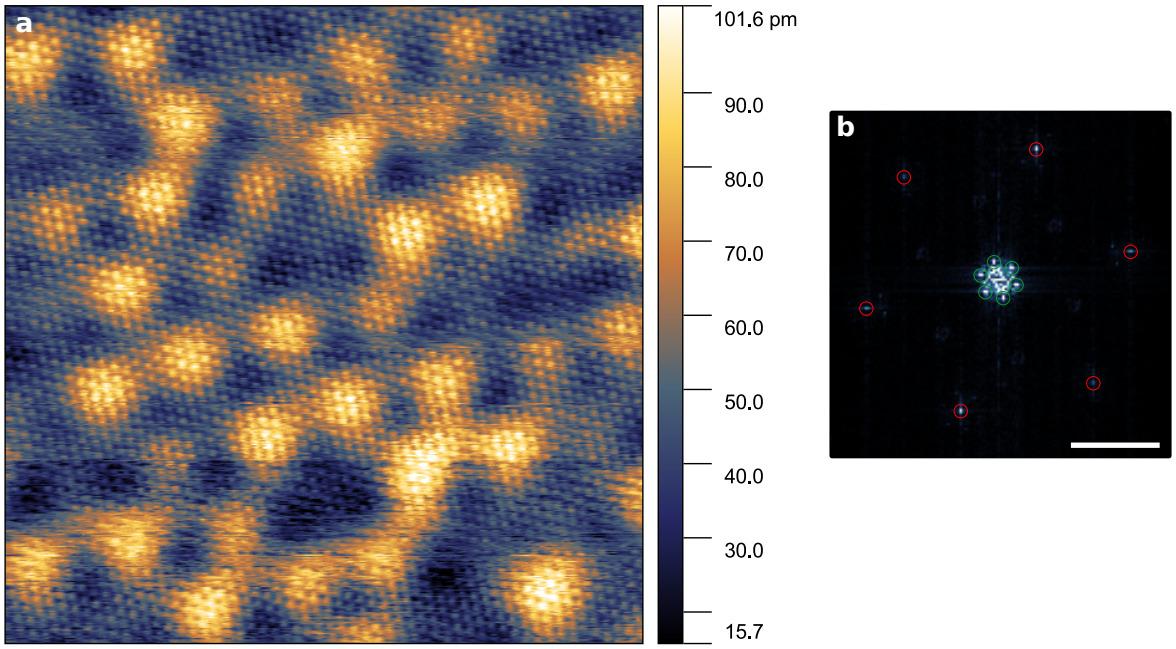

Figure 3.6: Topography image of the graphene substrate. **a** 15 nm × 15 nm topography scan recorded at V_b = 10 mV and I = 500 pA, showing the atomic lattice as well as the substrate induced 6x6-SiC modulation compatible with observations on bilayer graphene. **b** FFT of a. In green, the peaks corresponding to the 6x6-SiC modulation, in red the Bragg peaks of the graphene lattice. The scalebar is 2.5 nm^{-1}.

substrate. The precise nature of the intermediate, light blue plateau remains unclear. It could be a somehow intercalated graphene layer, a second graphene layer beginning to form next to the step edge with an unknown microscopic structure of the underlying SiC-graphene interface, etc. In principle, one could argue that this might be a tip artefact, reproducting the step of the substrate, but in that case we would expect to see the 6x6 modulation also on the light blue area.

Let us now consider a bit more in detail the graphene in the orange region of Figure 3.5. An atomically resolved 15 nm × 15 nm topography image of it is depicted in Figure 3.6 along with its two dimensional Fast Fourier Transform (FFT). From the FFT, we find that the periodicity of the modulation is about 7.4 times that of the graphene lattice. Using the graphene lattice constant of 2.45 Å[155], this gives a lattice constant of 1.8 nm for the modulation, in agreement within uncertainties with the theoretical value of 1.9 nm for the 6x6 modulation that is defined relative to the SiC substrate[153]. We can further take a look at the amplitude of the corrugation caused by the 6x6 modulation. Its peak to peak amplitude is about 40 to 50 pm, compatible with DFT calculations[153]. A last detail we observe is that the atomic lattice has a contrast such that one of the two graphene sublattices light up. This is in contrast to free-standing graphene (e.g. on hBN), where one observes both sublattices and the bonds between them. This sublattice symmetry breaking is caused by the AB (Bernal) stacking of the graphene layer on top of the buffer layer and is usually observed on a bilayer of graphene[156,157].

As a final side note, we remark the large size of the substrate terraces. In the 2.5 µm × 2.5 µm scan of Figure 3.7 a), only one step is visible in the very corner of the image. It's height is (4.7 ± 0.2) Å, so probably two bunched SiC steps of 2.5 Å each.

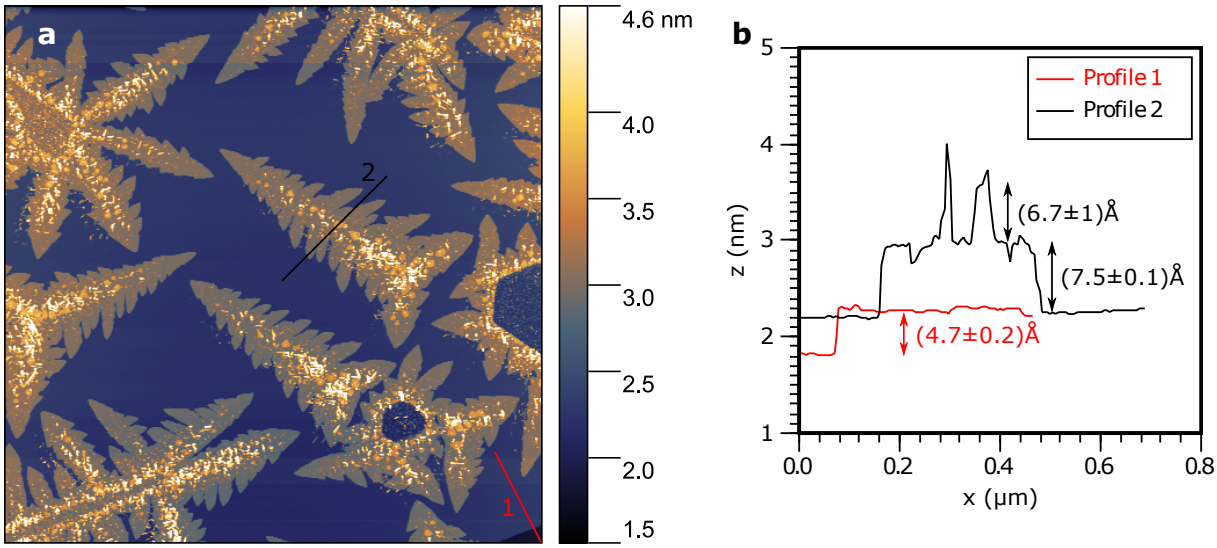

Figure 3.7: $NbSe_2$ islands on graphene. **a** $2.5\,\mu m \times 2.5\,\mu m$ topography STM scan of recorded at 750 mV and 20 pA. **b** height profiles as indicated on the left. Profile 1 shows a 4.7 Å high double step of the SiC substrate, profile 2 a 7.5 Å high $NbSe_2$ island with 6.7 Å high dirt which might be a second $NbSe_2$ layer.

NbSe2 Islands

On larger topography images, like the one depicted in Figure 3.7 a), we see the $NbSe_2$ islands (orange) that grew on top of the graphene substrate (blue). First, we note that, as expected from RHEED measurements, the surface is roughly 50 % covered with $NbSe_2$.
Second, taking a look at the height profile 2 in Figure 3.7 b), we note that the thickness of the islands is about 7.5 Å, which confirms that the islands are really made of monolayer $NbSe_2$[98]. Third, the islands on sample $NbSe_2$-Gr 2502 have a dendritic shape with lots of small branches whereas in other studies these islands look more compact[98] or even triangular[158]. This indicates that the adatom mobility during growth is low, leading to out-of-equilibrium shapes. At higher growth temperature, the islands would become more compact. However, the sticking coefficient decreases with temperature, resulting in a lower growth rate[158]. Be aware that around 600 °C, $NbSe_2$ undergoes an irreversible phase transition from the 2H to the 1T polymorph which is a Mott insulator (with a gap of 0.4 eV) and therefore not superconducting[159]. Since our sample is still nicely superconducting, we still have a 2H polymorph, so probably the temperature measurements of our growth is not directly comparable to the one from the cited study.
The fourth remark we make is that on top of the islands we see additional structures. The more or less homogeneous dark orange patches are, according to the profile 2 in Figure 3.7 b), about (6.7 ± 0.1) Å above the monolayer $NbSe_2$, and therefore most likely represent a second $NbSe_2$ layer. Apart from this, there are even higher and less regular structures in white, which are probably excessive Nb or $NbSe_2$. Our first hypothesis was that it is remaining Se from the capping layer. However, we could rule this out by heating the sample up to about 500 °C, far above the melting temperature of Se, in 9 annealing steps with increasing temperature and imaging the islands every time. We essentially did not observe any change induced by these annealing steps. Furthermore, the second sample $NbSe_2$-Gr 2529 presented in Appendix E for which the $NbSe_2$ growth was performed at a higher sample temperature, does not show this kind of structure. This corroborates the explanation that it is Nb or $NbSe_2$ that was not mobile enough to fully rearrange to its equilibrium position.

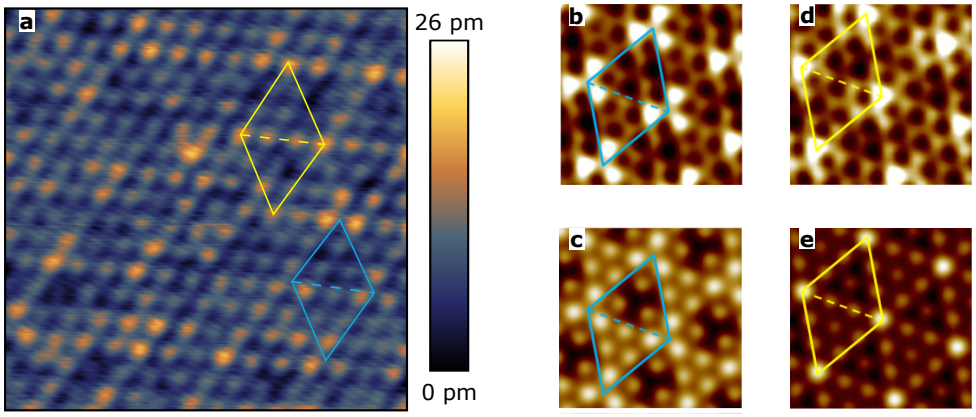

Figure 3.8: Charge density wave on monolayer $NbSe_2$. **a** Our atomically resolved $5\,nm \times 5\,nm$ STM scan at $V_b = 50\,mV$ and $I = 300\,pA$ exhibiting several patterns compatible with a charge density wave. **b-e** measurements (top) and simulations (bottom) of two phases of the charge density wave of bulk $2H$-$NbSe_2$ reprinted from[139]. The overlay highlights the resemblance between the bulk phases and our measurement on monolayer $NbSe_2$.

Let us now zoom back in on the atomic scale, but this time on the $NbSe_2$. The resulting topography scan resolving the individual atoms can be seen in Figure 3.8 a). Signs of a charge density wave are visible and form a superstructure of brighter atoms. We observe triplets of bright atoms (at the corners of the blue diamond), like in Figure 3.2 and like on bulk 2H-$NbSe_2$ depicted in Figure 3.8 b) and c). These triplets mark the corners of a triangular structure where one half of the triangles is a bit brighter than the other half. This reproduces very nicely the simulation shown in Figure 3.8 c). However, the CDW we observe is not very pronounced and seems to be spatially varying. At some positions, instead of a triplet of bright atoms it seems like only one atom is lighting up. One example is overlaid with the yellow diamond. This could correspond to one of the six other CDW phases that can coexist in $NbSe_2$. Possibly, the scanned area is just around a phase boundary between the two phases like it has been observed on bulk $NbSe_2$ [139]. Therefore, we confirm that the CDW exists in epitaxial monolayer $NbSe_2$ and that it does not differ notably from the bulk CDW.
From an experimental point of view, it is not easy to obtain atomic resolution on $NbSe_2$. The coupling between $NbSe_2$ and the graphene substrate seems to be very weak since, at large tunnel currents on the order of 1 nA at around 50 mV, we observed that an entire $NbSe_2$ island got displaced under the effect of the tip. Larger tunnel resistances and hence smaller sample-tip interactions as they have been used for the scans in Figure 3.2 seem to work better.

3.2.3 Spectroscopic features

Band structure

In Figure 3.9, we show two bias spectroscopies recorded on graphene. Let us first consider the red curve, recorded on the orange graphene area of Figure 3.5. On the eV scale, it shows the typical strongly asymmetric V-shape, usually observed for graphene on SiC[160]. As highlighted in the inset of the same figure, around zero bias, the spectrum has a symmetric gap with a width of approximately 84 mV at its bottom. This is also a typical feature observed on graphene on SiC which is caused by inelastic tunneling processes involving surface phonon and plasmon modes[157,161]. For monolayer graphene on SiC, substrate induced doping shifts the Dirac point to about $-0.39\,V$[162]. In multilayer graphene, the Dirac point can easily be estimated by its characteristic local minimum in the tunneling conductance[160,163,164]. As expected we observe such a minimum around $-0.4\,V$. However, features in the bias spectroscopy

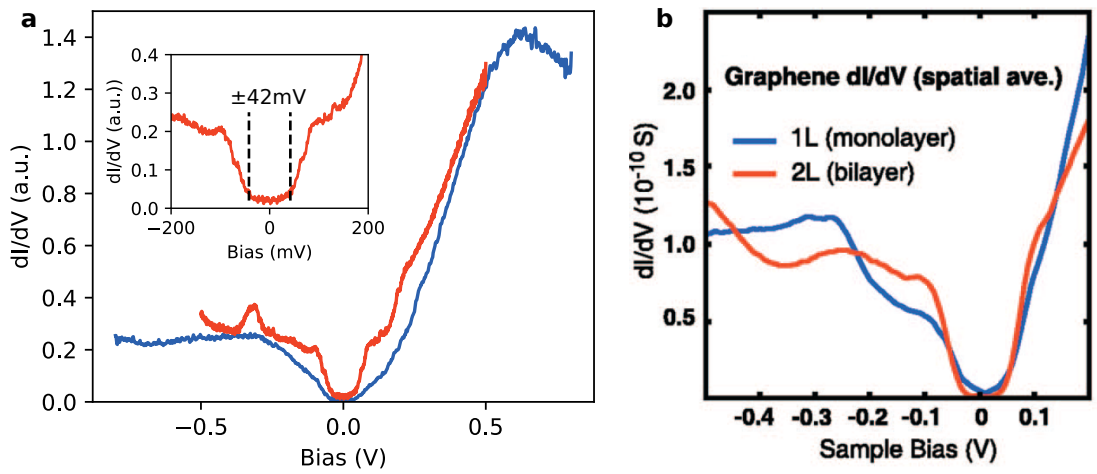

Figure 3.9: Bias spectrosocpy of graphene on SiC. **a** Measurements at different positions of our graphene sample. The inset shows a zoom on the zero bias gap which is symmetrical around zero. **b** Spatially averaged reference measurement from[157] showing the same kind of zero bias gap, electron-hole asymmetry and presence or absence of a local minimum around −0.4 V.

are usually strongly influenced by disorder and therefore spatially vary a lot[157], which is why we would need more statistics to ensure that the observed minimum is really the Dirac point. An unambiguous determination of the Dirac point can be obtained by tracing the dispersion relation using quasiparticle interferences[162,165] but this requires a lot more effort.
Let us now turn to the blue curve that was recorded far away on a different graphene area of the sample. In this curve, we can not identify a dip that could be attributed to the Dirac point. This might indicate that in this area we only have a monolayer of graphene, as reported by Lauffer et al.[163] as well as by Brar et al.[157] shown in Figure 3.9 b).

Moving on to spectroscopy measurements on monolayer $NbSe_2$, on a large bias range we find a spectrum as it is plotted in Figure 3.10 a). It exhibits several characteristic peaks and steps caused by van Hove (VH) singularities and flat regions of the conduction (C) and valence band (V) in the band structure depicted in Figure 3.10 c). They perfectly coincide with the spectrum measured by Dreher et al.[124] on the same system, shown in Figure 3.10 b), and are in agreement with Angle-Resolved PhotoEmission Spectroscopy (ARPES) measurements. Note that the positions of the annotated features in Figure 3.10 a) are exactly the same as in b).

Superconductivity

Let us now focus on spectroscopic features around zero bias, namely the superconducting gap. The spectrum in Figure 3.11 a) was recorded with a normal PtIr tip at 57 mK. It shows a well developed superconducting gap of approximately $\Delta = 380\,\mu\text{eV}$ which is in agreement with the $400(20)\,\mu\text{eV}$ reported by Dreher et al.[124] shown in Figure 3.1. The effective temperature of about 350 mK found in our fit is much higher than the cryostat temperature of 57 mK and also larger than the effective temperature of 140 mK we found during our benchmark measurements (see Section 2.6.2). This high electronic temperature was caused by bias noise induced in a badly shielded BNC cable used during this measurement. I identified this problem on a different sample after having finished the measurements on $NbSe_2$, so the gap should be remeasured on the next $NbSe_2$ sample using the good cable.

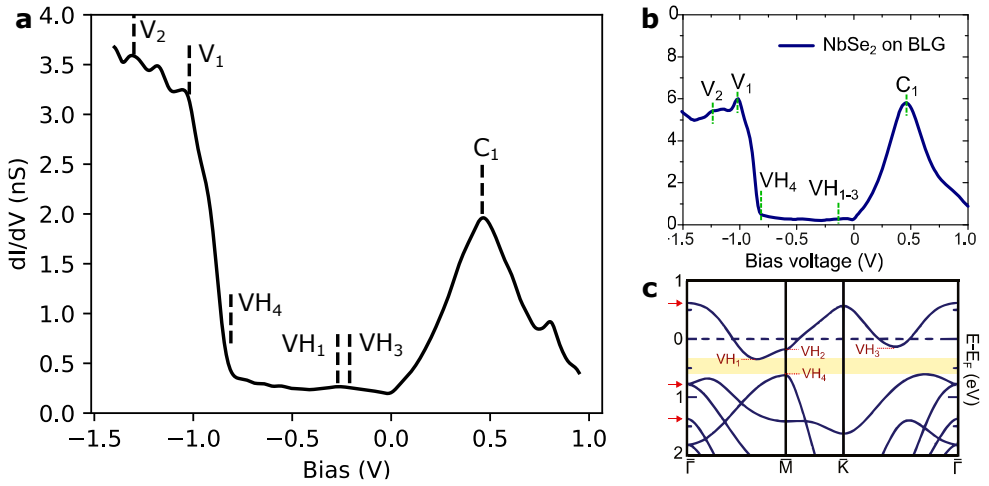

Figure 3.10: Bias spectrosocpy and band structure of $NbSe_2$. **a** Bias spectroscopy of monolayer $NbSe_2$ measured on our sample, showing the same characteristic features as in a previous study[124] shown in **b** and which can be explained by the band structure of free standing monolayer NbSe obtained by DFT[140] in **c**. The finite conductance between VH_4 and VH_1, i.e. inside the band gap of $NbSe_2$ is caused by the graphene substrate.

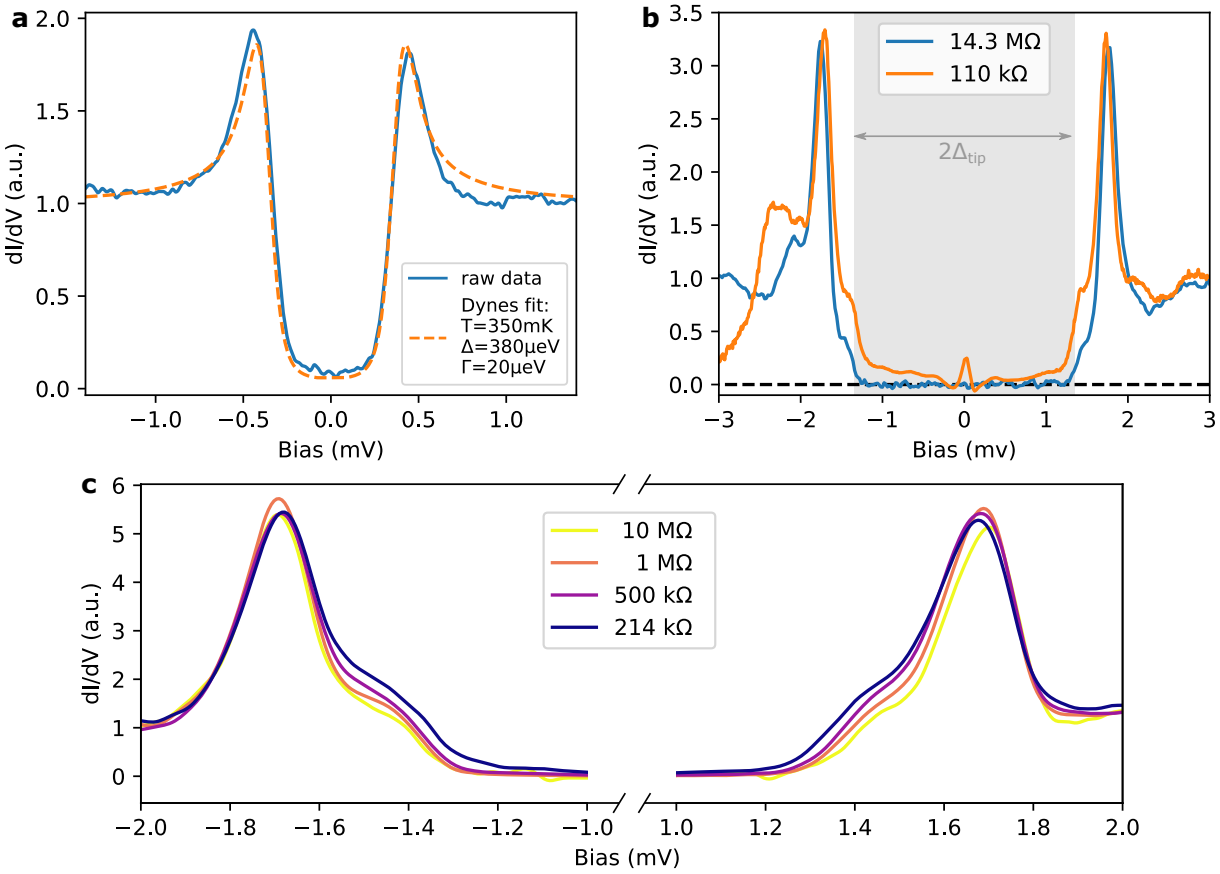

Figure 3.11: Superconductivity in monolayer $NbSe_2$ probed by STS. **a** NIS spectrum with a normal PtIr tip recorded at 57 mK, $V_b = 1.5\,\text{mV}$, $I = 1\,\text{nA}$, $V_{rms} = 15\,\mu\text{V}$. Unlike Dreher et al.[124] (Fig. 3.1 b) we do not observe peaks above the gap. **b** SIS spectrum measured with a Pb tip at 50 mK. At low resistance, the Josephson peak at zero bias emerges and the relative weight of the shoulder of the coherence peak at approximately $\pm 1.4\,\text{mV}$ increases compared to the measurement at larger resistance. The grayed area indicates the gap of the tip. **c** Tunneling resistance dependence measured at 54 mK. The spectra are rescaled to a normal state conductance of one.

The Dynes parameter[2] $\Gamma = 20\,\mu eV$ we need for fitting the finite conductance inside the gap is larger than the $\Gamma = 10\,\mu eV$ Dreher et al. report. As pointed out by ARPES at 1 K[136], the finite sub-gap conductance might originate from the anisotropic nature of the superconducting gap which includes gapless regions. However, we favor the interpretation that it is caused by inverse proximity effect from the intrinsically normal graphene below. Following the model by McMillan[146], the tunnel coupling between graphene and $NbSe_2$ results in the formation of a minigap $\Omega_N < \Delta_{NbSe_2}$ in graphene. Above Ω_N, one expects a finite density of states in the superconductor as well. As we will see in Subsection 3.2.4, the minigap could be on the order of $2\Omega_N = 140\,\mu eV$. The unfortunately high effective temperature of 350 mK leads to FWHM smearing of about 106 µeV such that we can not resolve the expected hard gap between $\pm 70\,\mu eV$. However, in a future measurement using the good wiring configuration, we can exploit the 140 mK effective temperature to check this hypothesis.

On larger bias windows than shown here[3], we do not observe a clear CDW gap of $\Delta_{CDW} \approx 4\,meV$ reported by Ugeda et al.[125] (see Figure 3.2). Our measurements are therefore more in line with the DFT calculations from Silva-Guillén et al.[140].

By coating the tip with Pb from a Pb (111) single crystal, we render it superconducting as well and can perform SIS spectroscopy. The observed bias spectroscopies are shown in Figure 3.11 b). Like for the case of the Pb-Pb junction presented in Section 2.6.2, all features are pushed outwards by the gap of the tip of approximately 1.35 meV[67] as indicated by the gray shade in the background. We find an unexpected shoulder of the coherence peaks inside the $NbSe_2$ gap whose tunnel resistance dependence is investigated further in Figure 3.11 c). There we see, that the relative weight of the shoulder increases slightly with decreasing resistance and hence by lowering the tip.
A trivial explanation of the occurrence of this shoulder could be the finite density of states observed in the NIS spectroscopies which, convoluted with the peaked DOS of the tip, would lead to peaks in the SIS spectroscopy at $\pm\Delta_{tip}$. Since we observe the shoulder at tunneling resistances as large as 10 MΩ and given that the change of the relative weight with tunneling resistance is rather small, we can exclude that it originates from Andreev reflection. Another hypothesis is that this signal stems from tunneling through the $NbSe_2$ layer into the normal quasiparticles of the graphene below. Z-Spectroscopy measurements on both materials show that the decay length Z_0 on graphene is roughly 20 % smaller compared to $NbSe_2$ (see Appendix E.5). Approaching the tip would therefore lead to a stronger increase of graphene's contribution to the tunnel current and thus be consistent with the observed tip height dependence. Eventually, the double peak structure might come from the anisotropic superconductivity of $NbSe_2$. In bulk $NbSe_2$ a similar structure has been observed[126]. The peak splitting there is about 0.4 meV compared to the 0.3 meV observed here. However, the gap in general is larger in bulk $NbSe_2$ due to the interlayer interactions. For properly attributing the peaks we observe to the same origin, simulations of a monolayer system would be required.

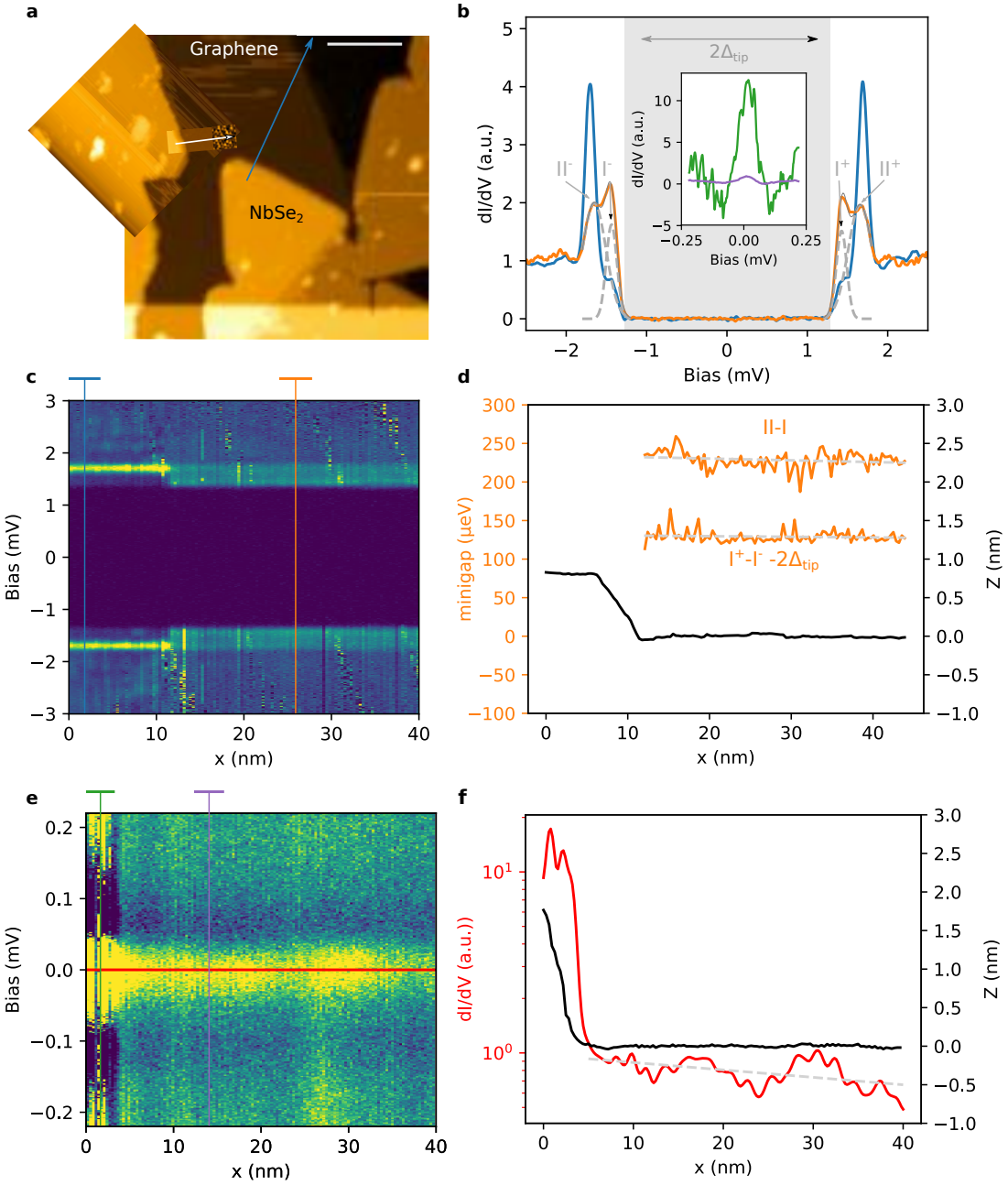

Figure 3.12: Proximity-induced superconductivity in graphene. **a** Topography scans of the investigated area. The line scan in e was measured along the white arrow. The map in c was measured at approximately the same position, but starting further into the $NbSe_2$ flake. The blue arrow indicates the approximate position of the measurements shown in Fig. E.2. Scale bar 50 nm. **b** Spatially averaged spectroscopies extracted from the map in c and e as indicated by the colored bars where the vertical line corresponds to the center position of the spectrum and the horizontal line on top to the length it is averaged on. The peaks of the spectrum on graphene (orange) fit well with a double Gaussian (gray) with $\mu_{I^\pm} = \pm 1.43\,\mathrm{mV}$, $\sigma_{I^\pm} = 65\,\mu\mathrm{V}$ and $\mu_{II^\pm} = \pm 1.65\,\mathrm{mV}$, $\sigma_{II^\pm} = 147\,\mu\mathrm{V}$. For the inset the curves are scaled to have the purple peak at 1. **c** Line scan recorded at $V_b = 3\,\mathrm{mV}$, $I = 300\,\mathrm{pA}$, $V_{rms} = 15\,\mu\mathrm{V}$. **d** Size of the minigap extracted from the peak positions of the double Gaussian fits exemplified in b. The dashed lines are linear fits giving (II-I): $-(-0.2 \pm 0.1)\,\mu\mathrm{eV nm^{-1}}\; x + (235 \pm 4)\,\mu\mathrm{eV}$ and ($I^+ - I^-$) assuming a tip gap of $\Delta_{tip} = 1.31\,\mathrm{meV}$: $(-8 \pm 8) \times 10^{-2}\,\mu\mathrm{eV nm^{-1}}\; x + (131 \pm 3)\,\mu\mathrm{eV}$. In black: topography for the line scan in c. **e** Line scan recorded at $V_b = 3\,\mathrm{mV}$, $I = 12\,\mathrm{nA}$, $V_{rms} = 15\,\mu\mathrm{V}$. **f** Amplitude of the Josephson peak along the red line in e. dashed gray: linear fit to the Josephson peak with a slope of $(-7.5 \pm 0.8) \times 10^{-3}\,\mathrm{nm^{-1}}$. In black: topography for map e.

3.2.4 Proximity superconductivity in graphene

As discussed in Section 3.1.4, the contact between the $NbSe_2$ and the graphene is expected to induce proximity superconductivity in graphene. Due to the large mobility of charge carriers in graphene, one can expect the effect to extend over much larger length scales than in normal metals.

In our experiment, we use a superconducting Pb tip for measuring bias spectroscopies at several hundred points along a line, starting on an $NbSe_2$ island and then moving onto the graphene and away from the $NbSe_2$ as indicated by the white arrow in Figure 3.12 a). We repeat the measurement with different conditions, each time focusing on a different aspect.

Let us start by considering the spectra at relatively large tunnel resistance of 10 MΩ in Figure 3.12 c). As expected from the topography scan, the line scan shows two regions, corresponding to the two different materials: the $NbSe_2$ on the left and the graphene on the right. Overall, both regions look spatially very homogeneous. On the $NbSe_2$, some oscillations outside the gap are visible. Two of these states are mapped over 60 nm × 60 nm in Appendix E.3.

The spatial average over about 10 nm on the $NbSe_2$ is plotted in blue in Figure 3.12 b). As discussed previously, it shows the coherence peaks at $\pm 1.69\,\mathrm{mV}$ corresponding to $\pm(\Delta_{\mathrm{tip}}+\Delta_{\mathrm{NbSe_2}})$. Since we have not characterized the tip on a metallic reference, we can not precisely disentangle the tip from the sample contributions for an accurate quantitative analysis of the gap size. On the contrary, let us use this measurement to estimate the gap of the tip. Recalling that the gap of $NbSe_2$ measured with the normal tip was 380 µeV we find $\Delta_{\mathrm{tip}} \approx 1.31\,\mathrm{mV}$, which is a reasonable value for Pb. We note that we once again observe the shoulder discussed in Figure 3.11.

Considering the orange spectrum in Figure 3.12 b) which represents the spatial average of spectra on graphene, we note a double peak structure. It fits very well with the sum of two Gaussians $\mu_{\mathrm{I}^\pm} = \pm 1.43\,\mathrm{mV}$, $\sigma_{\mathrm{I}^\pm} = \pm 65\,\mu\mathrm{V}$ and $\mu_{\mathrm{II}^\pm} = \pm 1.65\,\mathrm{mV}$, $\sigma_{\mathrm{II}^\pm} = \pm 147\,\mu\mathrm{V}$, where μ defines the peak position and σ its standard deviation. In the following, we will discuss two possible explanations for this double peak structure. Once again, since we do not know the precise tip density of states, we can not give a definitive conclusion on which of the hypothesis is the correct one.

The first possibility is that graphene has an induced hard gap around zero bias and shows a double peak structure like the measured convoluted signal. As we discussed in the theory Section 3.1.4, such kind of densities of states can occur in a closed short wire geometry (see Figure 3.3 a)). A short wire scenario could be explained in our case by a large coherence length in graphene due to its large charge carrier mobility together with the fact that our $NbSe_2$ islands are a maximum of a few hundred nanometers apart. Following this scenario, the minigap needs to be estimated from the data by determining the distance between the peaks I^+ and I^- and subtracting the gap of the tip density of states $2\Delta_{\mathrm{tip}} = 2.62\,\mathrm{meV}$ deduced from the measurement on $NbSe_2$. The spatial evolution of the resulting minigap size is represented by the lower orange curve of Figure 3.12 d). A linear fit yields $(-8\pm 8)\times 10^{-2}\,\mu\mathrm{eV nm^{-1}}\,x + (131\pm 3)\,\mu\mathrm{eV}$. Thus, there is no significant slope detectable on the length of 35 nm of our measurement.

The second scenario is that the density of states in the graphene does not reach zero even at the center of the gap, as it has been observed by previous STM measurements on proximity superconducting graphene (see Figure 3.3 b)). In this case, we observe a first peak (I) as soon as the Fermi energy of the sample is aligned with the coherence peak of the superconducting

[2] The Dynes formula models the superconducting DOS as $\rho_{\mathrm{Dynes}} = N_0 \left|\mathrm{Re}\left(\frac{E-i\Gamma}{\sqrt{(E-i\Gamma)^2-\Delta^2}}\right)\right|$ where N_0 is the normal state conductance, Γ the Dynes parameter and Δ the superconducting gap [166].

[3] see Appendix E.4 for an example

tip. The second peak (II) is then the actual coherence peak of the graphene density of states. Hence, for the determination of the minigap size we have to take the difference between the peaks I and II, which is plotted on the top of Figure 3.12 d). The linear fit to this data yields $-(-0.2 \pm 0.1)\,\mu\text{eV}\text{nm}^{-1}\,x + (235 \pm 4)\,\mu\text{eV}$. The uncertainty here is still large, but the slope is clearly negative, indicating the expected weakening of the pairing with increasing distance from the contact in a long wire scenario. Assuming an exponential decay, this would correspond to a decay length lying between 680 nm and 2.3 µm. Note that in this scenario, the gap on $NbSe_2$ measured here at the edge of the island would only be $1.69\,\text{meV} - 1.43\,\text{meV} = 260\,\mu\text{eV}$ and therefore much smaller than the 380 µeV observed by NIS spectroscopy further away from the edge. However, under the same assumptions, the other dataset in Appendix E.2 would give a $NbSe_2$ gap of 330 µeV.

Next, we present a novel approach for studying the proximity effect. For this, we reduce the tunneling resistance between the graphene and our superconducting tip from 10 MΩ down to 300 kΩ to enter the Josephson regime in which we can study how Cooper pair tunneling varies spatially. The measurement in Figure 3.12 e) shows a clear peak at zero bias on the $NbSe_2$ which continues with a lower intensity on graphene. Here as well, two spatially averaged spectra are extracted and plotted in the inset of Figure 3.12 b). Both, the green curve measured on $NbSe_2$ as well as the purple curve measured on graphene clearly show the peak at zero bias surrounded by two dips of negative conductance, as expected for the Josephson peak. Not surprisingly, the amplitude of the purple peak on the graphene is about 12 times weaker. Nevertheless, it is present and significantly larger than the noise floor. This provides an unambiguous proof that superconducting correlations exist in graphene. We can now look at the spatial variations of the peak amplitude along the zero bias line highlighted in red in Figure 3.12 e). The corresponding profile is shown in Figure 3.12 f), where it is compared with the topography measured at the same time. First of all, we see a strong correlation of the peak amplitude and the topography, i.e. the strong decrease of peak amplitude at the transition of $NbSe_2$ to graphene. From this, we conclude that the coupling between the two is not very strong and thus the transparency of the interface for Cooper pairs is rather low.

The linear fit of the peak amplitude on graphene drawn by a dashed gray line gives a slope of $(-7.5 \pm 0.8) \times 10^{-3}\,\text{nm}^{-1}$. Assuming once more an exponential decay, this would correspond to a decay length between 120 nm and 150 nm. Compared to the length scales deduced at larger tunneling bias, this range is much more in line with the observations of Natterer et al [144] shown in Figure 3.3 b). However, the fact that the line scan is approaching the next flake towards its end but does not show an increase in the Josephson amplitude raises further questions. The second dataset presented in Appendix E.2 does not show a decay over its length of 90 nm. Therefore, the data we have up to now is not conclusive. More statistics is necessary to gain a proper understanding of the important parameters. The corresponding measurements are ongoing and will hopefully shed light on this in the near future.

A last note concerns the black topography curve in Figure 3.12 f). Interestingly, the height difference between the $NbSe_2$ and the graphene is about 2 nm even though it is supposed to be about 0.8 nm for the single $NbSe_2$ layer as it is observed in Figure 3.12 d). Since the bias used for the height regulation is the same in d) and in f) this difference has to be explained by the Josephson current which is only significant in f). It contributes much stronger on $NbSe_2$ than on graphene. To obtain the same overall current, the tip therefore approaches the graphene more than the $NbSe_2$ which results in the increased step height observed in the topography data.

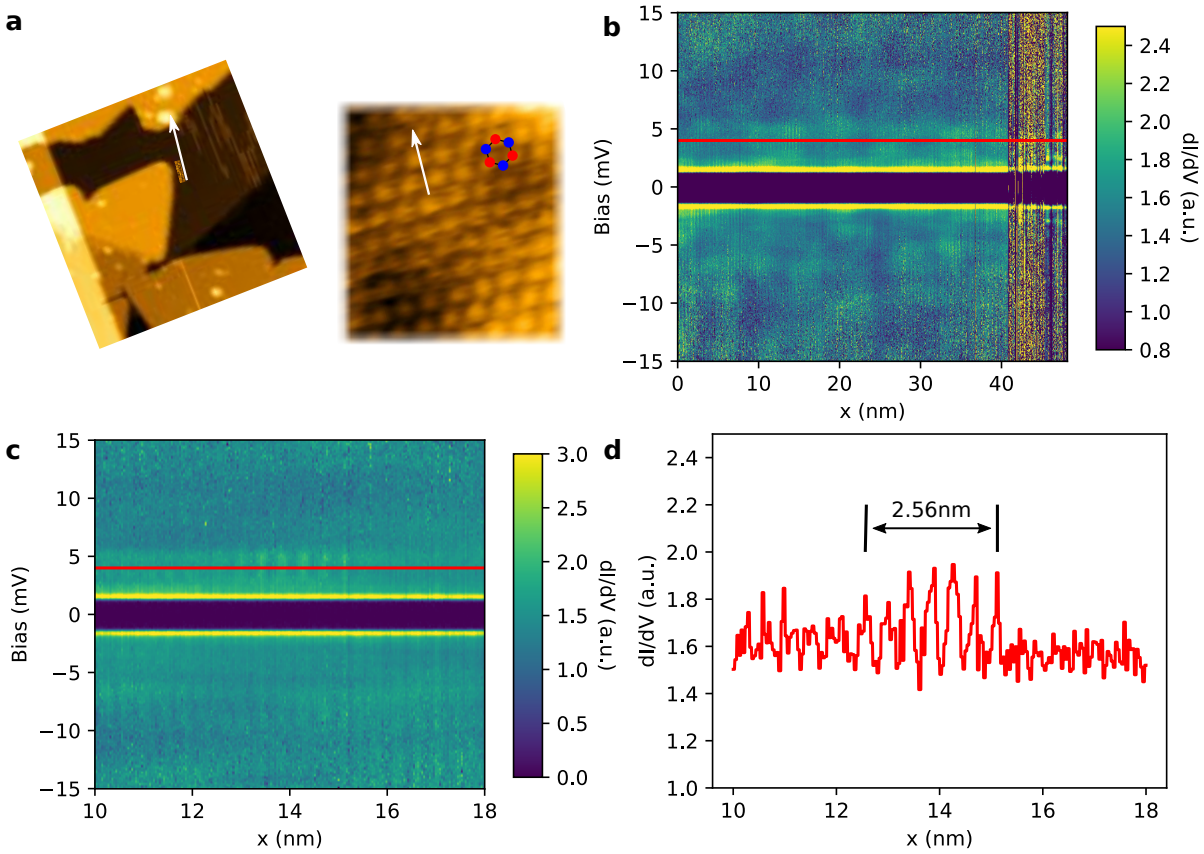

Figure 3.13: Sublattice polarized states in graphene. **a** Topography images of the area. Left large scale (arrow length: 50 nm). Right: zoom on the graphene lattice. The measurement direction is indicated by the white arrow and is about 1.4° from the armchair direction of the lattice. The overlay indicates the two sublattices A in red and B in blue. **b** Line scan recorded at a setpoint of$V_b = 15\,\mathrm{mV}$, $I = 8\,\mathrm{nA}$, $V_{rms} = 30\,\mu\mathrm{V}$ and $T = 55\,\mathrm{mK}$ showing an inhomogeneous density of states. At about 42 nm the scan transits to the $NbSe_2$ flake where the signal gets less stable. Marked states at 2.5 mV and -3 mV emerge. **c** Zoom on b revealing spatially oscillating DOS. **d** Constant bias cut at $V_b = 4\,\mathrm{mV}$ along the the profile highlighted in c. The oscillations have a wavelength of 4.3 Å.

3.2.5 Sublattice polarized states

As a last part of this study, we will have a look at spectroscopies on an intermediate bias range. Figure 3.13 shows a line scan over $\pm 15\,\mathrm{mV}$ recorded along a roughly 50 nm long line starting on graphene and ending on $NbSe_2$. The topography around the measurement position is depicted in Figure 3.13 a). The full line scan is plotted in Figure 3.13 b).
Let us first analyze the spectroscopies on graphene which span over a length of about 42 nm. In this area, we observe smooth inhomogeneities oscillating with a wavelength of about 5-10 nm outside of the superconducting gap which might be caused by intravalley scattering quasiparticle interferences, by impurities in the substrate or by charge puddles often observed in graphene[167]. However, a close look reveals additional small sub-nanometer oscillations. These are better visible in the zoomed plot of Figure 3.13 c). Figure 3.13 d) shows a constant bias profile extracted from Figure 3.13 c) at $V_b = 4\,\mathrm{mV}$ where these oscillations are nicely visible and which gives us a wavelength of 4.3 Å. To understand this number, let us come back to the atomically resolved image of graphene in Figure 3.13 a). The scan direction indicated by the white arrow is coincidentally almost perfectly aligned with the armchair direction of the graphene lattice (the misalignment is about 1.4°). Along this direction, the lattice has a periodicity of $\sqrt{3}a = 4.26\,\text{Å}$ where $a = 2.45\,\text{Å}$[155] is the graphene lattice constant. This corresponds exactly to the wavelength we observe in the line scan. Note that for each oscillation the tip comes across two carbon atoms from different sublattices. We conjecture that the state at 4 meV is partially sublattice polarized. It is not surprising to observe such kind of features in graphene on SiC because of the sublattice symmetry breaking caused by the Bernal stacking of the graphene on the buffer layer.

3.2.6 Summary

Let us briefly summarize the results of the preliminary data presented in this chapter.
The MBE growth of $NbSe_2$ on graphene was successful, yet with non-optimal growth conditions. Nevertheless, the superconducting spectra show a relatively large gap of $\Delta \approx 380\,\mu\mathrm{eV}$, pointing to a critical temperature of 2.5 K within BCS theory. This is not too far from the 3 K observed in exfoliated monolayers and proves the good quality of the grown film. A direct measurement of the critical temperature should be envisaged in the next experiments.
We found clean surface areas but the overall surface conditions can still be improved, potentially by lowering the residual gas pressure in the STM chamber. It seems like a cold sample is prone to degradation when exposed to the 10^{-8} mbar in the outer STM chamber for longer times.
Achieving atomically resolved topography scans is not easy, but we managed to obtain a few well resolved images and observed signs of a charge density wave. However, we did not find a clear signature of the corresponding 4 meV gap in spectroscopic measurements.
The graphene substrate looks as expected, both in topography as well as in spectroscopy. It seems like we have areas with bilayer and others with monolayer graphene coverage. In future studies, this could be exploited to systematically analyze if the graphene thickness is an important parameter for the $NbSe_2$ properties. Due to the contact to the superconducting $NbSe_2$, the graphene substrate is rendered superconducting as well. We confirmed this by observing the opening of a gap and by a novel approach using a superconducting tip to observe the transport of supercurrent through graphene over up to 100 nm. The observed gap decay with distance from the $NbSe_2$ indicates that although weak, the proximity effect in graphene might persist on micrometer lengthscales. A confirmation of this would require a sample with less $NbSe_2$

coverage to increase the distance between adjacent islands.
Overall, the measurements shown here provide a good understanding of the sample properties but a few open questions remain. The sample quality is very good so the first milestone of our project is already reached.

For the future, this encourages a continuation of the project, soon moving to more complex structures including magnetic impurities for the study of YSR states in this two-dimensional system. The first step would be adding 0D impurities like magnetic molecules or adatoms. As it has been done on bulk $NbSe_2$ already, one can then use the STM tip to build 1D chains or even slightly more complex structures. Two dimensional magnetic superstructures which might give rise to topological edge states could potentially be created by MBE growth of magnetic TMD islands.
For gaining a deeper understanding of the Ising superconductivity in monolayer $NbSe_2$, a study in finite magnetic field, inducing vortices might be interesting as well.

4 Quantum Hall Ferromagnetism in Graphene

Every experimental work knows dead times due to instrument break downs. In my case, one of the scanner motors of my STM described in Chapter 2 broke and the required maintenance at the manufacturer took about five months during which my project was on halt.
Fortunately, I was able to join and continue the project of Alexis Coissard working with Benjamin Sacépé in our group at Institut Néel. He was working on STM studies of graphene in the quantum Hall regime, such as imaging the edge states as well as the bulk lattice-scale order. Alexis had already measured graphene on hBN/SiO_2 and found the Kekulé ground state for this system. However, since transport measurements performed in the same group[168] had shown the possibility of inducing a phase transition in graphene on the high-k dielectric $SrTiO_3$ by tuning the applied magnetic field, the overall goal of the study was more ambitious, aiming at imaging the ground state order across this phase transition as well.
By the time I joined, Alexis had already fabricated STM compatible graphene samples on hBN/$SrTiO_3$ but he had measured only one of them, which did not give conclusive results and he did not have the time to measure the two other samples himself because of the approaching end of his PhD. This is why, after a detailed instruction by Alexis, I was mainly in charge of running the experiments on the two other hBN/$SrTiO_3$ samples where we found a charge density wave ground state at high magnetic field and a spin polarized ground state at low fields and hence were able to confirm the anticipated phase transition.

The results of this study are published under the following reference[169]:

A. Coissard, D. Wander, H. Vignaud, A. G. Grushin, C. Repellin, K. Watanabe, T. Taniguchi, F. Gay, C. B.Winkelmann, H. Courtois, H. Sellier and B. Sacépé
Imaging tunable quantum Hall broken-symmetry orders in graphene
Nature, vol. 605, pp. 51–56, May 2022.

Contents

4.1 State of the art

Graphene, a single layer of crystalline graphite, is a two dimensional layer of carbon atoms that form a hexagonal lattice. From a tight binding model, taking into account nearest and next-nearest neighbor hopping, one readily obtains its dispersion relation, plotted in Figure 4.1.
The Dirac cones with their linear dispersion around the Fermi energy develop at the K and K'

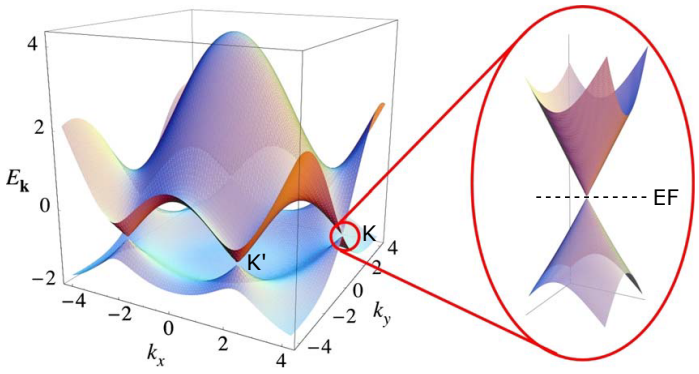

Figure 4.1: Graphene dispersion relation obtained from tight binding calculations considering nearest and next-nearest neighbor hopping. The particularity is the linear dispersion in the Dirac cones around the Fermi energy, highlighted in the inset. Reprinted with permission from [155].

points. Around these points, i.e. for $\mathbf{k} = \mathbf{K} + \mathbf{q}$ with $|\mathbf{q}| \ll |\mathbf{K}|$, the Hamiltonian of the system can be approximated by the 2D Dirac Hamiltonian

$$\hat{H}(\mathbf{q}) = \xi \hbar v_F \mathbf{q}.\boldsymbol{\sigma} \tag{4.1.1}$$

where $\xi = \pm 1$ denotes the valley (or isospin) stemming from the two equivalent sublattices A and B, $v_F \approx 1 \times 10^6\,\mathrm{m/s}$ the Fermi velocity and $\boldsymbol{\sigma}$ the Pauli matrices acting on the sublattice pseudospin. The resulting dispersion relation reads

$$E(q) = \hbar v_F q\ . \tag{4.1.2}$$

Formally, this equation is the same as the Dirac equation, describing the motion of a mass-less relativistic particle.
Experimentally, Novoselov et al. were the first to isolate a monolayer of graphene [170] and to show its linear dispersion and Dirac like behavior [171].

4.1.1 Graphene under perpendicular magnetic Field

When applying an external magnetic field, the Lorentz force confines electrons to circular trajectories which profoundly alters their dispersion and energy spectrum. Formally, this is taken into account by applying the Peierls substitution, i.e. replacing the canonical momentum $\mathbf{p} = \hbar\mathbf{q}$ by the kinetic momentum $\pi = \mathbf{p} + e\mathbf{A}$. The vector potential $\mathbf{A}$ has to be chosen such that $\mathbf{B} = \nabla \times \mathbf{A}$. For the Dirac like Hamiltonian of graphene in Equation 4.1.1, this leads to discrete Landau levels (LL) which disperse as

$$E_N = \mathrm{sign}(N)\ v_F \sqrt{2\hbar e |N| B} \tag{4.1.3}$$

with the level index $N \in \mathbb{Z}$ and the perpendicular magnetic field component B. In contrast to the conventional, parabolic 2DEG with $E_N = \hbar\omega_c(N + 1/2)$, we emphasize the $\sqrt{|N|}$ behavior

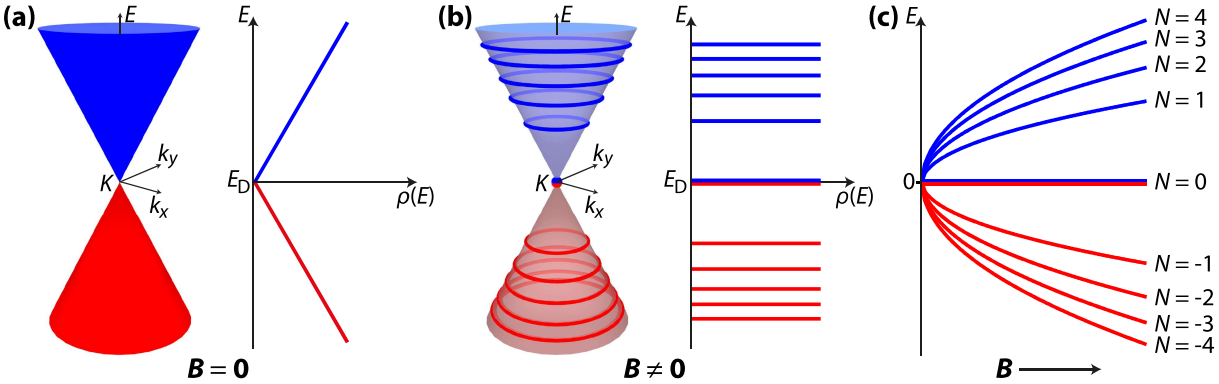

Figure 4.2: Dispersion and Landau Levels in graphene. (a) Low energy dispersion and density of states of graphene without external magnetic field. (b) In a finite perpendicular magnetic field, the density of states condenses to discrete, four fold degenerate Landau levels. (c) The magnetic field dependence of the Landau level's energies. Figure from[174].

and, most important for the following, the existence of the $N = 0$ Landau level (LL_0) residing at the Fermi energy which does not disperse with B and for which the wave function of each valley is localized only on one of the two sub-lattices[172,173]. Note that the electron spin and the above-mentioned isospin form an SU(4) isospin space, thus each Landau level is four fold degenerate.

To describe the filling of the Landau levels, we define the filling factor $\nu = n/n_B$ as the ratio between the electron density n and the flux density $n_B = B/\Phi_0$ where $\Phi_0 = h/e$ is the flux quantum. Note that $\nu = 0$ when the Fermi energy is at the Dirac point as it is the case in ideal, undoped graphene. Since each Landau level is four fold degenerate and the Fermi energy lies in the middle of the zeroth Landau level, $\nu = 2$ corresponds to a fully occupied LL_0, $\nu = 6$ to a fully occupied first level and so on.

The characteristic length scale for the cyclotron radius of LL_0 is the so called magnetic length l_B, given by

$$l_B = \sqrt{\frac{\hbar}{eB}} \approx 25.65\ \text{nm}/\sqrt{B[\text{T}]} \tag{4.1.4}$$

where, once again, B is the perpendicular component of the external magnetic field.

4.1.2 Quantum Hall Ferromagnetism

To introduce the concept of Quantum Hall ferromagnetism let us first consider a conventional quantum Hall system where Landau levels are only two fold degenerate due to the spin degree of freedom of the electrons. At half filling of a Landau level, an anti-symmetric orbital wave-function minimizes the Coulomb repulsion between the electrons. As a consequence of their fermionic nature, the overall wave function must be antisymmetric under particle exchange. Hence, the electron's spin-wave function must be symmetric resulting in an alignment of the spins and therefore a ferromagnetic order, from where the name Quantum Hall ferromagnetism originates[175]. Another way of describing the same phenomenon is to see the Landau levels as flat bands with quenched kinetic energy, where the density of states is quasi infinite. Let us recall the Stoner criterion which predicts a ferromagnetic order in a partially filled band if $D_F\ U > 1$, where D_F is the density of states at the Fermi energy and U the on-site Coulomb repulsion. In the case of a half-filled Landau level with the quasi-infinite density of states, we thus obtain ferromagnetic order no matter how small the interaction.

Returning to the $\nu = 0$ state in graphene with the SU(4) symmetry, the same principle applies

for both the spin and the isospin degree of freedom. Taking a look at the relevant energy scales at play, listed in Table 4.1, we observe that the dominant scale is the cyclotron gap, confining all relevant processes in the low energy limit to the states of the same Landau level index. The next energy scale is the exchange energy scaling proportionally to the Coulomb interaction and leading to the symmetry breaking mentioned before. However, due to the additional valley degree of freedom, not only ferromagnetic spin ordering is allowed. Another obvious alternative is a full valley polarization, equivalent to a full sublattice polarization in the zeroth Landau level. The resulting, so called charge density wave (CDW) is sketched in Figure 4.3, where both electrons per unit cell are localized on the same sublattice, forming a non-magnetic singlet. A thorough theoretical consideration finds two other possible broken-symmetry ground states[176]: the canted anti-ferromagnetic (CAF) state, where electrons are homogeneously distributed over the lattice sites and showing a tilted anti-ferromagnetic spin texture, and the Kekulé bond order, where the two electrons are localized on one out of the three inter-atom bonds.
Which state is finally realized in a real system depends on the delicate balance of all interactions at play. Therefore, even though their magnitude is much smaller then the Coulomb interaction, also the short-range electron-electron and electron-phonon interactions, which gap out the valley degree of freedom, as well as the Zeeman effect play an important role. The resulting phase diagram is sketched in Figure 4.3 in the interaction space. Unfortunately, the axes of this phase diagram do not have a simple experimental correspondence which makes it difficult to access the different regimes and to theoretically predict the ground state in real systems. Nevertheless, indirect transport measurements have managed to drive the system through a phase transition using two different strategies:

- by tilting the applied magnetic field to tune the Zeeman energy while keeping all other energies unchanged[177]
- by placing the graphene on a high k dielectric substrate to screen long range Coulomb interactions[168]

The common principle to these experiments is to bring the graphene to charge neutrality using a back-gate and to measure the transport across a micrometer sized sample at low bias voltages $eV_b < \Delta E^0$, where ΔE^0 is the gap between the occupied and the unoccupied states induced by the interactions we discussed above. In this case, the bulk of the sample is insulating and only the edge states where the bands bend due to the confinement potential can contribute to transport. Whether or not the edge excitations are gapped out or not depends on the bulk ground state[178–181]. However, these measurements can not unambiguously identify the bulk ground state because three of the four possible ground states lead to gapped edge excitations and thus an insulating charge-neutral graphene. Also, nontopological edge currents may be induced by charge accumulation on the edges[182] which makes the interpretation of transport data even more challenging. Arguing the other way around, the identification of the ground states would close this long-standing open and intensely debated question and facilitate the interpretation of (future) transport measurements.
The best way of doing so is to image the ground-state wave functions using a scanning tunneling microscope. In our study we aim at doing precisely that: image the quantum Hall broken-symmetry orders in different charge-neutral graphene systems.

Cyclotron gap	$E_{0-1} = v_F\sqrt{2\hbar e}\cdot\sqrt{B} \approx 36.3\,\text{meV}\cdot\sqrt{B[T]}$	spacing between the 0th and 1st Landau level
Exchange energy	$E_X \sim E_C = \frac{e^2}{4\pi\varepsilon_0\varepsilon_r l_B} \approx 56.2\,\text{meV}\cdot\frac{\sqrt{B[T]}}{\varepsilon_r}$	Pauli repulsion
Valley gap	$E_V \sim \frac{a}{l_B}E_C \approx 0.31\,\text{meV}\cdot\frac{B[T]}{\varepsilon_r}$	caused by short range electron-electron and electron-phonon interactions distorting the lattice
Spin gap	$E_Z = g\mu_B B \approx 0.116\,\text{meV}\cdot B_{tot}[T]$	Zeeman effect

Table 4.1: Energy scales in the zeroth Landau level of graphene in the Quantum Hall Regime. B is the perpendicular magnetic field component and B_{tot} the amplitude of the total magnetic field. $\varepsilon_r \approx 4$ for (hBN)/SiO_2.

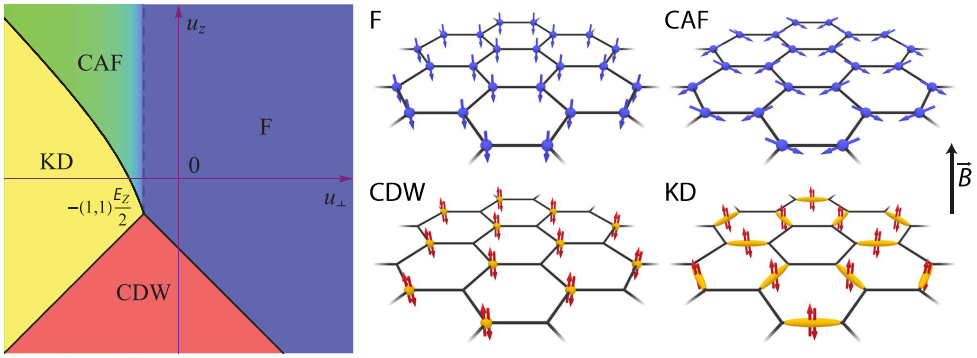

Figure 4.3: Phase diagram of the $\nu = 0$ quantum Hall state in graphene in the anisotropy energy space. Reprinted with permission from[176]. The sketches on the right give a schematic representation of the corresponding wave functions and their polarizations. Sketches from[174].

4.2 Imaging tunable quantum Hall broken-symmetry orders in charge-neutral graphene

All experiments presented in this section are performed at 4.2 K and under a perpendicular magnetic field of up to 14 T. Since the setup presented in Chapter 2 does not allow applying sufficiently high magnetic fields, we use a different low temperature SPM built by Benjamin Sacépé with support of Dominique Grand, Louis Veyrat and the SERAS service at CNRS. In principle, this setup shown in Figure 4.4 also provides a UHV sample preparation chamber and can reach mK temperatures using a dilution-insert. However, since graphene is very robust to ambient conditions, we do not require in-situ sample preparation. Furthermore, the energy-scales we are interested in for this study are in the meV range, so 4.2 K sample temperature are sufficiently low. We therefore work with the much simpler to use 4.2 K insert in a 7×10^{-1} mbar He atmosphere and only prevent condensation of residual gas on the sample during the cool-down from room temperature to 4.2 K by performing a light heating of about 200 mW using a heating resistance on the sample holder.
Figure 4.4 b) shows a picture of the home-made Pan-style SPM head. It is designed for combined STM and transport measurements which is why it is equipped with 24 sample lines and offers an AFM mode which can be used to localize the device on an insulating substrate.

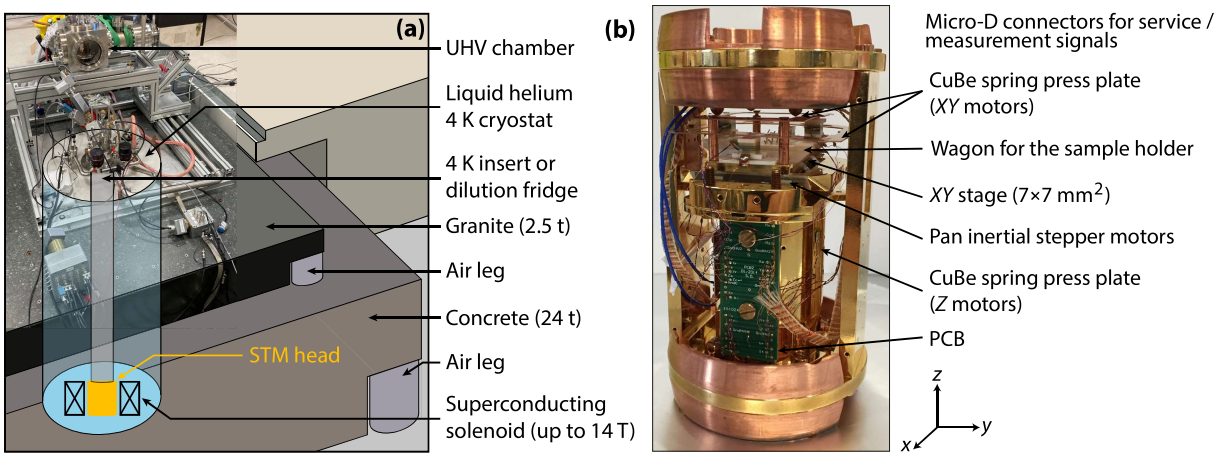

Figure 4.4: The high magnetic field SPM. (a) The refrigerator hosting the STM head surrounded by a 14 T superconducting solenoid. Vibration damping is achieved through a two level air damper system and large suspended masses. (b) Picture of the home-made Pan-style SPM head providing 24 contacts to the sample and a sample travel of 7 mm × 7 mm. Adapted from[174].

4.2.1 Device fabrication

Impurities in the graphene lead to scattering processes which introduce a disorder potential. For the observation of the interaction dominated physics such as the symmetry breaking in quantum Hall ferromagnetism, the disorder potential needs to be smaller than the exchange energy causing the symmetry breaking. We therefore need a device with little defects, or in other words, with a high charge carrier mobility[172]. Best mobilities in STM compatible graphene devices have been obtained by placing graphene on hexagonal boron nitride (hBN)[183], an insulating substrate with a lattice very similar to graphene and bonding only through Van-der-Waals forces to the graphene layer. The Gr/hBN/substrate devices for our work, sketched in Figure 4.5, were fabricated by Alexis Coissard using the Van-der-Waals transfer technique[174,184], widely employed in the graphene/2D Van-der-Waals heterostructure community and introduced at Institut Néel by Katrin Zimmermann[185]. Graphene and hBN flakes are exfoliated from bulk crystals by pressing the crystals on a SiO_2 surface using a scotch tape. Good flakes are chosen by optical microscopy and AFM and finally assembled together using a polypropylene carbonate stamp in a dedicated setup[174]. The stack, still stuck to the stamp, is then placed atop the substrate of choice. Finally, the stamp is sublimated during an annealing under vacuum conditions. Then, the gold top contacts (Cr/Au - 5/25 nm) as well as a millimeter-sized marker field are deposited on the sample using e-beam lithography, metal evaporation and lift-off. The last electrode is the Ti/Au (20/80 nm) back-gate, deposited on the back side of the $SrTiO_3$ substrate. Before mounting the sample on the STM sample holder, a final vacuum annealing is performed to remove resist-residues from the nano-fabrication. The marker fields form the large structured golden patch on the fully mounted and bonded sample shown in Figure 4.5. The markers are crucial to locating the micrometer sized graphene device on the millimeter sized chip using AFM because, initially, we can only roughly align tip and sample by eye. A detailed description of the markers can be found in Alexis Coissard's PhD thesis.[174]
Since we aim at driving the quantum phase transition by dielectric screening discussed above, Alexis fabricated samples using two different substrates: the standard SiO_2/Si^{++} for an unscreened configuration and the high-k dielectric $SrTiO_3$ which is expected to screen long range Coulomb interactions[168,186].

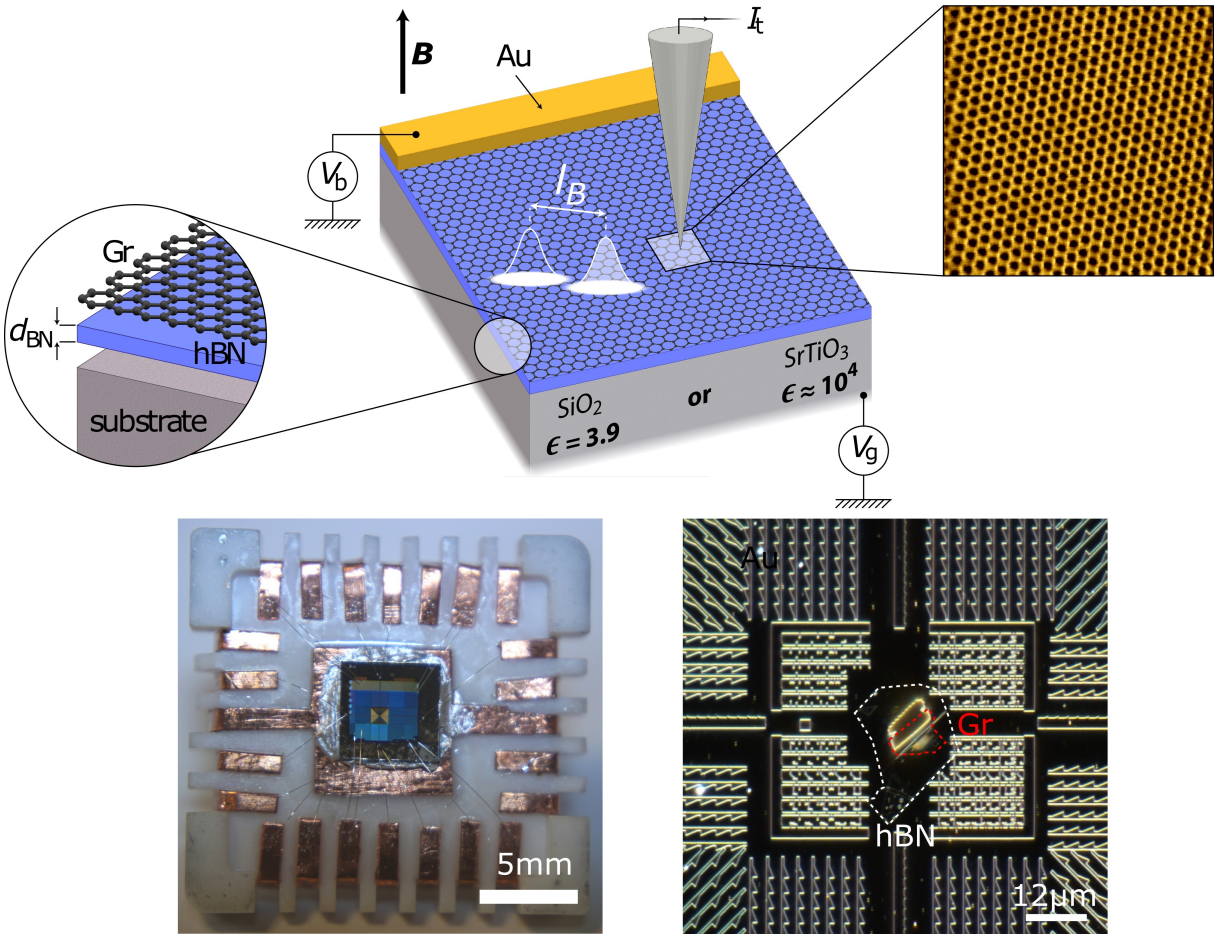

Figure 4.5: Device architecture. Top: Schematics of the investigated devices, consisting of a SiO_2 or a $SrTiO_3$ substrate, a few nanometer thick hBN flake and a Graphene monolayer which is contacted by a Au electrode. Adapted from[169]. Bottom left: photo of the sample mounted on its sample holder. Most of the sample surface is covered by the navigation markers made of Cr/Au. Bottom right: dark field optical image of the device AC24.

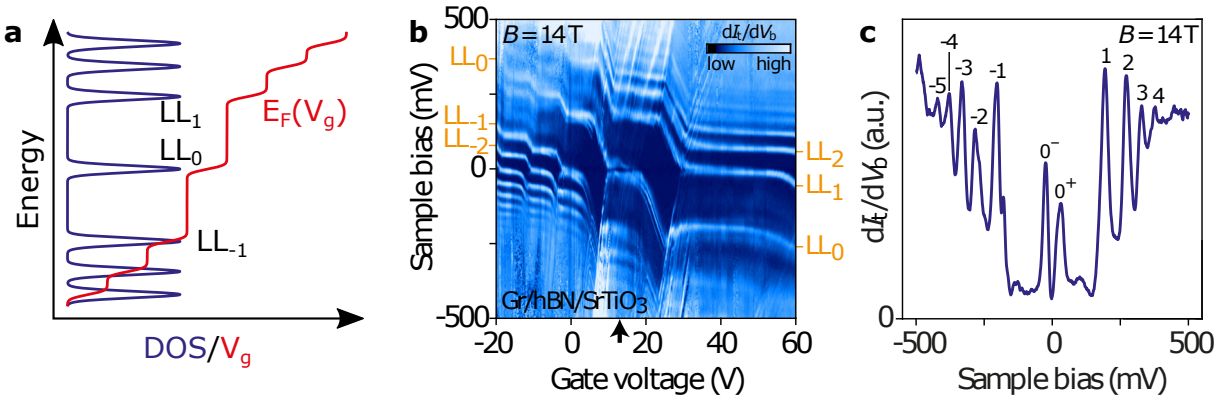

Figure 4.6: Landau level spectroscopy. **a** Sketch illustrating the Fermi-level pinning inside the Landau levels, as described by Equation 4.2.5. **b** Conductance map, showing the dispersion of the Landau levels with the back gate voltage. Around charge neutrality, i.e. when LL_0 crosses the Fermi energy, the interaction gap splits the LL_0. **c** Single tunneling spectrum at charge neutrality (13 V), indicated by the black arrow in b. Several Landau levels are well resolved and the splitting of LL_0 is very pronounced. b and c are adapted from [169].

4.2.2 LL tunneling spectroscopy

In this experiment, we want to investigate charge-neutral graphene. However, due to impurities and residues from nano-fabrication, the graphene is usually slightly doped and therefore not charge-neutral. This is why all samples possess a back-gate which allows us to tune the graphene's charge carrier density n through the field effect. We can approximately describe our back gate - dielectric - graphene system like a plane capacitor with dielectric constant ε_r over the dielectric thickness d on which we apply a voltage V_g giving the left-hand side of Equation 4.2.5. On the other hand, the induced charge carrier density is linked to the Fermi energy through the density of states ρ of the system as described by the right-hand side of the same equation.

$$\frac{\varepsilon_0 \varepsilon_r (V_g - V_{CNP})}{de} = n = \int_0^{E_F(V_g)} \rho(E) \mathrm{d}E \tag{4.2.5}$$

Here, ε_0 is the vacuum permittivity, e the electron charge, V_{CNP} the gate voltage at which graphene is at the charge neutrality point and $E = 0$ corresponds to the Dirac point.

The energy spectrum of the density of states of graphene in the quantum Hall regime is sketched in Figure 4.6 a). It is characterized by very well pronounced Landau level peaks and areas of almost vanishing density of states between them. Within the Landau level peaks, the Fermi energy moves very little as function of the applied gate due to the large density of states therein which thus pins E_F on a wide range of V_g. Once the Fermi energy leaves a Landau level, the low density of states implies a very rapid change with gate voltage until the next Landau level is reached. This leads to the step-like gate voltage dependence sketched in red in the same figure. Experimentally, we observe this behavior in conductance maps as the exemplary one depicted in Figure 4.6 b) where we measure a set of bias spectroscopies at different gate voltages. At $V_g = -20\,\mathrm{V}$ the Fermi energy lies in the Landau level -3 which we therefore observe at 0 V sample bias. The Fermi energy is pinned in the same Landau level up to about $V_g = -12\,\mathrm{V}$ and then transitions to LL_{-2} within approximately 2 V where it is again pinned for another 8 V of the back gate and so forth.

Measuring the full map allows us then to find the back gate voltage V_{CNP} at which the graphene is charge neutral. Since the Landau levels are four fold degenerate, the left edge of the LL_0 plateau corresponds to a filling factor $\nu = -2$ and the right edge to $\nu = 2$ accordingly. The

filling factor $\nu = 0$ is therefore reached in the middle of the plateau. In the case shown in Figure 4.6 this is at $V_g = 13\,V$ as indicated by the black arrow.
Around charge neutrality we observe the most important effect for the remainder of this work: the splitting of the LL_0 level and thus the opening of the interaction induced gap. This gap is also very well visible in the single spectrum at 13 V shown in Figure 4.6 c).
Furthermore, we observe a large asymmetry in the gate voltage extension of the Landau levels between negative and positive bias. This is caused by the non-linear dielectric constant of the $SrTiO_3$ substrate with electric field. As explained in the methods section of the paper[169], we can estimate the dielectric constant from the gate map and find that it decreases from about 12000 to 3000 over the applied gate range. Consequently, the gating effect becomes less efficient at high gate voltage and the plateaus are more and more extended.
Finally, between 10 V and 20 V and for $V_b > 250\,mV$, four lines with positive slope are visible. These are charging peaks stemming from quantum dots induced in the graphene by substrate or tip induced disorder potentials[187,188]. Each of the peaks corresponds to the charging of a single electron, which shows very visually the four fold degeneracy of each of the Landau levels. However, for our measurements these peaks are undesired, since they conceal the clean Landau level and interaction physics and therefore complicate the localization and estimation of the interaction gap. For this reason, whenever these peaks became too dominant, we discarded the measurement, reshaped the tip on the gold contact and/or moved to a different region on the sample to recover a gate map resembling the one shown here.
A small technical side note is that the $SrTiO_3$ substrate is piezo-electric[189]. Changing the gate voltage therefore changes the electric field and hence the thickness of the substrate. For a gate sweep from -40 V to 100 V the thickness changes by roughly 300 nm. For this reason, we hold the gate voltage fixed during the measurement time of each of the bias spectra and only change it between two bias spectra when the z-controller is enabled.
Summarizing, measuring the full gate dependence allows us to properly identify the Landau levels through their characteristic step like dispersion, discriminate parasitical additional peaks in the spectra and properly determine the gate voltage for obtaining charge neutrality. Measuring the full map is therefore indispensable to reliably extract the interaction induced gap that opens in the zeroth Landau level at charge neutrality.

4.2.3 Screening the long range Coulomb interaction

Transport measurements have shown that using the high-k dielectric substrate $SrTiO_3$, long range Coulomb interactions can be screened[186]. This leads to altered electronic properties of the $\nu = 0$ state, driving the system from a broken-symmetry state with gapped edge excitation to an ungapped, helical edge transport regime[168].
The first step of our STM investigation is therefore to quantify this substrate induced screening on the two different substrates (SiO_2 and $SrTiO_3$) and as function of magnetic field. In Section 4.1.2, we have seen that the symmetry breaking is dominated by the exchange interaction and thus the gap that opens is given by the Coulomb energy E_C through $\Delta E^0 = \sqrt{\pi/8} E_C$[190].
As explained in the previous section, we estimate the exchange gap by first taking a full gate map, to properly identify the charge neutrality point, and then extract the value of the gap from the individual spectrum at which the gap reaches its maximum, which corresponds to exact half filling of the zeroth Landau level[190]. This process is illustrated in Figures 4.7 a) and b). The estimated values as function of magnetic field and substrate are plotted in Figure 4.7 c). On SiO_2, the measurements follow the expected $\sqrt{\pi/8} E_C = \sqrt{\pi/8} \frac{e^2}{4\pi\varepsilon_0\varepsilon_r l_B} \propto \sqrt{B}$ behavior plotted

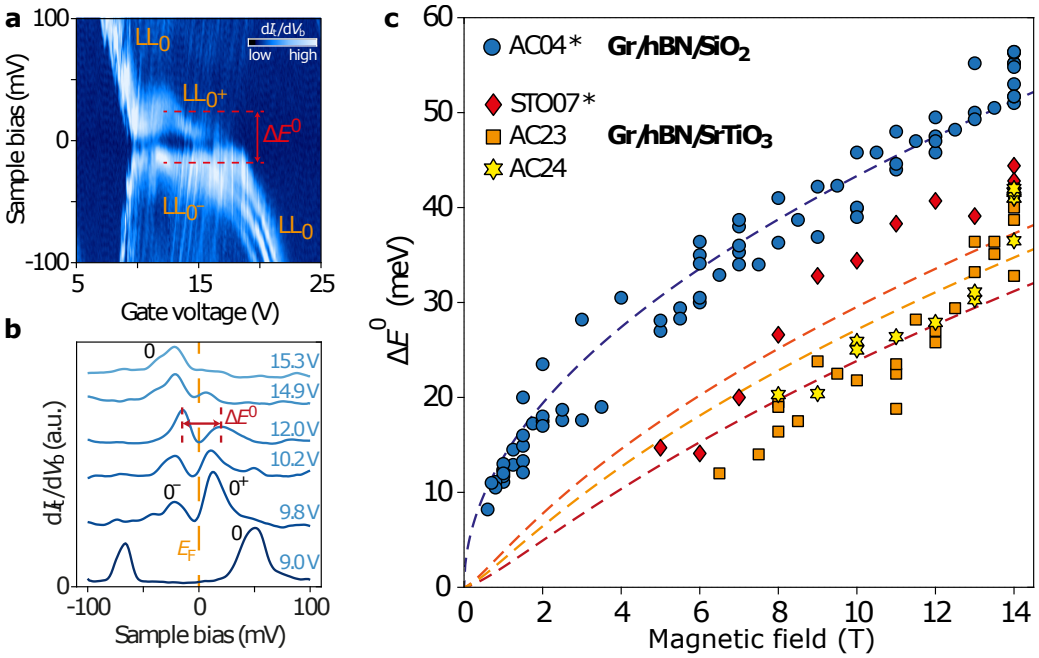

Figure 4.7: Screening the long range Coulomb interaction in graphene by the use of a high-k dielectric. **a** Zoom on the plateau of the LL_0. **b** Several individual bias spectra extracted from the map in a. The value of the interaction induced gap ΔE^0 is estimated from the peak distance of the individual spectrum where the gap is the largest. **c** The interaction induced gap is proportional to $\sqrt{B}$ for AC04 on a SiO_2 substrate whereas for the samples on $SrTiO_3$ it is proportional to the more complicated, hBN-thickness dependent $S(B) \times \sqrt{B}$. It is significantly decreased in its amplitude compared to SiO_2 which demonstrates the screening effect of the high-k substrate. Adapted from[169]. *: samples measured by Alexis Coissard.

by the dashed line. Here $\varepsilon_r = (\varepsilon_{BN}+1)/2 \approx (3.6+1)/2 = 2.3$ is the relative permittivity of the environment of the graphene, since there is the Boron Nitride on one side and vacuum on the other side. The fit to the experimental data yields $\varepsilon_r = 2.6$ close to the theoretical value and thus proves the validity of our gap determination method.
Moving on to the three other samples measured on $SrTiO_3$, we note a significantly smaller interaction gap than on the SiO_2 substrate. This demonstrates the screening effect by the substrate. Quantitative dielectric considerations taking into account the thin hBN flake between the $SrTiO_3$ and the graphene show that the effective, substrate screened Coulomb energy $\tilde{E}_C$ can be approximated by $\tilde{E}_C = E_C \times S(B)$ with the screening factor

$$S(B) \approx 1 - \frac{\varepsilon_{STO} - \varepsilon_r}{\varepsilon_{STO} + \varepsilon_r} \frac{l_B}{\sqrt{l_B^2 + 4d_{BN}^2}} \tag{4.2.6}$$

where d_{BN} is the hBN thickness[168].[1] This dependence is plotted in Figure 4.7 c) using the different hBN thicknesses of the three samples. Note that the screening effect is B-field dependent (since l_B is B-field dependent) and the strongest for small magnetic fields when $l_B \gg d_{BN}$. This will be particularly important later on when imaging the ground states as function of the applied magnetic field.

[1] The geometry used to derive this formula includes an infinitely thick top hBN layer not present on our sample. However, this should only lead to a small correction.

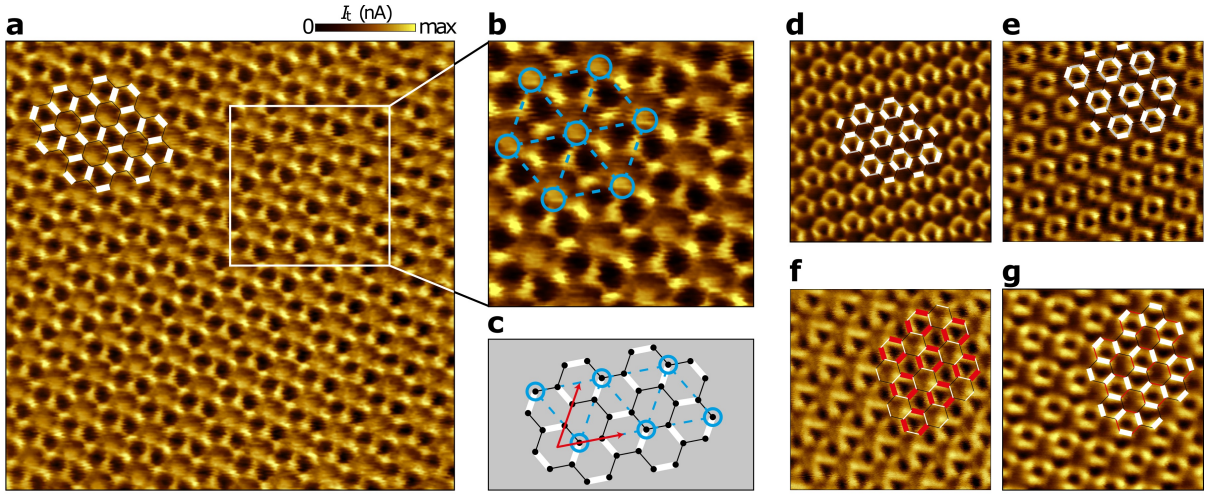

Figure 4.8: Kekulé density wave in unscreened charge-neutral graphene. **a** 5 nm × 5 nm constant height image at $B = 14\,\mathrm{T}$ and 25 mV showing the Kekulé bond order where the two electrons are localized on one out of three C-C bonds (structure sketched in overlay). **b** zoom of a featuring a secondary charge density wave order on a lattice matching the Kekulé lattice sketched in **c**. The red arrows indicate the basis vectors of the Kekulé lattice. **d**, **e** Two 3 nm × 3 nm images of asymmetric Kekulé patterns. d $B = 14\,\mathrm{T}$ and 2 mV, e $B = 3\,\mathrm{T}$ and 30 mV. **f**, **g** Two 3 nm × 3 nm images at $B = 14\,\mathrm{T}$ and 25 mV acquired at the same position a few minutes apart, demonstrating the transition between two out of three degenerate Kekulé configurations: red in f and white in g. Figure from [169].

4.2.4 Imaging the broken-symmetry orders

We now turn to the imaging of the orders of the zeroth Landau level's broken-symmetry states. As for the measurements above, the first step consists in estimating the gate voltage for charge neutrality of the graphene by measuring a full gate map. Coming back to charge neutrality is a bit more complicated on $SrTiO_3$ because it shows a hysteretic behavior. On these samples, we therefore always cycle the gate voltage along the same trajectory. For example, after completing the gate map from −20 V to 60 V, shown in Figure 4.6, to return to charge neutrality at 13 V, we first ramp the back gate to −20 V before coming back to 13 V. Furthermore, we approach charge neutrality in small steps and check again by measuring single bias spectroscopies.
We then measure constant height images at different bias voltages. At small positive bias, only LL_0^+ contributes to the current, and thus the image corresponds to the local density of states of this state. At larger bias $V_b \geq eE_1$, the first Landau level also contributes to the current and the regular honeycomb lattice is recovered, which we take as a proof that the structure measured at low bias is not a tip effect but the real structure of the ground state wave function.

Unscreened

Let us first consider the system with unscreened Coulomb interaction, i.e. graphene on SiO_2, which is the standard substrate for almost all transport experiments.[2] For this case, transport experiments pointed to a canted-antiferromagnetic ground state [177]. Magnon transmission experiments also suggested a magnetic ground state [191–193]. Surprisingly, we find the non-magnetic Kekulé bond order depicted in Figure 4.8 a). This is consistent with an independent STM study, carried out at the same time, which also observed a Kekulé order and a CAF skyrmion around a charged impurity [194], as well as measurements without back-gate on CVD grown multilayer graphene where the topmost layer is claimed to be electronically decoupled from the lower lay-

[2] The results on SiO_2 presented in this subsection have been measured by Alexis Coissard without contribution of my part and are presented here just for giving the complete picture of the study.

ers through a twist angle of about 13.7°[195]. The disagreement between transport and STM measurements is not yet understood and subject of ongoing research.
Note that the Kekulé order not always looks like the one in Figure 4.8 a). It can also look more like small circles as can be seen in Figure 4.8 e). Similar shapes were observed by Liu et al. around a valley skyrmion localized at a charged defect (compare with fig 4 D 1 and 2 of ref.[194]). Describing the valley order with a Bloch sphere representation $|\psi\rangle = \cos(\theta/2)|K\rangle + \sin(\theta/2)\exp(i\phi)|K'\rangle$, they show that the different shapes correspond to different phases ϕ between the wave functions of the two sublattices.
Interestingly, the Kekulé configuration can vary with time. Figure 4.8 f) and g) show the same area scanned a few minutes apart. Between the two images, the Kekulé configuration switched from the configuration with the strong red bonds in the overlay to the degenerate one highlighted by strong white bonds.

Taking a close look on the Kekulé order in Figure 4.8 a) and its zoom in b), we remark an additional unexpected structure, highlighted by blue circles. It consists of an increased local density of states on a lattice with $\sqrt{3}$ times the size of the atomic lattice, thus corresponding to the Kekulé lattice. This structure is sketched in Figure 4.8 c) as well. It resembles a charge density wave, which is why we call it K-CDW. This K-CDW is not always present and for the same position it can change with time, which is why it probably is neither caused by a tip effect nor by stationary substrate effects. At $B = 0$, a competition between Kekulé bond order and charge density wave are predicted by theory[196,197], however, at finite field corresponding theory work is still missing. Two other examples of asymmetric Kekulé orders are shown in Figure 4.8 d) and e). Fourier decomposition of the image (see Appendix F) reveals that this asymmetry also stems from the superposition of the K-CDW just like in Figure 4.8 a). This asymmetry can change with time (see extended data of ref.[169]), caused by a switch in the K-CDW order. We emphasize that due to the observation of this time dependence, substrate effects are very unlikely to be the origin of the asymmetries.

Weakly Screened

Let us now move on to the measurements on the second substrate, namely $SrTiO_3$. At large magnetic fields $B \gtrsim 7\,\mathrm{T}$ such that $l_B < d_{\mathrm{BN}}$, the long-range Coulomb interactions are weakly screened according to Equation 4.2.6.
In this regime, we observe the charge density wave shown in Figure 4.9. The most striking feature is the triangular lattice of dots with low tunnel current which corresponds to one of the two sublattices of graphene, visually demonstrating the strong sublattice polarization expected for this ground state.
In Figure 4.9 b), taken at a negative bias of $-20\,\mathrm{mV}$, as sketched in Figure 4.9 a), less current flows on the sublattice B highlighted by red dots in the overlay. Since at negative sample bias, we extract electrons from the sample, the sublattice B is unoccupied. When changing the sign of the bias by moving to 40 mV, the current is now reduced on the blue sublattice A. This is what we expect for the sublattice polarized charge density wave because at positive bias we inject electrons into the sample, which is not possible on the doubly occupied sublattice A.
If we increase the bias voltage further to 100 mV (Figure 4.9 d), we start imaging additional states supposedly from the first Landau level and therefore recover the full honeycomb lattice.
In addition, in the images b) and c) we note bright lines connecting the dark spots and forming a triangular structure. These lines correspond to a high local density of states of occupied

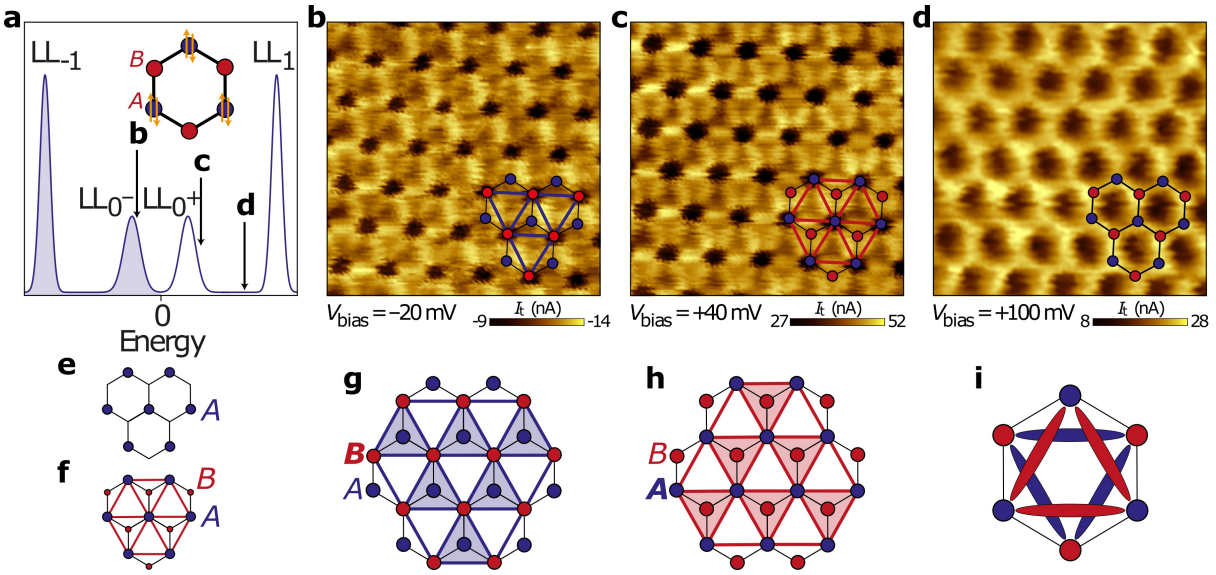

Figure 4.9: Charge Density Wave in the weakly screened regime. **a** Sketch of the Landau levels and the bias voltages corresponding to the scans b-d. Inset: sketch of the charge density wave and the color code for this figure: sublattice A in blue is doubly occupied, sublattice B in red is empty. **b-d** 1.5 nm × 1.5 nm constant-height STM scans acquired at 14 T. **b** At −20 mV, sublattice B appears as dark spots with bright bonds between them. **c** At 40 mV, sublattice A appears as dark spots with bright bonds between them. Note the inversion of the color scale from b to c which accounts for the change in sign of the applied bias voltage. **d** at 100 mV, the full honeycomb lattice is recovered. **e** Fully polarized CDW as predicted by ref.[176] vs CDW with partial sublattice polarization in **f** where a symmetry-allowed sublattice hopping asymmetry causes a triangular lattice. **g**,**h**, Sketches of the CDW structure of b and c. **i** Sketch of the triangular bond structure. Figure from[169]

states in b) and of empty states in c). A schematic representation of the line structure and its bias inversion behavior is sketched in Figure 4.9 i). This line structure connects second nearest neighbors of the honeycomb lattice, thus its symmetry is the same as for second nearest neighbor hopping terms. In the simple model presented in the introduction, which only takes into account the zeroth Landau level and no level mixing whatsoever, the charge density wave state is always fully sublattice polarized[176]. Second nearest neighbor hopping is then impossible since there are no states to hop to for the fully occupied sublattice and no states to hop from for the empty sublattice. The substructure we observe in our measurements is then impossible by symmetry. However, if we only have a partial sublattice polarization, second order hopping becomes possible and a triangular structure like the one we observe becomes plausible. A possible origin of this partial sublattice polarization could be Landau level mixing. In the zeroth Landau level, the wavefunctions at each valley are localized on one sublattice only, thus full valley polarization implies full sublattice polarization. However, in higher Landau levels this locking to the sublattice no longer holds, such that even a fully valley polarized state no longer resides on one sublattice only.

A close inspection of the triangular pattern reveals that the triangles hosting the omitted sublattice atoms appear a bit brighter than the other half of the triangles, consistent with the image of an increased local density of states around the atoms. This is highlighted by the shaded triangles in the structural sketches of Figures 4.9 g) and h).

The sample AC23 where the charge density wave was measured shows a Moiré superlattice caused by a rotation angle of about 11° between the hBN substrate and the graphene later. This Moiré is highlighted by white dashed circles in the measurement at 7 T of Figure 4.10. Since Moiré patterns are known to alter the electronic properties of graphene[198–201], the question arises if the charge density wave is caused by a sublattice symmetry breaking induced by this

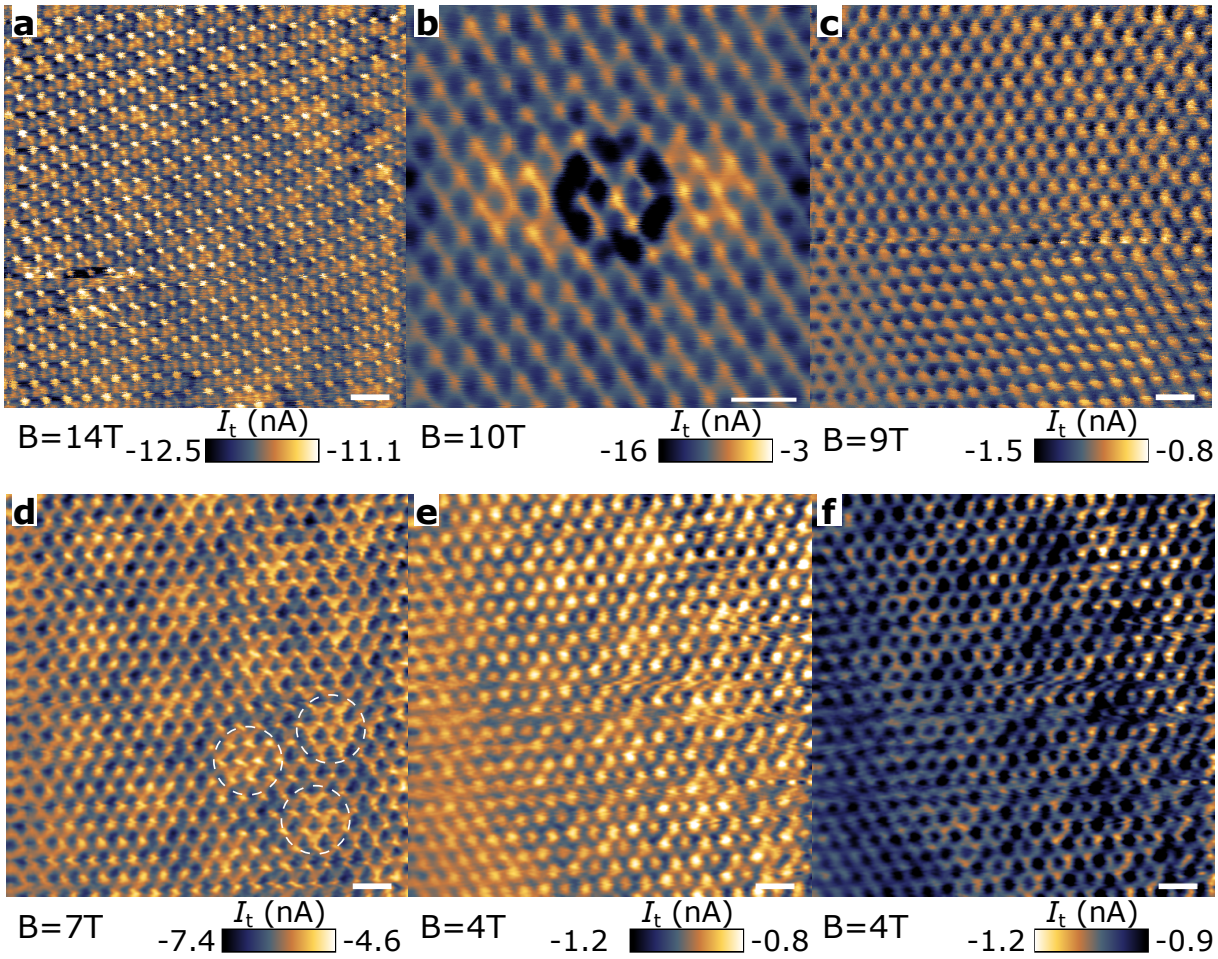

Figure 4.10: Field driven transition from the CDW order to a spin polarized state. All images are constant-height STM images recorded at −20 mV. **a-d** show a CDW, **e** and **f** a regular honeycomb lattice. **b** In addition to the CDW, we observe a localized impurity that appeared spontaneously during scanning, stayed for about 1 h and spontaneously disappeared again. It does not affect the CDW in the background. **d** The Moiré superlattice which is present in all scans is most pronounced here and is highlighted by white dashed circles. **f** shows the same scan as **e** but with inverted color map where the honeycomb is better visible. There is still a small sublattice polarization even in this case. Scale bars are 500 pm. The measurements have been performed at different locations and with different tips.

Moiré. If that was the case, we would expect the charge density wave to also be modulated on the Moiré length scale. However, we do not observe such a modulation. Furthermore, we do not see the Moiré on all images of the charge density wave. Finally, we also observed signatures of the charge density wave on a second sample (AC24), on which we did not find any Moiré superlattice (see Appendix F.2). Taking into account all these informations, we are convinced that the charge density wave we observed is not caused by the Moiré.

B-field driven transition to strong screening

Leaving behind the measurements at 14 T, we can further increase the substrate induced screening of the long range Coulomb interactions by decreasing the applied field. For this purpose we repeat the study shown above at several lower fields. The resulting series of images is depicted in Figure 4.10. We observe a clear sublattice polarization down to 7 T, but at 4 T mainly the regular honeycomb lattice is recovered. The honeycomb lattice is the fingerprint of a spin-polarized order for which both sublattices are equally occupied. While our STM measurements

are not spin sensitive and therefore do not allow identifying the exact nature of the spin order, transport measurements identified a ferromagnetic order at low field on the hBN/$SrTiO_3$ substrate[168]. This transport study observes a transition from the helical edge transport implying a ferromagnetic ground state to an insulating edge state compatible with the CAF order at around 3 T.
Despite the dominance of the honeycomb lattice, even at 4 T there is still a little sublattice polarization, which is better visible in the inverted contrast image in Figure 4.10 f). We interpret this as the coexistence of the two phases, which points to a first-order phase transition as predicted by theory[176].

Summary and Discussion

Summarizing the results presented in the last three sections, we observe three different regimes in our measurements each represented by one scan in Figure 4.11. Coming from an unscreened graphene on hBN/SiO_2, where we surprisingly observe a Kekulé bond order, we can screen the long range Coulomb interaction by changing the substrate to hBN/$SrTiO_3$. According to Equation 4.2.6, we can tune this screening with magnetic field. In the weakly screened regime at around ≈ 14 T, we observe a charge density wave order. Increasing the screening by lowering the magnetic field results in a spin polarized ground state, which transport measurements identified as the ferromagnetic order[168]. From these observations, we conjecture that with our experimental approach we are able to tune the interactions along a trajectory similar to the one sketched for illustrative purposes on the phase diagram in Figure 4.11. At very high magnetic fields $l_B \ll d_{\mathrm{BN}}$, not accessible in our setup, we expect the screening effect of the $SrTiO_3$ substrate to vanish and hence to recover the unscreened configuration with a Kekulé bond order on this substrate as well.
Previous, indirect transport measurements[177] in graphene on hBN/SiO_2 observed a Zeeman controlled transition from one of the three insulating to the conducting ferromagnetic edge state from wich they conjectured a CAF ground state. Our observation of the Kekulé order instead of the CAF in the corresponding regime contradicts this transition scenario as well as other experiments investigating spin-currents[202] and magnon transmission[191–193] that point to a magnetic ground state. However, a recent theoretical study shows that the CAF and the bond order can coexist[203], which might explain the experimental dissonance.
Our observation of unexpected subdominant orders in the Kekulé bond order as well as in the charge density wave order demonstrates the need for more elaborate modeling of the underlying physics.
The time dependent switches of the Kekulé bond order that occured during our measurements as well as skyrmion excitations observed in the same kind of system[194] point to the presence of depinning mechanisms and domain walls which might contribute to transport.

In general, as sketched in Figure 4.11, the broken symmetry states for the Kekulé and charge density order on the one hand and the ferromagnetic order on the other hand disperse in fundamentally different ways when approaching the edge. The presence or absence of a gap at Fermi energy at the sample edge profoundly alters the transport properties of macroscopic samples. This illustrates how relevant our study is to transport measurements and applications since it helps understanding the real nature of the ground-state orders.

A weak point of our study is that our STM tip is not sensitive to the spin orientation. For this reason we have to rely on transport measurements in similar samples for interpreting the nature

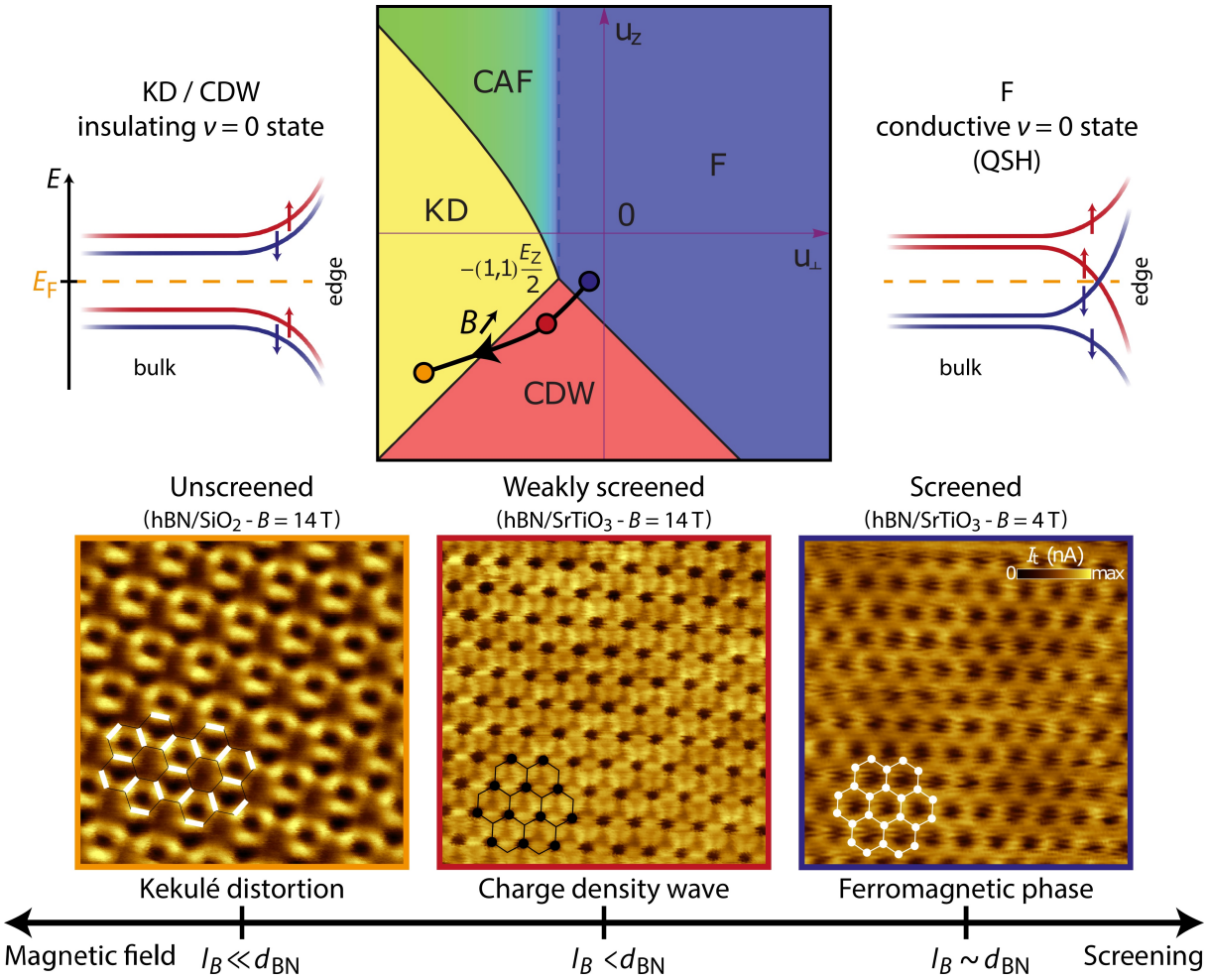

Figure 4.11: Screening induced phase transition from Kekulé distortion in the unscreened case via a charge density wave in the weak-screening regime to a ferromagnetic phase in the strong-screening regime. Bottom: constant-height STM images of the three different ground states. Center top: the proposed phase diagram trajectory realized in our experiment through changing the substrate and the applied magnetic field. Left and right: edge state dispersion of the different ground states leading to a gapped spectrum for the Kekulé and charge density wave and to helical edge state for the ferromagnetic order. Adapted from [174,176].

of the honeycomb lattice observed in the strong screening regime. In the future, spin-polarized STM measurements could directly image the spin texture to confirm this interpretation.
Another interesting continuation of our work could be to look at very clean samples at millikelvin temperatures to enter the fractional quantum Hall regime.

5 Conclusion and Outlook

Let us recall the main results presented in this work.

The first and main part of my work was the design, fabrication, testing and calibration of a UHV surface preparation chamber and its integration into the existing dilution refrigerator which required replacing the existing STM and wiring inside the refrigerator as well. Summarizing, the key features of the setup are:

- Surface Preparation
  - base pressure 2.2×10^{-10} mbar
  - sample annealing up to 1200 °C
  - sample cooling to liquid nitrogen temperatures
  - ion bombardment using Ar or Ne
  - e-beam metal evaporation, tested with In, Nb and Fe
  - molecule evaporation - sub monolayer MnPc evaporation demonstrated
  - sample storage for up to 5 samples
- STM / AFM
  - base temperature 50 mK
  - effective electronic temperature 140 mK
  - outside vacuum chamber pressure 10^{-9} mbar range during sample transfer
  - atomic resolution on Pb, $NbSe_2$ and graphene demonstrated
  - equipped with an RF antenna, photon assisted tunneling demonstrated
  - up to 10 DC sample lines for simultaneous transport measurements or gates
  - manipulation of single molecules with the STM tip demonstrated
  - magnetic field ready - soon up to approximately 2 T

Given the complexity of the system and problems of the components supplied by external companies, the proof of its proper functioning was a big success. During the last months of my thesis the system worked nicely and stable allowing the measurements summarized below.
There are a few improvements of the setup which are already being pursued. First, the installation of a new fully UHV-compatible superconducting coil to replace the broken old one. Second, not being designed for UHV conditions, the current dilution refrigerator still uses several viton o-rings and materials which are not optimized for UHV, resulting in a relatively high pressure which is often in the 10^{-8} mbar range and which depends a lot on efficient cryopumping. A new version of the dilution fridge designed for UHV conditions is being fabricated and will replace the old one within the next year. In the course of this, the STM chamber will also be equipped with an ionic pump so it will no longer depend on the cryo-pumping for maintaining the vacuum. In view of increasing helium prices, we also consider installing a local reliquefier to effectively make it a closed-cycle system.

In the second part, we started the rather long-term project of using monolayer $NbSe_2$ as a potential platform for topological superconductivity in different device geometries. I did the first step on the way to this long-term goal by characterizing the first samples grown by our collaborator Matthieu Jamet at CEA Grenoble. My measurements confirmed the expected sample

structure. I started with the graphene substrate which was grown on SiC. It exhibits the expected topographic and spectroscopic features such as the 6x6 modulation. We had to slightly adjust the initial $NbSe_2$ growth conditions to obtain clean monolayer samples. Nevertheless, the grown film quality is good, pointing to a large critical temperature of about 2.5 K estimated from the low temperature gap size. This value still needs to be confirmed by temperature dependent measurements. Surprisingly, I observed no charge density wave gap in the spectroscopy. The CDW topography signal was also rather weak. This should be studied more in detail on future samples. Finally, I also investigated the proximity superconductivity in graphene, demonstrating supercurrent flow over more than 100 nm and mapping the decay of the induced minigap which points to decoherence lengths on the order of a few micrometers in graphene.
My results establish a good understanding of the fundamental building block for future studies of heterosystems that might exhibit topological superconductivity. In a next step, we can deposit zero-dimensional impurities such as single MnPc molecules or iron atoms which are both available in the setup and whose deposition is already calibrated.

Finally, we discussed a very fruitful side project to which I contributed during a down time of my own setup: imaging the quantum Hall ground state orders in graphene. Not only did we answer the long standing question of which one of the four broken-symmetry state orders is actually realized in the standard Gr/hBN/SiO_2 samples (the Kekulé bond order), but we also managed to explore the phase diagram by means of a high-k dielectric that screens the Coulomb interactions. We also observed unexpected subdominant orders as well as time dependent switching behaviors which show that previous models have not grasped the full richness of this very complex many-body system. Apart from further theoretical work, it could be interesting to repeat similar measurements with a spin-polarized tip for being able to unambiguously discriminate all four lattice-scale orders. Another exciting project might be aiming at measuring very clean samples at millikelvin temperatures to enter the fractional quantum Hall regime.

A Surface coverage time - Full derivation

The goal of this appendix[1] is to derive equation 2.3.1, i.e. the time it takes for a (clean) surface to be covered with molecules as a function of temperature and pressure, assuming 100% sticking probability. This is a relevant question for the design and operation of a vacuum chamber in order to preserve a clean surface for the entire measurement time.

A.1 Theory

From the size of a unit cell, we can estimate the area occupied by one adsorbed molecule A_m. If we further know the incoming particle flux I, i.e. how many molecules impinge on a unit area of the surface per unit time, we can calculate the coverage rate. In the following discussion, we will assume a low coverage (wherever a molecule hits a surface, there is no other molecule yet which might prevent the incoming one from adsorbing) and a perfect adsorption (whatever arrives on the surface gets adsorbed). These are both worst case assumptions, hence the real coverage will be lower. The real adsorption probability, often called "sticking coefficient" is highly dependent on the material combination, the temperature and the energy and angle of the impinging molecule. Examples of experimental values are 2.6 % for He on graphite at low temperatures of around 4 K[204] or 95 % for CO on tungsten at 100 K[205].
With these assumptions, we can calculate the time until full coverage τ as

$$\tau = \frac{1}{I\,A_\mathrm{m}}.$$

Let us first consider the incoming particle flux I. Assuming an isotropic velocity distribution of the molecules in the gas phase, we can write the density of particles moving at a velocity v and at angles θ and ϕ with respect to the surface as $\mathrm{d}^3 n_{\theta,\phi,v} = n\frac{1}{4\pi}\sin\theta\ \mathrm{d}\theta\ \mathrm{d}\phi\ f(v)\mathrm{d}v$. Here, n denotes the overall particle density and $f(v,T)$ the normalized Maxwell-Boltzmann distribution. Therefore, we can write the total number of particles $\mathrm{d}^3 N_{\theta,\phi,v}$ arriving on an area element $\mathrm{d}A$ in the time $\mathrm{d}t$ as $\mathrm{d}^3 N_{\theta,\phi,v} = \mathrm{d}^3 n_{\theta,\phi,v}\mathrm{d}V(\theta,v)$. $\mathrm{d}V(\theta,v)$ is the volume element of particles with a speed v and at an angle of θ that moves in a time $\mathrm{d}t$ trough the surface area $\mathrm{d}A$. We can reformulate it as $\mathrm{d}V(\theta,v) = \mathrm{d}A\ \mathrm{d}z = \mathrm{d}A\ v_z\ \mathrm{d}t = \mathrm{d}A\ v\cos\theta\ \mathrm{d}\theta\ \mathrm{d}t$.

Now, we can finally write the incoming particle flux as

$$I = \frac{N}{\mathrm{d}A\ \mathrm{d}t} = \frac{1}{4\pi}\int_0^{\pi/2}\mathrm{d}\theta\int_0^{2\pi}\mathrm{d}\phi\,\sin\theta\ \cos\theta\int nvf(v)\mathrm{d}v = \frac{1}{4}n\bar{v}$$

denoting the average velocity $\bar{v} = \int_0^\infty vf(v)\mathrm{d}v$.

The Maxwell-Boltzmann distribution is given by $f(v) = \sqrt{\frac{2}{\pi}\left(\frac{m}{k_\mathrm{B}T}\right)^3}v^2\ \exp(-\frac{mv^2}{2k_\mathrm{B}T})$ which leads to an average velocity of (this is a Gaussian integral)

$$\bar{v} = \int_0^\infty vf(v)\mathrm{d}v = \frac{2}{\sqrt{\pi}}\sqrt{\frac{2k_\mathrm{B}T}{m}}.$$

[1] Source: lecture on Surface Physics 2017 at Karlsruhe Institut of Technology by Prof Dr Wulf Wulfhekel

In the final step, we make use of the ideal gas law $P = nk_BT$ and plug everything together, yielding

$$\tau = \frac{1}{I * A_m} = \frac{4k_BT}{P\frac{2}{\sqrt{\pi}}\sqrt{\frac{2k_BT}{m}}A_m} = \frac{\sqrt{2\pi mk_BT}}{PA_m}. \tag{A.1.1}$$

A.2 Numerics

If we assume an fcc lattice with a border length of 4 Å, we get an area of $16 \cdot 10^{-20}\text{m}^2$ per unit cell. Each unit cell hosts two lattice sites, such that the area per molecule is $8 \cdot 10^{-20}\text{m}^2$. We further assume the gas to be Nitrogen with a molecular mass of $m \approx 28\text{u} \approx 46.5 \cdot 10^{-27}\text{kg}$. Plugging these numbers in Equation A.1.1 for the two temperatures 300 K and 4 K gives the curves plotted in Figure A.1.

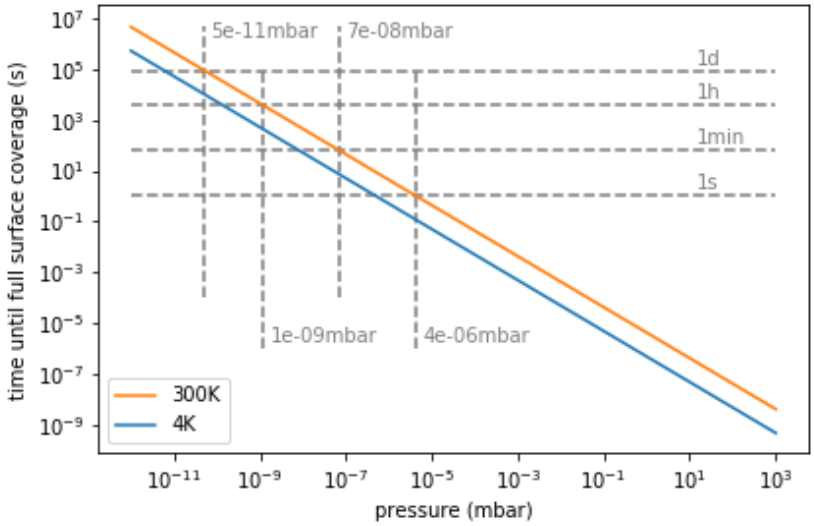

Figure A.1: Surface coverage time as function of pressure for 300 K (orange) and 4 K (blue), assuming Nitrogen gas.

For a colder gas at the same pressure, it takes a shorter time to cover the full surface because at lower temperature each molecule carries less energy and therefore less momentum. For this reason, a higher particle density is necessary to generate the same pressure. However, in a real setup, one observes a decreasing pressure when lowering the temperature. Therefore, the more reasonable assumption is that the particle density $n = \frac{N}{V}$ is the same. This is a worst case assumption because gasses tend to condense on cold surfaces and desorption and degassing are strongly suppressed, which is why the walls of a cold cryostat act as an additional cryo pump. According to the kinetic gas theory, the pressure is $P = nk_BT$ which implies

$$\frac{\tau_1}{\tau_2} = \frac{\sqrt{T_1}}{\sqrt{T_2}}\frac{T2}{T1} = \frac{\sqrt{T_2}}{\sqrt{T_1}}.$$

Hence, the time until full coverage at 4K is at least 8.7 times and at 100mK at least 55 times larger than at 300K. In reality, we expect this time to be even larger due to the discussed cryo pumping of the walls, but it is hard to quantitatively estimate the real pressure in the base temperature volume of the cryostat.

B SPM Motor calibration

The calibration of the piezo motors was performed using a sample patterned by lithography for the x and y axes. The z axis was calibrated on monoatomic steps of a Au (111) surface.
The directions of the axes can in principle be chosen arbitrarily. The choice we made here, and which is depicted in Figure B.1, ensures consistency between the coarse and fine motion and unmirrored imaging of sample features.

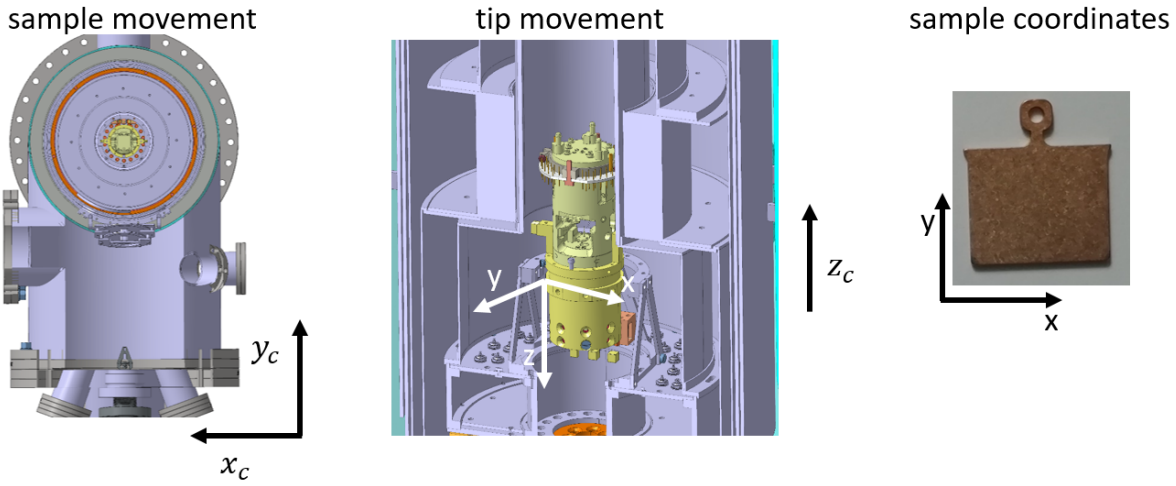

Figure B.1: Definition of the SPM axes. Their orientations are chosen in such a way that the imaging and the coarse motions are consistent with the sample coordinates. For instance, coarse steps in +X move the scan area towards larger x values on the sample, i.e. to the right.

	axis	300 K, 75 V	4 K, 200 V
tube	X	55.8 nm/V	10.6 nm/V
	Y	−52.6 nm/V	−10.3 nm/V
	Z	7.135 nm/V	1.34 nm/V
coarse	+X	201 nm/step	105 nm/step
	-X	179 nm/step	62 nm/step
	+Y	126 nm/step	32 nm/step
	-Y	171 nm/step	36 nm/step
	+Z	63 nm/step	<80 nm/step
	-Z	82 nm/step	<80 nm/step

Table B.1: Calibration of the SPM motors at the two standard operating temperatures. At 300 K, the coarse motors are driven with 75 V, at 4 K with 200 V.

C Main manipulator axes definitions

In principle, the position of the sample inside the chamber is defined by its three space coordinates as well as the three rotation angles. In practice, the rotation around the y axis (see Figure C.1) is prevented by construction, which leaves five degrees of freedom to be controlled.
The space coordinates, x, y and z can be adjusted by turning the corresponding lead screw. Each axis has a scale that allows reading the position with millimeter precision.
The rotation angle θ around the z axis can be adjusted by turning the orange knob in Figure C.1 c). It rotates the central part of the manipulator and leaves the outer part fix. Leak tightness is achieved through polished surfaces sliding on a series of viton o-rings equipped with differential pumping between adjacent o-rings.
The last degree of freedom is the rotation around the x-axis. This rotation is not desired and would ideally be prevented by the construction. However, the engineering tolerance in the x-y table in combination with the large lever of the manipulator arm (approx. 1.5 m), effectively allows a rotation of a few degree around the x-axis. Due to the length of the arm, this translates to several centimeter of displacement of the sample along the y-axis. For this reason, a precise sample positioning requires the control of this angle as well, which we achieve by measuring the height h of the adjustable support shown at the end of the manipulator in Figure C.1 b).

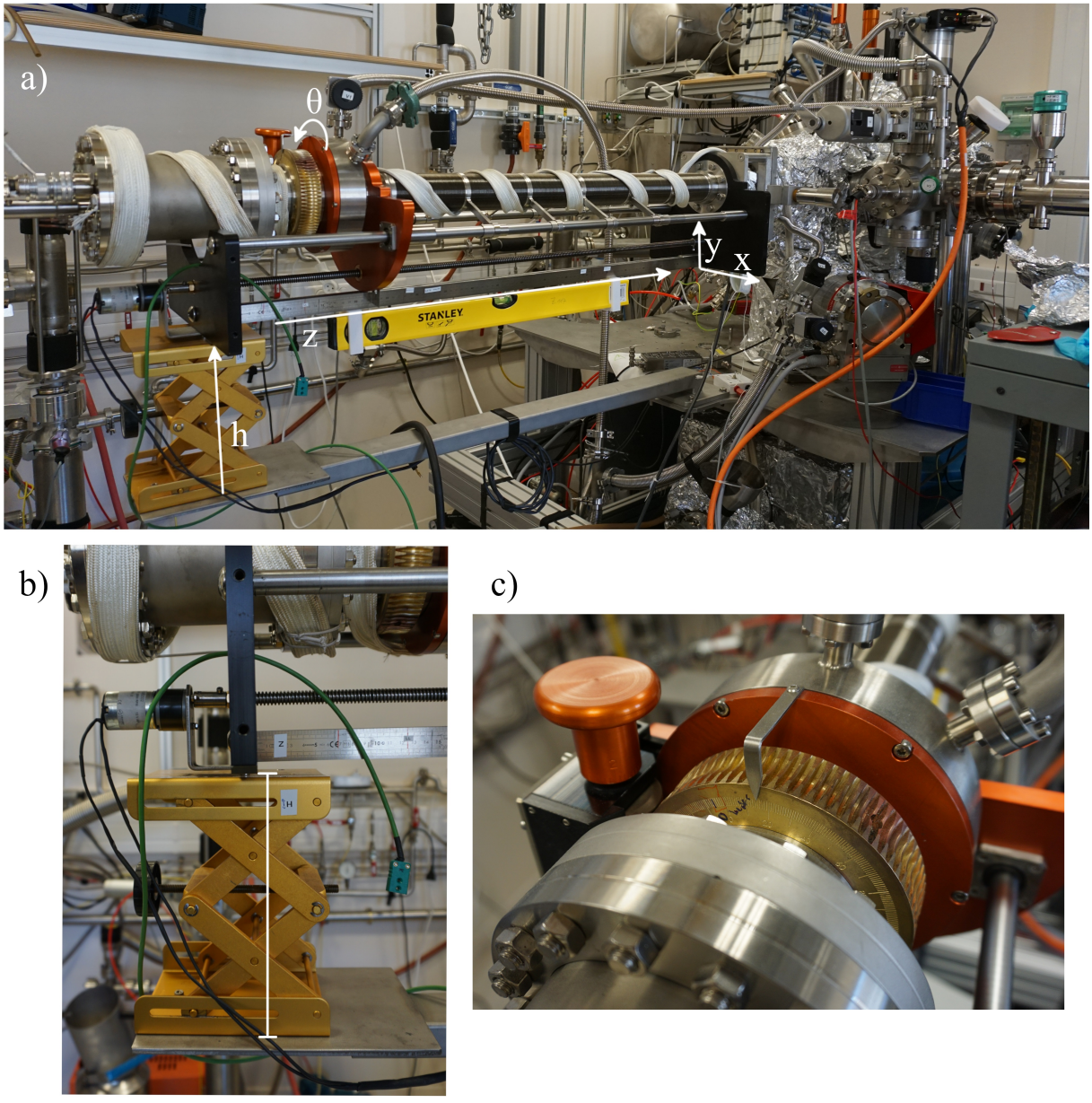

Figure C.1: Definition of the main manipulator's axes. a) Overview. x,y and z have their scales from where they can be read. b) h is measured from the stainless steel support to the lower edge of the black part of the manipulator. c) The rotation angle θ has an integrated scale as well.

D NIS spectroscopy on Pb (111)

Figure 2.23 c) shows an SIS spectroscopy of a Pb (111) surface measured with a Pb tip. This annex contains the corresponding NIS spectroscopy, shown in Figure D.1, measured with a normal Pt/Ir tip on the same Pb (111) surface.

This measurement was performed with a not optimized measurement environment inducing bias noise and thus a worse resolution than the best measurements shown in Chapter 2. Nevertheless, two peaks contributing to the density of states are distinguishable. Their position and spacing corresponds to what we expect from the SIS measurement and from the literature[66]. As expected from the band-structure calculations in the cited article, the Fermi surface with the larger gap contributes less to the tunneling conductance on the 111 surface.

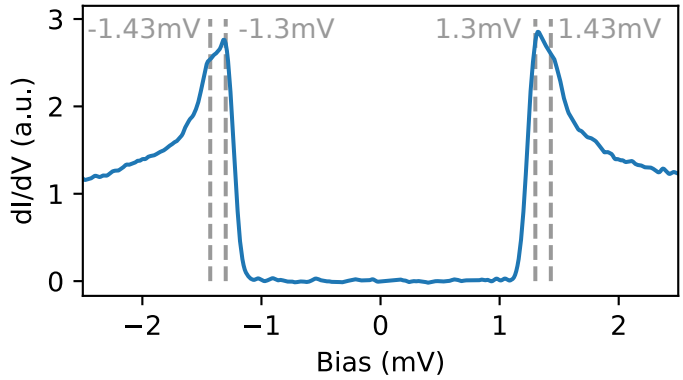

Figure D.1: NIS spectroscopy on Pb (111) using a Pt/Ir tip at 50 mK. We see the contribution of two peaks at around ± 1.3 mV and ± 1.43 mV. $I_{sp} = 1$ nA, $V_b = 5$ mV, $V_{ac,rms} = 15$ µV.

E Monolayer $NbSe_2$ - Supplementary Data

E.1 Islands on sample $NbSe_2$-Gr 2529

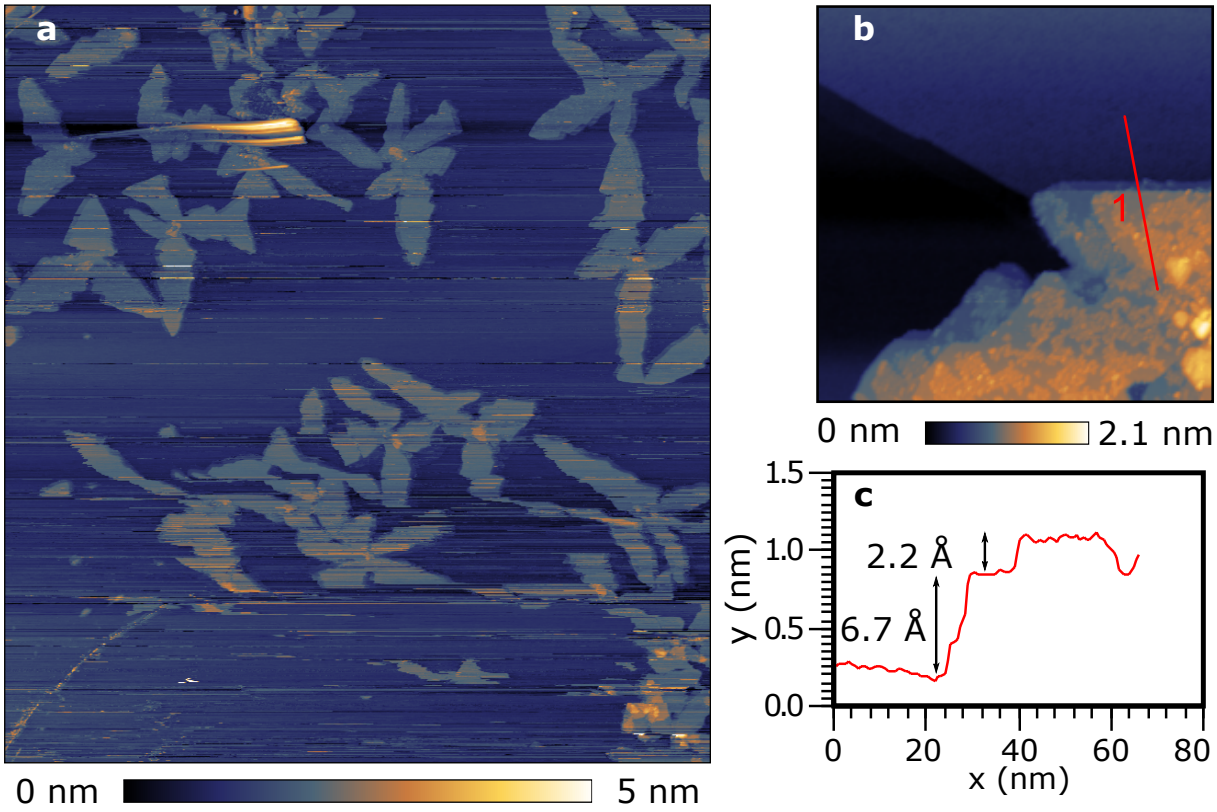

Figure E.1: 1.5 µm × 1.5 µm topography image of $NbSe_2$-Gr 2529. **a** There is no overgrown 'dirt' as on $NbSe_2$-Gr 2502 shown in Figure 3.7. A few bilayer $NbSe_2$ patches are visible in organge. **b** 150 nm × 150 nm topography image revealing small grainy dirt on top of $NbSe_2$. **c** Profile indicated in red in b. The dirt on top of $NbSe_2$ is about 2.2 Å thick, so probably a mono-atomic layer.

E.2 Proximity-induced superconductivity in graphene

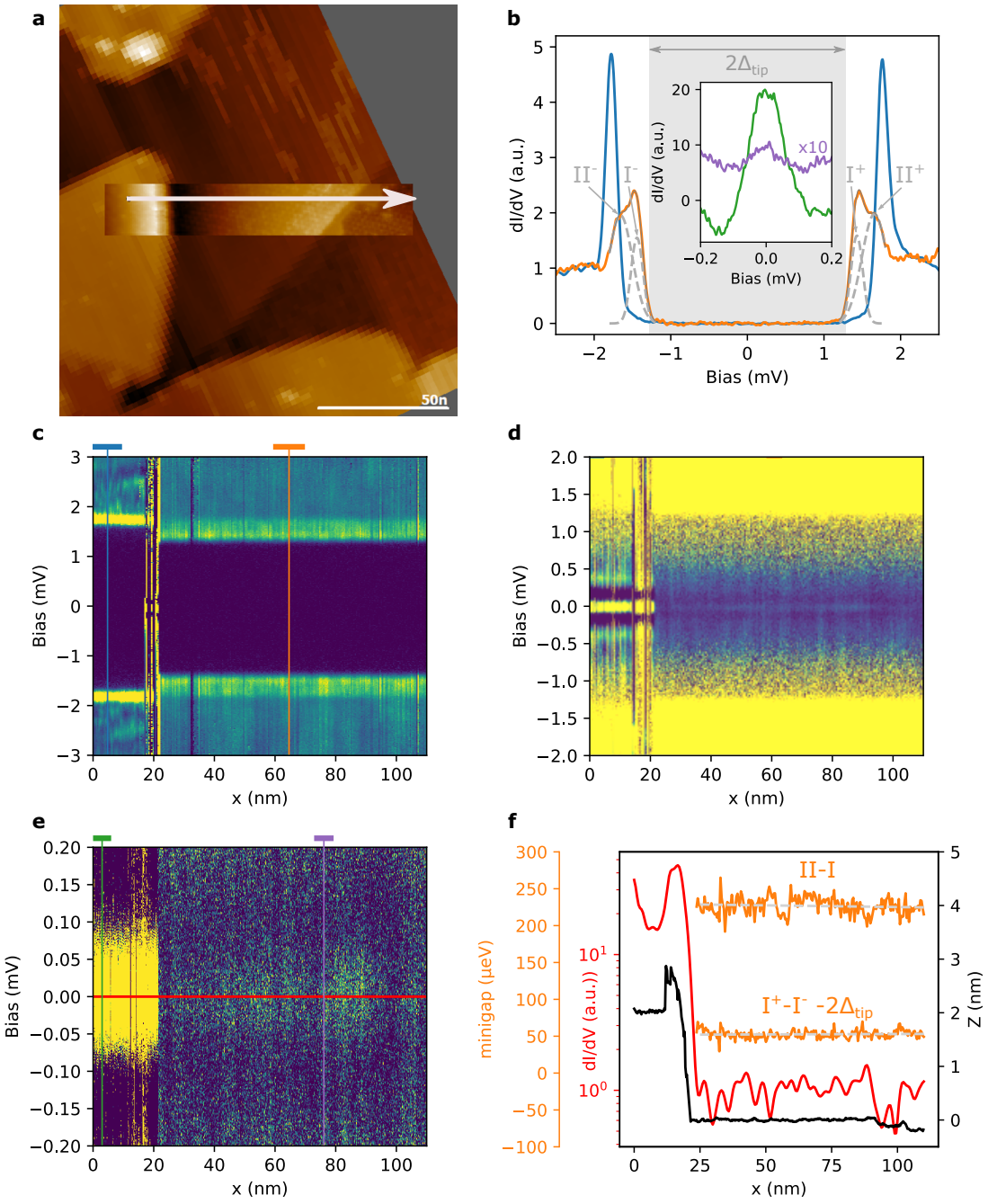

Figure E.2: Proximity-induced superconductivity in graphene. **a** Topography scan of the investigated area. The position of the spectroscopy maps in e-f is indicated by the white arrow. All maps start on $NbSe_2$ and transit to graphene at about 20 nm. At approximately 90 nm, there is a step in the substrate. **b** Spatially averaged spectroscopies (as indicated by the colored bars on top of c and e) extracted from the map in c and from e for the inset. The peaks of the spectrum on graphene (orange) fit well with a double Gaussian (gray) with $\mu_{I^\pm} = \pm 1.43\,\mathrm{mV}$, $\sigma_{I^\pm} = 77\,\mu\mathrm{V}$ and $\mu_{II^\pm} = \pm 1.66\,\mathrm{mV}$, $\sigma_{II^\pm} = 160\,\mu\mathrm{V}$. The purple peak in the inset is multiplied by ten for better visibility. **c-e** Line scans at **c** $V_b = 3\,\mathrm{mV}$, $I = 300\,\mathrm{pA}$, $V_{rms} = 15\,\mu\mathrm{V}$ **d**,**e** $I = 10\,\mathrm{nA}$ rest unchanged. **f** orange: size of the minigap extracted from the peak positions of the double Gaussian fits exemplified in b. The dashed lines are linear fits giving (II-I): $-(-0.5 \pm 0.3)\,\mu\mathrm{eV}\,x + (230 \pm 5)\,\mu\mathrm{eV}$ and ($I^+ - I^-$) assuming a tip gap of $\Delta_{tip} = 1.384\,\mathrm{meV}$: $(1 \pm 2) \times 10^{-2}\,\mu\mathrm{eV nm^{-1}}\,x + (52 \pm 1)\,\mu\mathrm{eV}$. red: Amplitude of the Josephson peak along the red line in e. dashed gray: linear fit to the Josephson peak with a slope of $5 \times 10^{-3}\,\mathrm{nm^{-1}}$. black: topography for map e.

E.3 Conductance maps on $NbSe_2$

Here we show two conductance maps taken on $NbSe_2$ at values corresponding to peaks above the superconducting gap. These peaks might originate from the collective modes from competing pairing instabilities observed by [99] or maybe just Friedel oscillations caused by the edge of the $NbSe_2$ flake.

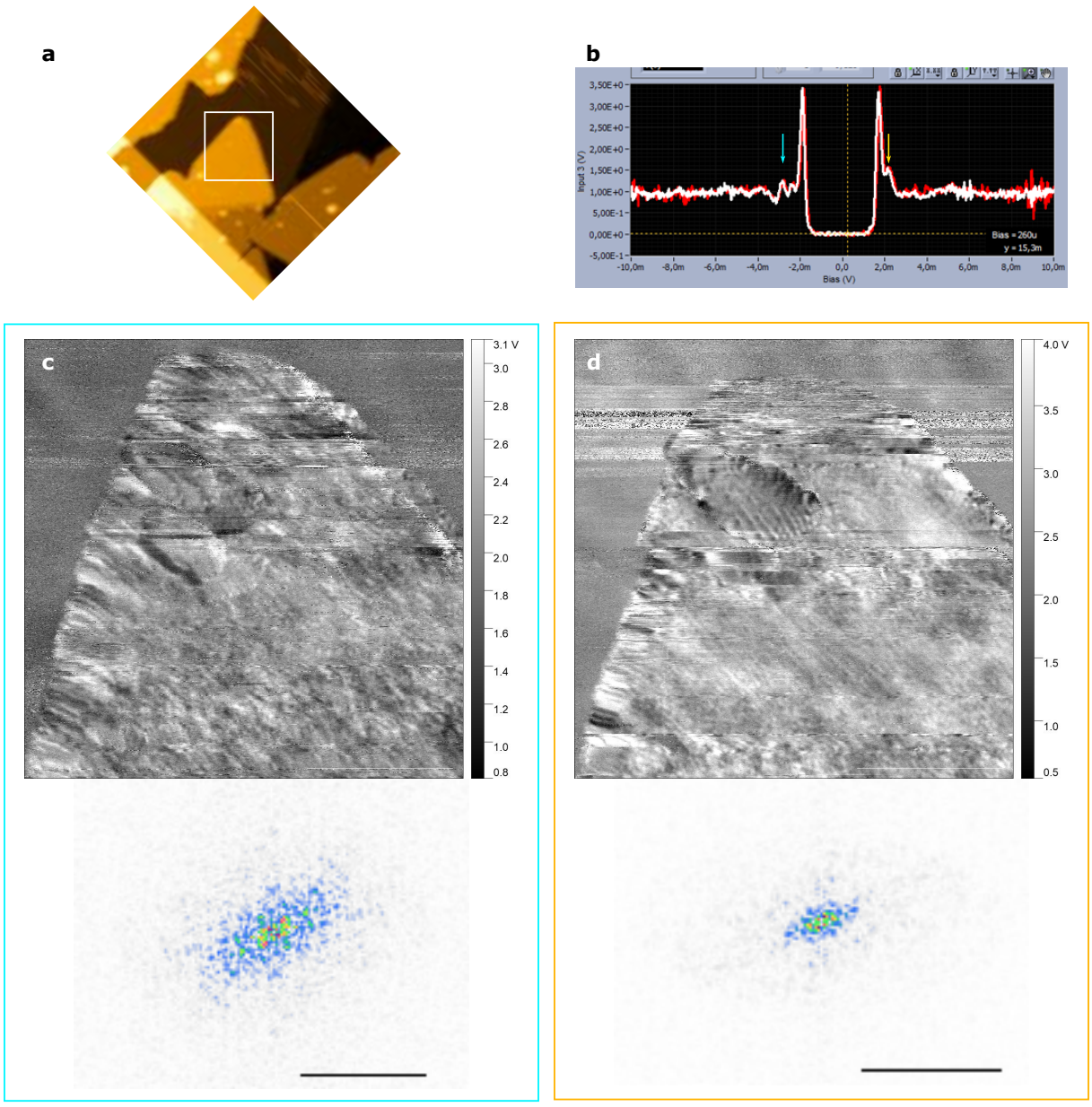

Figure E.3: Conductance maps of peaks above the gap. **a** Overview topography image of the surrounding area. Bright parts are $NbSe_2$. **b** SIS spectrum measured on $NbSe_2$ with a superconducting tip showing additional peaks outside the superconducting gap. The conductance maps corresponding to the bias voltages highlighted by arrows are plotted in c and d. **c,d** 60 nm × 60 nm conductance maps at $V_b = -2.8\,\text{mV}$ (c) and $V_b = 2.2\,\text{mV}$ (d) recorded at $I = 300\,\text{pA}$, $V_{rms} = 15\,\mu\text{V}$. A clear structure of the conductance is visible. The FFT of the $NbSe_2$ area is plotted below with a scalebar of $1\,\text{nm}^{-1}$.

E.4 Tunneling Spectroscopy of the CDW gap

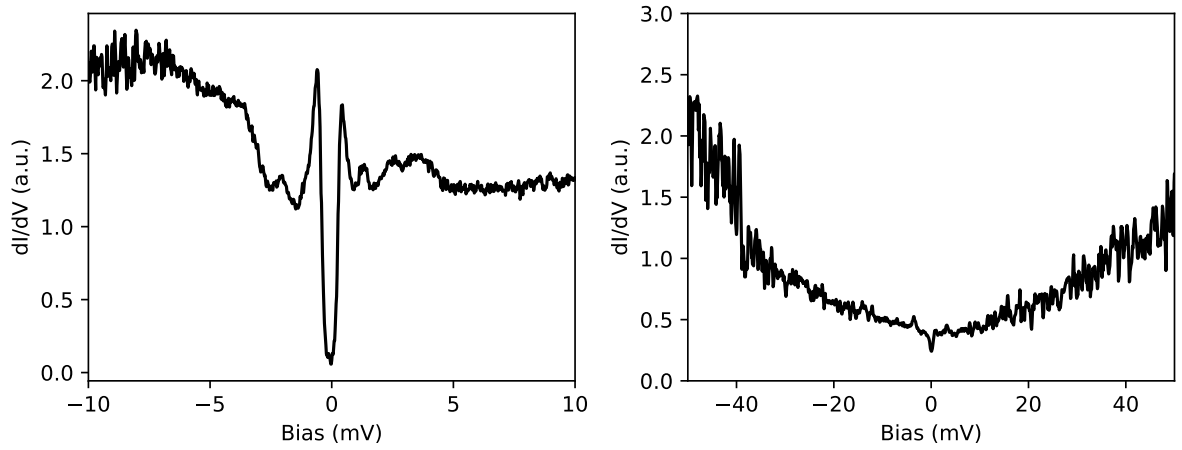

Figure E.4: Tunneling Spectroscopy on $NbSe_2$. Left: $V_b = 10\,mV$, $I = 2\,nA$, $V_{rms} = 15\,\mu V$, Right: $V_b = 80\,mV$, $I = 2\,nA$, $V_{rms} = 120\,\mu V$.

As mentioned in the main text, we did not observe a clear CDW gap in tunneling spectroscopy as it has been reported in literature (see Figure 3.2). Figure E.4 shows the tunneling spectroscopy measurement on $NbSe_2$ which would be the most compatible with a CDW gap of about 4 meV. We clearly see the superconducting gap of approximately 400 µeV at Fermi energy. At approximately $\pm 4\,mV$, there is a change in the DOS which could be caused by the CDW. However, the dip is not very pronounced and has not been clearly visible on other spectroscopies at different positions on the sample. Taking a look a the larger bias window on the right, we hardly see any dip either.

E.5 Z-Spectroscopy on $NbSe_2$ and graphene

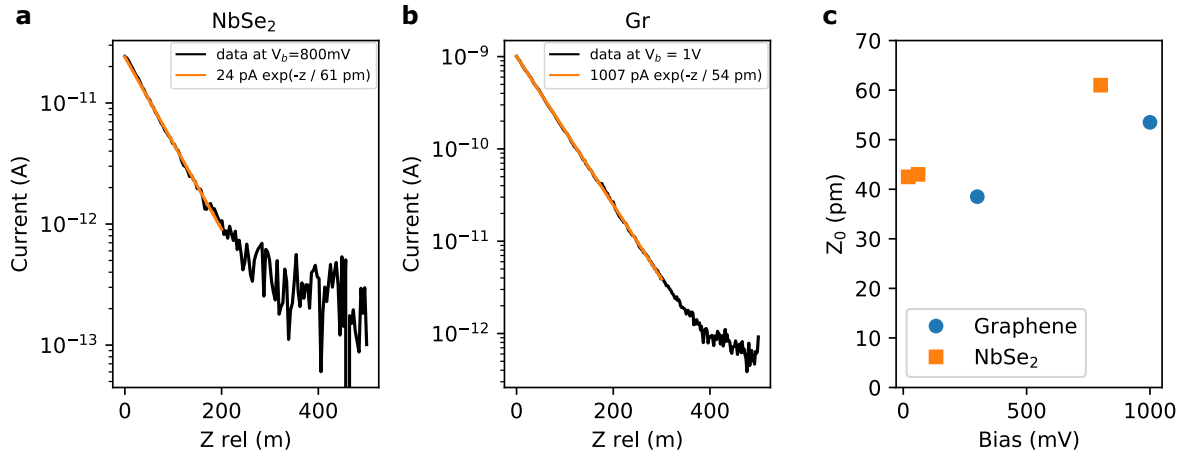

Figure E.5: Z-Spectroscopy on $NbSe_2$ and graphene. **a** Z-Spectroscopy on $NbSe_2$ at $V_b = 800\,mV$ fitted with an exponential fit yielding $Z_0 = 61\,pm$. **b** Z-Spectroscopy on graphene at $V_b = 1\,V$ fitted with an exponential fit yielding $Z_0 = 54\,pm$. **c** Z_0 versus bias voltage on both materials showing that Z_0 is systematically smaller on graphene than on $NbSe_2$.

In the simple 1D barrier model, the transmission probability through the vacuum barrier and thus the current decays with the tip-sample distance as $Z_0 = 2\sqrt{2m_e\Phi/\hbar^2}$. m_e is the electron mass and Φ the work function. This model works well if the tip and sample work-function Φ are the same and the applied bias is negligible ($V_b \ll \Phi$). If one of these conditions is not met, the barrier should be modeled by a trapezoid. Here we limit the discussion to the bias effect. Applying a bias leads to a tilt of the potential barrier and effectively decreases its height. Therefore, the observed decay length increases. This is what we observe in Figure E.5 c). However, the more important result for the discussion in the main text is that at a fixed bias voltage, the decay length on graphene is smaller than on $NbSe_2$.

F Quantum Hall Ferromagnetism in Graphene - Supplementary Data

F.1 Asymmetry of the Kekulé bond order

This section shows additional data of the Fourier decomposition of a symmetric Kekulé (Fig. F.1) and an asymmetric Kekulé (Fig. F.2). The main difference between the two lies in the central hexagon in the Fourier transform, highlighted in blue, which is has asymmetric amplitudes for the asymmetric Kekulé image whereas in the symmetric case the amplitudes are symmetric. We attribute this to the K-CDW on the $\sqrt{3}$ sized Kekulé lattice discussed in Section 4.2.4. Since a spontaneous direction change of the asymmetric Kekulé was observed (see Fig. 4.8 f-g), a substrate or tip induced asymmetry can be ruled out.

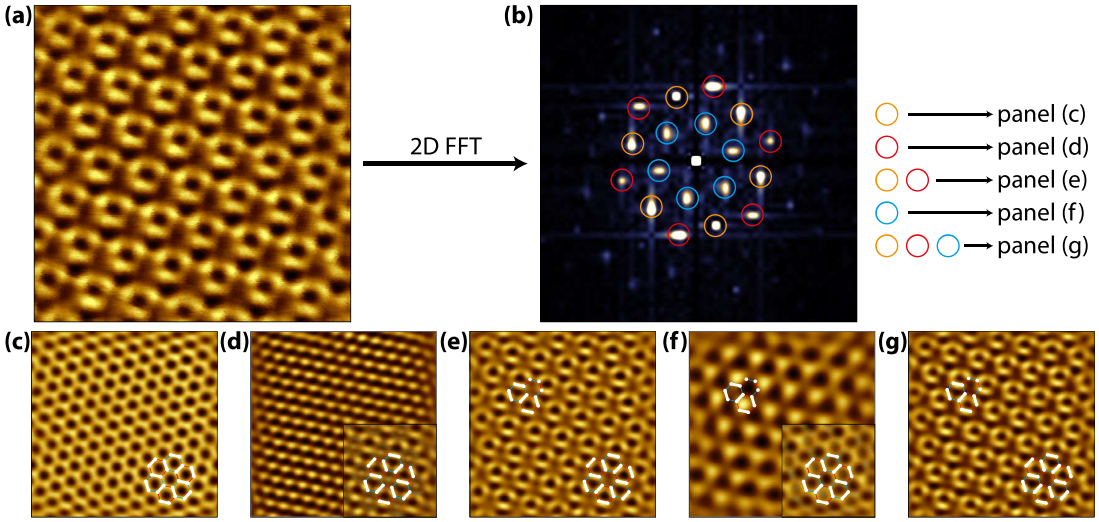

Figure F.1: FFT decomposition of the symmetric Kekulé. **(a)** Original constant height image. **(b)** 2D FFT of (a). **(c-g)** Filtered images only taking into account certain peaks of the FFT as listed in (b). The semi transparent insets of (d) and (f) superimpose the same area from (c). Image from[174].

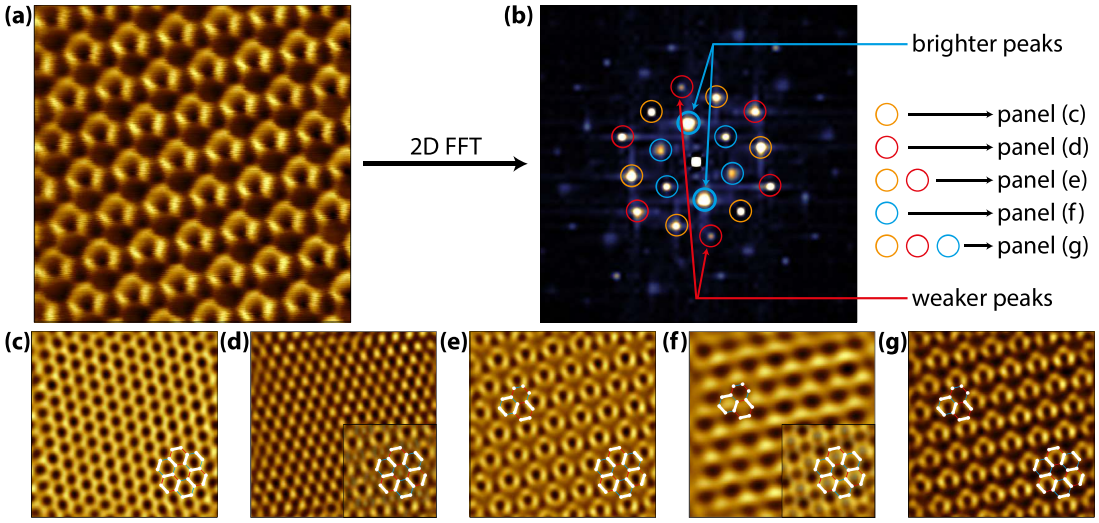

Figure F.2: FFT decomposition of the asymmetric Kekulé. **(a)** Original constant height image. **(b)** 2D FFT of (a). **(c-g)** Filtered images only taking into account certain peaks of the FFT as listed in (b). The semi transparent insets of (d) and (f) superimpose the same area from (c). Image from[174].

F.2 Charge Density Wave on AC24

To provide further evidence for the charge density wave pattern observed on sample AC23 and presented in detail in Section 4.2.4, we performed additional samples on a second sample called AC24 which has a hBN/$SrTiO_3$ substrate just like AC23. First, we remark on large area STM scans, as the one shown in Figure F.3, that this sample does not possess any Moiré superlattice. We then conduct the same study as on AC23, i.e. spectroscopy measurements to identify the charge neutrality point and scans at different bias voltages to image the broken symmetry ground state. The observed images represented in Figure F.4 point to the presence of a charge density wave at 14 T on the sample this sample as well. However, on this sample it was difficult to obtain good spectroscopy and imaging conditions at the same time, so we do not have as solid data as for AC23.

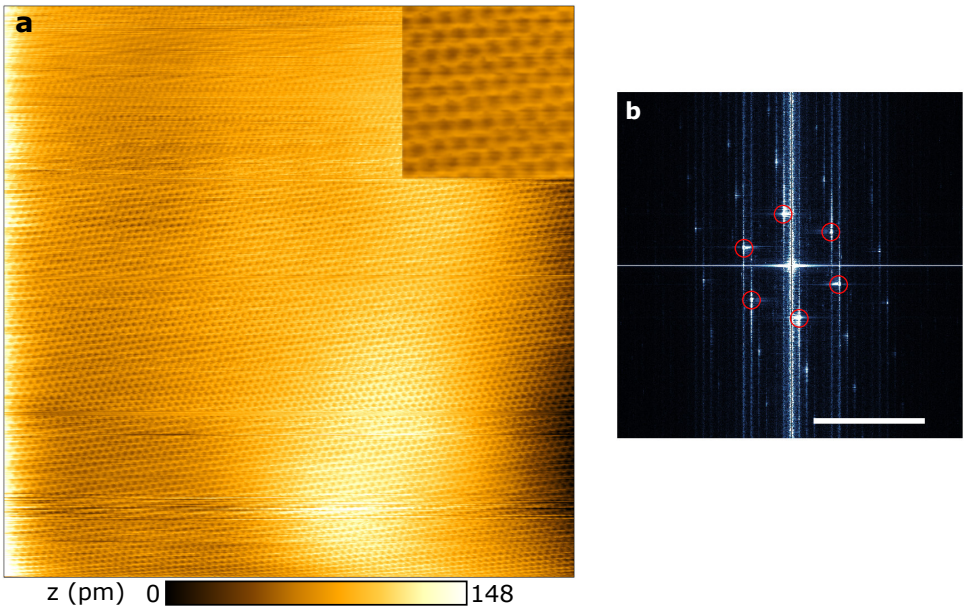

Figure F.3: **a** 20 nm × 20 nm STM constant current image recorded at 300 mV and 1 nA showing the graphene honeycomb lattice and no Moiré superlattice. The inset shows a 2 nm × 2 nm zoomed area. **b** FFT of a with the peaks corresponding to the honeycomb lattice highlighted in red. No small wave-vector superlattice can be observed. The scale bar is 10 nm^{-1}.

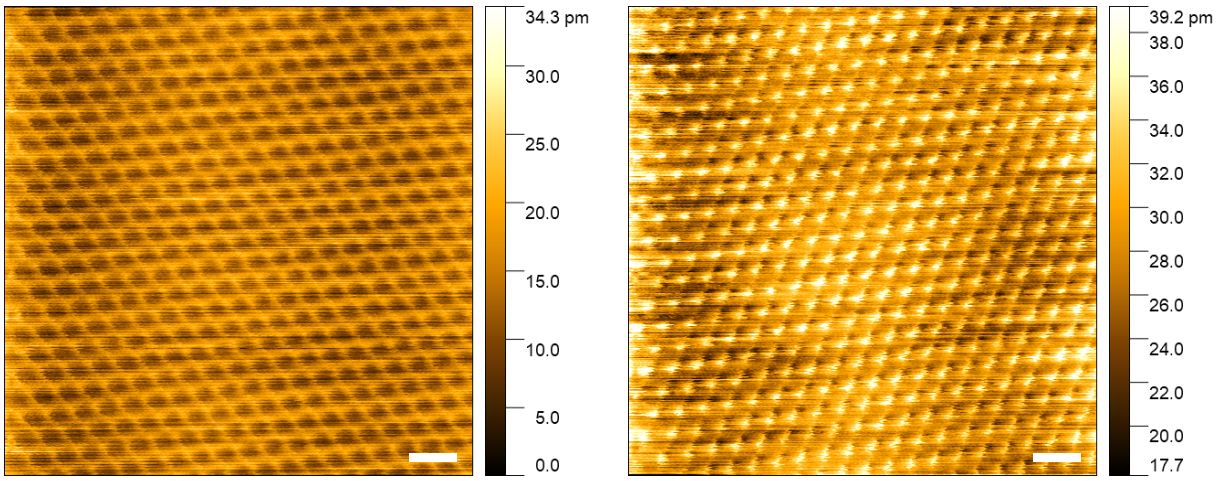

Figure F.4: STM scans of graphene at 14 T on sample AC24. Left: At −350 mV bias voltage we see the normal honeycomb lattice. Right: At −18 mV we observe a strong sublattice polarization compatible with a charge density wave.

Bibliography

[1] G. Binnig and H. Rohrer, "Scanning tunneling microscopy—from birth to adolescence," *Rev. Mod. Phys.*, vol. 59, pp. 615–625, July 1987. Publisher: American Physical Society.

[2] G. Binnig, H. Rohrer, C. Gerber, and E. Weibel, "7 × 7 Reconstruction on Si(111) Resolved in Real Space," *Phys. Rev. Lett.*, vol. 50, pp. 120–123, Jan. 1983. Publisher: American Physical Society.

[3] J. Tersoff and D. R. Hamann, "Theory and Application for the Scanning Tunneling Microscope," *Physical Review Letters*, vol. 50, pp. 1998–2001, June 1983.

[4] A. M. Baró, G. Binnig, H. Rohrer, C. Gerber, E. Stoll, A. Baratoff, and F. Salvan, "Real-Space Observation of the 2 × 1 Structure of Chemisorbed Oxygen on Ni(110) by Scanning Tunneling Microscopy," *Phys. Rev. Lett.*, vol. 52, pp. 1304–1307, Apr. 1984. Publisher: American Physical Society.

[5] F. Besenbacher, J. V. Lauritsen, and S. Wendt, "STM studies of model catalysts," *Nano Today*, vol. 2, pp. 30–39, Aug. 2007.

[6] A. L. de Lozanne, S. A. Elrod, and C. F. Quate, "Spatial Variations in the Superconductivity of Nb_3Sn Measured by Low-Temperature Tunneling Microscopy," *Phys. Rev. Lett.*, vol. 54, pp. 2433–2436, June 1985. Publisher: American Physical Society.

[7] O. Marti, G. Binnig, H. Rohrer, and H. Salemink, "Low-temperature scanning tunneling microscope," *Surface Science*, vol. 181, no. 1, pp. 230–234, 1987.

[8] M. Anders, M. Mück, and C. Heiden, "SEM/STM combination for STM tip guidance," *Ultramicroscopy*, vol. 25, no. 2, pp. 123–128, 1988.

[9] O. Guise, H. Marbach, J. T. Yates, M.-C. Jung, J. Levy, and J. Ahner, "Development and performance of the nanoworkbench: A four tip STM for conductivity measurements down to submicrometer scales," *Review of Scientific Instruments*, vol. 76, p. 045107, Apr. 2005. Publisher: American Institute of Physics.

[10] R. Wiesendanger, H.-J. Güntherodt, G. Güntherodt, R. J. Gambino, and R. Ruf, "Observation of vacuum tunneling of spin-polarized electrons with the scanning tunneling microscope," *Phys. Rev. Lett.*, vol. 65, pp. 247–250, July 1990. Publisher: American Physical Society.

[11] M. Johnson and J. Clarke, "Spin-polarized scanning tunneling microscope: Concept, design, and preliminary results from a prototype operated in air," *Journal of Applied Physics*, vol. 67, pp. 6141–6152, May 1990. Publisher: American Institute of Physics.

[12] M. Bode, M. Getzlaff, and R. Wiesendanger, "Spin-Polarized Vacuum Tunneling into the Exchange-Split Surface State of Gd(0001)," *Phys. Rev. Lett.*, vol. 81, pp. 4256–4259, Nov 1998.

[13] W. Wulfhekel and J. Kirschner, "Spin-polarized scanning tunneling microscopy on ferromagnets," *Applied Physics Letters*, vol. 75, pp. 1944–1946, Sept. 1999.

[14] N. García, A. M. Baró, R. Miranda, H. Rohrer, C. Gerber, R. G. Cantú, and J. L. Peña, "Surface Roughness Standards, Obtained with the Scanning Tunneling Microscope Operated at Atmospheric Air Pressure," *Metrologia*, vol. 21, pp. 135–138, Jan. 1985. Publisher: IOP Publishing.

[15] R. Sonnenfeld and P. K. Hansma, "Atomic-Resolution Microscopy in Water," *Science*, vol. 232, no. 4747, pp. 211–213, 1986. _eprint: https://www.science.org/doi/pdf/10.1126/science.232.4747.211.

[16] M. Crommie, C. Lutz, D. Eigler, and E. Heller, "Quantum corrals," *Quantum Complexity in Mesoscopic Systems*, vol. 83, pp. 98–108, May 1995.

[17] E. Liebhaber, L. M. Rütten, G. Reecht, J. F. Steiner, S. Rohlf, K. Rossnagel, F. von Oppen, and K. J. Franke, "Quantum spins and hybridization in artificially-constructed chains of magnetic adatoms on a superconductor," *Nature Communications*, vol. 13, p. 2160, Apr 2022.

[18] N. Moussy, H. Courtois, and B. Pannetier, "Local spectroscopy of a proximity superconductor at very low temperature," *Europhysics Letters (EPL)*, vol. 55, pp. 861–867, Sept. 2001. Publisher: IOP Publishing.

[19] H. Le Sueur, *Cryogenic AFM-STM for mesoscopic physics*. Theses, Université Pierre et Marie Curie - Paris VI, Sept. 2007.

[20] M. Assig, M. Etzkorn, A. Enders, W. Stiepany, C. R. Ast, and K. Kern, "A 10 mK scanning tunneling microscope operating in ultra high vacuum and high magnetic fields," *Review of Scientific Instruments*, vol. 84, p. 033903, Mar. 2013. Publisher: American Institute of Physics.

[21] H. Hess, R. Robinson, and J. Waszczak, "STM spectroscopy of vortex cores and the flux lattice," *Physica B: Condensed Matter*, vol. 169, pp. 422–431, Feb. 1991. Reprinted with permission from Elsevier.

[22] C. R. Ast, B. Jäck, J. Senkpiel, M. Eltschka, M. Etzkorn, J. Ankerhold, and K. Kern, "Sensing the quantum limit in scanning tunnelling spectroscopy," *Nature Communications*, vol. 7, p. 13009, Dec. 2016.

[23] S. Misra, B. B. Zhou, I. K. Drozdov, J. Seo, L. Urban, A. Gyenis, S. C. J. Kingsley, H. Jones, and A. Yazdani, "Design and performance of an ultra-high vacuum scanning tunneling microscope operating at dilution refrigerator temperatures and high magnetic fields," *Review of Scientific Instruments*, vol. 84, no. 10, p. 103903, 2013.

[24] H. von Allwörden, A. Eich, E. J. Knol, J. Hermenau, A. Sonntag, J. W. Gerritsen, D. Wegner, and A. A. Khajetoorians, "Design and performance of an ultra-high vacuum spin-polarized scanning tunneling microscope operating at 30 mk and in a vector magnetic field," *Review of Scientific Instruments*, vol. 89, no. 3, p. 033902, 2018.

[25] D. Wong, S. Jeon, K. P. Nuckolls, M. Oh, S. C. J. Kingsley, and A. Yazdani, "A modular ultra-high vacuum millikelvin scanning tunneling microscope," *Review of Scientific Instruments*, vol. 91, no. 2, p. 023703, 2020.

[26] M. Fernández-Lomana, B. Wu, F. Martín-Vega, R. Sánchez-Barquilla, R. Álvarez Montoya, J. M. Castilla, J. Navarrete, J. R. Marijuan, E. Herrera, H. Suderow, and I. Guillamón, "Millikelvin scanning tunneling microscope at 20/22 t with a graphite enabled stick–slip approach and an energy resolution below 8 μev: Application to conductance quantization at 20 t in single atom point contacts of al and au and to the charge density wave of 2h–nbse2," *Review of Scientific Instruments*, vol. 92, no. 9, p. 093701, 2021.

[27] Y. J. Song, A. F. Otte, V. Shvarts, Z. Zhao, Y. Kuk, S. R. Blankenship, A. Band, F. M. Hess, and J. A. Stroscio, "Invited review article: A 10 mk scanning probe microscopy facility," *Review of Scientific Instruments*, vol. 81, no. 12, p. 121101, 2010. Reprinted with the permission of AIP Publishing.

[28] T. Balashov, M. Meyer, and W. Wulfhekel, "A compact ultrahigh vacuum scanning tunneling microscope with dilution refrigeration," *Review of Scientific Instruments*, vol. 89, no. 11, p. 113707, 2018. Reprinted with the permission of AIP Publishing.

[29] G. C. Ménard, S. Guissart, C. Brun, S. Pons, V. S. Stolyarov, F. Debontridder, M. V. Leclerc, E. Janod, L. Cario, D. Roditchev, P. Simon, and T. Cren, "Coherent long-range magnetic bound states in a superconductor," *Nature Physics*, vol. 11, pp. 1013–1016, Dec. 2015.

[30] J. Halbritter, "On the oxidation and on the superconductivity of niobium," *Applied Physics A Solids and Surfaces*, vol. 43, pp. 1–28, May 1987.

[31] R. Calder and G. Lewin, "Reduction of stainless-steel outgassing in ultra-high vacuum," *British Journal of Applied Physics*, vol. 18, p. 15, May 1967.

[32] T. Fauster, ed., *Oberflächenphysik: Grundlagen und Methoden*. München: Oldenbourg Verlag, 2013.

[33] J. Cai, P. Ruffieux, R. Jaafar, M. Bieri, T. Braun, S. Blankenburg, M. Muoth, A. P. Seitsonen, M. Saleh, X. Feng, K. Müllen, and R. Fasel, "Atomically precise bottom-up fabrication of graphene nanoribbons," *Nature*, vol. 466, pp. 470–473, July 2010.

[34] L. Grill, M. Dyer, L. Lafferentz, M. Persson, M. V. Peters, and S. Hecht, "Nano-architectures by covalent assembly of molecular building blocks," *Nature Nanotechnology*, vol. 2, pp. 687–691, Nov. 2007.

[35] K. Logan, "Optimising the Assembly of an Ultra-High Vacuum Capable and Single-Electron Transistor Implementable Low Temperature Scanning Tunnelling Microscope," Master's thesis, Grenoble INP phelma, Imperial College London, May 2020.

[36] D. Longo, *Engineering topological states in arrays of magnetic molecules in interaction with a 2D superconductor*. Theses, Sorbonne Université, May 2019.

[37] J. Bauer, J. I. Pascual, and K. J. Franke, "Microscopic resolution of the interplay of Kondo screening and superconducting pairing: Mn-phthalocyanine molecules adsorbed on superconducting Pb(111)," *Physical Review B*, vol. 87, p. 075125, Feb. 2013.

[38] S. Martin, *Systèmes nanoélectroniques hybrides: Cartographies de la densité d'états locale*. PhD thesis, Institut Néel CNRS/UJF/Grenoble INP, Grenoble, Dec. 2012.

[39] R. Radebaugh and J. Siegwarth, "Dilution refrigerator technology," *Cryogenics*, vol. 11, pp. 368–384, Oct. 1971.

[40] S. Samaddar, *Charge disorder and screening in graphene*. PhD thesis, Université Grenoble Alpes, Grenoble, Oct. 2015.

[41] A. De Cecco, *Quantum electronics in nanostructures explored by Scanning Probe Microscopy*. PhD thesis, Université Grenoble Alpes, Grenoble, Oct. 2018.

[42] W. Demtröder, *Experimentalphysik 1*. Springer-Lehrbuch, Berlin, Heidelberg: Springer Berlin Heidelberg, 2013.

[43] R. Sharma, *Superconductivity: Basics and Applications to Magnets*, vol. 214 of *Springer Series in Materials Science*. Cham: Springer International Publishing, 2015.

[44] J. Olson, "Thermal conductivity of some common cryostat materials between 0.05 and 2 K," *Cryogenics*, vol. 33, pp. 729–731, July 1993.

[45] J. Weisend II, ed., *Cryostat Design: Case Studies, Principles and Engineering*. International Cryogenics Monograph Series, Cham: Springer International Publishing, 2016.

[46] G. Ventura and M. Perfetti, *Thermal Properties of Solids at Room and Cryogenic Temperatures*. International Cryogenics Monograph Series, Dordrecht: Springer Netherlands, 2014.

[47] M. Thalmann, H.-F. Pernau, C. Strunk, E. Scheer, and T. Pietsch, "Comparison of cryogenic low-pass filters," *Review of Scientific Instruments*, vol. 88, p. 114703, Nov. 2017.

[48] K. Bladh, D. Gunnarsson, E. Hürfeld, S. Devi, C. Kristoffersson, B. Smålander, S. Pehrson, T. Claeson, P. Delsing, and M. Taslakov, "Comparison of cryogenic filters for use in single electronics experiments," *Review of Scientific Instruments*, vol. 74, pp. 1323–1327, Mar. 2003.

[49] J. M. Martinis, M. H. Devoret, and J. Clarke, "Experimental tests for the quantum behavior of a macroscopic degree of freedom: The phase difference across a Josephson junction," *Physical Review B*, vol. 35, pp. 4682–4698, Apr. 1987.

[50] A. B. Zorin, "The thermocoax cable as the microwave frequency filter for single electron circuits," *Review of Scientific Instruments*, vol. 66, pp. 4296–4300, Aug. 1995.

[51] M. B. Steer, *Microwave and RF design: a systems approach*. Raleigh, N.C: SciTech Pub, 2010. OCLC: ocn419263300.

[52] D. C. Glattli, P. Jacques, A. Kumar, P. Pari, and L. Saminadayar, "A noise detection scheme with 10 mK noise temperature resolution for semiconductor single electron tunneling devices," *Journal of Applied Physics*, vol. 81, pp. 7350–7356, June 1997.

[53] J.-F. Ge, M. Ovadia, and J. E. Hoffman, "Achieving low noise in scanning tunneling spectroscopy," *Review of Scientific Instruments*, vol. 90, p. 101401, Oct. 2019.

[54] N. Gaillard, *Etude des propriétés morphologiques, electriques et chimiques ¡br /¿de l'Interface Métal/Isolant et de leur impact sur les performances ¡br /¿de la capacité TiN/Ta2O5/TiN*. Theses, Université Joseph-Fourier - Grenoble I, Dec. 2006.

tex.hal_id: tel-00142484 tex.hal_version: v1 tex.pdf: https://tel.archives-ouvertes.fr/tel-00142484/file/N.Gaillard-These.pdf.

[55] E. A. Mechtly, "Properties of Materials," in *Reference Data for Engineers*, pp. 4–1–4–33, Elsevier, 2002.

[56] R. Gross and A. Marx, *Festkörperphysik*. De Gruyter Oldenbourg, 2 ed., 2014.

[57] H. P. Klug, "A.Redetermination of the Lattice Constant of Lead," *Journal of the American Chemical Society*, vol. 68, pp. 1493–1494, Aug. 1946.

[58] N. Hatter, *Fundamental properties of molecules on surfaces Molecular switching and interaction of magnetic molecules with superconductors*. PhD thesis, Freie Universität Berlin, Dec. 2016.

[59] B. Chen, X. Duan, H. Wang, J. Du, Y. Zhou, C. Xu, Y. Zhang, L. Zhang, M. Wei, Z. Xia, C. Cao, J. Dai, M. Fang, and J. Yang, "Large magnetoresistance and superconductivity in α-gallium single crystals," *npj Quantum Materials*, vol. 3, p. 40, Dec. 2018.

[60] W. De Haas and J. Voogd, "On the superconductivity of the gallium," *Commun. Phys. Lab. Univ. Leiden*, vol. 199, pp. 733–734, 1929.

[61] D. Campanini, Z. Diao, and A. Rydh, "Raising the superconducting Tc of gallium: *In situ* characterization of the transformation of α-Ga into β-Ga," *Physical Review B*, vol. 97, p. 184517, May 2018.

[62] C. Tonnoir, A. Kimouche, J. Coraux, L. Magaud, B. Delsol, B. Gilles, and C. Chapelier, "Induced Superconductivity in Graphene Grown on Rhenium," *Physical Review Letters*, vol. 111, p. 246805, Dec. 2013.

[63] E. Mazaleyrat, S. Vlaic, A. Artaud, L. Magaud, T. Vincent, A. Cristina Gómez-Herrero, S. Lisi, P. Singh, N. Bendiab, V. Guisset, P. David, S. Pons, D. Roditchev, C. Chapelier, and J. Coraux, "How to induce superconductivity in epitaxial graphene via remote proximity effect through an intercalated gold layer," *2D Materials*, vol. 8, p. 015002, Oct. 2020.

[64] H. le Sueur and P. Joyez, "Room-temperature tunnel current amplifier and experimental setup for high resolution electronic spectroscopy in millikelvin scanning tunneling microscope experiments," *Review of Scientific Instruments*, vol. 77, p. 123701, Dec. 2006.

[65] J. G. Rodrigo, H. Suderow, and S. Vieira, "On the use of STM superconducting tips at very low temperatures," *The European Physical Journal B*, vol. 40, pp. 483–488, Aug. 2004.

[66] M. Ruby, B. W. Heinrich, J. I. Pascual, and K. J. Franke, "Experimental Demonstration of a Two-Band Superconducting State for Lead Using Scanning Tunneling Spectroscopy," *Physical Review Letters*, vol. 114, p. 157001, Apr. 2015.

[67] B. W. Heinrich, L. Braun, J. I. Pascual, and K. J. Franke, "Protection of excited spin states by a superconducting energy gap," *Nature Physics*, vol. 9, pp. 765–768, Dec. 2013.

[68] T. M. Klapwijk, G. E. Blonder, and M. Tinkham, "Explanation of subharmonic energy gap structure in superconducting contacts," *Physica B+C*, vol. 109-110, pp. 1657–1664, 1982.

[69] M. Octavio, M. Tinkham, G. E. Blonder, and T. M. Klapwijk, "Subharmonic energy-gap structure in superconducting constrictions," *Physical Review B*, vol. 27, pp. 6739–6746, June 1983.

[70] T. Proslier, A. Kohen, Y. Noat, T. Cren, D. Roditchev, and W. Sacks, "Probing the superconducting condensate on a nanometer scale," *Europhysics Letters (EPL)*, vol. 73, pp. 962–968, mar 2006.

[71] N. Bergeal, J. Lesueur, M. Aprili, G. Faini, J. P. Contour, and B. Leridon, "Pairing fluctuations in the pseudogap state of copper-oxide superconductors probed by the Josephson effect," *Nature Physics*, vol. 4, pp. 608–611, Aug 2008.

[72] M. T. Randeria, B. E. Feldman, I. K. Drozdov, and A. Yazdani, "Scanning Josephson spectroscopy on the atomic scale," *Physical Review B*, vol. 93, p. 161115, Apr. 2016.

[73] E. Berg, E. Fradkin, and S. A. Kivelson, "Charge-4e superconductivity from pair-density-wave order in certain high-temperature superconductors," *Nature Physics*, vol. 5, pp. 830–833, Nov. 2009.

[74] Y. Matsuda and H. Shimahara, "Fulde–Ferrell–Larkin–Ovchinnikov State in Heavy Fermion Superconductors," *Journal of the Physical Society of Japan*, vol. 76, p. 051005, May 2007.

[75] B. Sacépé, T. Dubouchet, C. Chapelier, M. Sanquer, M. Ovadia, D. Shahar, M. Feigel'man, and L. Ioffe, "Localization of preformed Cooper pairs in disordered superconductors," *Nature Physics*, vol. 7, pp. 239–244, Mar. 2011.

[76] K. K. Gomes, A. N. Pasupathy, A. Pushp, S. Ono, Y. Ando, and A. Yazdani, "Visualizing pair formation on the atomic scale in the high-Tc superconductor $Bi_2Sr_2CaCu_2O_{8+\delta}$," *Nature*, vol. 447, pp. 569–572, May 2007.

[77] S. H. Pan, E. W. Hudson, and J. C. Davis, "Vacuum tunneling of superconducting quasiparticles from atomically sharp scanning tunneling microscope tips," *Applied Physics Letters*, vol. 73, pp. 2992–2994, Nov. 1998.

[78] M. Xu, Y. Takano, T. Hatano, M. Kitahara, and D. Fujita, "The fabrication of MgB_2 superconducting STM tips," *Physica C: Superconductivity*, vol. 388-389, pp. 117–118, May 2003.

[79] O. Naaman, W. Teizer, and R. C. Dynes, "Fluctuation Dominated Josephson Tunneling with a Scanning Tunneling Microscope," *Physical Review Letters*, vol. 87, p. 097004, Aug. 2001.

[80] V. Mourik, K. Zuo, S. M. Frolov, S. R. Plissard, E. P. A. M. Bakkers, and L. P. Kouwenhoven, "Signatures of Majorana Fermions in Hybrid Superconductor-Semiconductor Nanowire Devices," *Science*, vol. 336, pp. 1003–1007, May 2012.

[81] A. Das, Y. Ronen, Y. Most, Y. Oreg, M. Heiblum, and H. Shtrikman, "Zero-bias peaks and splitting in an Al–InAs nanowire topological superconductor as a signature of Majorana fermions," *Nature Physics*, vol. 8, pp. 887–895, Dec. 2012.

[82] R. S. Deacon, Y. Tanaka, A. Oiwa, R. Sakano, K. Yoshida, K. Shibata, K. Hirakawa, and S. Tarucha, "Tunneling Spectroscopy of Andreev Energy Levels in a Quantum Dot Coupled to a Superconductor," *Physical Review Letters*, vol. 104, p. 076805, Feb. 2010.

[83] E. J. H. Lee, X. Jiang, M. Houzet, R. Aguado, C. M. Lieber, and S. De Franceschi, "Spin-resolved Andreev levels and parity crossings in hybrid superconductor–semiconductor nanostructures," *Nature Nanotechnology*, vol. 9, pp. 79–84, Jan. 2014.

[84] A. Jellinggaard, K. Grove-Rasmussen, M. H. Madsen, and J. Nygård, "Tuning Yu-Shiba-Rusinov states in a quantum dot," *Physical Review B*, vol. 94, p. 064520, Aug. 2016.

[85] E. J. H. Lee, X. Jiang, R. Žitko, R. Aguado, C. M. Lieber, and S. De Franceschi, "Scaling of subgap excitations in a superconductor-semiconductor nanowire quantum dot," *Physical Review B*, vol. 95, p. 180502, May 2017.

[86] L. Schneider, M. Steinbrecher, L. Rózsa, J. Bouaziz, K. Palotás, M. dos Santos Dias, S. Lounis, J. Wiebe, and R. Wiesendanger, "Magnetism and in-gap states of 3d transition metal atoms on superconducting Re," *npj Quantum Materials*, vol. 4, p. 42, Dec. 2019.

[87] E. Liebhaber, S. Acero González, R. Baba, G. Reecht, B. W. Heinrich, S. Rohlf, K. Rossnagel, F. von Oppen, and K. J. Franke, "Yu–Shiba–Rusinov States in the Charge-Density Modulated Superconductor $NbSe_2$," *Nano Letters*, vol. 20, pp. 339–344, Jan. 2020.

[88] O. Peters, N. Bogdanoff, S. Acero González, L. Melischek, J. R. Simon, G. Reecht, C. B. Winkelmann, F. von Oppen, and K. J. Franke, "Resonant Andreev reflections probed by photon-assisted tunnelling at the atomic scale," *Nature Physics*, vol. 16, pp. 1222–1226, Dec. 2020.

[89] S. A. González, L. Melischek, O. Peters, K. Flensberg, K. J. Franke, and F. von Oppen, "Photon-assisted resonant Andreev reflections: Yu-Shiba-Rusinov and Majorana states," *Physical Review B*, vol. 102, p. 045413, July 2020.

[90] P. K. Tien and J. P. Gordon, "Multiphoton Process Observed in the Interaction of Microwave Fields with the Tunneling between Superconductor Films," *Physical Review*, vol. 129, pp. 647–651, Jan. 1963.

[91] S. Müllegger, S. Tebi, A. K. Das, W. Schöfberger, F. Faschinger, and R. Koch, "Radio Frequency Scanning Tunneling Spectroscopy for Single-Molecule Spin Resonance," *Physical Review Letters*, vol. 113, p. 133001, Sept. 2014.

[92] S. Baumann, W. Paul, T. Choi, C. P. Lutz, A. Ardavan, and A. J. Heinrich, "Electron paramagnetic resonance of individual atoms on a surface," *Science*, vol. 350, pp. 417–420, Oct. 2015.

[93] S. Loth, M. Etzkorn, C. P. Lutz, D. M. Eigler, and A. J. Heinrich, "Measurement of Fast Electron Spin Relaxation Times with Atomic Resolution," *Science*, vol. 329, pp. 1628–1630, Sept. 2010.

[94] L. M. Veldman, L. Farinacci, R. Rejali, R. Broekhoven, J. Gobeil, D. Coffey, M. Ternes, and A. F. Otte, "Free coherent evolution of a coupled atomic spin system initialized by electron scattering," *Science*, vol. 372, pp. 964–968, May 2021.

[95] X. Xi, Z. Wang, W. Zhao, J.-H. Park, K. T. Law, H. Berger, L. Forró, J. Shan, and K. F. Mak, "Ising pairing in superconducting $NbSe_2$ atomic layers," *Nature Physics*, vol. 12, pp. 139–143, Feb. 2016.

[96] C.-w. Cho, J. Lyu, L. An, T. Han, K. T. Lo, C. Y. Ng, J. Hu, Y. Gao, G. Li, M. Huang, N. Wang, J. Schmalian, and R. Lortz, "Nodal and nematic superconducting phases in NbSe2 monolayers from competing superconducting channels," *arXiv:2003.12467*, 2020.

[97] A. Hamill, B. Heischmidt, E. Sohn, D. Shaffer, K.-T. Tsai, X. Zhang, X. Xi, A. Suslov, H. Berger, L. Forró, F. J. Burnell, J. Shan, K. F. Mak, R. M. Fernandes, K. Wang, and V. S. Pribiag, "Two-fold symmetric superconductivity in few-layer $NbSe_2$," *Nature Physics*, vol. 17, pp. 949–954, Aug. 2021.

[98] C. Rubio-Verdú, A. M. García-García, H. Ryu, D.-J. Choi, J. Zaldívar, S. Tang, B. Fan, Z.-X. Shen, S.-K. Mo, J. I. Pascual, and M. M. Ugeda, "Visualization of Multifractal Superconductivity in a Two-Dimensional Transition Metal Dichalcogenide in the Weak-Disorder Regime," *Nano Letters*, vol. 20, pp. 5111–5118, July 2020.

[99] W. Wan, P. Dreher, D. Muñoz-Segovia, R. Harsh, H. Guo, A. J. Martínez-Galera, F. Guinea, F. de Juan, and M. M. Ugeda, "Observation of Superconducting Collective Modes from Competing Pairing Instabilities in Single-Layer $NbSe_2$," *Advanced Materials*, p. 2206078, 2022.

[100] J. Alicea, "New directions in the pursuit of Majorana fermions in solid state systems," *Reports on Progress in Physics*, vol. 75, p. 076501, June 2012. Publisher: IOP Publishing.

[101] M. Sato and Y. Ando, "Topological superconductors: a review," *Reports on Progress in Physics*, vol. 80, p. 076501, May 2017. Publisher: IOP Publishing.

[102] K. Flensberg, F. von Oppen, and A. Stern, "Engineered platforms for topological superconductivity and Majorana zero modes," *Nature Reviews Materials*, vol. 6, pp. 944–958, Oct. 2021.

[103] A. Y. Kitaev, "Unpaired Majorana fermions in quantum wires," *Physics-Uspekhi*, vol. 44, pp. 131–136, Oct. 2001.

[104] B. Jäck, Y. Xie, and A. Yazdani, "Detecting and distinguishing Majorana zero modes with the scanning tunnelling microscope," *Nature Reviews Physics*, vol. 3, pp. 541–554, Aug. 2021.

[105] G. C. Ménard, S. Guissart, C. Brun, R. T. Leriche, M. Trif, F. Debontridder, D. Demaille, D. Roditchev, P. Simon, and T. Cren, "Two-dimensional topological superconductivity in Pb/Co/Si(111)," *Nature Communications*, vol. 8, p. 2040, Dec. 2017.

[106] A. Palacio-Morales, E. Mascot, S. Cocklin, H. Kim, S. Rachel, D. K. Morr, and R. Wiesendanger, "Atomic-scale interface engineering of Majorana edge modes in a 2D magnet-superconductor hybrid system," *Science Advances*, vol. 5, no. 7, p. eaav6600, 2019. _eprint: https://www.science.org/doi/pdf/10.1126/sciadv.aav6600.

[107] B. Huang, G. Clark, E. Navarro-Moratalla, D. R. Klein, R. Cheng, K. L. Seyler, D. Zhong, E. Schmidgall, M. A. McGuire, D. H. Cobden, W. Yao, D. Xiao, P. Jarillo-Herrero, and X. Xu, "Layer-dependent ferromagnetism in a van der Waals crystal down to the monolayer limit," *Nature*, vol. 546, pp. 270–273, June 2017.

[108] S. Kezilebieke, M. N. Huda, V. Vaňo, M. Aapro, S. C. Ganguli, O. J. Silveira, S. Głodzik, A. S. Foster, T. Ojanen, and P. Liljeroth, "Topological superconductivity in a van der Waals heterostructure," *Nature*, vol. 588, pp. 424–428, Dec. 2020.

[109] J. V. Barth, "Molecular Architectonic on Metal Surfaces," *Annual Review of Physical Chemistry*, vol. 58, pp. 375–407, May 2007. Publisher: Annual Reviews.

[110] K. J. Franke, G. Schulze, and J. I. Pascual, "Competition of Superconducting Phenomena and Kondo Screening at the Nanoscale," *Science*, vol. 332, pp. 940–944, May 2011.

[111] A. García Corral, D. M. T. van Zanten, K. J. Franke, H. Courtois, S. Florens, and C. B. Winkelmann, "Magnetic-field-induced transition in a quantum dot coupled to a superconductor," *Phys. Rev. Research*, vol. 2, p. 012065, Mar. 2020. Publisher: American Physical Society.

[112] L. Farinacci, G. Ahmadi, G. Reecht, M. Ruby, N. Bogdanoff, O. Peters, B. W. Heinrich, F. von Oppen, and K. J. Franke, "Tuning the Coupling of an Individual Magnetic Impurity to a Superconductor: Quantum Phase Transition and Transport," *Phys. Rev. Lett.*, vol. 121, p. 196803, Nov. 2018. Publisher: American Physical Society.

[113] M. Ruby, Y. Peng, F. von Oppen, B. W. Heinrich, and K. J. Franke, "Orbital Picture of Yu-Shiba-Rusinov Multiplets," *Phys. Rev. Lett.*, vol. 117, p. 186801, Oct. 2016. Publisher: American Physical Society.

[114] D.-J. Choi, C. Rubio-Verdú, J. de Bruijckere, M. M. Ugeda, N. Lorente, and J. I. Pascual, "Mapping the orbital structure of impurity bound states in a superconductor," *Nature Communications*, vol. 8, p. 15175, Aug. 2017.

[115] J. Homberg, A. Weismann, R. Berndt, and M. Gruber, "Inducing and Controlling Molecular Magnetism through Supramolecular Manipulation," *ACS Nano*, vol. 14, pp. 17387–17395, Dec. 2020. Publisher: American Chemical Society.

[116] S. Lu, H. Nam, P. Xiao, M. Liu, Y. Guo, Y. Bai, Z. Cheng, J. Deng, Y. Li, H. Zhou, G. Henkelman, G. A. Fiete, H.-J. Gao, A. H. MacDonald, C. Zhang, and C.-K. Shih, "PTCDA Molecular Monolayer on Pb Thin Films: An Unusual π-Electron Kondo System and Its Interplay with a Quantum-Confined Superconductor," *Phys. Rev. Lett.*, vol. 127, p. 186805, Oct. 2021. Publisher: American Physical Society.

[117] L. Malavolti, M. Briganti, M. Hänze, G. Serrano, I. Cimatti, G. McMurtrie, E. Otero, P. Ohresser, F. Totti, M. Mannini, R. Sessoli, and S. Loth, "Tunable Spin–Superconductor Coupling of Spin 1/2 Vanadyl Phthalocyanine Molecules," *Nano Letters*, vol. 18, pp. 7955–7961, Dec. 2018. Publisher: American Chemical Society.

[118] M. Ruby, B. W. Heinrich, Y. Peng, F. von Oppen, and K. J. Franke, "Wave-Function Hybridization in Yu-Shiba-Rusinov Dimers," *Phys. Rev. Lett.*, vol. 120, p. 156803, Apr. 2018. Publisher: American Physical Society.

[119] Nadj-Perge Stevan, Drozdov Ilya K., Li Jian, Chen Hua, Jeon Sangjun, Seo Jungpil, MacDonald Allan H., Bernevig B. Andrei, and Yazdani Ali, "Observation of Majorana fermions in ferromagnetic atomic chains on a superconductor," *Science*, vol. 346, pp. 602–607, Oct. 2014. Publisher: American Association for the Advancement of Science.

[120] L. Schneider, P. Beck, T. Posske, D. Crawford, E. Mascot, S. Rachel, R. Wiesendanger, and J. Wiebe, "Topological Shiba bands in artificial spin chains on superconductors," *Nature Physics*, vol. 17, pp. 943–948, Aug. 2021.

[121] Kim Howon, Palacio-Morales Alexandra, Posske Thore, Rózsa Levente, Palotás Krisztián, Szunyogh László, Thorwart Michael, and Wiesendanger Roland, "Toward tailoring Majorana bound states in artificially constructed magnetic atom chains on elemental superconductors," *Science Advances*, vol. 4, p. eaar5251, May 2018. Publisher: American Association for the Advancement of Science.

[122] L. Schneider, S. Brinker, M. Steinbrecher, J. Hermenau, T. Posske, M. dos Santos Dias, S. Lounis, R. Wiesendanger, and J. Wiebe, "Controlling in-gap end states by linking nonmagnetic atoms and artificially-constructed spin chains on superconductors," *Nature Communications*, vol. 11, p. 4707, Sept. 2020.

[123] S. Kezilebieke, M. Dvorak, T. Ojanen, and P. Liljeroth, "Coupled Yu–Shiba–Rusinov States in Molecular Dimers on $NbSe_2$," *Nano Letters*, vol. 18, pp. 2311–2315, Apr. 2018. Publisher: American Chemical Society.

[124] P. Dreher, W. Wan, A. Chikina, M. Bianchi, H. Guo, R. Harsh, S. Mañas-Valero, E. Coronado, A. J. Martínez-Galera, P. Hofmann, J. A. Miwa, and M. M. Ugeda, "Proximity Effects on the Charge Density Wave Order and Superconductivity in Single-Layer $NbSe_2$," *ACS Nano*, vol. 15, pp. 19430–19438, Dec. 2021.

[125] M. M. Ugeda, A. J. Bradley, Y. Zhang, S. Onishi, Y. Chen, W. Ruan, C. Ojeda-Aristizabal, H. Ryu, M. T. Edmonds, H.-Z. Tsai, A. Riss, S.-K. Mo, D. Lee, A. Zettl, Z. Hussain, Z.-X. Shen, and M. F. Crommie, "Characterization of collective ground states in single-layer $NbSe_2$," *Nature Physics*, vol. 12, pp. 92–97, Jan. 2016. https://doi.org/10.1038/nphys3527.

[126] A. Sanna, C. Pellegrini, E. Liebhaber, K. Rossnagel, K. J. Franke, and E. K. U. Gross, "Real-space anisotropy of the superconducting gap in the charge-density wave material 2H-$NbSe_2$," *npj Quantum Materials*, vol. 7, p. 6, Jan. 2022.

[127] L. Huder, *Link between structural and electronic properties of moirés of graphene studied by scanning tunneling microscopy*. Theses, Université Grenoble Alpes, Nov. 2017. Issue: 2017GREAY083.

[128] G. R. Yazdi, T. Iakimov, and R. Yakimova, "Epitaxial Graphene on SiC: A Review of Growth and Characterization," *Crystals*, vol. 6, no. 5, 2016.

[129] T. Straub, T. Finteis, R. Claessen, P. Steiner, S. Hüfner, P. Blaha, C. S. Oglesby, and E. Bucher, "Charge-Density-Wave Mechanism in $2H$-$NbSe_2$: Photoemission Results," *Phys. Rev. Lett.*, vol. 82, pp. 4504–4507, May 1999. Publisher: American Physical Society.

[130] D. W. Shen, Y. Zhang, L. X. Yang, J. Wei, H. W. Ou, J. K. Dong, B. P. Xie, C. He, J. F. Zhao, B. Zhou, M. Arita, K. Shimada, H. Namatame, M. Taniguchi, J. Shi, and D. L. Feng, "Primary Role of the Barely Occupied States in the Charge Density Wave Formation of $NbSe_2$," *Phys. Rev. Lett.*, vol. 101, p. 226406, Nov. 2008. Publisher: American Physical Society.

[131] S. V. Borisenko, A. A. Kordyuk, V. B. Zabolotnyy, D. S. Inosov, D. Evtushinsky, B. Büchner, A. N. Yaresko, A. Varykhalov, R. Follath, W. Eberhardt, L. Patthey, and H. Berger, "Two Energy Gaps and Fermi-Surface "Arcs" in $NbSe_2$," *Phys. Rev. Lett.*, vol. 102, p. 166402, Apr. 2009. Publisher: American Physical Society.

[132] T. M. Rice and G. K. Scott, "New Mechanism for a Charge-Density-Wave Instability," *Phys. Rev. Lett.*, vol. 35, pp. 120–123, July 1975. Publisher: American Physical Society.

[133] C. M. Varma and A. L. Simons, "Strong-Coupling Theory of Charge-Density-Wave Transitions," *Phys. Rev. Lett.*, vol. 51, pp. 138–141, July 1983. Publisher: American Physical Society.

[134] T. Valla, A. V. Fedorov, P. D. Johnson, P.-A. Glans, C. McGuinness, K. E. Smith, E. Y. Andrei, and H. Berger, "Quasiparticle Spectra, Charge-Density Waves, Superconductivity, and Electron-Phonon Coupling in 2H-$NbSe_2$," *Phys. Rev. Lett.*, vol. 92, p. 086401, Feb. 2004. Publisher: American Physical Society.

[135] F. Weber, S. Rosenkranz, J.-P. Castellan, R. Osborn, R. Hott, R. Heid, K.-P. Bohnen, T. Egami, A. H. Said, and D. Reznik, "Extended Phonon Collapse and the Origin of the Charge-Density Wave in 2H-$NbSe_2$," *Phys. Rev. Lett.*, vol. 107, p. 107403, Sept. 2011. Publisher: American Physical Society.

[136] D. J. Rahn, S. Hellmann, M. Kalläne, C. Sohrt, T. K. Kim, L. Kipp, and K. Rossnagel, "Gaps and kinks in the electronic structure of the superconductor 2H-$NbSe_2$ from angle-resolved photoemission at 1 K," *Phys. Rev. B*, vol. 85, p. 224532, June 2012. Publisher: American Physical Society.

[137] Soumyanarayanan Anjan, Yee Michael M., He Yang, van Wezel Jasper, Rahn Dirk J., Rossnagel Kai, Hudson E. W., Norman Michael R., and Hoffman Jennifer E., "Quantum phase transition from triangular to stripe charge order in $NbSe_2$," *Proceedings of the National Academy of Sciences*, vol. 110, pp. 1623–1627, Jan. 2013. Publisher: Proceedings of the National Academy of Sciences.

[138] C. J. Arguello, E. P. Rosenthal, E. F. Andrade, W. Jin, P. C. Yeh, N. Zaki, S. Jia, R. J. Cava, R. M. Fernandes, A. J. Millis, T. Valla, R. M. Osgood, and A. N. Pasupathy, "Quasiparticle Interference, Quasiparticle Interactions, and the Origin of the Charge Density Wave in 2H-$NbSe_2$," *Phys. Rev. Lett.*, vol. 114, p. 037001, Jan. 2015. Publisher: American Physical Society.

[139] B. Guster, C. Rubio-Verdú, R. Robles, J. Zaldívar, P. Dreher, M. Pruneda, J. n. Silva-Guillén, D.-J. Choi, J. I. Pascual, M. M. Ugeda, P. Ordejón, and E. Canadell, "Coexistence of Elastic Modulations in the Charge Density Wave State of 2*H*-$NbSe_2$," *Nano Letters*, vol. 19, pp. 3027–3032, May 2019. Reprinted adapted with permission from American Chemical Society.

[140] J. n. Silva-Guillén, P. Ordejón, F. Guinea, and E. Canadell, "Electronic structure of 2*H*-$NbSe_2$ single-layers in the CDW state," *2D Materials*, vol. 3, p. 035028, Sept. 2016. Publisher: IOP Publishing.

[141] F. Zheng, Z. Zhou, X. Liu, and J. Feng, "First-principles study of charge and magnetic ordering in monolayer 2H-$NbSe_2$," *Phys. Rev. B*, vol. 97, p. 081101, Feb. 2018. Publisher: American Physical Society.

[142] C.-S. Lian, C. Si, and W. Duan, "Unveiling Charge-Density Wave, Superconductivity, and Their Competitive Nature in Two-Dimensional $NbSe_2$," *Nano Letters*, vol. 18, pp. 2924–2929, May 2018. Publisher: American Chemical Society.

[143] H. le Sueur, P. Joyez, H. Pothier, C. Urbina, and D. Esteve, "Phase Controlled Superconducting Proximity Effect Probed by Tunneling Spectroscopy," *Phys. Rev. Lett.*, vol. 100, p. 197002, May 2008. Publisher: American Physical Society. https://doi.org/10.1103/PhysRevLett.100.197002.

[144] F. D. Natterer, J. Ha, H. Baek, D. Zhang, W. G. Cullen, N. B. Zhitenev, Y. Kuk, and J. A. Stroscio, "Scanning tunneling spectroscopy of proximity superconductivity in epitaxial multilayer graphene," *Phys. Rev. B*, vol. 93, p. 045406, Jan. 2016. Publisher: American Physical Society
https://doi.org/10.1103/PhysRevB.93.045406.

[145] Y. Oda and H. Nagano, "Meissner effect in Cu of thick Cu clad Nb," *Solid State Communications*, vol. 35, no. 8, pp. 631–634, 1980.

[146] W. L. McMillan, "Tunneling Model of the Superconducting Proximity Effect," *Phys. Rev.*, vol. 175, pp. 537–542, Nov. 1968. Publisher: American Physical Society.

[147] H. Courtois, P. Gandit, and B. Pannetier, "Proximity-induced superconductivity in a narrow metallic wire," *Phys. Rev. B*, vol. 52, pp. 1162–1166, July 1995. Publisher: American Physical Society.

[148] B. Pannetier and H. Courtois, "Andreev Reflection and Proximity effect," *Journal of Low Temperature Physics*, vol. 118, pp. 599–615, Mar. 2000.

[149] K. D. Usadel, "Generalized Diffusion Equation for Superconducting Alloys," *Phys. Rev. Lett.*, vol. 25, pp. 507–509, Aug. 1970. Publisher: American Physical Society.

[150] H. B. Heersche, P. Jarillo-Herrero, J. B. Oostinga, L. M. K. Vandersypen, and A. F. Morpurgo, "Bipolar supercurrent in graphene," *Nature*, vol. 446, pp. 56–59, Mar. 2007.

[151] X. Du, I. Skachko, and E. Y. Andrei, "Josephson current and multiple Andreev reflections in graphene SNS junctions," *Phys. Rev. B*, vol. 77, p. 184507, May 2008. Publisher: American Physical Society.

[152] E. Cortés-del Río, J. L. Lado, V. Cherkez, P. Mallet, J.-Y. Veuillen, J. C. Cuevas, J. M. Gómez-Rodríguez, J. Fernández-Rossier, and I. Brihuega, "Observation of Yu–Shiba–Rusinov States in Superconducting Graphene," *Advanced Materials*, vol. 33, p. 2008113, June 2021. Publisher: John Wiley & Sons, Ltd.

[153] F. Varchon, P. Mallet, J.-Y. Veuillen, and L. Magaud, "Ripples in epitaxial graphene on the Si-terminated SiC(0001) surface," *Phys. Rev. B*, vol. 77, p. 235412, June 2008. Publisher: American Physical Society.

[154] Y. Baskin and L. Meyer, "Lattice Constants of Graphite at Low Temperatures," *Phys. Rev.*, vol. 100, pp. 544–544, Oct. 1955. Publisher: American Physical Society.

[155] A. H. Castro Neto, F. Guinea, N. M. R. Peres, K. S. Novoselov, and A. K. Geim, "The electronic properties of graphene," *Rev. Mod. Phys.*, vol. 81, pp. 109–162, Jan. 2009. Publisher: American Physical Society
https://doi.org/10.1103/RevModPhys.81.109.

[156] P. Mallet, F. Varchon, C. Naud, L. Magaud, C. Berger, and J.-Y. Veuillen, "Electron states of mono- and bilayer graphene on SiC probed by scanning-tunneling microscopy," *Phys. Rev. B*, vol. 76, p. 041403, July 2007. Publisher: American Physical Society.

[157] V. W. Brar, Y. Zhang, Y. Yayon, T. Ohta, J. L. McChesney, A. Bostwick, E. Rotenberg, K. Horn, and M. F. Crommie, "Scanning tunneling spectroscopy of inhomogeneous electronic structure in monolayer and bilayer graphene on SiC," *Applied Physics Letters*, vol. 91, p. 122102, Sept. 2007. Publisher: American Institute of Physics. Reprinted with the permission of AIP Publishing.

[158] A. Rajan, K. Underwood, F. Mazzola, and P. D. C. King, "Morphology control of epitaxial monolayer transition metal dichalcogenides," *Phys. Rev. Materials*, vol. 4, p. 014003, Jan. 2020. Publisher: American Physical Society.

[159] Y. Nakata, K. Sugawara, R. Shimizu, Y. Okada, P. Han, T. Hitosugi, K. Ueno, T. Sato, and T. Takahashi, "Monolayer 1*T*-$NbSe_2$ as a Mott insulator," *NPG Asia Materials*, vol. 8, pp. e321–e321, Nov. 2016.

[160] Q. Wang, W. Zhang, L. Wang, K. He, X. Ma, and Q. Xue, "Large-scale uniform bilayer graphene prepared by vacuum graphitization of 6H-SiC(0001) substrates," *Journal of Physics: Condensed Matter*, vol. 25, p. 095002, Jan. 2013. Publisher: IOP Publishing.

[161] Y. Zhang, V. W. Brar, F. Wang, C. Girit, Y. Yayon, M. Panlasigui, A. Zettl, and M. F. Crommie, "Giant phonon-induced conductance in scanning tunnelling spectroscopy of gate-tunable graphene," *Nature Physics*, vol. 4, pp. 627–630, Aug. 2008.

[162] P. Mallet, I. Brihuega, S. Bose, M. M. Ugeda, J. M. Gómez-Rodríguez, K. Kern, and J. Y. Veuillen, "Role of pseudospin in quasiparticle interferences in epitaxial graphene probed by high-resolution scanning tunneling microscopy," *Phys. Rev. B*, vol. 86, p. 045444, Jul 2012.

[163] P. Lauffer, K. V. Emtsev, R. Graupner, T. Seyller, L. Ley, S. A. Reshanov, and H. B. Weber, "Atomic and electronic structure of few-layer graphene on SiC(0001) studied with scanning tunneling microscopy and spectroscopy," *Phys. Rev. B*, vol. 77, p. 155426, Apr. 2008. Publisher: American Physical Society.

[164] P. Lauffer, K. V. Emtsev, R. Graupner, T. Seyller, and L. Ley, "Molecular and electronic structure of PTCDA on bilayer graphene on SiC(0001) studied with scanning tunneling microscopy," *physica status solidi (b)*, vol. 245, pp. 2064–2067, Oct. 2008. Publisher: John Wiley & Sons, Ltd.

[165] G. M. Rutter, J. N. Crain, N. P. Guisinger, T. Li, P. N. First, and J. A. Stroscio, "Scattering and Interference in Epitaxial Graphene," *Science*, vol. 317, no. 5835, pp. 219–222, 2007.

[166] R. C. Dynes, V. Narayanamurti, and J. P. Garno, "Direct Measurement of Quasiparticle-Lifetime Broadening in a Strong-Coupled Superconductor," *Physical Review Letters*, vol. 41, pp. 1509–1512, Nov. 1978.

[167] S. Samaddar, I. Yudhistira, S. Adam, H. Courtois, and C. B. Winkelmann, "Charge Puddles in Graphene near the Dirac Point," *Phys. Rev. Lett.*, vol. 116, p. 126804, Mar. 2016. Publisher: American Physical Society.

[168] L. Veyrat, C. Déprez, A. Coissard, X. Li, F. Gay, K. Watanabe, T. Taniguchi, Z. Han, B. A. Piot, H. Sellier, and B. Sacépé, "Helical quantum Hall phase in graphene on $SrTiO_3$," *Science*, vol. 367, pp. 781–786, 2020.

[169] A. Coissard, D. Wander, H. Vignaud, A. G. Grushin, C. Repellin, K. Watanabe, T. Taniguchi, F. Gay, C. B. Winkelmann, H. Courtois, H. Sellier, and B. Sacépé, "Imaging tunable quantum Hall broken-symmetry orders in graphene," *Nature*, vol. 605, pp. 51–56, May 2022.

[170] K. S. Novoselov, D. Jiang, F. Schedin, T. J. Booth, V. V. Khotkevich, S. V. Morozov, and A. K. Geim, "Two-dimensional atomic crystals," *Proceedings of the National Academy of Sciences of the United States of America*, vol. 102, p. 10451, July 2005.

[171] K. Novoselov, A. Geim, S. Morozov, D. Jiang, M. Katsnelson, I. Grigorieva, S. Dubonos, and A. Firsov, "Two-dimensional gas of massless Dirac fermions in graphene," *Nature*, vol. 438, pp. 197–200, 2005.

[172] K. Nomura and A. H. MacDonald, "Quantum Hall Ferromagnetism in Graphene," *Phys. Rev. Lett.*, vol. 96, p. 256602, 2006.

[173] J. Alicea and M. P. A. Fisher, "Graphene integer quantum Hall effect in the ferromagnetic and paramagnetic regimes," *Phys. Rev. B*, vol. 74, p. 075422, Aug. 2006.

[174] A. Coissard, *The many-body ground states of the graphene quantum Hall effect and their edge channels*. PhD thesis, Université Grenoble Alpes, Grenoble, Nov. 2021.

[175] M. O. Goerbig, "Electronic Properties of Graphene in a Strong Magnetic Field," *Reviews of Modern Physics*, vol. 83, pp. 1193–1243, Nov. 2011. arXiv: 1004.3396.

[176] M. Kharitonov, "Phase diagram for the $\nu = 0$ quantum Hall state in monolayer graphene," *Phys. Rev. B*, vol. 85, p. 155439, 2012. https://doi.org/10.1103/PhysRevB.85.155439.

[177] A. F. Young, J. D. Sanchez-Yamagishi, B. Hunt, S. H. Choi, K. Watanabe, T. Taniguchi, R. C. Ashoori, and P. Jarillo-Herrero, "Tunable symmetry breaking and helical edge transport in a graphene quantum spin Hall state," *Nature*, vol. 505, pp. 528–532, 2014.

[178] D. A. Abanin, P. A. Lee, and L. S. Levitov, "Spin-Filtered Edge States and Quantum Hall Effect in Graphene," *Phys. Rev. Lett.*, vol. 96, p. 176803, 2006.

[179] D. A. Abanin, P. A. Lee, and L. S. Levitov, "Charge and spin transport at the quantum Hall edge of graphene," *Solid State Communications*, vol. 143, no. 1, pp. 77–85, 2007.

[180] M. Kharitonov, "Edge excitations of the canted antiferromagnetic phase of the $\nu = 0$ quantum Hall state in graphene: A simplified analysis," *Phys. Rev. B*, vol. 86, p. 075450, 2012.

[181] A. Knothe and T. Jolicoeur, "Edge structure of graphene monolayers in the $\nu = 0$ quantum Hall state," *Phys. Rev. B*, vol. 92, p. 165110, 2015.

[182] A. Aharon-Steinberg, A. Marguerite, D. J. Perello, K. Bagani, T. Holder, Y. Myasoedov, L. S. Levitov, A. K. Geim, and E. Zeldov, "Long-range nontopological edge currents in charge-neutral graphene," *Nature*, vol. 593, pp. 528–534, May 2021.

[183] C. R. Dean, A. F. Young, I. Meric, C. Lee, L. Wang, S. Sorgenfrei, K. Watanabe, T. Taniguchi, P. Kim, K. L. Shepard, and J. Hone, "Boron nitride substrates for high-quality graphene electronics," *Nature Nanotechnology*, vol. 5, pp. 722–726, Oct. 2010.

[184] L. Wang, I. Meric, P. Y. Huang, Q. Gao, Y. Gao, H. Tran, T. Taniguchi, K. Watanabe, L. M. Campos, D. A. Muller, J. Guo, P. Kim, J. Hone, K. L. Shepard, and C. R. Dean, "One-Dimensional Electrical Contact to a Two-Dimensional Material," *Science*, vol. 342, pp. 614–617, 2013.

[185] K. Zimmermann, *Quantum point contact in high mobility graphene*. Theses, Université Grenoble Alpes, June 2016. Issue: 2016GREAY008.

[186] N. J. G. Couto, B. Sacépé, and A. F. Morpurgo, "Transport through Graphene on $SrTiO_3$," *Phys. Rev. Lett.*, vol. 107, p. 225501, Nov. 2011. Publisher: American Physical Society.

[187] S. Jung, G. M. Rutter, N. N. Klimov, D. B. Newell, I. Calizo, A. R. Hight-Walker, N. B. Zhitenev, and J. A. Stroscio, "Evolution of microscopic localization in graphene in a magnetic field from scattering resonances to quantum dots," *Nature Physics*, vol. 7, no. 3, pp. 245–251, 2011.

[188] C. Gutiérrez, D. Walkup, F. Ghahari, C. Lewandowski, J. F. Rodriguez-Nieva, K. Watanabe, T. Taniguchi, L. S. Levitov, N. B. Zhitenev, and J. A. Stroscio, "Interaction-driven quantum Hall wedding cake-like structures in graphene quantum dots," *Science*, vol. 361, pp. 789–794, 2018.

[189] D. E. Grupp and A. M. Goldman, "Giant Piezoelectric Effect in Strontium Titanate at Cryogenic Temperatures," *Science*, vol. 276, pp. 392–394, 1997.

[190] Z. F. Ezawa, *Quantum Hall Effects*. World Scientific Publishing, 2013.

[191] D. S. Wei, T. van der Sar, S. H. Lee, K. Watanabe, T. Taniguchi, B. I. Halperin, and A. Yacoby, "Electrical generation and detection of spin waves in a quantum Hall ferromagnet," *Science*, vol. 362, pp. 229–233, 2018.

[192] P. Stepanov, S. Che, D. Shcherbakov, J. Yang, R. Chen, K. Thilahar, G. Voigt, M. W. Bockrath, D. Smirnov, K. Watanabe, T. Taniguchi, R. K. Lake, Y. Barlas, A. H. MacDonald, and C. Ning Lau, "Long-distance spin transport through a graphene quantum Hall antiferromagnet," *Nature Physics*, vol. 14, pp. 907–911, 2018.

[193] A. Assouline, M. Jo, P. Brasseur, K. Watanabe, T. Taniguchi, T. Jolicoeur, P. Roche, D. C. Glattli, N. Kumada, F. D. Parmentier, and P. Roulleau, "Unveiling excitonic properties of magnons in a quantum Hall ferromagnet," 2021. Published: *arXiv*:2102.02068.

[194] X. Liu, G. Farahi, C.-L. Chiu, Z. Papic, K. Watanabe, T. Taniguchi, M. P. Zaletel, and A. Yazdani, "Visualizing broken symmetry and topological defects in a quantum Hall ferromagnet," *Science*, vol. 375, no. 6578, pp. 321–326, 2022. _eprint: https://www.science.org/doi/pdf/10.1126/science.abm3770.

[195] S.-Y. Li, Y. Zhang, L.-J. Yin, and L. He, "Scanning tunneling microscope study of quantum Hall isospin ferromagnetic states in the zero Landau level in a graphene monolayer," *Phys. Rev. B*, vol. 100, p. 085437, 2019.

[196] J. Motruk, A. G. Grushin, F. de Juan, and F. Pollmann, "Interaction-driven phases in the half-filled honeycomb lattice: An infinite density matrix renormalization group study," *Phys. Rev. B*, vol. 92, p. 085147, 2015.

[197] S. Capponi and A. M. Läuchli, "Phase diagram of interacting spinless fermions on the honeycomb lattice: A comprehensive exact diagonalization study," *Phys. Rev. B*, vol. 92, p. 085146, 2015.

[198] M. Yankowitz, J. Xue, D. Cormode, J. D. Sanchez-Yamagishi, K. Watanabe, T. Taniguchi, P. Jarillo-Herrero, P. Jacquod, and B. J. LeRoy, "Emergence of superlattice Dirac points in graphene on hexagonal boron nitride," *Nature Physics*, vol. 8, pp. 382–386, May 2012.

[199] Y. Cao, V. Fatemi, A. Demir, S. Fang, S. L. Tomarken, J. Y. Luo, J. D. Sanchez-Yamagishi, K. Watanabe, T. Taniguchi, E. Kaxiras, R. C. Ashoori, and P. Jarillo-Herrero, "Correlated insulator behaviour at half-filling in magic-angle graphene superlattices," *Nature*, vol. 556, pp. 80–84, 2018.

[200] Y. Cao, V. Fatemi, S. Fang, K. Watanabe, T. Taniguchi, E. Kaxiras, and P. Jarillo-Herrero, "Unconventional superconductivity in magic-angle graphene superlattices," *Nature*, vol. 556, pp. 43–50, 2018.

[201] U. Zondiner, A. Rozen, D. Rodan-Legrain, Y. Cao, R. Queiroz, T. Taniguchi, K. Watanabe, Y. Oreg, F. von Oppen, A. Stern, E. Berg, P. Jarillo-Herrero, and S. Ilani, "Cascade of phase transitions and Dirac revivals in magic-angle graphene," *Nature*, vol. 582, pp. 203–208, 2020.

[202] S. Takei, A. Yacobi, B. I. Halperin, and Y. Tserkovnyak, "Spin Superfluidity in the $\nu = 0$ Quantum Hall State of Graphene," *Phys. Rev. Lett.*, vol. 116, p. 216801, 2016.

[203] A. Das, R. K. Kaul, and G. Murthy, "Coexistence of Canted Antiferromagnetism and Bond Order in $\nu = 0$ Graphene," *Phys. Rev. Lett.*, vol. 128, p. 106803, Mar. 2022. Publisher: American Physical Society.

[204] P. Taborek and L. J. Senator, "Helium on graphite: Low-temperature desorption kinetics and sticking coefficient," *Phys. Rev. Lett.*, vol. 56, pp. 628–631, Feb. 1986. Publisher: American Physical Society.

[205] C. Kohrt and R. Gomer, "Adsorption of CO on the (110) plane of tungsten; temperature dependence of the sticking coefficient and absolute surface coverages," *Surface Science*, vol. 40, no. 1, pp. 71–84, 1973.